

Response to the reviewer comments on the revised version 15.02.2017

Dear Dr. Stenke,

we have revised the manuscript according to your and the reviewer comments. Please find our detailed responses below. We hope that the manuscript now fulfills all requirements and can be published.

Thank you very much,

Katja Matthes and Bernd Funke (on behalf of all co-authors)

Comments by the editor from December 20th 2016:

Dear Katja Matthes,

your efforts in revising your manuscript according to the referees' comments are very much appreciated. I agree with the referee that the manuscript has clearly improved compared to the previous version. However, there are still some open questions that need clarification before the paper can be finally accepted. Attached I am sending you the referee's comments on the revised version.

Furthermore, I would like to ask you for clarification of the following point: At a project meeting last week there was a talk on solar irradiance observations and data sets. In the presentation it was mentioned that the CMIP6 solar forcing data set is not exactly the mean of the NRLSSI2 and SATIRE data sets as stated in your manuscript, but that somehow modified data sets had been used for the CMIP6 solar forcing data. Could you please comment on this? In case the cited NRLSSI2 and SATIRE data sets had indeed been modified for the CMIP6 input data, the applied modifications have to be documented in the paper. The description of the data sets should be sufficiently complete and precise to allow traceability of methods and results by other scientists.

Yes, it is correct that the NRL and SATIRE datasets in the CMIP6 solar forcing dataset are not identical with the published individual datasets by the two groups. The use of this for CMIP6 modified version of the datasets have been documented, but we have highlighted it even more in the manuscript (in the abstract, the data description section, and in the conclusions). We also added this to the netcdf headers of the published datasets to make sure that there is no confusion. We hope that this has now been sufficiently clarified.

Finally, the editors handling manuscripts on CMIP6 data sets have been asked to make sure that the data are uploaded to ESGF and that the DOIs are cited in the paper before final acceptance. I checked the solarisheppa website, but could not find a link to ESGF or DOIs of the data sets. Please make sure that these information are made available, also in the paper.

Meanwhile the data has been uploaded to ESGF (<https://pcmdi.llnl.gov/search/input4mips/>). This has been clarified in Section 7 (Data

Availability). Regarding DOIs, the infrastructure that will be issuing DOIs for the CMIP6 contributed data is currently still in development. It is hoped that DOIs will be come available soon.

Best regards,
Andrea Stenke

Referee's Report on the revised version

Many thanks to the authors for taking many of my numerous suggestions into account and for making substantial changes to the manuscript. It has improved considerably compared with the first version. Many parts of the manuscript, such as that on particle forcings, are well balanced, well written and a pleasure to read. I do not agree with some of the arguments/answers put forward by the authors, but am willing to let them pass in the interests of time. However, there are still two important issues to be clarified/dealt with before the manuscript can be published. There are also a few minor points that the authors may care to look at. Let me begin with the two major issues still present in the revised version of the manuscript.

1. Description of the SOLID composite and Fig. 3: The authors are to be lauded for substantially extending the description of the SOLID composite and for introducing a table describing which data sets have been used. They have now also given a reference to Haberreiter et al. (2017) in which a more detailed description is promised. This is a significant improvement over the first version of the manuscript. All the same, there are still a number of unanswered questions.

For example, the manuscript states that the significant deviations of the SOLID composite from the observations shown in Fig. 3 are explained by the existence of other datasets listed in Table 1, but not shown in Fig. 3. Coincidentally, these other, not shown, datasets almost exactly compensate the difference between the data that are plotted and CMIP6. If this is indeed the case, then the authors are to be congratulated, but from the brief description in the paper, it does not become clear how this happens. For instance, the disagreement between SOLID and SORCE/SIM in the 200-400 nm range is explained by averaging with SORCE/SOLSTICE. However, SORCE/SOLSTICE data are only available shortward of 309 nm (Table 1 in the manuscript), whereas much of the flux variability measured by SIM in the 200-400 nm range comes from the 309-400 nm domain not covered by SOLSTICE (see Fig. 1 from Haigh et al. 2010). According to the manuscript this flux should enter SOLID with weight 1 so that it remains unclear why SOLID is so different from the SIM data.

Likely this and other questions that I still have will be resolved by the more detailed description in the manuscript submitted to JGR by Haberreiter et al. (2017), which unfortunately is not accessible. I therefore ask the authors to make this paper available to me via the editor, to enable evaluating the strengths and weaknesses of this approach. The information likely provided there will hopefully quickly clarify the issues and questions I still have regarding the SOLID composite.

Thanks for asking for further clarification. We apologize that our previous answer was not complete. The datasets that are available for the 200-400nm spectral range are: NIMBUS7/SBUV (170-399nm), NOAA9/SBUV (170-399nm), NOAA11/SBUV2 (170-399nm), SME/UV (115-302.5nm), SORCE/SIM (240- 2412.3 nm), SORCE/SOLSITCE (115-309nm), UARS/SOLSTICE (115.5 - 410.5 nm) and UARS/SUSIM (115.5 - 410.5 nm). (Note that following the comment of a reviewer, NOAA16/SBUV2 has been taken out). Through the temporal extension of all these datasets, and their subsequent scale-wise

decomposition and recomposition these datasets all enter into the final SOLID composite and moderate the SIM data. So, up to 415 nm, the weight of SIM is smaller than 1. This explains why the SOLID composite is in good agreement with CMIP6. SIM data do get a weight of "1" if no other dataset is available.

We are happy to provide the manuscript for Haberreiter et al. (2017), which hopefully answers the other open questions.

2. Future scenarios: Section 3 has improved, but is still substantially weaker than most of the rest of the paper. It also remains misleading, maybe partly because the authors seem to have misunderstood my comments in the last report. I apologize if they were unclear. Let me try to be clearer this time. In spite of the "scenarios" in the title, large parts of Sect. 3 give a false sense that in effect some kind of prediction of future solar activity is being made. True, in the revised version "predict" has been replaced by "forecast" in a few places, but dictionaries (e.g., Collins English dictionary) use the two words synonymously (although they do have somewhat different meanings in meteorology). Also, in spite of these changes in name, a lot of trouble is taken (and quite some text has been added) to argue that the two provided time series are reliable forecasts and not just scenarios.

We agree with the reviewer that there was some confusion about the terminology of using "forecast" and "prediction". We have changed the text in section 3 significantly in order to avoid confusion. We provide a scenario for future solar activity, this terminology is perfectly in line with the IPCC terminology for greenhouse gas scenarios. For the scenario construction we use time series analysis, that are forecasts, in order to come up with a likely scenario under the assumption that past statistical behaviour of the Sun can be extrapolated into the future.

However, uncertainties in the adopted approach are likely strongly underestimated. For me the claimed ability to predict or forecast solar activity on longer timescales, although even the amplitude of the next cycle cannot be predicted reliably by dynamo models (or by other means except partly from the strength of the polar fields during the previous minimum), is an assumption, and not a statement of fact, as the current version purports it to be. Assumptions should be clearly identified as such to the reader. On the basis of this assumption and various purely statistical models the authors then "forecast" future solar activity, while the assumption itself remains completely untested in this paper and very poorly tested otherwise. E.g., given the many unknowns affecting the solar dynamo and consequently the very wide variety of dynamo models that have found their way into the recent literature, it may be questioned whether the predictions of any one current dynamo model will stand the test of time.

Even if this basic assumption of Sect. 3 were correct, it is unclear that any of the statistical methods used by the authors, or an ensemble of such methods, will be any good in predicting solar activity in 50, 100 or 300 years. I cannot find a reliable reason for the belief apparently held by the authors that purely statistical "more elaborate reconstruction schemes" will give the correct behavior a number of cycles down the line, while failing already at the next cycle.

The trouble with all the methods used by the authors is that they have not been tested on solar activity on the time scales of interest to the authors (and cannot be properly tested for 50, or 100 years, or even longer periods without waiting that length of time). Therefore, the value of all these extrapolations, be they called

“predictions” or “forecasts”, is fairly limited.

Take the argument that the Sun has just left a grand maximum and is now likely to stay at a low level of activity and consider the recent revision of the sunspot number. Until a new consensus is reached a number of different sunspot number data sets vie with each other, some of which do not even agree with the statement that the last 6-7 decades was a grand maximum. E.g., according to Svalgaard and Schatten (2016) there have been at 3 episodes since the Maunder minimum, when the activity was approximately as high as in the last 60-70 years. Therefore, the authors possibly have been extrapolating on the basis of wrong assumptions regarding past solar activity. Please note that I am not arguing that Svalgaard and Schatten are correct, but that currently even the sunspot number record is very much under debate, placing a big question mark behind some of the assumptions made here (which, yet again, are sold for a fact). Consequently, the uncertainties in the extrapolations made in the present paper are much larger than the authors acknowledge.

We would like to note here that our forecasts are based on Phi rather than SSN.

In summary, I am arguing that the “forecasts” or “scenarios” of future activity proposed here are reasonable-looking courses that future activity may possibly take, but they are not more probable than any number of other such scenarios. This is because we do not have reliable, i.e. thoroughly and successfully tested means of forecasting solar activity on the timescales of interest. To be clear, I am not arguing that the authors remove or change their time series (although they show only part of the possible range of solar activity in the upcoming decades, thus restricting the range of solar forcing in CMIP6 climate runs). Rather I am arguing that the authors acknowledge that these are 2 of many equally possible scenarios.

It is necessary to strongly tone down the claims that actual forecasts of activity are presented, removing the impression that the time series being provided are better than many other time series that could be proposed. Ideally, much of the introductory part of Sect. 3, as well as almost the entire Sect. 3.1 should be removed. This could become part of a separate paper in an appropriate journal. In such a paper the authors could provide more details, much more stringent tests etc. It could allow readers to estimate the reliability of the employed statistical methods when applied to solar data.

However, as this means a major rewrite of this section, I would be satisfied if the authors changed the text to reflect the fact that what they are proposing really are to some extent random scenarios and should not be taken as reliable forecasts or predictions.

We have updated the text along the lines you suggest. However, we would like to highlight that our scenarios are not just random (which would have made our task much easier). Nor are they predictions. They describe a likely scenario of solar activity.

Minor issues

1. page 2. lines 1-2: The manuscript still contains the confusing sentence about CMIP6 “statistically indistinguishable from available observations”. The answer to the referee explains what the authors mean by this. Such an explanation should also be added to the manuscript to avoid confusing readers

We removed this confusing sentence in the abstract and expanded that part to be more specific in the respective section where Fig. 1 is described.

2. page 3. lines 30-31. The sentence it is still not fully correct. Please note that

Usoskin et al. (2014) do not discuss TSI reconstruction. Possibly the authors mean reconstructions of solar activity?

We failed to correct this in the previous version by replacing TSI with solar activity, with our apologies.

3. SATIRE-TS has been converted everywhere to SATIRE, but SATIRE-TS is still mentioned in the legends of Figures 1, 2, 4, 6 (see previous report).

Thank you for pointing this out. This has now been corrected.

4. page 11, lines 25-28. "In both models, the historical reconstructions are sensitive to the assumptions made when constraining them to direct (satellite era) observations that suffer from large uncertainties. This mainly explains why these models differ before 1990 by an offset." Which assumptions are meant? Why do they lead to an offset? Please explain in the manuscript.

NRLTSI2 has been trained with TSI data from SORCE/TIM whereas SATIRE has mainly used the PMOD composite to assess its performance. This, by itself, may already explain why the two models behave differently before the 1990's. We cut out some text because this is not the main message we want to convey.

5. page 8. line 16. "a disk-integrated ratio of the core to the-wings of the Mg II emission line at 280 nm". This is not how the Mg II index is defined (a disk integrated ratio is not the same as the ratio of disk integrated quantities); see the paper by Viereck et al. (2001), cited in the same sentence of the revised manuscript. Please correct.

Thank you, we corrected this.

6. Figure 4 may be misleading to some readers, as the sum of the SSI variability of the various models does not seem to be the same (and hence cannot all be equal to the TSI variability). This is likely because the IR is missing. I would propose to (ideally) add the IR band to the figure (as done by Ermolli et al. 2013, although a larger wavelength coverage would be better), or to at least point this out in the text.

We added the following sentence to the description of Fig. 4 to avoid confusion: "Please note that the sum of the SSI variability of the various models is not equal to the TSI variability since the IR part is missing in Fig. 4."

Solar Forcing for CMIP6 (v3.2)

Katja Matthes^{1,2}, Bernd Funke³, Monika E. Andersson¹⁸, Luke Barnard⁴, Jürg Beer⁵, Paul Charbonneau⁶, Mark A. Clilverd⁷, Thierry Dudok de Wit⁸, Margit Haberreiter⁹, Aaron Hendry¹⁴, Charles H. Jackman¹⁰, Matthieu Kretzschmar⁸, Tim Kruschke¹, Markus Kunze¹¹, Ulrike Langematz¹¹, Daniel R. Marsh¹⁹, Amanda C. Maycock¹², Stergios Misios¹³, Craig J. Rodger¹⁴, Adam A. Scaife¹⁵, Annika Seppälä¹⁸, Ming Shangguan¹, Miriam Sinnhuber¹⁶, Kleareti Tourpali¹³, Ilya Usoskin¹⁷, Max van de Kamp¹⁸, Pekka T. Verronen¹⁸, and Stefan Versick¹⁶

¹GEOMAR Helmholtz Centre for Ocean Research Kiel, Kiel, Germany

²Christian-Albrechts Universität zu Kiel, Kiel, Germany

³Instituto de Astrofísica de Andalucía (CSIC), Granada, Spain

⁴University of Reading, Reading, United Kingdom

⁵EAWAG, Dübendorf, Switzerland

⁶University of Montreal, Canada

⁷British Antarctic Survey (NERC), Cambridge, UK

⁸LPC2E, CNRS and University of Orléans, France

⁹Physikalisch-Meteorologisches Observatorium Davos/World Radiation Center, Davos, Switzerland

¹⁰Emeritus, NASA Goddard Space Flight Center, Greenbelt, MD, U.S.A.

¹¹Freie Universität Berlin, Berlin, Germany

¹²University of Leeds, Leeds, UK

¹³Laboratory of Atmospheric Physics, Aristotle University of Thessaloniki, Thessaloniki, Greece

¹⁴Department of Physics, University of Otago, Dunedin, New Zealand

¹⁵Met Office Hadley Centre, Fitz Roy Road, Exeter, Devon, UK

¹⁶Karlsruhe Institute of Technology, Karlsruhe, Germany

¹⁷ReSoLVE Centre of Excellence and Sodankylä Geophysical Observatory, University of Oulu, Finland

¹⁸Finnish Meteorological Institute, Helsinki, Finland

¹⁹National Center for Atmospheric Research, Boulder, CO, USA

Correspondence to: Katja Matthes (kmatthes@geomar.de)

Abstract. This paper describes the [recommended](#) solar forcing dataset for CMIP6 and highlights changes with respect to ~~the CMIP5 recommendation~~. The solar forcing is provided for radiative properties, namely, total solar irradiance (TSI), solar spectral irradiance (SSI), the F10.7 index, as well as particle forcing, ~~with~~ [including](#) geomagnetic indices Ap and Kp, and ~~ionisation~~ [ionization](#) rates to account for effects of solar protons, electrons and galactic cosmic rays. This is the first time that

5 a recommendation for solar-driven particle forcing ~~is~~ [has been](#) provided for a CMIP exercise. The solar forcing datasets are provided at daily and monthly resolution separately for the CMIP6 [preindustrial control](#), historical (1850–2014) and future (2015–2300) simulations. ~~The datasets include~~ [For the preindustrial control simulation, both constant and time-varying solar forcing components are provided, with the latter including variability on 11-year and shorter timescales but no long-term changes. For the future, we provide a realistic scenario of what solar behavior could be, as well as](#) an additional extreme

10 Maunder minimum-like sensitivity scenario, ~~as well as a constant and a time-varying forcing for the preindustrial control~~

~~simulation~~. This paper describes the forcing datasets and also provides detailed recommendations as to their implementation in ~~the different forcing components in current~~ climate models.

~~The~~ ~~For the historical simulations, the~~ TSI and SSI time series are defined as the average of two solar irradiance models ~~that are adapted to CMIP6 needs~~: an empirical one (NRLTSI2 / NRLSSI2) and a semi-empirical one (SATIRE). A new and lower
5 TSI value is recommended: the contemporary solar cycle-average is now 1361.0 W/m². The slight negative trend in TSI ~~during the last three over the three most recent~~ solar cycles in ~~the~~ CMIP6 ~~is statistically indistinguishable from available observations and only leads to dataset leads to only~~ a small global radiative forcing of -0.04 W/m². In the 200–400 nm ~~wavelength~~ range, which is ~~also~~ important for ozone photochemistry, ~~the~~ CMIP6 ~~solar forcing dataset~~ shows a larger solar cycle variability contribution to TSI than ~~in~~ CMIP5 (50% as compared to 35%).

10 We compare the ~~climatic effects of the~~ CMIP6 ~~solar forcing~~ dataset to its CMIP5 predecessor by using timeslice experiments of two chemistry-climate models and a reference radiative transfer model. The ~~changes-differences~~ in the long-term ~~evolution of the mean~~ SSI in the CMIP6 dataset, as compared to CMIP5, impact on climatological stratospheric conditions (lower short-wave heating rates (-0.35 K/day at the stratopause), cooler stratospheric temperatures (-1.5 K in the upper stratosphere), lower
15 ozone abundances in the lower stratosphere (-3%), and higher ozone abundances (+1.5% in the upper stratosphere and lower mesosphere). Between the maximum and minimum phases of the 11-year solar cycle, there is an increase in shortwave heating rates (+0.2 K/day at the stratopause), temperatures (~1 K at the stratopause), and ozone (+2.5% in the upper stratosphere) in the tropical upper stratosphere using the CMIP6 forcing dataset. This solar cycle response is slightly larger, but not statistically significantly different from that for the CMIP5 forcing dataset.

CMIP6 models with a well-resolved shortwave radiation scheme are encouraged to ~~use SSI, as well as prescribe SSI~~
20 ~~changes and include~~ solar-induced ~~ozone signals~~ ~~stratospheric ozone variations~~, in order to better represent solar climate variability compared to models that only prescribe TSI and/or exclude the solar-ozone response. ~~Monthly~~ ~~We show that monthly~~ mean solar-induced ozone variations ~~will also be incorporated into the~~ ~~are implicitly included in the SPARC/CCMI~~ CMIP6 Ozone Database for ~~historical simulations, which is derived from transient chemistry-climate model simulations and has been developed for~~ climate models that do not calculate ozone interactively. CMIP6 models ~~with~~ ~~without chemistry that perform~~
25 ~~a preindustrial control simulation with time-varying solar forcing will need to use a modified version of the SPARC/CCMI Ozone Database that includes solar variability. CMIP6 models with~~ interactive chemistry are ~~also~~ encouraged to use the particle forcing ~~datasets~~, which will allow the potential long-term ~~effect-effects~~ of particles to be addressed for the first time. The consideration of particle forcing has been shown to significantly improve the representation of reactive nitrogen and ozone variability in the polar middle atmosphere, eventually resulting in further improvements ~~of~~ ~~in~~ the representation of solar climate
30 variability ~~in global models~~.

1 Introduction

Solar variability affects the Earth's atmosphere in numerous, and often intricate ways through changes in the radiative and energetic particle forcing (Lilensten et al., 2015). For many years, the role of the Sun in climate model simulations was reduced to its sole total radiative output, named Total Solar Irradiance (TSI), and this situation prevailed in the assessment reports of the IPCC until 2007 (Alley et al., 2007). However, there has been growing evidence for other aspects of solar variability to be major players for climate, in particular Solar Spectral Irradiance (SSI) variations and, more recently, Energetic Particle Precipitation (EPP).

For about a decade, studies involving stratospheric resolving (chemistry) climate models have included SSI variations (e.g., Haigh, 1996; Matthes et al., 2003, 2006; Austin et al., 2008; Gray et al., 2010). Whereas relative TSI variations in the 11-year solar cycle are small, about 0.1%, SSI changes are wavelength dependent, and may vary by up to 10% at 200 nm in the ultraviolet (UV) wavelength range (Lean, 1997). Variations in UV radiation over the solar cycle have significant impacts on the radiative heating and ozone budget of the middle atmosphere (Haigh, 1994).

Through dynamical feedback mechanisms solar forcing can also influence the lower atmosphere and the ocean (e.g., Gray et al., 2010). Therefore, its importance is becoming increasingly evident, in particular for regional climate variability (e.g., Gray et al., 2010; Seppälä et al., 2014). Together with volcanic activity, solar variability is an important external source of natural climate variability. Because of its prominent 11-year cycle, solar variability on time scales of years, and beyond may offer a degree of predictability for regional climate and could therefore help reduce uncertainties in decadal climate predictions.

However, there are still uncertainties in the observed atmospheric signals of solar variability (Mitchell et al., 2015a) and its transfer mechanism(s) to the surface. Proposed transfer mechanisms include changes in TSI and SSI, as well as in solar-driven energetic particles (e.g., Seppälä et al., 2014). In addition, recent work suggests a lagged response in the North Atlantic/European sector due to atmosphere-ocean coupling (e.g., Gray et al., 2013; Scaife et al., 2013), as well as a synchronisation of decadal variability in the North Atlantic Oscillation (NAO) by the solar cycle (Thieblemont et al., 2015). Lagged responses have been also attributed to particle effects (Seppälä and Clilverd, 2014) and hence the observed solar surface signal could be a combination of top-down solar UV and particle as well as bottom-up atmosphere-ocean mechanisms.

Since some of the climate models run under the previous fifth Coupled Model Intercomparison Project (CMIP5) included the stratosphere and the mesosphere for the first time, and were thus able to capture the so-called "top-down" mechanism for solar-climate coupling, both TSI and SSI variations were recommended by the WCRP/SPARC SOLARIS-HEPPA activity (<http://solarisheppa.geomar.de/cmip5>). Recent modeling efforts have made progress in defining the pre-requisites to simulate solar influence on regional climate more realistically (e.g., Gray et al., 2013; Scaife et al., 2013; Thieblemont et al., 2015), but the lessons learned from CMIP5 show that a more process based analysis of climate models within CMIP6 is required to better understand the differences in model responses to solar forcing (e.g., Mitchell et al., 2015b; Misios et al., 2016; Hood et al., 2015). In particular, the role of solar-induced ozone changes and the need for a suitable resolution of climate model radiation schemes to capture SSI variations is becoming increasingly evident, and will be touched upon in this paper. In addition we will for the first time provide the solar-driven energetic particle forcing together and consistent with the radiative forcing.

The quantitative assessment of radiative solar forcing has been systematically hampered so far by the large uncertainties and the instrumental artifacts that plague SSI observations, and to a lesser degree TSI observations (e.g., Ermolli et al., 2013; Solanki et al., 2013). Another problem is the sparsity of the observations, which started in the late 1970s only with the satellite era. These problems have deprived us of the hindsight that is needed to properly assess variations on time scales that are relevant for climate studies. Another issue is the uncertainty regarding their absolute level. Since CMIP5, the nominal TSI has been reduced to $1361.0 \pm 0.5 \text{ W/m}^2$, see (Prša et al., 2016), and also (Kopp and Lean, 2011). This adjustment has inevitable implications for understanding the Earth's radiation budget.

On multi-decadal time scales, proxy reconstructions of ~~the TSI~~ solar activity reveal occasional phases of unusually low or high solar activity, which are respectively called grand solar minima and maxima (Usoskin et al., 2014). Of particular interest in this regard is the future evolution of long-term solar activity. Solar activity reached unusually high levels in the second half of the twentieth century, so that one could expect subsequent activity to fall back to levels closer to the historical mean, an expectation buttressed by the low amplitude of current activity cycle 24. Moreover, some recent empirical long-term forecast even predict a phase of very low activity in the second half of the twenty-first century – perhaps akin to the 1645-1715 Maunder Minimum (Abreu et al., 2008; Barnard et al., 2011; Steinhilber et al., 2012). However, how deep and how long such phase of low solar activity would be is still largely uncertain. Recent studies have investigated the climate impacts of a large reduction in solar forcing over the 21st century, revealing only a small impact on a global scale (Feulner and Rahmstorf, 2010; Anet et al., 2013; Meehl et al., 2013). However, a systematic assessment of the regional impacts of a more realistic future solar forcing is still to be done. For example, on regional scales, a future grand solar minimum could potentially reduce Arctic amplification (Chiodo et al., 2016) and reduce long-term warming trends over western Europe (Ineson et al., 2015).

The above-mentioned uncertainty in the SSI is particularly challenging in the UV band (Ermolli et al., 2013). All climate model intercomparison studies relied so far on the NRLSSI1 dataset (Lean, 2000). However, it is becoming increasingly evident that its solar cycle variability in the UV part of the spectrum may be too low as compared to updated and more recent SSI reconstructions by models such as NRLSSI2 (Coddington et al., 2016) and SATIRE (Yeo et al., 2014). Recent studies have emphasized the sensitivity to UV forcing changes due to top down effects (Ermolli et al., 2013; Langematz et al., 2013; Ineson et al., 2015; Thieblemont et al., 2015; Maycock et al., 2015; Ball et al., 2016), thereby stressing the need for a state-of-the-art representation of the SSI, and in particular the UV band, in the CMIP6 solar forcing recommendation. For that reason, we will focus on the SSI uncertainty and possible impacts of the higher SSI variability in CMIP6 with respect to the CMIP5 solar forcing recommendation (<http://solarisheppa.geomar.de/cmip5>).

Analysis of model simulations and observations have shown a response of global surface temperature to TSI variations over the 11-year solar cycle of about 0.1 K (Lean and Rind, 2008; Misios et al., 2016). However, the observed lag and the spatial pattern of the solar cycle response are poorly represented in CMIP5 models (e.g., Mitchell et al., 2015b; Misios et al., 2016; Hood et al., 2015).

In addition, (Gray et al., 2010) report that previous long-term variations in solar forcing used in some experiments (Alley et al., 2007) may be too weak due to an unfortunate choice of epoch (around 1750) for the preindustrial solar forcing, as this was a period of relatively high solar activity.

More recently, it has become better established that there is a solar response in the Arctic Oscillation (AO) and NAO from the top-down mechanism (Shindell et al., 2001; Kodera, 2002; Matthes et al., 2006; Woollings et al., 2010; Lockwood et al., 2010; Ineson et al., 2011; Langematz et al., 2013; Ineson et al., 2015; Maycock et al., 2015; Thieblemont et al., 2015). Earlier models often employed a lower vertical domain, missing key physical processes by which solar signals in the stratosphere
5 couple to surface winter climate. However, some of the more recent studies using stratosphere resolving (chemistry) climate models confirm a stratospheric downward influence on the NAO from solar variability, in particular associated with changes in UV radiation and possibly through interaction with stratospheric ozone (e.g., Matthes et al., 2006; Rind et al., 2008; Ineson et al., 2011; Chiodo et al., 2012; Langematz et al., 2013; Thieblemont et al., 2015; Ineson et al., 2015). Some of these studies also suggest weaker model responses than are apparent in observations, although with large uncertainty (e.g., Gray et al., 2013;
10 Scaife et al., 2013).

Another very important solar forcing mechanism after electromagnetic radiation is energetic particle precipitation (Gray et al., 2010; Lilensten et al., 2015). Although the impact of EPP on the atmosphere is well documented, it had been ignored in solar forcing recommendations for earlier phases of CMIP. The term EPP encompasses particles with very different origins: solar, magnetospheric, and from beyond the solar system. These particles are mainly protons and electrons, and occasionally
15 α -particles, and heavier ions.

Solar protons with energies of 1 MeV to several hundreds of MeV are accelerated in interplanetary space during large solar perturbations called coronal mass ejections (Reames, 1999; Richardson and Cane, 2010). These sporadic events, also known as solar proton events (SPEs), are associated with the presence of complex sunspots, and are therefore more frequent during solar maximum.

20 Auroral electrons originate from the Earth's magnetosphere, and are accelerated to energies of 1-30 keV during auroral substorms (Fang et al., 2008). Sudden enhancements of their flux occurs during geomagnetic active periods, which are more frequent 1-2 years after peak of the 11-year solar cycle. Medium-energy electrons are accelerated to energies of a few hundred keV during geomagnetic storms in the terrestrial radiation belts (Horne et al., 2009). Precipitation of middle energy electrons can be triggered both by solar coronal mass ejections, and high-speed solar wind streams, leading to more frequent events
25 near solar maximum and during the declining phase of the solar cycle. Particle precipitation, regardless of its origin, is thus modulated by solar activity, and varies with the solar cycle. However, these intermittent variations take place on different timescales, and at different altitude regions. Their sources and variability have recently been reviewed by Mironova et al. (2015).

EPP affects the ~~ionisation~~ionization levels in the polar middle and upper atmosphere, leading to significant changes of the chemical composition. In particular, the production of odd nitrogen and odd hydrogen species causes changes in ozone abundances via catalytic cycles, potentially affecting temperature and winds (see, e.g., the review by Sinnhuber et al., 2012). Recent model studies and the analysis of meteorological data have provided evidence for a dynamical coupling of this signal to the lower atmosphere, leading to particle-induced surface climate variations on a regional scale (e.g., Seppälä et al., 2009; Baumgaertner et al., 2011; Rozanov et al., 2012; Maliniemi et al., 2014).

The third, and most energetic components of EPP is represented by galactic cosmic rays (GCR), which mainly consist of protons with energies from hundreds of MeV to TeV. This continuous flux of particles is the main source of **ionisation** ionization in the troposphere and lower stratosphere. GCRs are deflected by the solar magnetic field, and hence their flux is anti-correlated with the solar cycle. Laboratory-based studies have confirmed the existence of ion-mediated aerosol formation and growth rates; however, the connection between GCR ionization and cloud production, and therefore convection, is still under debate. Meanwhile, the chemical impact via ozone-depleting catalytic cycles and subsequent dynamical forcing is rather well understood (Calisto et al., 2011; Rozanov et al., 2012).

The effect of various components of EPP on surface climate is an emerging research topic. However, the particle impact on regional climate may be comparable to that of the UV forcing (Seppälä and Clilverd, 2014). One of the major challenges here is to quantify the long-term climate impact of such local and mostly intermittent particle precipitations.

The uncertainties in the solar forcing itself are compounded by possible errors in the simulated climate response to this forcing in models (e.g., Stott et al., 2003; Scaife et al., 2013). Possible errors in climate model responses could be related to biases in the representation of dynamical processes and dynamical variability, the inability of model radiation schemes to properly resolve SSI changes (Forster et al., 2011), or to the missing or inadequate representation of UV and particle-induced ozone signals (Hood et al., 2015). Any comparison of climate model simulations with observations could be affected by a combination of these possible sources of error. In addition, the comparison of models with observations is inhibited by the insufficient length of the observational records, and in some cases model simulations.

This paper will provide the first complete overview on solar forcing (radiative, particle and ozone forcing) recommendations for CMIP6 from preindustrial times to the future and provides in this respect an advance to earlier MIPs (CMIP5, CCMVal, CCMII) as it gives a complete and state-of-the-art overview on our current understanding of solar variability and provides the dataset in a user-friendly way.

Section 2 presents the historical to present-day solar forcing dataset with individual subsections on solar irradiance (Section 2.1) and particle forcing (Section 2.2). Section 3 provides a description of the future solar forcing recommendation, section 4 on the pre-industrial control forcing and section 5 finally a description of the solar induced ozone signal. A summary with respect to differences to the CMIP5 recommendation is given in section 6.

2 Historical (to Present) Forcing Data (1850-2014)

In this section we first describe the solar irradiance dataset (including the TSI, the F10.7 decimetric radio index, and the SSI, see Sec. 2.1), and subsequently address the energetic particle datasets (including solar protons, auroral electrons, medium-energy electrons, and galactic cosmic rays, see Sec. 2.2).

2.1 Solar Irradiance (TSI, SSI, and F10.7)

This subsection starts with a description of the available TSI and SSI datasets from two different solar irradiance models (NRLSSI and SATIRE), and one observational estimate (SOLID), before introducing the CMIP6 recommendation. Afterwards

a recommendation on how to implement the solar irradiance forcing in CMIP6 models is provided. An evaluation of the comparison between different SSI forcing datasets with a focus on CMIP5 and CMIP6 solar irradiance recommendations in a line-by-line model and two state-of-the-art CCMs, i.e. CESM1(WACCM) and EMAC, is performed at the end to highlight the effects of solar irradiance variability on the atmosphere, and possible effects on atmospheric dynamics all the way to the ocean.

5 2.1.1 Description of Solar Irradiance Datasets

NRLTSI2 and NRLSSI2

The Naval Research Laboratory (NRL) family of SSI models (Lean, 2000; Lean et al., 2011) is based on the premise that changes in solar irradiance from background quiet Sun conditions can be described by a balance between bright facular, and dark sunspot features on the solar disk. These two contributions are determined by linear regression between solar proxies, and direct observations of TSI and SSI by satellite missions such as SORCE (Rottman, 2005). These models are thus empirical.

Both the TSI and the SSI consist of a baseline solar contribution, with a wavelength-dependent contribution. The Magnesium (MgII) index, for example, represents the contribution of bright faculae, whereas the sunspot area represents the contribution of sunspots. The time dependency in TSI and SSI thus emerges from the temporal variability in the solar proxies. SORCE measurements at solar minimum conditions are the basis for the adopted quiet Sun irradiance (Kopp and Lean, 2011) in NRLSSI2.

The recently updated version of the NRL models, named NRLTSI2 (for TSI only) and NRLSSI2, have been transitioned to the National Centers for Environmental Information (NCEI) as part of their Climate Data Record (CDR) Program (see <http://www.ngdc.noaa.gov>), and operational updates are provided on a near quarterly basis. Coddington et al. (2016) describe the model algorithm, the uncertainty estimation approach, and comparisons to observations in detail. Please note that our version slightly differs from the one published by Coddington et al. (2016) by using a different scaling factor between the sunspot area as measured by the Royal Greenwich Observatory (from 1874-1976) and the NOAA/USAF Solar Observing Optical Network (SOON) since 1966. The future release of NRLSSI2 will use the same scaling factor as the version we use.

In NRLSSI2, a multiple linear regression approach of solar proxy inputs with observations of TSI from SORCE/TIM (Kopp et al., 2005), and observations of SSI from the SORCE/SOLSTICE (McClintock et al., 2005) and SORCE/SIM (Harder et al., 2005) instruments is used to determine the scaling coefficients that convert the proxy indices to irradiance variability. Concerns for the long-term stability of the SORCE SSI observations (Lean and DeLand, 2012) that are not shared with regard to the SORCE TSI record mean the wavelength-dependent scaling coefficients used in the NRLSSI2 model are derived for solar rotation time scales (i.e. the SSI observations and the proxy indices are detrended with an 81-day running mean). However, because regression coefficients derived from detrended SSI time series differ from those developed from non-detrended SSI time series, a further adjustment is required to extend the SSI variability from solar rotational to solar cycle time scales. In NRLSSI2, this adjustment is made by a linear scaling that is constrained by the TSI variability. This adjustment is made in the separate facular and sunspot proxy records and the magnitude of the adjustment is smaller than the assumed uncertainty in

the proxy indices themselves. In this approach, the integral of the SSI tracks the TSI; however, the relative facular and sunspot contributions at any given wavelength are not constrained to match their specific TSI contributions.

The NRLTSI2 and NRLSSI2 irradiances also include a speculated long-term facular contribution that produces a secular (i.e., underlying the solar activity cycle) net increase in irradiance from a small accumulation of total magnetic flux. This secular impact is specific to historical time scales (i.e., prior to 1950) and is consistent with simulations from a magnetic flux transport model (Wang et al., 2005).

SATIRE

The SATIRE (Spectral And Total Irradiance REconstruction) family of semi-empirical models assumes that the changes in the solar spectral irradiance are driven by the evolution of the photospheric magnetic field (Fligge et al., 2000; Krivova et al., 2003, 2011). The model makes use of the calculated intensity spectra of the quiet Sun, faculae and sunspots generated from model solar atmospheres with a radiative transfer code (Unruh et al., 1999). SSI at a particular time is given the sum of these spectra, weighted by the fractional solar surface that is covered by faculae and sunspots, as apparent in solar observations.

The implementation of SATIRE employing solar images in visible light, and solar magnetograms (magnetic field intensity and polarity) is termed SATIRE-S (Wenzler et al., 2005; Ball et al., 2012; Yeo et al., 2014), and that based on the sunspot number ([SSN](#)) is SATIRE-T (Krivova et al., 2010). Individual records are accessible at ~~-.In order to guarantee the homogeneity of our past and future SSI reconstructions, we use here~~ <http://www2.mps.mpg.de/projects/Sun-climate/>. ~~We use here SATIRE-S for the space age (available from 1974 to 2015). Prior to 1974 the CMIP6 SATIRE data was calculated with the same SATIRE-T, driven by the same sunspot number record-~~ ~~model (Krivova et al., 2010), however, using daily SSN (Version 1) instead of Group SSN (GSNN) (Hoyt and Schatten, 1998) while keeping all other inputs (including sunspot area) identical to the original version. We shall henceforth call this model SATIRE in the following.~~

On decadal to centennial time scales, SATIRE reproduces observations such as: the composite of the Lyman- α line at 121.5 nm (since 1947, Woods et al., 2000), the measured solar photospheric magnetic flux (since 1967), the empirically reconstructed solar open magnetic flux (since 1845, Lockwood et al., 2014), and the ^{44}Ti activity in stony meteorites (Krivova et al., 2010; Vieira et al., 2011; Yeo et al., 2014).

SATIRE and NRLSSI2 are internally consistent, in the sense that the integral of the modeled spectral ~~irradiance~~ irradiances equals the TSI. These are among the best model reconstructions we currently have. Note, however, that both models reconstruct the SSI prior to the space age by assuming the relationship between sunspot number and SSI to be time-invariant. The model-uncertainty associated with this assumption is difficult to quantify. For that reason, it is not included in the uncertainties that are provided with the model datasets, which ~~might~~ may therefore be underestimated.

30 Proxies Used

Both NRLSSI2 and SATIRE rely on the sunspot number when no other solar proxies are available. For the CMIP6 composite, we decided to rely on version 1.0 of the international sunspot number (from <http://www.sidc.be/silso>), even though a newer version 2.0 recently came out (Clette et al., 2014). Indeed, SSI models have not yet been thoroughly trained and tested with

this new sunspot number. Recent results by Kopp et al. (2016) suggest that this revision has little impact after 1885, and leads to greater solar-cycle fluctuations prior.

In NRLSSI2 the proxy index for facular brightening is the composite MgII index from the University of Bremen. The MgII index (Viereck et al., 2001) is ~~a disk-integrated~~ the core-to-wing ratio of the ~~core-to-the-wings-of-the~~ disk-integrated MgII emission line at 280 nm, ~~and~~. This quantity is used by many models as a UV proxy. The MgII index is available from 1978 onwards; values prior to that are estimated from the sunspot number.

In NRLSSI2 and in SATIRE, the proxy index for sunspot darkening is the sunspot area as recorded by ground-based observatories in white light images since 1882 (Lean et al., 1998). The sunspot darkening prior to 1882 is estimated from the sunspot number.

10 SOLID Composite

The task at hand – to determine the most likely temporal variation in SSI – is challenged by the paucity of direct SSI observations, and the numerous instrumental ~~artefacts~~ artifacts that affect these observations. Recently, this task has been addressed by an international consortium, which has produced an observational SSI composite (Haberreiter et al., 2017). This SOLID¹ composite is the first of its kind to include a large ensemble of observations, which are listed in Table 1. These observations are combined by using a probabilistic approach, without any model input. We consider this observational composite here mainly as an independent means for comparing the SSI reconstructions. While it is premature to use this composite as a benchmark for testing ~~the~~ models, it definitely represents the most comprehensive description to date of SSI observations (Haberreiter et al., 2017).

The making of this composite involves several steps. First, the SSI datasets as provided by the instrument teams (see the list of instruments in Table 1) are pre-processed, e.g., corrected for outliers and aligned in time. Furthermore, the short-term and long-term uncertainties of the SSI time series are determined. These steps are detailed in (Schöll et al., 2016).

Second, for each individual dataset all data gaps are filled by expectation-maximization (Dudok de Wit, 2011). This approach makes use of observed proxies representing the SSI variation of different wavelength ranges in the solar spectrum, as listed in Table 2. We emphasize here that the gap-filling is ~~a purely statistical method, as no physical assumption goes into it~~ required here to decompose the records into different time-scales; at the end, the interpolated values are excluded from the composite. Third, each individual time series is decomposed by wavelet transform into 13 time scales $a = 2^j$, with j being the level of the scale. These scales go from 1 day (Level 0) to 11.2 years (Level 12). For each time scale, the uncertainty is determined by taking into account the short-term and long-term uncertainties. Fourth, the recomposed records are recombined by calculating the weighted average for each scale thereby taking into account the scale-dependent and wavelength-dependent uncertainties. Finally, the SSI composite is obtained by adding up the averaged temporal scales. Additionally, the time-dependent and wavelength-dependent uncertainties are also summed-up. The SOLID composite is currently available for the time frame of November 8, 1978 to December 31, 2014; for further details see (Haberreiter et al., 2017).

¹FP7 SPACE Project *First European SOLar Irradiance Data Exploitation (SOLID)*; <http://projects.pmodwrc.ch/solid/>

Table 1. SSI datasets used for the SOLID composite. The first column gives the instrument, the second column the spectral band, and the third column the temporal coverage of the observations.

Name of the instrument	Wavelength range [nm]	Observation Period
GOES13/EUVS	11.7–123.2	07/2006–10/2014
GOES14/EUVS	11.7–123.2	07/2009–11/2012
GOES15/EUVS	11.7–123.2	04/2010–10/2014
ISS/SolACES	16.5–57.5	01/2011–03/2014
NIMBUS7/SBUV	170.0–399.0	11/1978–10/1986
NOAA9/SBUV2	170.0–399.0	03/1985–05/1997
NOAA11/SBUV2	170.0–399.0	12/1988–10/1994
NOAA16/SBUV2 170.0–406.2 10/2000–04/2003 SDO/EVE	5.8–106.2	04/2010–10/2014
SME/UV	115.5–302.5	10/1981–04/1989
SNOE/SXP	4.5	03/1998–09/2000
SOHO/CDS	31.4–62.0	04/1998–06/2010
SOHO/SEM	25.0–30.0	01/1996–06/2014
SORCE/SIM	240.0–2412.3	04/2003–05/2015
SORCE/SOLSTICE	115.0–309.0	04/2003–05/2015
SORCE/XPS	0.5–39.5	04/2003–05/2015
TIMED/SEE-EGS	27.1–189.8	02/2002–02/2013
TIMED/SEE-XPS	1.0–9.0	01/2002–11/2014
UARS/SOLSTICE	119.5–419.5	10/1991–09/2001
UARS/SUSIM	115.5–410.5	10/1991–08/2005

Table 2. Proxies used in addition to the original SSI data in order to fill in data gaps.

Name of proxy	Origin (Observatory)	relevant for
30.0 cm radio flux	Nobeyama/Toyokawa	UV
15.0 cm radio flux	Nobeyama/Toyokawa	UV
10.7 cm radio flux	Penticton/Ottawa	UV
8.2 cm radio flux	Nobeyama/Toyokawa	UV
3.2 cm radio flux	Nobeyama/Toyokawa	UV
sunspot darkening	Greenwich/SOON netw.	VIS

Our aim was to keep this composite fully independent from existing models. This means that no SSI models have been used to correct the observational data, which are taken at their face value, without any correction.

One challenge of this - as with any statistical - approach is its reliance on the number of independent datasets. While for the past decades several missions were dedicated to measuring the UV band of the solar spectrum, the picture becomes bleaker when considering recent observations in the visible and near-UV parts of the spectrum. After 2003, the only remaining observations are from *SORCE/SIM*, whose out-of-phase behavior (Harder et al., 2009) is controversial (Lean and DeLand, 2012; Ermolli et al., 2013). Let us therefore stress that the *SOLID* composite is based on observations only, and will necessarily undergo revisions as new physical constraints are incorporated, or new versions of the datasets are released.

2.1.2 CMIP6 Recommended Solar Irradiance Forcing

NRLSSI and *SATIRE* are not the only available models for reconstructing the SSI (Ermolli et al., 2013). However, they are the only ones that have been widely tested, and can easily cover the 1850–2300 time span for CMIP6 with one single and continuous record. The resulting homogeneity in time is a major asset of our reconstructions, and a necessary condition for obtaining a realistic solar forcing.

NRLSSI and *SATIRE* agree well on time scales of days to months, but exhibit more pronounced differences on longer time scales, which have fueled a debate (e.g. Yeo et al., 2015) that is unlikely to settle soon. The two models have been derived independently, and as of today there is no consensus regarding their relative performance. In this context, and for the time being, the most reasonable approach (in a maximum likelihood sense) consists in averaging their reconstructions, weighted by their uncertainty. Since in addition we are lacking uncertainties that can be meaningfully compared, our current recommendation is to simply take the arithmetic mean of the two model datasets: (i) the empirical model *NRLTSI2* and *NRLSSI2* (Coddington et al., 2016), and (ii) the semi-empirical model *SATIRE* (Yeo et al., 2014). Note that multi-model averaging is a widely-used practice in climate [modelling-modeling](#) (e.g Smith et al., 2013).

For historical data (Jan 1, 1850 – Dec 31, 2014) both models rely, as described above, on one or several of: the international sunspot number *V1.0*, sunspot area distribution (after 1882), solar photospheric magnetic field (after 1974), and the *MgII* index (after 1978). Since *NRLSSI2* and *NRLTSI2* have yearly averages only before 1882, we reconstructed sub-yearly variations by using an *ARMAX* (AutoRegressive Moving Average with eXogeneous input) model (Box et al., 2015) that uses the sunspot number as input.

The EUV band (10-121 nm) is required for CMIP6 but is not provided by *NRLSSI2* and *SATIRE*, whose shortest wavelength is 115.5 nm. We thus added it with spectral bins from 10.5-114.5 nm by using a nonlinear regression from the SSI in the 115.5–123.5 nm band, trained with *TIMED/SEE* data from 2002 to 2011. This is further detailed in Appendix A.

In some climate models the EUV flux is parameterised as a function of the *F10.7* index, which is the daily radio flux at 10.7 cm from Penticton Observatory, adjusted to 1 AU, and measured daily since 1947 (Tapping, 2013). For practical purposes, we also provide this index. Values prior to 1947 are obtained by multi-linear regression to the first 20 principal components of the SSI and application of minor non-linear adjustments. Let us note that while the *F10.7* index is a good proxy for EUV variability on daily to yearly time scales, this may not be true anymore on multi-decadal time scales. As of today, the lack of

direct EUV observations does not allow us to constrain its long-term evolution, whereas the F10.7 index at solar minimum has not significantly varied since 1947, when its first measurements started.

The dataset, together with a technical description, and a routine for how to read and integrate the SSI data to the radiation bands used in climate models can be found at <http://solarisheppa.geomar.de/cmip6>. In addition, a recommendation on how to
5 implement the SSI changes in the models is provided in the Appendix B. A detailed description of the CMIP6 solar irradiance forcing in TSI and SSI, and a comparison to the CMIP5 recommendation is presented in the following.

Total Solar Irradiance (TSI)

Figure 1 presents time series of the TSI from the CMIP5, CMIP6, and the original NRLTSI2 and SATIRE datasets, along with one observational composite from PMOD (version 42.64.1508)². We stress that all the data are taken at their face value, using
10 their latest version, without any adjustments or scaling, except for NRLTSI1, whose value we uniformly reduced by 5 W/m² to account for the new recommendation for average TSI (see below).

All TSI records agree well on daily to yearly time scales, and in some cases (e.g. NRLTSI1 and NRLTSI2) they match as well on multi-decadal time scales. The major difference arises in the long-term ~~behaviour~~behavior of SATIRE and NRLTSI2, which impacts the CMIP6 composite, and leads to a weaker trend as compared to the CMIP5 recommendation (which was based on
15 NRLTSI1 only). In both models, the historical reconstructions are sensitive to the assumptions made when constraining them to direct (satellite era) observations that suffer from large uncertainties. ~~This mainly explains why these models differ before 1990 by an offset.~~ There is no consensus yet as to which one better represents long-term solar variability, and this is what motivated us to average them for making the CMIP6 composite.

More subtle differences between the different TSI datasets arise in the satellite era, especially with the unusually deep
20 solar minimum that occurred in 2008-2010: the NRLTSI2 model has a weak negative trend between successive solar minima, whereas the SATIRE reconstruction exhibits a larger one. The resulting trend in the CMIP6 composite is comparable to the observational TSI composite from PMOD (grey area). Figure 1 does not show any model uncertainties, because these are either absent or difficult to compare. We do provide uncertainties, however, for the observational PMOD composite, based on
25 the $\pm 1\sigma$ confidence interval, which highlights how delicate it is to constrain them by observational data.

After CMIP5, the recommended value of the average TSI during solar minimum was reduced from 1365.4 ± 1.3 W/m² to a lower value of 1360.8 ± 0.5 W/m² after reexamination by Kopp and Lean (2011), later confirmed independently by Schmutz et al. (2013). Based on this, the International Astronomical Union recently recommended 1361.0 ± 0.5 W/m² as the nominal value of the TSI, averaged over solar cycle 23, which lasted from 1996 to 2008 (Prša et al., 2016). Our CMIP6 composite
30 complies with this recommendation.

To summarise for the TSI: the CMIP6 and CMIP5 recommendations are comparable on decadal and sub-decadal time scales. They differ, however, by a weaker secular trend in CMIP6. Between 1980 and 1880, the difference TSI(CMIP6)-TSI(CMIP5)

²<https://www.pmodwrc.ch/pmod.php?topic=tsi/composite/SolarConstant>

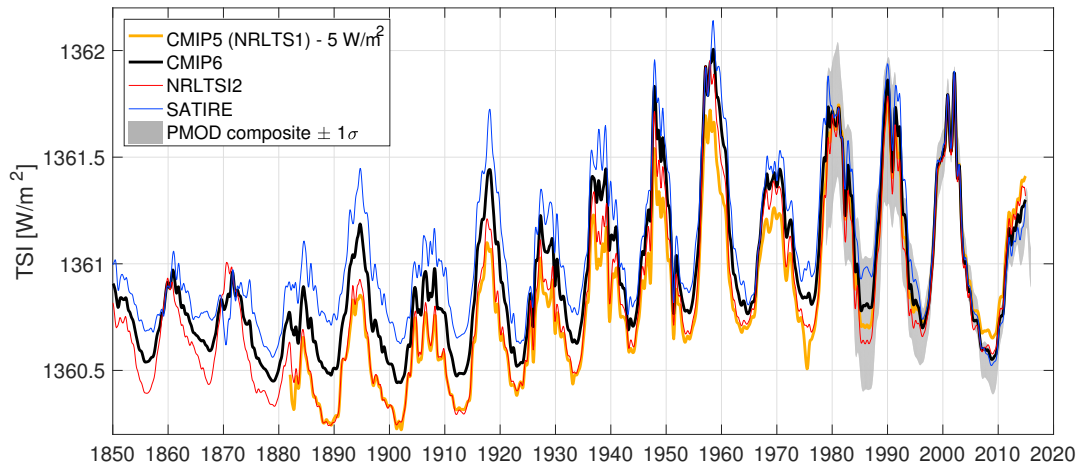


Figure 1. Comparison of several TSI reconstructions, showing 6-month running averages of: the NRLTSI1 record (reference for CMIP5, and thus continuing after the 2010 end date of CMIP5), the CMIP6 composite, and the reconstructions from the NRLTSI2, and SATIRE models. Also shown is the observational composite from PMOD (version 42.64.1508) with a $\pm 1\sigma$ confidence interval. A negative offset of -5 W/m^2 has been applied to the NRLTSI1 record to account for the change in average TSI that occurred between CMIP5 and CMIP6.

progressively increases from 0.1 to 0.4 W/m^2 (after correcting the aforementioned 5 W/m^2 offset in CMIP5). This results in a weaker change in solar forcing, which will be detailed in Sec. 2.1.3.

To estimate the impact of these different trends on the radiative forcing (RF), we have conducted a high spectral resolution calculation using a single profile with a line-by-line radiative transfer code (libradtran) described in more detail below. This indicated an instantaneous change in downward solar flux of -0.16 W/m^2 over the 1986-2009 period for the combined CMIP6 dataset. A crude estimate of the global mean forcing from this change is -0.04 W/m^2 , which is relatively small in comparison to other forcings over this period.

Solar Spectral Irradiance (SSI)

To investigate differences and similarities between the SSI datasets, following Ermolli et al. (2013), we concentrate on four specific wavelength ranges, 120–200 nm (UV1), 200–400 nm (UV2), 400–700 nm (VIS), and 700–1000 nm (NIR), with special emphasis on the CMIP5 (i.e. NRLSSI1) and the CMIP6 (average of NRLSSI2 and SATIRE) datasets. These ranges are relevant for climate studies, see for example Table 3 below. Figure 2 shows the SSI time series from 1880 through 2014. Note that we added vertical offsets by adjusting the mean values to facilitate their comparison, using CMIP6 as a reference. We note that:

- The long-term increase from 1880 to 1980 is similar in all datasets (NRLSSI1 might appear to have larger long-term increase in the VIS but this is mostly caused by different solar cycle amplitudes). SATIRE predicts a slightly larger increase in the UV2 ($+0.03 \text{ W/m}^2$ with respect to NRLSSI2) from 1880 to 1930 compensated by a smaller increase in the VIS. NRLSSI2 has a larger but still small increase ($+0.075 \text{ W/m}^2$ with respect to SATIRE) in the NIR from 1880 to

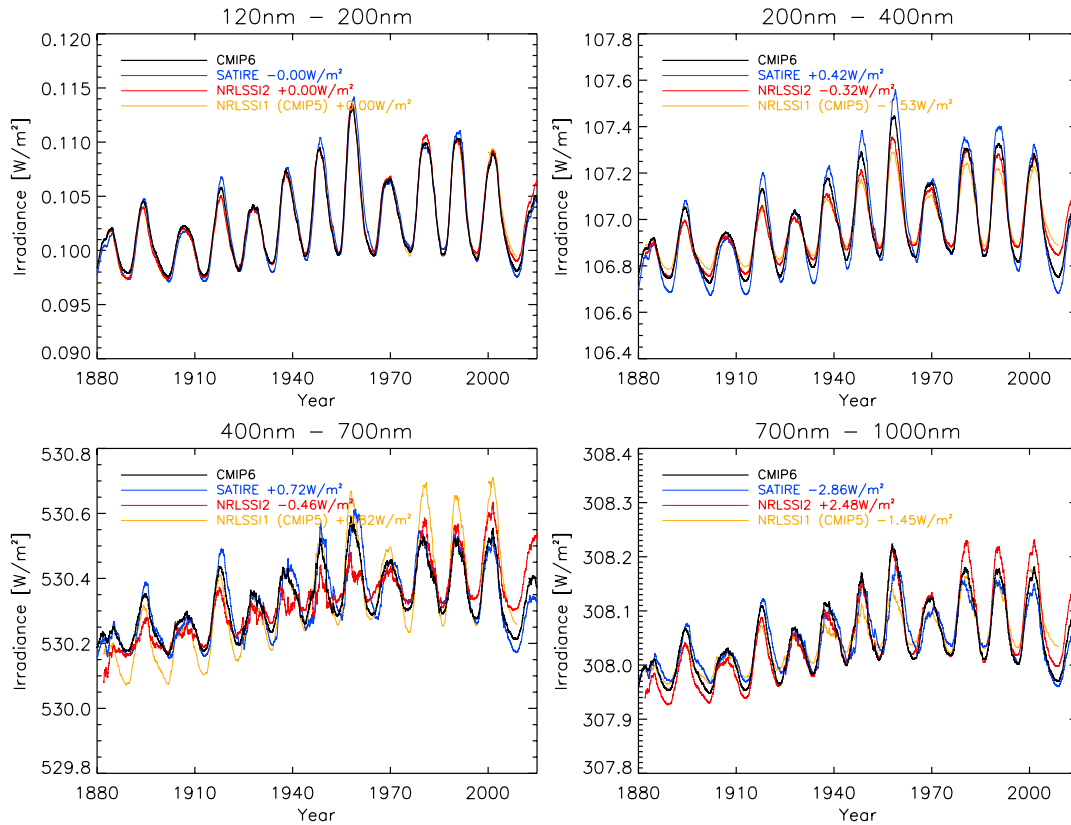


Figure 2. SSI time series from 1882 to 2014, integrated over following wavelength ranges: 120-200 nm (top left), 200-400 nm (top right), 400-700 nm (bottom left), and 700-1000 nm (bottom right). An offset, indicated in the legend, has been added to each time series, to ease visualisation. All time series are running averages over 2 years.

present, which was also present in NRLSSI1 (CMIP5). Before 1970, NRLSSI2 shows less smoothed cycles with respect to the other models in the visible. The major difference on the long-term trend comes from SATIRE after 1985 (see below).

- As already described for the TSI ~~behaviour~~ behavior above (Fig. 1), SATIRE predicts a significant downward trend of the baseline for the last three solar cycles, as can be seen by comparing the SSI at solar minima between cycles 21 & 22 (1985), 22 & 23 (1995), and 23 & 24 (2008). NRLSSI2 does not predict significant variations and therefore the recommended CMIP6 time series has a slower downward trend than SATIRE in the recent cycles. This trend was not apparent in the dataset recommended for CMIP5.
- The solar cycle variability in CMIP6 exceeds that of CMIP5, particularly in the UV2 and NIR ranges, while it is approximately the inverse in the VIS. The change in the NRLSSI model can be explained by the use of new, and higher-quality data from the *SORCE* mission on the rotational timescale in NRLSSI2, while NRLSSI1 was based on data from older

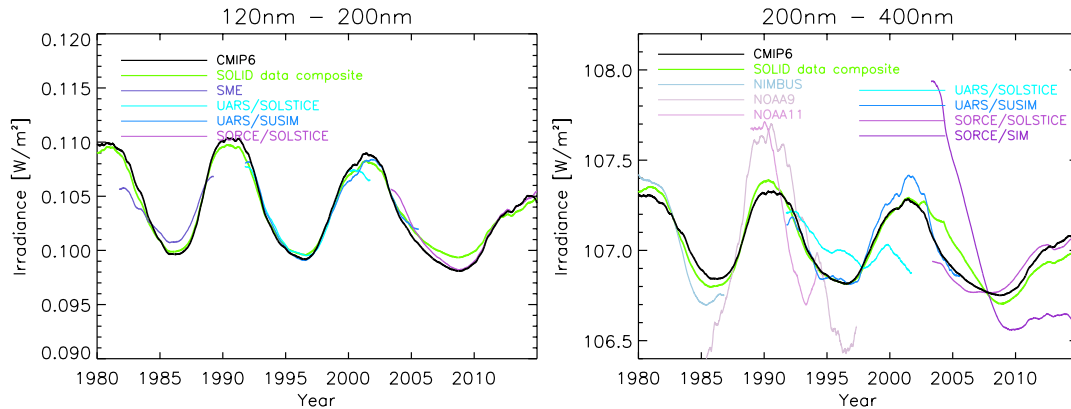


Figure 3. CMIP6 recommended SSI time series (black) from 1980 to 2015 together with the SOLID data composite (green) and relevant instrument observations for the following wavelength bins: 120nm–200nm (left), 200nm–400nm (right). The SOLID and instrument time series have been adjusted to match the average level of the CMIP6 time series. Note that SOFCE/SOSLTICE only covers 200nm-309nm and SOFCE/SIM only 240nm-400nm. All time series are running averages over 2 years.

satellite missions. In the UV2, SATIRE predicts larger solar cycle amplitudes, which can be explained by a larger weight of the network at these wavelengths.

In Figure 2, the apparently less regular solar cycle reconstruction by NRLSSI2 between 1940 and 1960 is most likely caused by the transition from one sunspot record to another in that model, (see Coddington et al., 2016).

5 Figure 3 compares our CMIP6 dataset with the observational SOLID composite (see description above) and some direct SSI satellite observations. Generally speaking, the observations and observation-based composite agree very well with each other, and the CMIP6 dataset up to 200 nm. Larger cycle variations than in the CMIP6 SSI occur above about 200 nm in the observations. Such discrepancies are inherent to the observation of small variations over eleven years. On the right panel of Fig. 3, one can notice the different influence of the various datasets on the SOLID composite, as a consequence of their
 10 uncertainty at different scales. For example, the SOFCE/SIM data have only a minor (but significant) effect on the long-term variations of the composite. In the VIS and NIR part of the spectrum, the only available measurements are from the SOFCE/SIM instrument, whose solar-cycle variation is controversial (Lean and DeLand, 2012) and hence should be considered with great caution.

Figure 4 shows the contribution of the different wavelength ranges to TSI variations between solar maximum on November
 15 1989 (solar cycle 22) and solar minimum on November 1994 (between cycles 22 and 23) for the different solar irradiance models. Both extrema are averaged over 81 days. We use the same spectral bands and color coding as in Fig. 2 of the review by Ermolli et al. (2013). The latter figure, though, applies to the next solar cycle, when SOFCE/SIM is operating. Our dates coincide with the ones chosen in the CCM timeslice experiments, see Section 2.1.3. Please note that the sum of the SSI variability of the various models is not equal to the TSI variability because the IR part is missing in Figure 4.

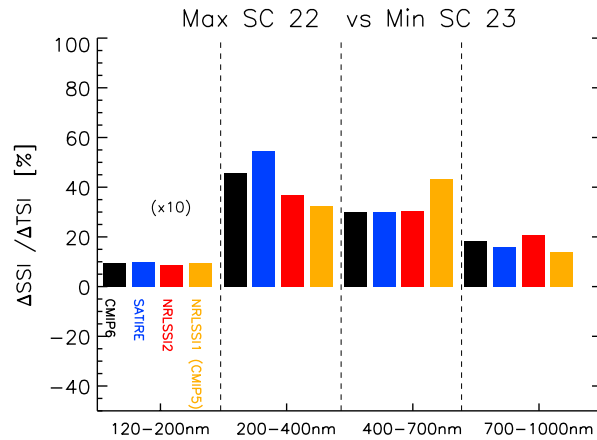


Figure 4. Contribution in percent of various wavelength ranges to the TSI variability between the maximum of cycle 22 and the minimum between cycles 22 and 23. Contributions between 120 nm and 200 nm have been multiplied by 10 for improved visibility. Maximum and minimum values have been taken over an 81-day period centered on November 1989 and on November 1994, respectively.

Both SSI models agree very well for the 120-200 nm wavelength range. Discrepancies arise for wavelengths longward of 200 nm, as already discussed in Fig. 2. In the 200-400 nm range, the SATIRE model shows the largest variability, followed by NRLSSI2, and NRLSSI1. This results in a CMIP6 variability that is larger than for CMIP5, 45% as compared to 32% (Fig. 4). In the VIS range this reverses, CMIP6 shows a smaller variability than CMIP5 (30% as compared to 40%). Remarkable is also the very good agreement between NRLSSI2 and SATIRE. In the NIR CMIP6 shows slightly larger variability than CMIP5. The implications of these different spectral variabilities on the atmospheric heating and ozone chemistry and subsequent thermal and dynamical effects with respect to both, climatological differences between CMIP5 and CMIP6 as well as the solar cycle signals in CMIP5 and CMIP6 will be discussed in section 2.1.3.

Figure 5 illustrates the reconstruction of the EUV band by comparing spectra obtained at high and low levels of solar activity, and by showing the historical reconstruction of the band-integrated flux. As explained in Section 2.1.2, we estimate the EUV flux by nonlinear regression from the SSI at longer UV wavelengths, using the first seven years of observations from TIMED/SEE. Not surprisingly, this reconstruction agrees well with the observations from TIMED/SEE. However, by lack of other long-duration EUV observations that are of sufficient radiometric quality, it is very difficult to assess the quality of our reconstruction. For the same reason, multi-decadal variations are poorly constrained, and in particular, the presence of trends remains largely unknown. Note that wavelengths below 28 nm require more caution, since they rely on TIMED/XPS observations that were partly degraded (Woods et al., 2005). One future improvement of our dataset involves reconstructions of the EUV band that are based more advanced models such as NRLEUV2 (Lean et al., 2011).

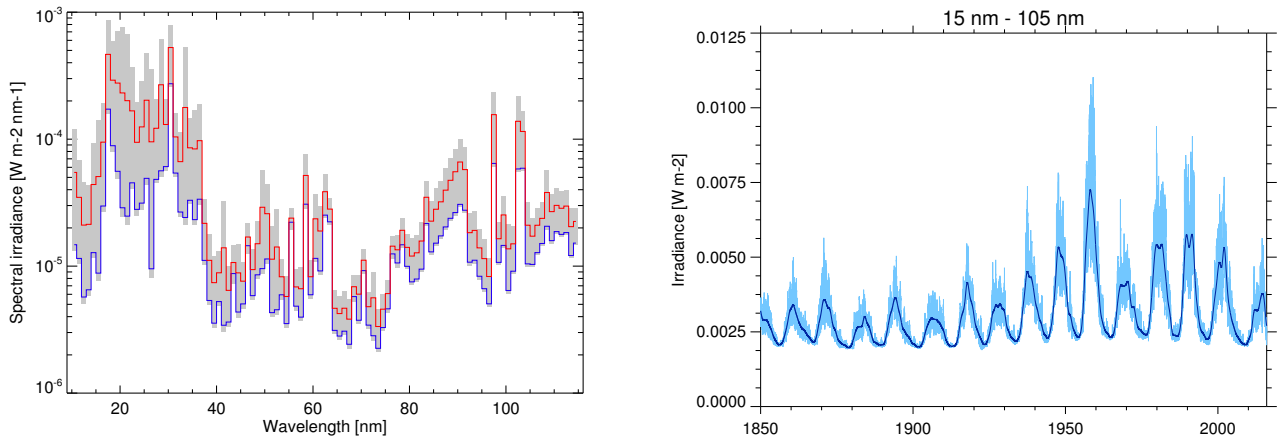


Figure 5. Left: EUV spectra for 20 November 2008 (corresponding to low solar activity conditions, in blue) and 8 February 2002 (corresponding to high solar activity conditions, in red). The full spectral variability range during 1850–2015 is grey-shaded. Right: Time series of the EUV irradiance integrated from 15–105 nm. The thick blue line corresponds to annual averages.

2.1.3 Evaluation of SSI Datasets in Climate Models

Providing a first assessment of implications employing the SSI recommended for CMIP6 in comparison to CMIP5, we present results of two state-of-the-art chemistry climate models (CCM): – the Whole Atmosphere Community Climate Model (CESM1(WACCM); Marsh et al., 2013) – and the ECHAM/MESSy Atmospheric Chemistry model (EMAC; Jöckel et al., 2010, 2016). Additionally, we include results of single-profile radiative transfer calculations performed with the line-by-line radiative transfer code *libradtran* (Mayer and Kylling, 2005). We use the latter to present estimates of direct SW radiative heating impacts neglecting the ozone chemistry feedback which is included in the CCM results.

Chemistry-Climate Model Descriptions

WACCM: The Whole Atmosphere Community Climate Model (version 4; Marsh et al., 2013) is an integrative part of the *Community Earth System Model* suite (version 1.0.6; Hurrell et al., 2013). CESM1(WACCM) is a “high-top” CCM covering an altitude range from the surface to the lower thermosphere, i.e. up to 5×10^{-6} hPa equivalent to approx. 140 km. It is an extension of the *Community Atmospheric Model* (CAM4; Neale et al., 2013) with all its physical parametrisations. For this study the model is integrated with a horizontal resolution of $1.9^\circ \text{lat} \times 2.5^\circ \text{lon}$ and 66 levels in the vertical. CESM1(WACCM) contains a middle atmosphere chemistry module based on the Model for Ozone and Related Chemical Tracers (MOZART3; Kinnison et al., 2007). It contains all members of the O_x , NO_x , HO_x , ClO_x , and BrO_x chemical groups as well as tropospheric source species N_2O , H_2O , CH_4 , CFCs and other halogen components (59 species and 217 gas-phase chemical reactions in total). Its photolysis scheme resolves 100 spectral bands in the UV and VIS range (121–750 nm) (see also Tab. 3). The SW radiation module is a combination of different parametrisations. Above approx. 70 km the spectral resolution is identical to the photolysis scheme (plus the parametrisation of Solomon and Qian, 2005, based on F10.7cm solar radio flux to account for

EUV irradiances). Below approx. 60 km the SW radiation of CAM4 is retained, employing 19 spectral bands between 200 and 5,000 nm (Collins, 1998). For the transition zone (60-70 km) SW heating rates are calculated as weighted averages of the two approaches. Tab. 3 contains an overview of the SW radiation and photolysis schemes in comparison to EMAC, the second CCM utilized for this study. CESM1(WACCM) features relaxation of stratospheric equatorial winds to an observed or
5 idealized Quasi-Biennial Oscillation (QBO; Matthes et al., 2010).

EMAC: The ECHAM/MESSy Atmospheric Chemistry (EMAC) model is a CCM that includes sub-models describing tropospheric and middle atmospheric processes and their interaction with oceans, land and human influences (Jöckel et al., 2010). It uses the second version of the Modular Earth Submodel System (MESSy2) to link multi-institutional computer codes. The core atmospheric model is the 5th generation European Centre Hamburg general circulation model (ECHAM5, Roeckner
10 et al., 2006). For the present study we applied EMAC (ECHAM5 version 5.3.02, MESSy version 2.51, Jöckel et al., 2016) in the T42L47MA-resolution, i.e. with a spherical truncation of T42 (corresponding to a quadratic Gaussian grid of approx. 2.8 by 2.8 degrees in latitude and longitude) with 47 hybrid pressure levels up to 0.01 hPa (~80 km). The applied model setup comprises, among others, the submodels: MECCA, JVAL, RAD/RAD-FUBRAD, and QBO. MECCA (Module Efficiently
15 Calculating the Chemistry of the Atmosphere) (Sander et al., 2011a) provides the atmospheric chemistry model. JVAL (Sander et al., 2014) provides photolysis rate coefficients based on updated rate coefficients recommended by JPL (Sander et al., 2011b). RAD/RAD-FUBRAD (Dietmüller et al., 2016) provides the parameterisation of radiative transfer based on Fouquart and Bonnel (1980) and Roeckner et al. (2003) (RAD). For a better resolution of the UV-VIS spectral band RAD-FUBRAD is used for pressures lower than 70 hPa, increasing the spectral resolution in the UV-VIS from one band to 106 bands (Nissen et al., 2007; Kunze et al., 2014). Tab. 3 presents more details of the SW radiation and photolysis schemes in comparison to WACCM. The
20 submodel QBO is used to relax the zonal wind near the equator towards the observed zonal wind in the lower stratosphere (Giorgetta and Bengtsson, 1999).

CCM Experimental Design

The CCM simulations with CESM1(WACCM) and EMAC are identically conducted in atmosphere-only timeslice configuration. This means, the external forcings such as the solar and the anthropogenic forcing are fixed for the whole simulation
25 period, that is 45 model years plus spin-up (~5 years for EMAC, ~3 years for CESM1(WACCM)). Concentrations of greenhouse gases (GHGs) and ozone-depleting substances (ODS) are set to constant conditions representative for the year 2000. The lower-boundary forcing is specified by the mean annual cycle of SSTs and sea-ice of the decade 1995-2004 derived from the *HadISST1.1*-dataset (Rayner et al., 2003). All simulations are nudged towards an observed (EMAC) or idealized 28-months varying (CESM1(WACCM)) QBO. The only difference between the simulations is in the solar forcing. Four simulations
30 for each of the following SSI datasets have been performed with EMAC and WACCM: CMIP6-SSI, its constituent datasets NRLSSI2 (Coddington et al., 2016) and SATIRE (Krivova et al., 2010; Yeo et al., 2014), as well as NRLSSI1 (Lean, 2000). The latter was recommended as solar forcing for CMIP5 including a uniform scaling of the spectrum to match TSI measurements of the *Total Irradiance Monitor* (TIM) instrument. As one emphasis of this study is to highlight differences to the previous

Table 3. Summary of spectral resolution of the SW radiation and photolysis schemes in EMAC and CESM1(WACCM). Boundaries of spectral intervals and further refinement in brackets when larger than one.

Spectral region	Gases	CESM1(WACCM)	EMAC
SW radiation ^{*,+}			
Lyman- α	O ₂		[121-122]
Schumann-Runge continuum	O ₂		[125-175] (3)
Schumann-Runge bands	O ₂		[175-205]
Herzberg cont./Hartley bands	O ₂ , O ₃	[200-245]	[206.5-243.5] (15)
Hartley bands	O ₃	[245-275] (2)	[243.5-277.5] (10)
Huggins bands	O ₃	[275-350] (4)	[277.5-362.5] (18)
UV-A/Chappuis bands	O ₃	[350-700] (2)	[362.5-690] (58)
Near Infrared/Infrared	O ₂ , O ₃ , CO ₂ , H ₂ O	[700-5000] (10)	[690-4000] (3)
Photolysis			
Lyman- α		[121-122]	[121-122]
Schumann-Runge continuum		[122-178.6] (20)	
Schumann-Runge bands		[178.6-200] (12)	[178.6-202]
Herzberg cont./Hartley bands		[200-241] (15)	[202-241]
Hartley bands		[241-291] (14)	[241-289.9]
Huggins bands		[291-305.5] (4)	[289.9-305.5]
UV-B		[305.5-314.5] (3)	[305.5-313.5]
UV-B/UV-A		[314.5-337.5] (5)	[313.5-337.5]
UV-A/Chappuis bands		[337.5-420] (17)	[337.5-422.5]
Chappuis bands		[420-700] (9)	[422.5-682.5]

^{*}Note that given bands for CESM1(WACCM) apply below ~ 65 km only. The resolution of the SW radiation code above ~ 65 km corresponds to the resolution of the photolysis scheme. ⁺Note that given bands from 121–690 nm for EMAC apply at pressures lower than 70 hPa only. At pressures larger than 70 hPa there is one band extending from 250–690 nm.

phase of CMIP we employed NRLSSI1 including this scaling and refer to it as NRLSSI1(CMIP5) in the following. Runs for each of the four dataset have been performed with both CCMs for a solar minimum timeslice and a solar maximum timeslice, respectively. For solar maximum timeslices, SSIs averaged over Nov. 1989 are used (maximum of solar cycle 22) while for the solar minimum timeslices averages over Nov. 1994 are chosen. The latter does not match the absolute minimum of solar cycle 5 21/22 (Jun. 1996). However, solar activity in Nov. 1994 was already close to the minimum. The differences in solar activity between our solar minimum and solar maximum timeslices for the respective datasets are within a range of 0.988 W/m² for NRLSSI1(CMIP5) to 1.057 W/m² for NRLSSI2.

It should be noted that these experiments will illustrate only one part of solar influence on climate. Given the atmosphere-only set-up of the runs, oceanic absorption of (mainly visible) solar irradiance and subsequent heating and feedbacks to the atmosphere – the so-called bottom-up mechanism (see Gray et al., 2010, and references therein) – is not represented in our simulations. Therefore we focus only on stratospheric signals and "top-down" dynamically induced responses in the troposphere.

5 A second constraint of this study's experimental set-up is the choice of one solar cycle. Solar activity and hence spectral irradiance vary between different solar cycles. However, these differences are relatively small as compared to a typical solar cycle amplitude and will probably not affect the main results of this study. It should also be noted that the timeslice simulations were designed as a sensitivity study to test the impact of the different solar input datasets. They do not represent the full feedbacks of transient CMIP6 simulations.

10 Radiative Transfer Model libradtran

Radiative transfer calculations were performed with the high resolution model libradtran (Mayer and Kylling, 2005), which is a library of radiative transfer equation solvers widely used for UV and heating rate calculations (www.libradtran.org). Libradtran was configured with the pseudo-spherical approximation of the DISORT solver, which accounts for the sphericity of the atmosphere, running in a six-streams mode. Calculations pertain to a cloud- and aerosol-free tropical atmosphere (0.56°N),

15 the surface reflectivity is set to a constant value of 0.1 and effects of Rayleigh scattering are enabled. The atmosphere is partitioned into 80 layers extending from the surface to 80km. The model output is annual averages of spectral heating rates from 120 nm to 700 nm in 1 nm spectral resolution, calculated according to the recommendations for the Radiation Intercomparison of the Chemistry-Climate Model Validation Activity (CCMVal) (Forster et al., 2011). As for the CCM simulations described above, calculations of the heating rates were performed for CMIP6-SSI, SATIRE, NRLSSI2 and NRLSSI1(CMIP5). The same
20 climatological ozone profile is specified for both solar maximum and minimum conditions in order to assess the direct effects in atmospheric heating by SSI variations only. As such, the line-by-line calculations do not take into account the positive ozone feedback with the solar cycle and SW heating rate changes are expected to be weaker compared to the signatures in the two CCM simulations.

Methods

25 The analyses presented in the following consist of differences between climatologies derived from the various simulations. Given the timeslice configuration of the CCM runs with all external forcings equal except for the SSI dataset, we assume that statistically significant differences of two climatologies are the result of the differing solar irradiance forcings. Confidence intervals (95%) as presented in Figs. 6 and 8 as well as statistical significances ($p < 5\%$) as marked in Figs. 10 and 11 are based on 1000-fold bootstrapping. Confidence intervals in Figs. 6 and 8 are only given for the CCM-results related to CMIP6 SSI.

Climatological Differences to CMIP5

Although all solar irradiance reconstructions subject to this analysis agree fairly well in TSI (see Fig. 1), they disagree significantly with respect to the spectral distribution of energy input, i.e. the shape of the solar spectrum. This is obvious from the offsets noted in Fig. 2 for the different spectral regions above 200 nm. Hence, we focus first on the climatological differences between the solar forcing in CMIP5 and CMIP6. We therefore compare the minimum timeslice simulations from the two CCMs and libradtran in Fig. 6 with respect to the climatological annual mean SW heating rates, as well as the temperatures, and ozone concentrations between the two CCMs resulting from CMIP6-SSI, NRLSSI2, and SATIRE, respectively, as differences to equivalent simulations forced by NRLSSI1(CMIP5). The profiles represent the tropical (averaged over 25°S-25°N) stratosphere and mesosphere (100–0.01 hPa) for annual mean conditions for the CCMs and libradtran.

Employing CMIP6-SSI results into significantly decreased radiative heating of large parts of the mesosphere and stratosphere (above 10 hPa) compared to NRLSSI1(CMIP5). Whereas the largest differences can be found at the stratopause with approx. -0.35 K/day according to both CCMs, and even more -0.42 K/day for libradtran (without any ozone chemistry feedback), libradtran and EMAC yield slightly increased SW heating rates below ~7 hPa and 10 hPa, respectively. This weaker SW heating in the new CMIP6 SSI dataset in the upper stratosphere and the stronger heating in the lower stratosphere are confirmed by the wavelength dependent percentage changes between the CMIP6 and CMIP5 SSI datasets with respect to the radiation and photolysis schemes (Fig.7). Regardless of the number of bands in the radiation code, both models show a smaller percentage difference of -5% below about 300nm and weaker or negligible differences above 300nm (Fig.7).

Significant differences in radiative heating throughout the stratosphere related to the three state-of-the art SSI reconstructions are produced only with radiation codes of high spectral resolution such as in libradtran or – to a lesser degree – in EMAC (for the middle to lower stratosphere). Comparisons between CMIP6-SSI and its constituents NRLSSI2 and SATIRE in WACCM and EMAC lead to the conclusion that the choice of the CCM and its specific radiation and photolysis scheme is more important than the choice of the SSI dataset with respect to SW heating rates. In addition the ozone chemistry damps the SW heating response in the CCMs as compared to libradtran which misses the ozone feedback. Less SW radiation below 300nm reduces ozone production (note also the reduced photolysis rates around 240nm in Fig.7) and hence less ozone is available to absorb SW radiation and results in a relative cooling of the upper stratosphere.

Corresponding to the SW heating rate differences, large parts of the stratosphere and mesosphere are significantly cooler (up to -1.6K at the stratopause) in simulations using CMIP6-SSI compared to NRLSSI1(CMIP5) irradiances. Note that libradtran results are shown for the SW heating rate differences only, as temperature and ozone profiles are prescribed for the radiative transfer calculations. No significant differences in temperature are found when employing NRLSSI2 or SATIRE instead of CMIP6-SSI in CESM1(WACCM) which has a coarser spectral resolution in the SW heating parameterization than EMAC (Tab.3 and Fig.7). EMAC instead simulates significantly lower (higher) temperatures in the stratosphere when using NRLSSI2 (SATIRE) than CMIP6-SSI forcing and in general a warmer stratosphere (and cooler stratopause and mesosphere) than CESM1(WACCM).

The impact of CMIP6-SSI as compared to NRLSSI1(CMIP5) irradiance changes on ozone are more complicated. In the middle tropical stratosphere, ozone concentrations are significantly lower (peaking at ~ 7 hPa with approx. -3.2%). In contrast, ozone concentrations around the stratopause are significantly higher for CMIP6-SSI ($+0.8\%$ and $+1.6\%$ according to EMAC and CESM1(WACCM), respectively) than under NRLSSI1(CMIP5) irradiances. Despite the considerable differences in spectral resolution of the photolysis schemes (Tab.3 and Fig.7)), for larger parts of the stratosphere below about 3hPa, CESM1(WACCM) and EMAC agree fairly well. For both models the SATIRE irradiances show larger signals than NRLSSI2 irradiances with the signal for CMIP6 in between. The ozone signals start to differ at and above the stratopause, probably due to the more detailed photolysis code and the higher model top in CESM1(WACCM) as compared to EMAC. The ozone signal is much more uncertain with respect to the different SSI forcings than the SW heating rate and the temperature signals.

In summary, the CMIP6-SSI irradiances lead to lower SW heating rates, lower temperatures as well as smaller ozone signals in the lower stratosphere and larger ozone signals in the upper stratosphere and lower mesosphere than the CMIP5-SSI irradiances. Differences between the three tested SSI datasets occur in the SW heating rates only with a very high spectral resolution of the radiation code (libradtran, EMAC) and more prominent for ozone in a similar way for both CCMs, i.e. stronger effects occur for SATIRE than NRLSSI2. These direct radiative effects in the tropical stratosphere lead to a weakening of the meridional temperature gradient and hence to a statistically significant weakening of the stratospheric polar night jet in early winter (not shown).

Impacts of Solar Cycle Variability

The second question tackled by this evaluation is the atmospheric impact of the 11-year solar cycle using different SSI irradiance reconstructions. A special focus lies on the comparison of the new CMIP6 dataset with its predecessor NRLSSI1(CMIP5). Fig. 8 provides annual mean tropical (25°S - 25°N) profiles analogue to Fig. 6 but now illustrating differences between perpetual solar maximum and perpetual solar minimum conditions according to simulations forced by the various SSI-datasets.

All models and SSI-forcings produce the well-known solar cycle impact of enhanced SW heating at solar maximum throughout the upper stratosphere and mesosphere. Differences to solar minimum forcing peak at the stratopause with approx. $+0.19$ to $+0.23$ K/day. Only the libradtran-calculations – that do not include any ozone-feedback – yield considerably weaker responses.

According to libradtran and CESM1(WACCM), CMIP6-SSI produces slightly higher SW heating rate differences than NRLSSI1(CMIP5). However, for EMAC this is not the case. For both CCMs and libradtran, the usage of SATIRE leads to strongest solar cycle induced SW heating rate signals, while NRLSSI2 is associated with the weakest response (though not significantly different from NRLSSI1(CMIP5) for EMAC and libradtran).

Temperatures in the tropical stratosphere and mesosphere are generally higher during solar maximum than during phases of low solar activity. A local maximum of temperature differences is found at the stratopause with positive differences of 0.8 - 1.0 K compared to solar minimum. According to both CCMs, CMIP6-SSI forcing yields slightly higher temperatures (up to $+0.2$ K in the mesosphere in CESM1(WACCM)) for the stratopause region and the (lower) mesosphere than NRLSSI1(CMIP5). However, most of these differences are statistically not significant. Comparing CMIP6-SSI-forced results with its components NRLSSI2 and SATIRE yields heterogeneous results. According to EMAC, NRLSSI2 leads to a slightly weaker so-

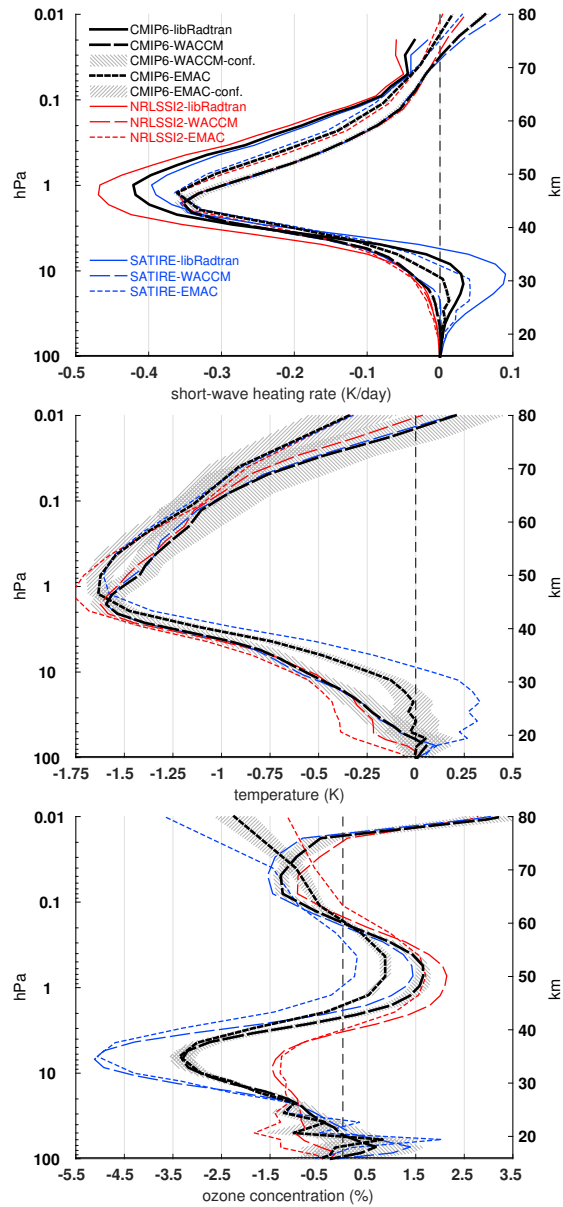


Figure 6. Impact of solar forcing for perpetual solar minimum conditions according to CMIP6 (black) as well as constituent NRLSSI2 (red) and SATIRE (blue) datasets on climatological (annual mean) profiles of SW heating rates (top), temperature (center), and ozone concentrations (bottom) averaged over the tropics (25°S – 25°N) when compared to NRLSSI1(CMIP5) solar forcing; derived from simulations with CESM1(WACCM) (long-dashed), EMAC (short-dashed), and libradtran radiative transfer calculations (solid, only top panel) only shown for SW heating rates; 95% confidence intervals for CMIP6 simulations (hatched) estimated by bootstrapping.

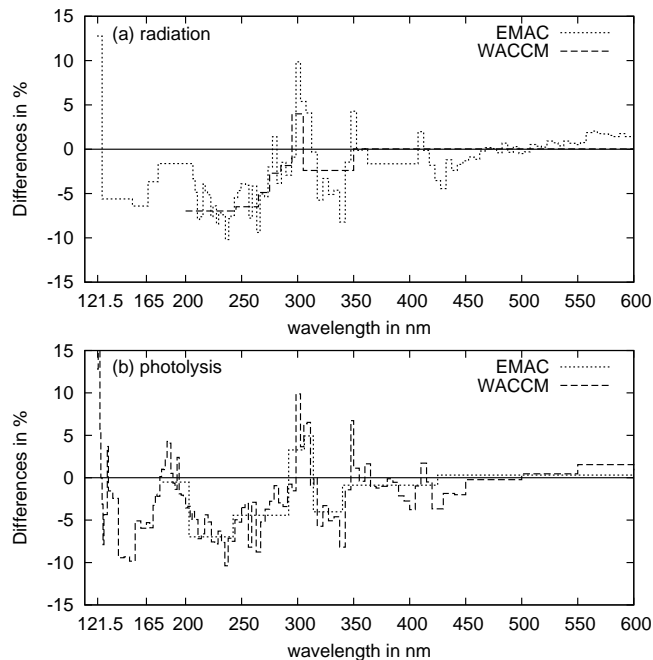


Figure 7. CMIP6 SSI differences of the solar irradiance in % for perpetual solar minimum conditions compared to CMIP5(NRLSSI1). Top: in the spectral resolution of the radiation schemes; bottom: in the spectral resolution of the photolysis schemes of EMAC (short-dashed) and CESM1(WACCM) (long-dashed).

lar cycle response throughout the stratosphere, while the mesospheric response is stronger than SATIRE and CMIP6-SSI. CESM1(WACCM)-results show that the stratospheric (up to approx. 2 hPa) solar cycle response to CMIP6-SSI-forcing in temperature is slightly weaker than in both, NRLSSI2- and SATIRE-driven simulations. As opposed to that, simulations forced by SATIRE and CMIP6-SSI yield very similar warming signals in the mesosphere while NRLSSI2 produces a (significantly) weaker response in the mesosphere.

The solar cycle signal in ozone is very consistent for most parts of the stratosphere and mesosphere with respect to the SSI datasets. More important for the solar ozone signals seems to be the choice of the CCM (with its specific photolysis scheme, see also Fig. 9), especially for the lower stratosphere (10 hPa and below). In the lower mesosphere however, the dataset induced differences are larger than the model-induced ones. All analyzed combinations of CCMs and forcing datasets agree very well on the (relative) peak of the ozone response (+2.3-2.5%) to the solar cycle at 3-5 hPa. In the lower mesosphere (0.2-1 hPa) CMIP6-SSI (and SATIRE) lead to a significantly weaker solar cycle ozone response (+0.3-0.5% at 0.5 hPa) than NRLSSI1(CMIP5) (and NRLSSI2; +0.6-0.8% at 0.5 hPa). For the lower stratosphere (below 7 hPa) both CCMs agree that SATIRE leads to strongest solar cycle ozone signals, though still within the uncertainty associated with CMIP6-SSI-forced simulations. The comparison between CMIP6-SSI and NRLSSI1(CMIP5) yields no unequivocal result: CESM1(WACCM) exhibits a secondary maximum ozone response at approx. 70 hPa that is weaker with CMIP6-SSI than with NRLSSI1(CMIP5)

while the opposite is seen in EMAC. Given the large uncertainty in the lower stratospheric solar ozone signal, we can only conclude that the signal is positive.

In summary, the CMIP6-SSI irradiance forcing leads to slightly enhanced solar cycle signals in SW heating rates, temperatures as well as ozone than the CMIP5-SSI irradiance forcing. In general, differences between the different SSI datasets are statistically not significant. Note that statistically significant differences in the irradiance amplitude between CMIP5 and CMIP6-SSI irradiances are particularly observed between 300 and 350nm, a wavelength region important for ozone destruction (below 320nm) consistently in both CCMs (Fig. 9).

The direct radiative effects in the tropical stratosphere from the CMIP6-SSI dataset, i.e. enhanced solar cycle signals in SW heating rates, temperatures, and ozone in the tropical upper stratosphere lead to the expected strengthening of the meridional temperature gradient and hence to a statistically significant stronger stratospheric polar night jet which propagates poleward and downward during winter from December through January (Fig. 10) and significantly affects the troposphere with a positive AO-like signal developing in late winter, i.e. January and February (Fig. 11). This signal is very similar and statistically significant for both CCMs, therefore the ensemble mean of both models is shown. Besides the radiative impact of the solar cycle, also energetic particles have an impact on the atmosphere and will be discussed in the following.

2.2 Particle Forcing

Precipitating energetic particles ionize the neutral atmosphere leading to the formation of NO_x ($[\text{N}] + [\text{NO}] + [\text{NO}_2]$) and HO_x ($[\text{H}] + [\text{OH}] + [\text{HO}_2]$) (Porter et al., 1976; Rusch et al., 1981; Solomon et al., 1981) as well as of some more minor species (Verronen et al., 2008; Funke et al., 2008; Winkler et al., 2009; Verronen et al., 2011a; Funke et al., 2011) due to both dissociation and ionization of the most abundant species, as well as due to complex ion chemistry reaction chains. The formation of NO_x and HO_x radicals leads to catalytic ozone loss that further triggers changes of the thermal and dynamical structure of the middle atmosphere. Energetic Particle Precipitation (EPP) introduces thus chemical changes to the middle atmospheric composition and can therefore only be considered explicitly in climate simulations that employ interactive chemistry. In the following we provide recommendations for the consideration of EPP effects in CCMs separately for auroral and radiation belt electrons (Sec. 2.2.1), for solar protons (Sec. 2.2.2), and for galactic cosmic rays (Sec. 2.2.3). In most cases, particle forcing can be expressed in terms of ion pair production rates. Recommendations for their implementation into chemistry schemes are provided in Sec. 2.2.4.

2.2.1 Geomagnetic Forcing (Auroral and Radiation Belt Electrons)

Energetic particles are trapped in the space around the Earth dominated by the geomagnetic field (known as the magnetosphere). The loss of electrons into the atmosphere is termed “electron precipitation”. Due to the Earth’s magnetic field configuration electron precipitation occurs mainly in the polar auroral and sub-auroral regions, i.e., at geomagnetic latitudes typically higher than 50° . Enhanced loss fluxes are associated with geomagnetic storms, which can occur randomly, and also with periodicity’s ranging from the ~ 27 day solar rotation to the 11-year solar cycle, and even to multi-decadal timescales. The altitudes at which precipitating electrons deposit their momentum are dependent on their energy spectrum, with lower energy particles impacting

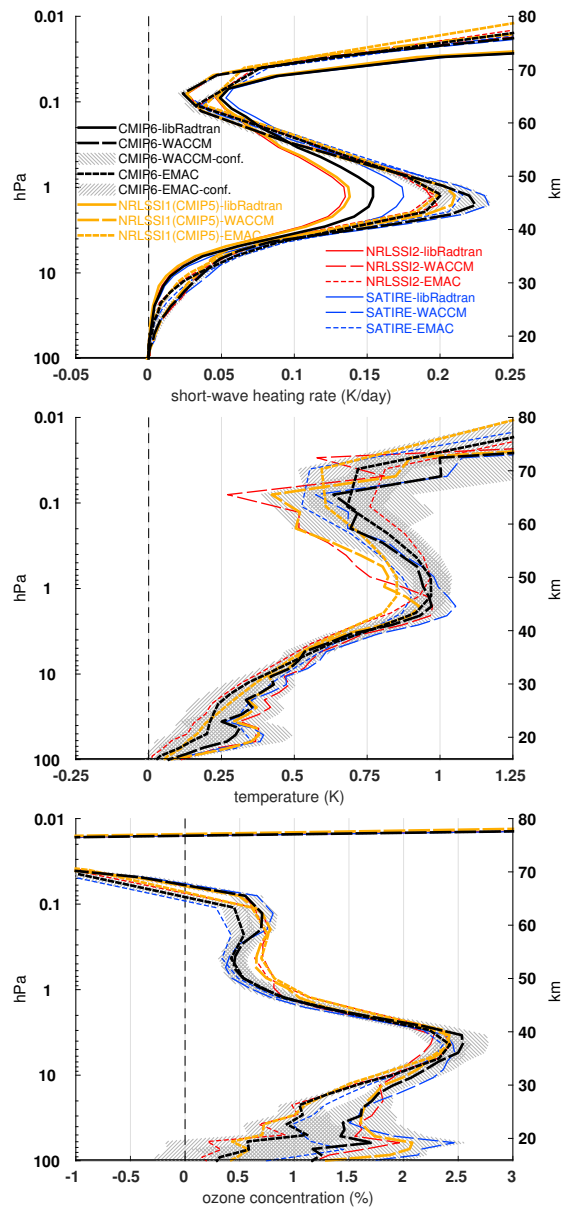


Figure 8. Impact of the 11-year solar cycle (differences between perpetual solar maximum and solar minimum experiments) on climatological (annual mean) profiles of shortwave heating rates (top), temperature (center), and ozone concentrations (bottom) averaged over the tropics (25°S – 25°N) according to CMIP6 (black) and CMIP5 (yellow) solar forcing as well as NRLSSI2 (red) and SATIRE (blue) derived from simulations with CESM1(WACCM) (long-dashed), EMAC (short-dashed), and libradtran radiative transfer calculations (solid; only in the top panel); 95% confidence intervals for CMIP6 simulations (hatched) estimated by bootstrapping.

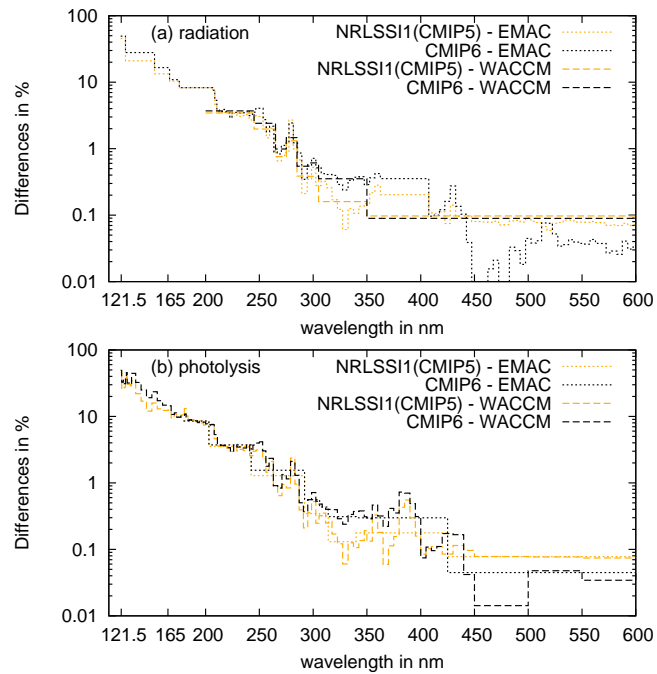


Figure 9. SSI differences in % for the solar amplitude between perpetual solar maximum and perpetual solar minimum conditions. Top: in the spectral resolution of the radiation schemes; bottom: in the spectral resolution of the photolysis schemes of EMAC (short-dashed) and CESM1(WACCM) (long-dashed).

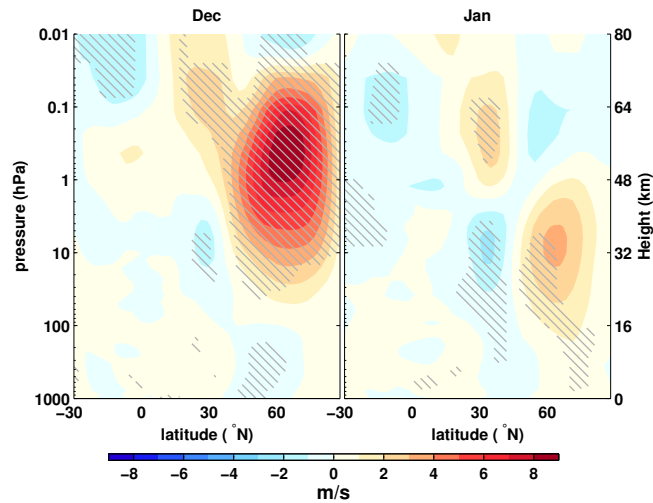


Figure 10. Zonal mean zonal wind response to the 11-year solar cycle according to CMIP6-SSI in December and January as “ensemble mean” of CESM1(WACCM) and EMAC simulations; hatched areas denote statistical significances ($p < 5\%$) of shown differences.

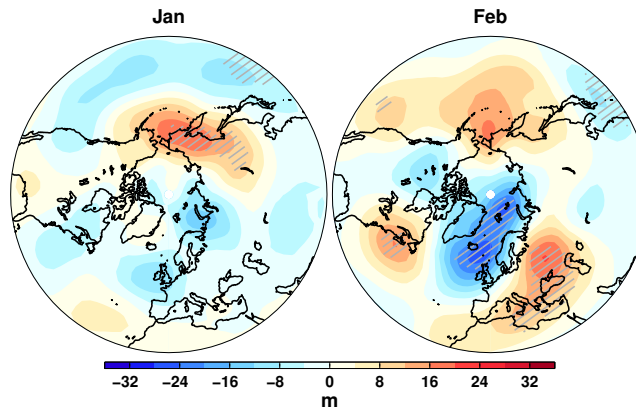


Figure 11. 500 hPa geopotential height response to the 11-year solar cycle according to CMIP6-SSI in January and February as “ensemble mean” of CESM1(WACCM) and EMAC simulations; hatched areas denote statistical significances ($p < 5\%$) of shown differences.

the atmosphere at higher altitudes than those with higher energies (e.g. Turunen et al., 2009). Auroral electrons, originating principally from the plasma sheet, have energies < 10 keV and affect the lower thermosphere (95–120 km). Processes that occur in the outer radiation belt typically generate mid-energy electron (MEE) precipitation within the energy range ~ 10 keV to several MeV, affecting the atmosphere at altitudes of ~ 50 –100 km (Codrescu et al., 1997).

5 Odd nitrogen, produced by precipitating electrons, is long-lived during polar winter and can then be transported down from its source region into the stratosphere, to altitudes well below 30 km. This has been postulated already by Solomon et al. (1982) and observed many times (Callis et al., 1996; Randall et al., 1998; Siskind, 2000; Funke et al., 2005; Randall et al., 2007). This so-called EPP “indirect effect” contributes significant amounts of NO_y to the polar middle atmosphere during every winter in both hemispheres, however, with varying magnitude ranging from a few percent up to 40% (Randall et al., 2009; Funke et al.,
 10 2014a). Its consideration in climate models with their upper lid in the mesosphere, thus not covering the entire EPP source region, requires the implementation of an upper boundary condition (UBC) that accounts for the transport of NO_x into the model domain, as discussed below.

Stratospheric ozone loss due to electron-induced NO_x production in the upper mesosphere /lower thermosphere and subsequent downward transport has been postulated by model experiments many times (Solomon et al., 1982; Schmidt et al., 2006;
 15 Marsh et al., 2007; Baumgaertner et al., 2009; Reddmann et al., 2010; Semeniuk et al., 2011; Rozanov et al., 2012). However, observational evidence for EPP-induced variations of stratospheric ozone linked to geomagnetic activity, **characterised**
characterized by a negative anomaly moving down with time during polar winter, have been given only very recently (Fytterer et al., 2015a; Damiani et al., 2016).

In addition, mesospheric ozone effects have been observed (Andersson et al., 2014a; Fytterer et al., 2015b) which are caused
 20 by HO_x increases during MEE precipitation (Verronen et al., 2011b). Although the HO_x -driven response is short-lived, the frequency of MEE events is large enough to cause solar cycle variability in ozone (Andersson et al., 2014a). HO_x response is seen at magnetic latitudes connected to the outer radiation belts, with e.g. the yearly amount of HO_x varying with the observed

magnitude of precipitation (Andersson et al., 2014b). The consideration of the effects of MEE on atmospheric species other than NO_x , HO_x , and ozone have not been investigated in detail to date, but they can be expected to be qualitatively similar to those caused by solar proton events (SPEs) (Verronen and Lehmann, 2013).

5 The impact of magnetospheric particles on the atmosphere is strongly linked to the strength of geomagnetic activity; this has been shown both for the direct production of NO in the thermosphere (Marsh et al., 2004; Hendrickx et al., 2015) and mesosphere (Sinnhuber et al., 2016), for mesospheric OH production (Fytterer et al., 2015b), and for the EPP indirect effect (Sinnhuber et al., 2011; Funke et al., 2014a). Geomagnetic activity can be constrained over centennial time scales by means of proxy data provided by geomagnetic indices. Since our forcing dataset for magnetospheric particle precipitation relies on these indices, their reconstruction and homogenisation is discussed first.

10 Reconstruction of Geomagnetic Indices

Geomagnetic indices provide a measure of the level of geomagnetic activity resulting from the response of the magnetosphere-ionosphere system to variability in the solar and near-Earth solar wind forcings. Many geomagnetic indices have been constructed and different indices are sensitive to different aspects of magnetospheric and ionospheric dynamics (Mayaud, 1980). The Kp and Ap geomagnetic indices (Bartels, 1949) are directly related by a quasi-logarithmic conversion; they are proxies for the global level of geomagnetic activity, and are used as inputs to parameterisations of magnetospheric particle precipitation. For the historical solar forcing data, daily values of the Kp and Ap indices from 1850 to 2014 are required. However, these indices, as provided by the International Service of Geomagnetic Indices (<http://isgi.unistra.fr/>), have only been produced from 1932 onwards. It is not possible to directly and consistently extend the Kp and Ap indices prior to 1932, as they use data from 13 geomagnetic observatories around the globe, and these data are unavailable further back in time. So, before 1932 the Kp and Ap indices must be estimated from other geomagnetic indices. The aa index (Mayaud, 1972) is the most appropriate choice, as it was constructed to be as similar as possible to the Ap index on annual timescales (Lockwood et al., 2013). However, the original aa-index only extends back to 1868 (also available from <http://isgi.unistra.fr/>), and so an extension (Nevanlinna, 2004) to the aa-index is also employed, extending it back to 1844 by use of the Ak indices from the Helsinki geomagnetic observatory, spanning 1844–1912. In addition, we implement a correction to the aa-index to account for a change in the derivation of the index in 1957, see (Lockwood et al., 2014).

On larger than annual timescales, the response of the aa and Ap indices is similar, and the indices are positively linearly correlated. However, on daily timescales the relationship between aa and Ap is not linear, and also displays a regular annual variation. Therefore, to estimate the daily Ap indices during the period 1868–1931, we used piecewise polynomial fits between the daily Ap and aa values for the period 1932 — present, for each calendar month. These fits were then extrapolated to estimate the Ap values between 1868 and 1931 from the aa values. This process was repeated to estimate the relationship between the Ak indices provided by Nevanlinna (2004), and the Ap values estimated from the aa index. The piecewise polynomial fits for each calendar month were calculated using the overlap period between the Ak and estimated Ap records, 1868–1912. These were then extrapolated to estimate Ap in the period 1850–1867. Figure 12 shows the time series of the reconstructed Ap index and the aa and Ak indices used for extension back to 1850.

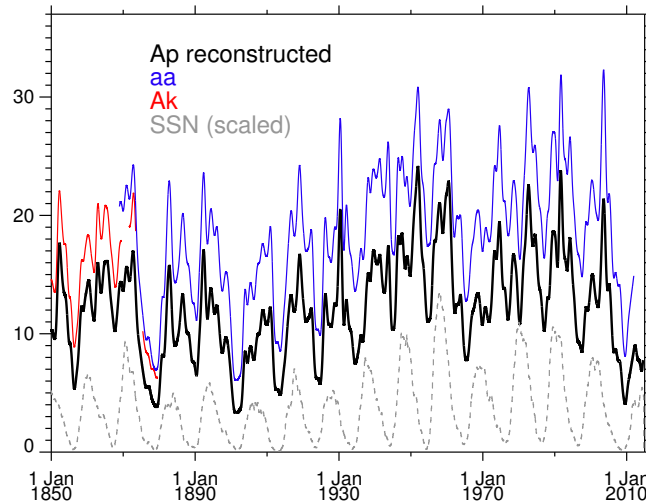


Figure 12. Time series of the reconstructed Ap index (black), together with the aa (blue) and Ak (red) indices used for its reconstruction, with comparison to the sunspot number variability (SSN scaled by a factor of 0.067, grey dashed). All the data have been smoothed with a 365-day running mean. Note that the reconstructed Ap includes the original Ap data from the International Service of Geomagnetic Indices since 1932.

The daily Kp index for the period 1868–1931 was estimated by using the monthly piecewise polynomial aa-Ap fits to estimate the 3-hourly ap-index values from the aa index values. These 3-hour ap values were then converted to the corresponding Kp indices, from which the daily mean was calculated. Since only daily Ak data is available, such an approach is not possible for the period 1850–1867, and so here the daily estimates of Ap, derived from Ak, are directly converted into daily Kp. The quasi-logarithmic nature of the conversion between the hourly Kp and ap indices, means that calculating daily values of Kp in this manner results in lower values than the standard method of averaging the eight 3-hourly values in a day, resulting in a slight bias in the Kp estimates. A statistical correction for this bias was employed by estimating the bias using the difference between the aa-derived Kp and the Ak-derived Kp for the period 1868–1912. The estimated bias was then subtracted from the Ak-derived Kp estimates for the period 1850–1867.

10 Auroral Electrons

Lower thermospheric nitric oxide production by auroral electron precipitation can only be considered explicitly in CCMs extending up to 120 km or higher. There were only a few Earth system models of this characteristic in CMIP5 and it is expected that the number of such models will not increase significantly within CMIP6. Most of the models falling into this category use parameterizations for the calculation of auroral ~~ionisation~~ ionization rates or NO productions in the polar cusp and polar cap (Schmidt et al., 2006; Marsh et al., 2007). Those parameterisations are typically driven by geomagnetic indices and we hence recommend the use of the extended Ap or Kp time series described above.

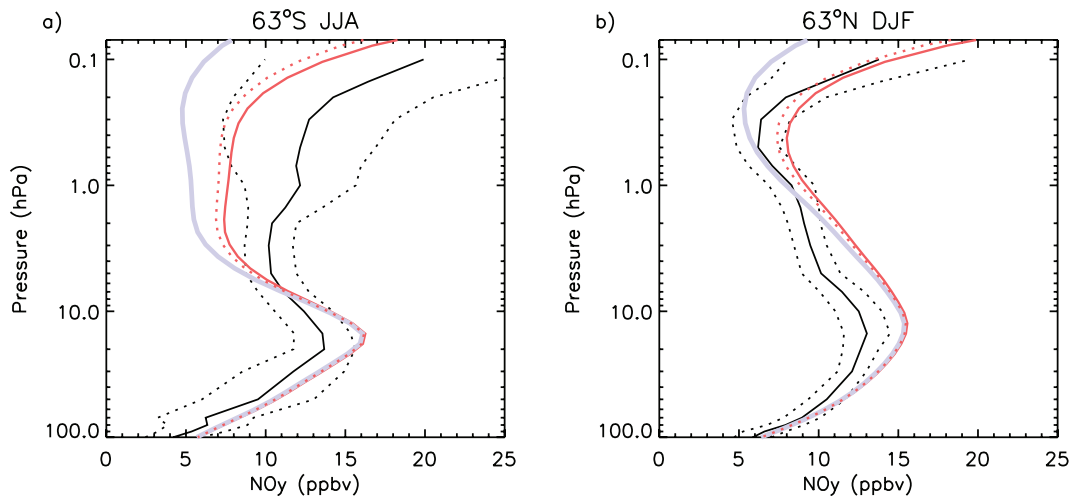


Figure 13. Comparison of 2004–2009 wintertime polar NO_y climatology between ACE-FTS observations and SD-WACCM simulations. Solid black line is ACE, black dots are the average standard deviation of the monthly means. Grey line is WACCM with weak transport of auroral NO_y from the lower thermosphere and no mesospheric production by medium energy electrons (MEE), dot-red line is stronger NO_x transport but no production by MEE, red line is stronger NO_x transport and production by MEE.

Figure 13 demonstrates the improvement in 2004–2009 wintertime polar NO_y [modelling-modeling](#) when production due to electron precipitation is included. The simulations are from the SD-WACCM model version 4 (Marsh et al., 2013) nudged to the NASA Global Modeling and Assimilation Office Modern-Era Retrospective Analysis for Research and Applications (MERRA) (Rienecker et al., 2011) dynamics, and they are compared to observations from the ACE-FTS instrument (Jones et al., 2011). The auroral electron contribution was calculated with a Kp-based parameterisation and was further controlled through eddy diffusion affecting the NO_x descent from lower thermosphere. MEE [ionisation-ionization](#) and NO_x production was calculated using electron flux observations from the NOAA SEM-2 medium energy proton and electron detector (MEPED) instrument onboard the POES spacecraft (Evans and Greer, 2000), using methods described in more detail in the following MEE section. Enhancing the transport of auroral NO_x from the lower thermosphere and including the mesospheric NO_x production by MEE clearly improves the wintertime NO_y near the stratopause. Around 0.1 hPa, modelled NO_y increases by 100% in both hemispheres, which leads to better agreement with ACE-FTS. Both auroral electrons and MEE have a clear impact, although the auroral contribution is larger. However, it should be noted that 2004–2009 was a period of weak MEE in general, and during other periods of stronger MEE the contributions become more equal such that the effect on model NO_y is stronger (not shown).

15 Mid-Energy Electrons (MEE) from the Radiation Belts

Highly energetic particles trapped in the radiation belts mainly consist of electrons and protons, forming inner and outer belts separated by a "slot" region (Van Allen and Frank, 1959). The outer radiation belt (located 3.5–8 Earth radii from the Earth's

centre) is highly dynamic, with electron fluxes changing by several orders of magnitude on timescales of hours to days (e.g. Morley et al., 2010). These changes are caused by the acceleration and loss of energetic electrons, through enhancements in radial diffusion and wave-particle interactions, during and after geomagnetic storms (e.g. Reeves et al., 2003). Storm-driven dynamic variations in the underlying cold plasma density influence the effectiveness of such processes in different regions of the inner magnetosphere (e.g. Summers et al., 2007).

In order to ~~characterise~~characterize the electron precipitation into the atmosphere since 1850 it is necessary to develop a model that uses in-situ satellite observations from the modern era. The most comprehensive, long-duration, and appropriate set of observations are provided by the NOAA SEM-2 MEPED instrument onboard the POES spacecraft (Evans and Greer, 2000; Rodger et al., 2010a). The MEPED instrument covers an energy range from 50 eV to 2700 keV. In this study we are primarily concerned with measurements made with the three medium energy integral electron detectors, i.e., >30, >100, and >300 keV, as the lower "auroral" energy range has been well ~~characterised~~characterized in previous work. The SEM-2 instrument has been flown on low-Earth orbiting (~800 km) Sun-synchronous satellites since 1998, with up to 6 instruments operating simultaneously on occasion. Electron precipitation fluxes from the outer radiation belt are measured with the 0° detectors, which are mounted approximately parallel to the Earth-centre-to-satellite vector.

Improved calibration of the SEM-2 detectors has been undertaken by Yando et al. (2011) using ~~modelling~~modeling techniques contained in the GEANT-4 code to determine the detector geometric conversion factor, or detector efficiency (following the original work described in Evans and Greer, 2000).

Further treatment of the data requires correction for the false counts caused by incident proton fluxes, which we undertake using the technique described in Lam et al. (2010). These calibration and corrections have been tested through comparison with other satellite (e.g. Whittaker et al., 2014b) and ground-based observations (e.g. Rodger et al., 2013; Neal et al., 2015). We convert the satellite position into the geomagnetic latitude parameter L (McIlwain, 1961) using the International Geomagnetic Reference Field IGRF (see Appendix C), and bin the precipitating flux data into zonal means with 0.25 L resolution from L = 2–10 (40–75° geomagnetic latitude).

Using observed electron flux data in 2002–2012, a precipitation model for radiation belt electrons was created by van de Kamp et al. (2016). The precipitation model was fit to the corrected observations of the MEPED/POES detectors following the approach outlined in Whittaker et al. (2014a). In the CMIP6 application of this model, the Ap index is used as the driving input parameter. Ap defines the level of magnetospheric disturbance and the location of the plasmapause, both of which are needed to calculate precipitating electron fluxes at different magnetic latitudes. Thus, the reconstructed Ap record, as described earlier, can be readily used to create a continuous electron precipitation time series for the whole CMIP6 period. As output, the model provides daily spectral parameters of precipitation: integrated flux at energies above 30 keV and a power-law spectral gradient. A test of high-energy resolved precipitating electron flux measurements made by the DEMETER satellite found that the power-law fit consistently provides the best representation of the flux (Whittaker et al., 2013). The model output has been shown to compare well with the spectral parameters derived from POES satellite data (van de Kamp et al., 2016).

An atmospheric ~~ionisation~~ionization data set has been calculated based on the Ap-based precipitation model, using a computationally fast ~~ionisation~~ionization parameterisation (Fang et al., 2010) and atmospheric composition from the NRLMSISE-00

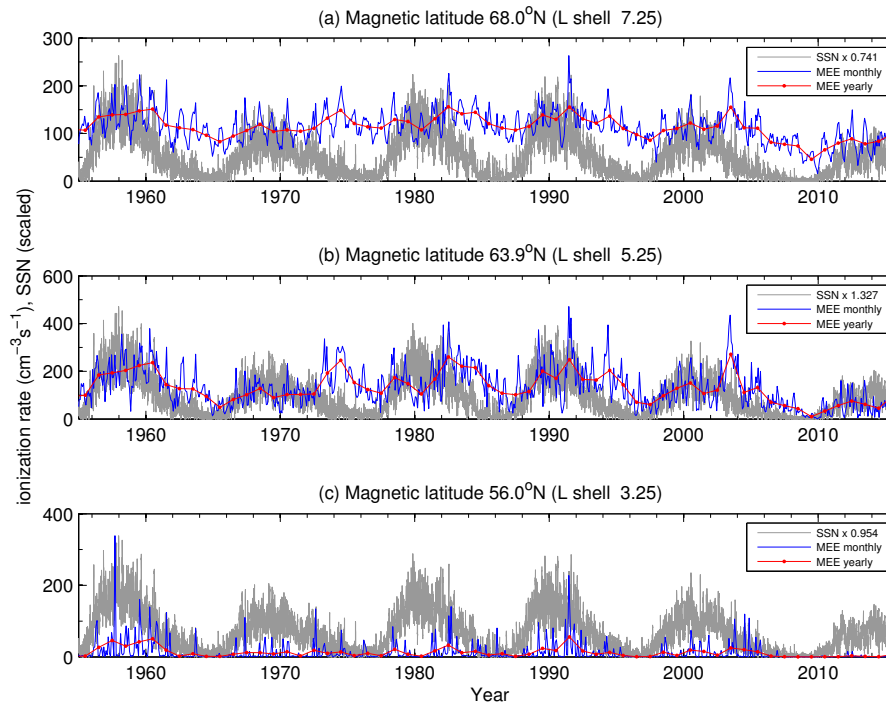


Figure 14. Examples of solar cycle variability of modeled, Ap-driven MEE ionization at ≈ 80 km altitude, with comparison to the sunspot number variability (SSN, scaled).

model (Picone et al., 2002). This calculation considered MEE (30–1000 keV) with maximum energy deposition at altitudes between about 60 and 90 km (van de Kamp et al., 2016). Note that the ionization parameterisation does not consider the contribution of Bremsstrahlung which could be significant only at altitudes below 50 km (Frahm et al., 1997).

Figure 14 shows examples of solar cycle variability of the modeled atmospheric MEE ionization rates at ≈ 80 km altitude. At 68° magnetic latitude (L shell 7.25), MEE precipitation is mostly driven by magnetic substorms and the solar cycle variability is relatively weak, except in around 2009 and the mid 1960s when extended periods of very low geomagnetic activity occurred. At 64° (L shell 5.25), precipitation is driven by high-speed solar wind streams. A more clear solar cycle variability can be seen with maximum ionization lagging the sunspot maximum by 1–2 years. At 56° (L shell 3.25), precipitation is mainly driven by coronal mass ejections which lead to more of an event-type behavior. Relatively infrequent ionization peaks are contrasted with long periods of very low ionization. Similar behavior is seen at other altitudes as well (not shown).

In the following, we demonstrate with examples the MEE impact in WACCM simulations. The purpose is to present a proof of concept, i.e., show that the MEE ionization data set can be used in chemistry-climate modeling, and is producing the expected direct effect in the mesosphere. We simulated the 2002–2012 period, including the Ap-driven MEE **ionisation ionization** rates, and analysed mesospheric OH and ozone responses at 0.040–0.015 hPa (approx. 70–80 km in altitude). This altitude region was selected because of the clear and direct MEE impact seen in satellite observations (e.g. Andersson et al.,

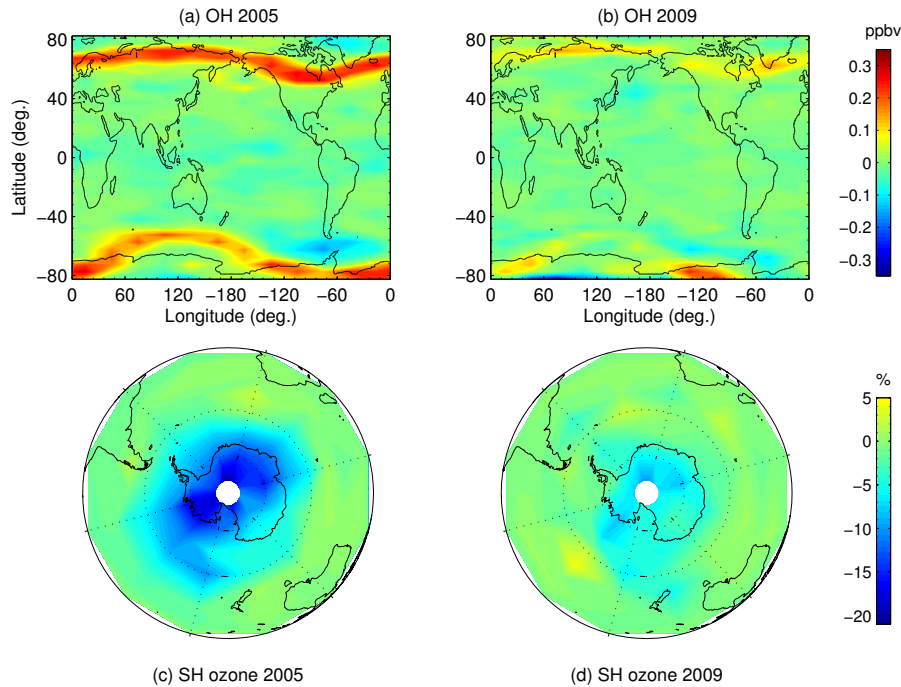


Figure 15. (a) and (b) Difference in yearly median OH mixing ratios at about 70–80 km between SD-WACCM runs with and without MEE ionization. (c) and (d) Relative differences in Southern Hemispheric wintertime mean O_3 at about 70–80 km between SD-WACCM runs with and without MEE ionization.

2014a, b; Fytterer et al., 2015b; Sinnhuber et al., 2016). WACCM version 4 (see above) was used with $1.9^\circ \times 2.5^\circ$ horizontal resolution extending from the surface to 5.9×10^{-6} hPa (≈ 140 km geometric height) in the specified dynamics mode, nudged to MERRA reanalysis at every dynamics time step below about 50 km.

Figures 15a and 15b show global differences in yearly median OH mixing ratios due to MEE. Distinct features on the map are the stripes of enhanced values at magnetic latitudes between 55° and 75° (both hemispheres) which connect through the magnetic field to the outer radiation belt. The impact decreases from 2005 to 2009 due to the decline in geomagnetic activity and MEE precipitation (as shown in Figure 14). These features are of expected quality and magnitude, and similar to those based on Microwave Limb Sounder (MLS) data analysis (Andersson et al., 2014b).

Figures 15c and 15d show relative differences in wintertime (MJJA) mean ozone due to MEE in the Southern Hemisphere. As expected, ozone is affected at high polar latitudes. In 2009, when MEE precipitation was weak, a maximum of 5–10% decrease is seen near the south pole relative to a reference WACCM simulation. In 2005, with much stronger MEE precipitation, the effect reaches up to 10–20% and covers the whole polar cap above about 60° latitude. The magnitude of the 2005 response, tens of percent, is comparable to that seen in MLS observations (Andersson et al., 2014a).

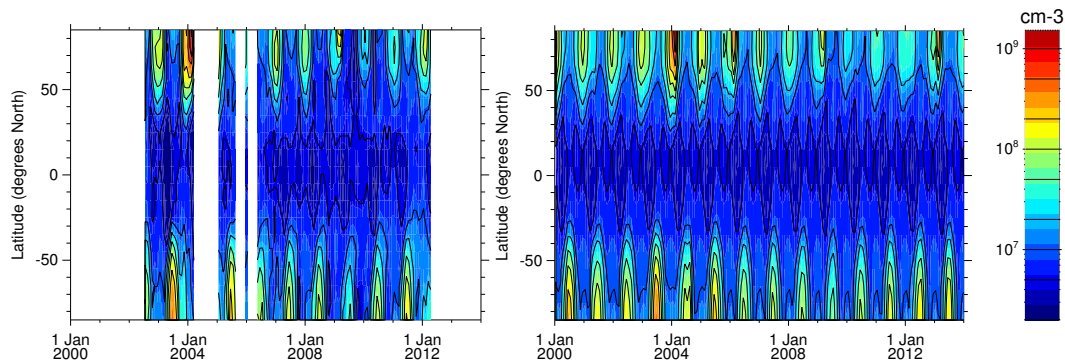


Figure 16. Latitude-time sections of NO_y concentrations observed by MIPAS (left) and from the UBC model (right) at 0.1 hPa.

The EPP Indirect Effect: Odd Nitrogen Upper Boundary Condition

Those models with their upper lid in the mesosphere, i.e., which do not represent the entire EPP source region, require an odd nitrogen upper boundary condition (UBC), accounting for EPP productions higher up, in order to allow for simulating the introduced EPP indirect effect in the model domain. Odd nitrogen UBCs have been previously used in CCMs. In some model studies, the UBC was taken directly from NO_x observations (e.g., Reddmann et al., 2010; Salmi et al., 2011), which, however, implies the restriction to the relatively short time period spanned by the observations. In other cases, a simple parameterisation in dependence of the seasonally averaged Ap index (Baumgaertner et al., 2009) was employed (e.g., Baumgaertner et al., 2011; Rozanov et al., 2012), enabling extended simulations over multi-decadal time periods. We recommend the use of the UBC model described in Funke et al. (2016) which is designed for the latter application and represents an improved parameterisation due to its more detailed representation of geomagnetic modulations, latitudinal distribution, and seasonal evolution. This semi-empirical model for computing time-dependent global zonal mean NO_y concentrations (in units of cm^{-3}) or EPP- NO_y molecular fluxes (in units of $\text{cm}^{-2} \text{s}^{-1}$) at pressure levels within 1–0.01 hPa and is available at <http://solarisheppa.geomar.de/solarisheppa/cmip6>.

The UBC model has been trained with the EPP- NO_y record inferred from Michelson Interferometer for Passive Atmospheric Sounding (MIPAS) observations (Funke et al., 2014a). Inter-annual variations of the EPP indirect effect at a given time of the winter are related to variations of the EPP source strength, the latter being considered to depend linearly on the Ap index. A finite impulse response approach is employed to describe the impact of vertical transport on this modulation. Interannual variations of the EPP- NO_y seasonal dependence, driven by variations of chemical losses and transport patterns, are not considered in the standard mode of the UBC model. Optionally, episodes of accelerated descent associated with Elevated Stratopause (ES) events in Arctic winters can be considered by means of a dedicated parameterisation, taking into account the dependence of the EPP- NO_y amounts and fluxes on the event timing (Holt et al., 2013). Although its application is recommended in principle, we note that it requires the implementation of the UBC model into the climate model system since ES events cannot be predicted in free-running model simulations. Further, the ES detection criterion might need to be tuned for each individual model system.

We recommend to prescribe NO_y concentrations, as this has already been tested successfully in a CCM. As an example, Fig. 16 shows the NO_y concentrations from the UBC model at 0.1 hPa in comparison with the MIPAS observations. Care has to be taken when balancing $[\text{NO}_y] = [\text{NO}] + [\text{NO}_2] + [\text{NO}_3] + [\text{HNO}_3] + 2[\text{N}_2\text{O}_5] + [\text{ClONO}_2]$ in order to avoid model artifacts at the upper boundary (primarily triggered by the loss reaction of NO_2 with atomic oxygen). The simplest way to achieve this is to set $[\text{NO}] = [\text{NO}_y]$ while forcing the concentrations of all other NO_y species to be zero. Note that below the vertical domain where NO_y is prescribed, MEE ionization still might occur and its consideration (as described before) is recommended. However, its consideration should be strictly limited to this vertical range since at and above the UBC, MEE is already implicitly accounted for by the prescribed NO_y from the observation-based UBC model.

The UBC was tested in the EMAC CCM version 2.50 (see also Sec. 2.1.2 and Jöckel et al., 2010) with a T42L90 resolution. NO_y concentrations were prescribed as NO in the uppermost four model boxes at pressure levels from 0.09 to 0.01 hPa. NO_y . There, NO_2 was set to zero to suppress artificial NO_2 buildup. The model was run from 1999 to 2010 in the specified dynamics mode, nudged to ERA-Interim reanalysis data (Dee et al., 2011) below 1 hPa. A special treatment of ES events was disabled in the UBC model and SPEs were not considered. A comparison of polar NO_y from EMAC with MIPAS observations is shown in Fig. 17 for 0.1 hPa (just below the prescription altitudes) and 1 hPa. A very good agreement between model predictions and observations is found at 0.1 hPa in both hemispheres, with the exception of periods of large SPEs (October/November 2003) in both hemispheres and ES events (January 2004 and February 2009) in the Northern Hemisphere. At 1 hPa, the agreement is still very good during winter, but EMAC underestimates the summer maximum of NO_y slightly. This is also observed in the base model run without employing the UBC (see Fig. 17).

The interannual variation of ozone in the stratosphere and lower mesosphere has been investigated in this model in a similar way as for a three-satellite composite (Fyterer et al., 2015a). The ozone difference between Austral winters with high and low geomagnetic activity during 2005–2010 is shown in Fig. 18 for 27-day running means relative to the mean of all years. This period has been chosen because of its low SSI variability. Cross-correlations between SSI and particle impact are thus minimized. EMAC results are in excellent agreement with the observations as provided in Fyterer et al. (2015a, Figure 5), showing a clear negative ozone anomaly of 5-10% moving down from the upper stratosphere to below 10 hPa (~ 30 km) from July to October. Below, a positive anomaly of smaller amplitude is observed both in EMAC and the three-satellite composite which might be due to a combination of self-healing, dynamical feedbacks, and chemical feedbacks (NO_x -induced chlorine buffering in the processed "ozone hole" area).

2.2.2 Solar Protons

Solar eruptive events sometimes result in large fluxes of high-energy solar protons at the Earth, especially near the maximum and declining periods of activity of a solar cycle. This disturbed time, wherein the solar proton flux is generally elevated for a few days, is known as a solar proton event (SPE). Solar protons are guided by the Earth's magnetic field and impact both the northern and southern polar cap regions ($>60^\circ$ geomagnetic latitude, e.g., see Jackman and McPeters, 2004). These protons can impact the neutral middle atmosphere (stratosphere and mesosphere) and produce both hydrogen radicals and reactive nitrogen constituents.

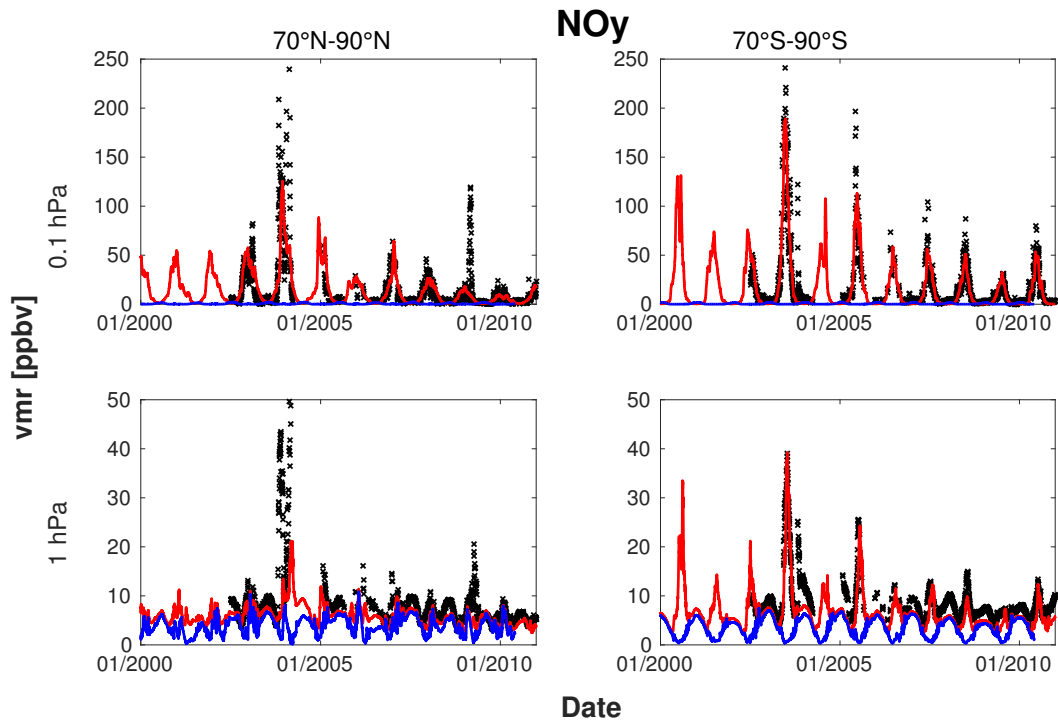


Figure 17. Comparison of NO_y from MIPAS observations and different EMAC model runs at $70\text{--}90^\circ\text{N}$ (left) and $70\text{--}90^\circ\text{S}$ (right) for 0.1 hPa (upper panel) and 1 hPa (lower panel), from 2000–2010. Black crosses: MIPAS observations. Red line: EMAC with the MIPAS-derived UBC for NO_y (see text); blue line: EMAC without UBC for NO_y .

The ozone response due to very large SPEs is fairly rapid and substantial and has been observed during and after numerous events to date (e.g., Weeks et al., 1972; Heath et al., 1977; McPeters et al., 1981; Thomas et al., 1983; Solomon et al., 1982; McPeters and Jackman, 1985; Jackman et al., 1990, 1995, 2001, 2005b, 2008, 2011, 2014; López-Puertas et al., 2005a; Rohen et al., 2005; Seppälä et al., 2006; Krivolutsky et al., 2008; Funke et al., 2011; von Clarmann et al., 2013). Ozone within the polar caps ($60\text{--}90^\circ\text{S}$ or $60\text{--}90^\circ\text{N}$ geomagnetic) is generally depleted to some extent in the mesosphere and upper stratosphere (e.g., Jackman et al., 2005b) within hours of the start of the SPE and can last for months beyond the event at lower altitudes in the stratosphere.

Decreases in mesospheric and upper stratospheric ozone are mostly caused by SPE-induced HO_x increases, which were predicted to occur over 42 years ago (e.g., see Swider and Keneshea, 1973). Direct measurements of SPE-caused OH and HO_2 enhancements have confirmed these early predictions (e.g., Verronen et al., 2006; Damiani et al., 2008; Jackman et al., 2011, 2014). Other observations of increased H_2O_2 (Jackman et al., 2011) and of chlorine-containing constituents HOCl (an increase, see von Clarmann et al., 2005; Jackman et al., 2008; Damiani et al., 2008, 2012; Funke et al., 2011) and HCl

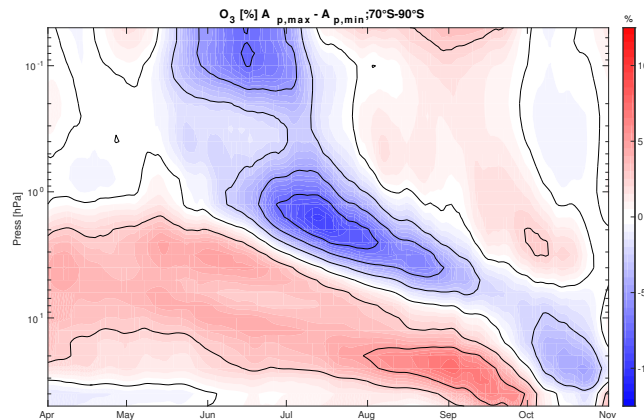


Figure 18. Ozone interannual variation due to geomagnetic forcing in 2005-2011 from EMAC model run using the MIPAS-derived UBC for NO_y . Shown are 27-day running means of the mean of the three years with highest – mean of the three years with lowest geomagnetic activity averaged over 70-90°S. EMAC results are in excellent agreement with O_3 observations using a three-satellite composite for the same period of time (see Figure 5 in Fytterer et al., 2015a).

(a decrease, see Winkler et al., 2009; Damiani et al., 2012) support the SPE-caused HO_x enhancement theory. Since HO_x constituents have relatively short lifetimes (hours), these SPE-enhanced species have only a short-term impact on ozone.

The SPE-induced NO_y enhancements, on the other hand, cause a much lengthier reduction in ozone, given their much longer atmospheric lifetime (\sim months) in the stratosphere. SPE-caused NO_x increases have been shown in several studies (e.g., McPeters, 1986; Zadorozhny et al., 1992, 1994; Randall et al., 2001; López-Puertas et al., 2005a; Jackman et al., 1995, 2005b, 2008, 2011, 2014; Funke et al., 2011; von Clarmann et al., 2013; Friederich et al., 2013). Other NO_y constituents like HNO_3 , HNO_4 , N_2O_5 , and ClONO_2 (e.g., López-Puertas et al., 2005b; Jackman et al., 2008; Funke et al., 2011; Damiani et al., 2012; von Clarmann et al., 2013) as well as the total NO_y family (e.g., Funke et al., 2011, 2014a, b) have also been shown to increase as a result of large SPEs. Additionally, N_2O has been measured to increase as a result of large SPEs (Funke et al., 2008; von Clarmann et al., 2013).

Solar proton fluxes have been measured by a number of satellites in interplanetary space or in orbit around the Earth. The National Aeronautics and Space Administration (NASA) Interplanetary Monitoring Platform (IMP) series of satellites provided measurements of proton fluxes from 1963–1993. IMPs 1-7 were used for the fluxes from 1963-1973 (Jackman et al., 1990) and IMP 8 was used for the fluxes from 1974–1993 (Vitt and Jackman, 1996). The National Oceanic and Atmospheric Administration (NOAA) Geostationary Operational Environmental Satellites (GOES) were used for proton fluxes from 1994–2014 (e.g., Jackman et al., 2005a, 2014).

Other precipitating particles are associated with SPEs, besides protons. These include alpha particles, which comprise, on average (but this value may vary from event to event) about 10% of the positively charged solar particles, other ions, which account for less than 1% of the remainder, and electrons (e.g., Mewaldt et al., 2005). Only solar protons are included in

energy deposition computations given in this paper. Please note that other charged particles could add modestly to this energy deposition in the middle atmosphere during SPEs.

The proton fluxes of energies 1-300 MeV were used to compute daily average ion pair production profiles using an energy deposition scheme first discussed in Jackman et al. (1980). The scheme includes the deposition of energy by the protons and
5 assumes 35 eV are required to produce one ion pair (Porter et al., 1976). Note that this approach misses development of the atmospheric cascade (Sec. 2.2.3). This process, crucial for GCRs, is minor for SPEs in the upper atmosphere but may contribute modestly to the energy deposition in the lower stratosphere.

The dataset for daily average ion pair production rates at 60–90° geomagnetic latitudes from SPEs was computed over a 52 year time period (1963–2014), when proton flux measurements from satellites were available. A longer-term dataset for
10 these SPE-caused ion pair production rates was created for the 1850–1962 time period using activity levels of the measured sunspots over the solar cycles. SPEs are much more frequent during years of maximum solar activity and vice versa. This longer-term dataset was reconstructed for years 1850–1962 in a random way using solar activity levels combined with the 52-year calculated SPE-caused ion pair production. Thus, an historical record of atmospheric forcing by SPEs in the form of a daily average ion pair production rate is available over the entire period 1850–2014 for use in global models.

15 2.2.3 Galactic Cosmic Rays

The Earth's atmosphere is continuously irradiated by Galactic cosmic rays (GCR), which consist mostly of protons and α -particles with a small amount of heavier fully ionized species up to iron and beyond. These cosmic rays originate from galactic (mostly supernova shocks) and exotic extra-galactic sources and may have an energy up to 10^{20} eV but the bulk energy is in the range of several GeV/nucleon. While the GCR flux can be assumed (at time scales shorter than thousands of year) constant
20 and isotropic in the interstellar space, it is subject to strong modulations within the heliosphere (the region of about 200 AU across hydromagnetically controlled by the solar wind and the heliospheric magnetic field). This modulation is driven by solar magnetic activity – the stronger the solar activity, the lower is the GCR flux near the Earth. This flux is often described by the so-called force-field model (Caballero-Lopez and Moraal, 2004) parameterized via the time-variable modulation potential ϕ and the fixed shape of the local interstellar spectrum (see, e.g., Usoskin et al., 2005, for more details). Typically, the value of
25 the modulation potential is defined by fitting data from the world-wide network of ground-based neutron monitors calibrated to fragmentary space-borne measurements of GCR energy spectra. These data are available since 1951 or, with caveats of using the ground-based ionization chambers, since 1936 (Usoskin et al., 2011).

Before impinging on the Earth's atmosphere, GCR are additionally deflected by the geomagnetic field.

This shielding is usually parameterized in the form of the effective geomagnetic rigidity cutoff, so that only particles with
30 rigidity/energy exceeding the cutoff can penetrate to the atmosphere at a given location while less energetic particles are fully rejected (Cooke et al., 1991).

When energetic cosmic rays enter the atmosphere, they initiate a nucleonic-muon-electromagnetic cascade in the atmosphere, ionizing ambient air. As a sub-product of this cascade cosmogenic isotopes such as ^{14}C , ^{10}Be and others can be pro-

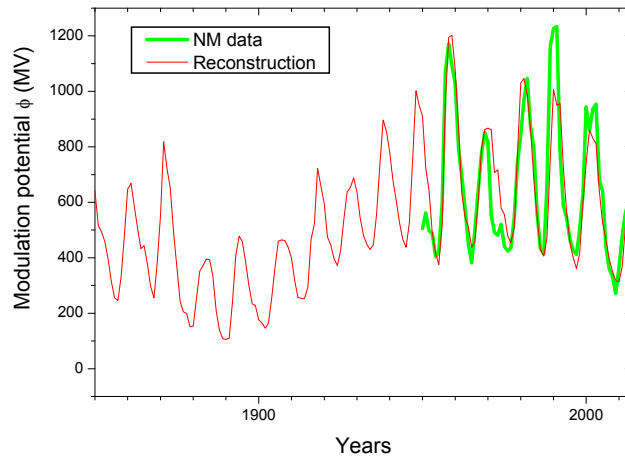


Figure 19. Time series of the reconstructed heliospheric modulation potential ϕ including solar cycle variations. The thick green line is the modulation potential reconstructed for the period 1951–2014 using data from the worldwide neutron monitor (NM) network (Usoskin et al., 2011).

duced. These cosmogenic isotopes are long-lived and can be used for the reconstruction of solar activity over several thousand years (see Sec. 3).

Between the surface and 25–30 km cosmic rays are the main source of atmospheric ionization (Mironova et al., 2015) causing the production of NO_x and HO_x . The influence of GCRs on atmospheric chemistry has been investigated in several model studies (Krivolutsky et al., 2002; Calisto et al., 2011; Rozanov et al., 2012; Mironova et al., 2015; Jackman et al., 2015). GCR-induced ozone reductions of more than 10% in the tropopause region and up to a few percent in the polar lower stratosphere have been reported. The potential impact on surface climate has been studied by Calisto et al. (2011) and Rozanov et al. (2012).

The process of development of the atmospheric cascade, initiated by energetic cosmic rays, is complicated and needs to be modelled using direct Monte-Carlo simulations of all the processes involved in the development of the cascade, including all types of interactions, scattering and decay of various species. We note that older models based on empirical parameterisations or on solution of Boltzmann-type equations may introduce significant biases in the results, especially in the lower atmosphere. Accordingly, we use a full Monte-Carlo model CRAC:CRII (Usoskin and Kovaltsov, 2006; Usoskin et al., 2010) based on the CORSIKA Monte-Carlo package. A similar result can be obtained with the PLANETOCOSMIC (Desorgher et al., 2005) based on the GEANT package. The agreement between the two models has been verified (Usoskin et al., 2009) to be within 10%.

GCR ion pair production rates are provided as a function of the barometric pressure and geomagnetic latitude and were calculated from the modulation potential values ϕ of the 9400-year long record by Steinhilber et al. (2012). Since this dataset has a 22-year time resolution, it has been interpolated to interannual time scales to resolve individual solar cycles, based on

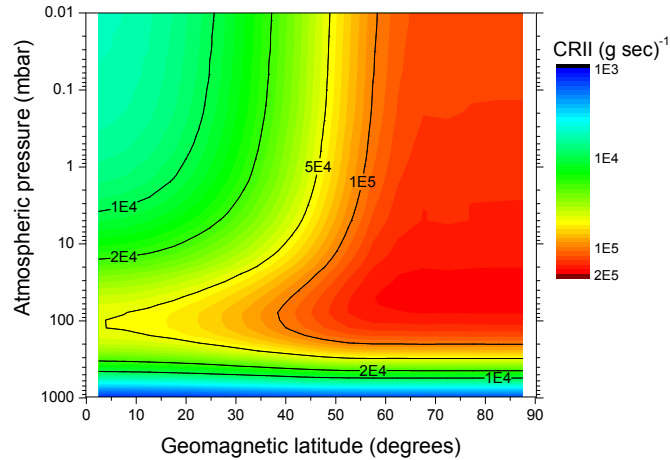


Figure 20. Calculated annual mean ion pair production rate for the year 2014 as a function of barometric pressure and geomagnetic latitude. Computations were done using the CRAC:CRII model.

the sunspot numbers (see Fig. 19). One can see that this agrees well with the values of ϕ reconstructed using data from the worldwide network of neutron monitors (NM) (Usoskin et al., 2011). An example of the calculated ionisation-ionization rate is shown in Fig. 20. The ionisation-ionization maximizes in polar regions at heights of 15–20 km, while in the equatorial region the maximum of ionisation-ionization occurs at about 12 km (note that in case of using ionization per cm^3 , the ionisation ionization maximizes at about 10 km in the equatorial region and 12 km over the poles).

2.2.4 Implementation of Chemical Changes Induced by Particle-Induced Ionisationionization

MEE, SPE, and GCR-induced atmospheric ionisation-ionization is expressed in the CMIP6 forcing dataset in terms of ion pair production rates (IPR). Note that IPR data are provided in units of ion pairs per gram per second as a function of the barometric pressure. These units are natural for the ionisation-ionization processes and are mostly independent of the atmospheric conditions. Conversion into units of $\text{cm}^{-3} \text{s}^{-1}$ (by multiplying with mass density) should be done on the model grid ideally at each time step, but at least once per day. Recommendations for the projection of ion pair production rates onto geographic coordinates can be found in Appendix C.

Particle-induced ionisation-ionization causes, along with the generation of the ion pairs, the production of NO_x and HO_x . As a basic approach, we recommend to consider these NO_x and HO_x productions in CCMs with interactive chemistry by using the parameterisations provided by Porter et al. (1976) and Solomon et al. (1981), respectively. More detailed information about these approaches is provided in Appendix D and E. Recommendations for the implementation of EPP effects on minor species are given in Appendix F.

3 Future Scenarios (2015-2300)

One of the key questions in the CMIP6 project is our ability to assess future climate changes given climate variability, predictability and uncertainties in scenarios. In CMIP5, climate projections were based on a stationary Sun scenario, obtained by simply repeating solar cycle 23, which ran from April 1996 till June 2008 (Lean and Rind, 2009). Clearly, such a stationary scenario is not representative of true solar activity, which exhibits cycle-to-cycle variations, and trends. Therefore, in CMIP6 we decided to ~~include~~ replace it by a more realistic ~~solar forcing, and provide two different scenarios:-~~

- ~~- a reference (REF) scenario with the most likely level of solar activity ;-~~
- ~~- an extreme (EXT) scenario with an exceptionally low level of solar activity, corresponding to the lower 5th percentile of all forecasts. This extreme scenario is meant to be used for sensitivity studies.-~~

~~There are several reasons why our extreme scenario is a low one. First, the Sun just exited a high amplitude one, called grand solar maximum, and several empirical studies suggest that it is very unlikely to return to one in the next 300 years (Abreu et al., 2008; Barnard et al., 2011; Steinhilber et al., 2012). Secondly, dynamo models of the solar cycle indicate that grand maxima are more likely to be followed by a grand minimum than by another grand maximum. And thirdly, when we generated an ensemble of 1000 scenarios with two of the empirical models to be described below (the different runs were based on different training intervals and model parameters) none of the forecasts gave rise to a grand maximum within the next century.~~ scenario for future solar activity exhibiting variability at all time scales. As will become clear below, this scenario provides a plausible course of solar activity until 2300 given what has been observed in the past and does not aim at predicting what the level of solar activity will actually be.

~~The main challenge consists in forecasting~~ As of today, predicting solar activity up to ~~2300.~~ 2300 is very challenging, if not impossible. Ever since the solar cycle was first observed, people have been trying to predict what future cycles may look like. Prediction methods were empirical, and at best could give some clue of what the amplitude of the next cycle could be (Petrovay, 2010). This situation prevailed until the early 21st century, when physical models of the magnetic dynamo that drives solar activity started unveiling a more realistic picture (Charbonneau, 2010). Many were confident that in a near future one would be able to predict the solar cycle several decades ahead. The unusually long solar cycle number 23 that ended in 2009, and the weak one (~~nr~~Nr. 24) that followed came as a surprise, and manifested our evident lack of understanding of the solar cycle. ~~As of today, even predicting the cycle amplitude one cycle ahead remains a major challenge (Pesnell, 2012).~~

~~In this context, Given the difficulty in~~ predicting solar activity several tens of cycles ahead may seem like a hopeless task. However, erratic as the solar cycle may be, solar activity on multi-decadal time scales (i.e. averaged over solar cycles) does exhibit some regularity, which may be used to predict it, see for example (Hanslmeier and Brajša, 2010) and references therein even one cycle ahead (Pesnell, 2012) one may wonder whether it even makes sense to consider longer horizons. The solar cycle is driven by the solar dynamo, by which the dynamical interactions of flows and magnetic fields in the solar convection zone lead to periodic reversals of polarity of the solar magnetic field (Charbonneau, 2010). One of its consequences is the emergence of regions with enhanced magnetic field, namely sunspots, whose number are the most widely known proxy

for solar activity. During that emergence process, the predominantly toroidal magnetic field generates a dipole moment, which in turns generates a new toroidal magnetic component through rotational shearing. Because these inductive processes are operating in the turbulent environment of the solar convection zone, memoryless stochastic forcing of the dynamo is certainly present ~~at some level~~. Nonetheless, memory effects associated with these periodic reversals play a major role in determining solar variability on multi-decadal time scales, and to some degree are decoupled from the short-term variability. This is our prime motivation for ~~considering predictions attempting to estimate future solar activity~~ on multi-decadal time scales. ~~Entry into grand minima typically involves extended excursions at the edge of the attractor defining normal cyclic behavior, with associated higher-than-average cycle amplitudes, until collapse to the trivial solution (or transition to another low-amplitude attractor) is triggered; this behavior is known as intermittency, and in this context a grand maximum is usually more likely to be followed by a grand minimum than by another grand maximum (e.g. Passos et al., 2012)~~ as basis for our scenario construction.

There are two ~~approaches for constraining such predictions~~ possible approaches for constructing future scenarios of solar activity. One is to learn from solar dynamo models, and the other is to infer from past variations of solar activity. Recent years have witnessed significant advances in solar dynamo modeling, and the development of several physical models (Charbonneau, 2014). Most models exhibit some persistence in the solar cycle-averaged level of activity, with a memory of up to a few cycles. However, among models that do succeed in producing deep activity minima similar to the Maunder minimum, most show onsets occurring surprisingly fast, typically within one or two cycles. ~~At present these models are still not detailed enough to warrant their use in producing physics-based forecasts. The second approach consists in making a probabilistic statement about future solar activity based on present conditions and by learning from past variations of solar activity. The latter are not totally random and exhibit some degree of regularity which can be exploited by means of time series analysis techniques (Brockwell and Davis, 2010), assuming that the statistical behavior of the Sun is invariant on the time scales under consideration. This enables us to build an ensemble of empirical forecasts and define from these what we call in the following a scenario, namely a realistic and plausible course of solar activity, based on assumptions about how this activity will develop. Let us stress that our scenarios are meant to provide a realistic evolution of solar forcing up to 2300: they are forecasts of what could happen, and do not aim at describing what will happen.~~

We construct two different scenarios for future solar activity:

- a reference (REF) scenario with a plausible level of solar activity and realistic variability;
- an extreme (EXT) scenario with an exceptionally low level of solar activity. This extreme scenario is meant to be used for sensitivity studies.

Two extreme scenarios would have been preferable for bracketing the possible range of future solar variability. However, the enormous computational effort to analyze such sensitivity scenarios within CMIP6 makes it necessary to restrict ourselves to one single extreme scenario.

There are several reasons why our extreme scenario is a low one. First, the Sun just exited a period of high activity, called grand solar maximum, and several empirical studies suggest that it is likely to be low or moderate in the near future (Abreu et al., 2008; Barnard et al., 2011; Steinhilber et al., 2012). Secondly, empirical studies indicate that grand maxima are

more likely to be followed by a grand minimum than by another grand maximum (Inceoglu et al., 2016). Entry into grand minima typically involves extended excursions at the edge of the attractor defining normal cyclic behavior, with associated higher-than-average cycle amplitudes, until collapse to the trivial solution (or transition to another low-amplitude attractor) is triggered; this behavior is known as intermittency, and in this context a grand maximum is usually more likely to be followed

5 by a grand minimum than by another grand maximum (e.g. Passos et al., 2012). And thirdly, when we generated an ensemble of 1000 scenarios with the empirical models to be described below (the different runs were based on different training intervals and model parameters) none of the scenarios constructions/analyses gave rise to a grand maximum within the next century.

The best gauge of past solar variability is the production rate of the ^{14}C and ^{10}Be cosmogenic isotopes (Usoskin, 2013), as already described in Sec. 2.2.3. The level of activity is ~~usually-sometimes~~ expressed in terms of the modulation potential Φ

10 (~~Usoskin, 2008; Beer et al., 2012~~)(Beer et al., 2012), which is intimately related to the open solar magnetic flux. There exist today different records of cosmogenic isotopes, which are gradually improving as new observations are being added, and underlying assumptions, such as the strength of the geomagnetic dipole, are better constrained. Here, we consider the 9400-year long record by Steinhilber et al. (2012), which is a composite of ^{14}C and ^{10}Be data, and is available from <http://www.ncdc.noaa.gov/paleo/forcing.html>. The record is sampled every 22 years, and runs from 7439 BC till 1977 AD. For ~~making~~

15 ~~better-predictions~~constructing the most likely scenario, we want our historic observations to end as close as possible to the present. ~~Therefore we extended the record~~This record was extended from 1977 to 1999, using the geomagnetic reconstruction of the open solar flux (Lockwood et al., 2014). The geomagnetic reconstruction provides annual values of the open solar flux back to 1845, and we extrapolate the linear regression between the 22-year boxcar smoothed geomagnetic reconstruction and the cosmogenic reconstruction to provide an estimate of the cosmogenic Φ in 1999.

20 Figure 21 displays the complete modulation potential record, which exhibits occasional periods of low solar activity (i.e. grand solar minima) separated by periods during which the fluctuations seem more erratic. It is noteworthy that the Sun was more active during ~~the~~ recent decades (the modern grand maximum) than during most of the other periods (Solanki et al., 2004).

In the following, we consider three ~~different-independent~~ (and mostly complementary) ~~approaches for predicting-forecast~~ methods for extending Φ up to 300 years ahead, and use their weighted average as the most likely value. To convert these

25 22-year averages of Φ into quantities that are relevant for climate forcing, we first convert the 22-year averaged modulation potential into an average sunspot number using the method described in (Usoskin et al., 2014). Historic solar cycles ~~that have the same are then scaled to match this~~ average sunspot number and are subsequently stitched together to obtain a ~~record with daily-resolved sunspot numbers~~future sunspot record. Using the latter, we estimate the SSI, and particle forcing, as described in Sec. 3.5.

30 ~~According to solar dynamo models, the~~The solar-cycle averaged modulation potential (and the sunspot number) cannot be meaningfully predicted more than ~~one solar cycle ahead~~. ~~The autocorrelation function of the observed modulation potential indeed decays exponentially with a characteristic time of 48 ± 5 years. This quantity can be interpreted as the time beyond which successive values become uncorrelated. As we shall see below, two of our three prediction methods exhibit prediction horizons of approximately 60 years. The deterministic harmonic model maintains substantial predictive capacity on much~~

35 ~~longer time scales because by construction it assumes the potential to vary periodically. To the best of our knowledge, no~~

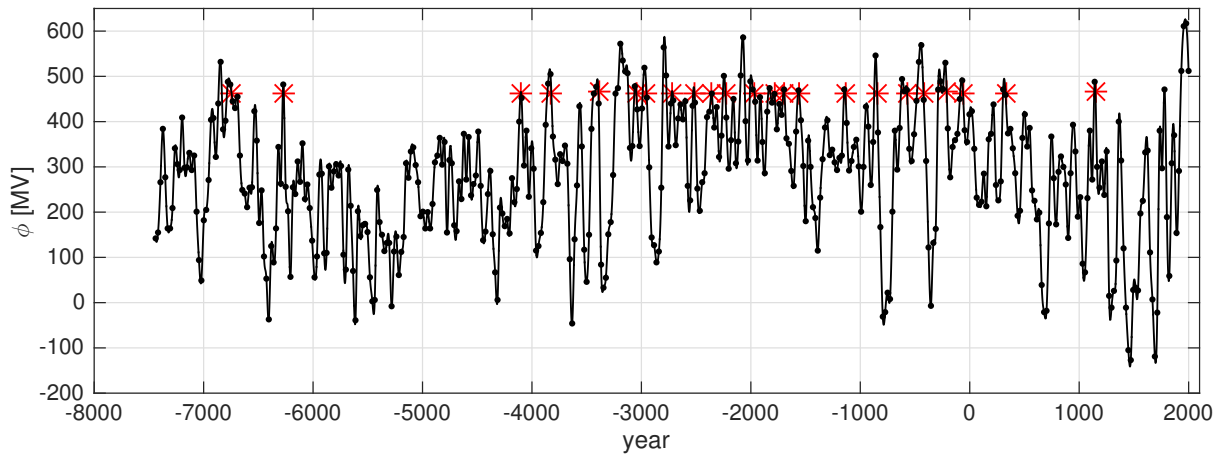


Figure 21. Modulation potential record Φ [MV] used for forecasting-constructing future scenarios of solar activity. What matters is the relative variation in Φ , which reflects that in the TSI: large values of Φ correspond to grand solar maxima, whereas low values correspond to grand solar minima. Red stars refer to the events used in the analogue forecast, see Sec. 3.1.1. Negative values of the modulation potential are unphysical, but occur in the original record because of our poor knowledge of the cosmic ray spectrum during deep solar minima.

~~method, except for harmonic ones, has been able to provide meaningful forecasts that go beyond this 60-year horizon. For that reason, we shall from now on speak in terms of forecast rather than prediction, and concentrate on scenarios of solar activity: a few solar cycles ahead (e.g. Kremliovsky, 1995; Petrovay, 2010). Thus, whatever is discussed further is only a plausible scenario not pretending to be a prediction with any degree of confidence.~~

5 3.1 ~~Forecast~~ Statistical Methods

Here we construct the reference (REF) and extreme (EXT) solar activity scenarios by applying three ~~prediction methods~~ empirical time series techniques to the heliospheric modulation potential ~~time-series record~~ produced by Steinhilber et al. (2012). The reason for choosing three techniques only out of many is motivated by our desire to build an ensemble of reasonable ~~forecasts-scenarios~~ that involve different assumptions. We consider these three techniques to reflect a fair range of possibilities for the future evolution of the heliospheric modulation potential, and it would be impractical to include an exhaustive set of techniques. The ones we consider ~~have been widely advocated for making predictions with climate data (Mudelsee, 2010) but do so in completely different ways~~ are widely used in different contexts (Brockwell and Davis, 2010). The first one (analogue forecast) is ~~non-parametric~~ non-parametric and does not make any assumptions on linearity; the second one (autoregressive model) is parametric and linear; and the third one (harmonic model) is parametric too, but can handle nonlinear systems. Below we describe each of them, before detailing how the two scenarios were constructed.

3.1.1 Analogue Forecast

The analogue forecast (AF) is calculated with a simple non-parametric technique, known across disciplines by various names including compositing, superposed-epoch analysis, conditional sampling and Chree analysis. In a data sequence that exhibits a low amplitude response to a specific trigger event, the response may be obscured by sources of random variability. The AF technique aims to reveal the response to a specific trigger event by averaging the responses to many occurrences of the trigger event, such that over many events random variability will be suppressed and the response will emerge (Laken and Čalogović, 2013). Barnard et al. (2011) used this technique with the Steinhilber et al. (2012) Φ record to estimate the possible future Φ evolution given the expected decline from the grand solar maximum that persisted through the late 20th century. Here we perform an updated version of the procedure employed by Barnard et al. (2011).

Defining grand solar maxima in the Φ record as any period above the 90th percentile of the Φ distribution (462 MV), identifies 23 grand solar maxima in the Φ record prior to the most recent one. Here the declines from the grand solar maxima are used as the event triggers from which the AF is calculated, and these times are marked on the Φ time series shown in Figure 21 by red stars. Figure 21 also shows that the most recent values in the Φ record have not yet fallen below grand solar maxima threshold. Therefore, as the end date of the most recent grand solar maxima is not known, it must be estimated, to provide a date from which the AF applies. The grand solar maximum end date was estimated to be 2004, by extrapolating the regression of the 22-yr smoothed Lockwood et al. (2014) annual geomagnetic reconstruction of the open solar flux onto the Steinhilber et al. (2012) Φ record. So the [forecast-construction of the scenarios](#) was applied from 2004 onwards and interpolated onto the dates required to continue 22-year sample sequence defined by the Φ record.

3.1.2 Autoregressive Model

Autoregressive (AR) models are widely used in time series [forecasting-analysis](#) (Box et al., 2015). These linear parametric models assume that variations can be described by means of a linear stochastic difference equation, so that future values are expressed as a linear combination of present and past values. In our context, we have

$$\hat{\Phi}_{k+h} = a_1\Phi_{k-1} + a_2\Phi_{k-2} + \dots + a_p\Phi_{k-p}, \quad (1)$$

where Φ_k is the heliospheric modulation potential (after subtracting its time average) at the k 'th time step, and $\hat{\Phi}_{k+h}$ is its value predicted $h \geq 0$ time steps ahead. Since Φ_k is measured with a cadence of 22 years, each value of k corresponds to a 22-year time step. AR models are capable of describing a variety of dynamical behavior, including oscillations, red noise, etc. The main free parameter is the model order p , for which there exist several selection criteria (Ljung, 1997). In our case, we obtain $p = 20$. According to this value, our [forecasts-scenarios](#) are based on observations that go back at most 440 years into the past.

Because AR models are linear, they cannot properly describe nonlinear dynamical effects such as the occasional occurrence of grand solar minima, which appear as a different mode of solar activity (Usoskin et al., 2014). To partly overcome this limitation, we train the model by considering time intervals whose conditions are similar to those prevailing at the end of the

20th century. More specifically, we train the model by using only observations that belong to either of the 23 time intervals $[t_{GSM} - 1100\text{years}, t_{GSM} + 1100\text{years}]$ $[t_{GSM} - 1100\text{years}, t_{GSM} + 1100\text{years}]$ that are centered on the same occurrences t_{GSM} of the 23 grand solar maxima as in the analogue forecast (see Sec. 3.1.1, and Fig. 21). We exclude observations that follow t_{GSM} by up to 300 years in order to give us a means for testing the prediction on a time interval that is (mostly) independent of the one the model has been trained on. The only exception in this list is the last grand solar maximum of the late 20th century, for which we do not have future observations available. The 2200-year duration of the time interval is the shortest one below which the performance of the AR model starts degrading.

This independence of the intervals on which the model is trained and then tested (called cross-validation (Hastie et al., 2009)) is essential for it and allows to test the performance of the model and define confidence intervals that truly reflect the difference between the constructed and actual course of solar activity.

Using AR models, we now forecast-construct the heliospheric potential 22, 44, \dots , 308 years ahead by training a different model for each value of the forecast-scenario horizon h in Eq. 1. The forecast-error, which is the usual metric for describing forecast-performance-the performance of the scenario construction, is classically defined as

$$s(h) = \sqrt{\langle (\hat{\Phi}_{k+h} - \Phi_{k+h})^2 \rangle}, \quad (2)$$

where the ensemble average $\langle \dots \rangle$ runs over all 23 grand solar maxima. Clearly, the AR model can be improved in several ways. One of them consists in modelling-modeling the full record of the heliospheric potential, and use threshold AR models to account for mode changes. These issues will be addressed in a forthcoming publication.

3.1.3 Harmonic Model

Several studies have reported the existence of periodicities in cosmogenic solar proxies, with outstanding periods of approximately 87 years (known as the Gleissberg cycle), 208 years (de Vries cycle), 350 years, and more (McCracken et al., 2013). The origin of these elusive periodicities has been hotly debated, and is beyond the scope of our study. Steinhilber and Beer (2013) successfully used them to model solar activity on multi-decadal time scales, and produced a 500 year forecast-extension of the heliospheric potential. We consider the same approach, and thus assume that the dynamical evolution of the heliospheric potential obeys a deterministic model.

$$\hat{\Phi}_k = b_0 + \sum_{i=1}^N (b_i \sin(2\pi t_k/T_i) + c_i \cos(2\pi t_k/T_i)). \quad (3)$$

We parameterize and train this harmonic model in a way that is similar to the preceding AR model. First, we select 2600-year intervals that are centered on the timings t_{GSM} of each of the 23 grand solar maxima, and exclude the 300 years that follow each t_{GSM} . In contrast to the AR model, however, we estimate the model coefficients separately for each interval in order to account for possible phase drifts. To select the periods T , and reduce their number, we start from an initial set of $N = 19$ periods of less than 2200 years, taken either from McCracken et al. (2013), or obtained from spectral analysis. We then estimate the forecast-error-error of this method after discarding one period at a time, only keeping those that do not lead to a significant

increase of the ~~forecast~~ error. Finally, we end up with a set of 12 periods of {88, 105, 130, 150, 197, 208, 233, 285, 353, 509, 718, 974} years. Likewise, the ~~forecast~~ error is used to fix the 2600-year duration of the intervals. Longer intervals give a better statistic, but result in a poorer fit because of possible phase drifts in short-period oscillations.

3.2 Summary of ~~Forecasts~~Statistical Methods

- 5 Figure 22A shows the results of the AF, AR and HM ~~forecasts~~methods, as well as the observed Φ record from 1845-1999. All three methods ~~forecast~~reveal a decrease in solar activity out to approximately 2100. In the HM model, oscillations with largest amplitudes occur, on average, at 88, 208, and 285 years, and so periodicities are clearly present in the HM~~forecast~~. In contrast, ~~forecasts~~scenario constructions obtained from the AF and AR models tend to converge toward a climatological mean.

3.3 ~~Prediction~~Errors of Statistical Methods

- 10 The error of each ~~prediction~~ method was assessed with a bootstrap approach. Defining grand solar maxima as any period in the Φ record larger than the 90th percentile of the Φ distribution, there are 23 other grand solar maxima in the Φ record prior to the one that persisted through the late 20th century. For each ~~prediction~~ method, hindcasts were made for the 308 years following the decline from each prior grand solar maximum. For each method and each grand solar maximum, the models were trained analogously to the descriptions above, such that no Φ data from within the prediction window is used to generate each hindcast.
- 15 The typical error in each ~~prediction~~ method as a function of prediction horizon was then calculated as the root mean square of the error of the 23 hindcasts at each prediction horizon.

- Although not used in the scenario construction, a simple persistence forecast and the corresponding error was also calculated, to serve as a benchmark to compare the AF, AR and HM methods against. The typical ~~prediction~~ error as a function of prediction horizon for the AF, AR, HM and persistence (PS) methods is shown in Figure 22C. The AF, AR and HM methods have similar error levels and each quickly ~~outperforms~~outperform the simple persistence model. For most of the prediction window, the AR method shows the lowest error, although the error in the HM decreases near a prediction horizon of 220 years, arguably due to the strength of the de Vries cycle, a 208 year periodicity observed in the power spectrum of the Φ record, and an important component of the HM model.
- 20

3.4 Scenario Construction

- 25 The REF scenario was calculated as the weighted average of the AF, AR and HM ~~predictions~~results for the current grand solar maximum, where the ~~prediction~~ errors shown in Figure 22C were used as the weightings. Here again, the maximum likelihood estimate of the average scenario is obtained simply by making a weighted average of the AF, AR and HM ~~predictions~~. ~~A different approach was used~~results. The REF scenario can thus be considered as a realistic description of what future solar activity could be, without claiming to be an actual prediction of solar activity. We used a different approach to calculate the
- 30 EXT scenario: the AF, AR and HM methods were used to generate hindcasts of the 23 prior grand solar maxima, also for a 308 year prediction window. The extreme scenario was then calculated as the 5th percentile of the 3×23 hindcasts at each

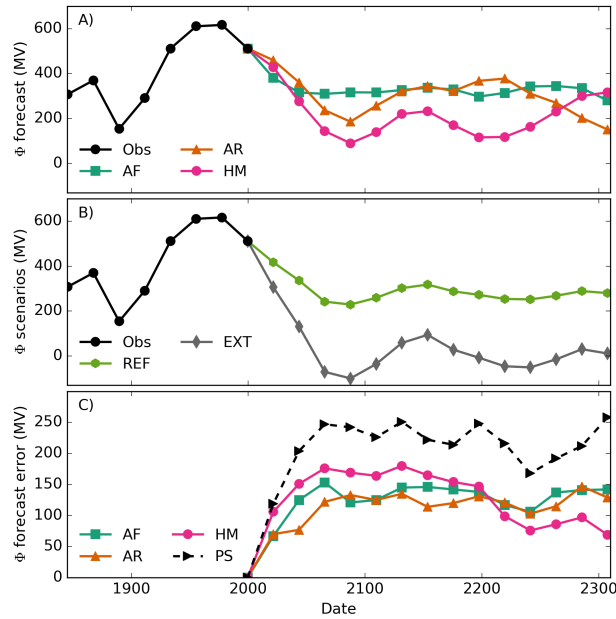


Figure 22. A) Observations of Φ (Obs) from 1850 until 1999, and the three forecasts-scenarios from 1999 until 2300, from the analogue forecast (AF), auto-regressive model (AR) and harmonic analysis (HM) methods. B) The CMIP6 reference scenario (REF) and extreme scenario (EXT). C) The forecast-error for the AF, AR, HM and PS methods, estimated by employing a bootstrap hindcast approach, calculating the root-mean-square of the hindcast errors for 23 prior grand solar maxima in the ϕ record. The occurrence of unphysical negative values comes from the original modulation potential data, and not necessarily from the prediction-methods, see Fig. 21.

prediction horizon. The REF and EXT scenarios are shown in Figure 22B. Let us stress again that EXT scenario is meant to be used primarily for sensitivity studies, in contrast to the REF scenario, which is the reference one.

Figure 22B shows that both scenarios start with a phase of low solar activity, which extends from approximately 2050 to 2110. In the reference scenario, the deepest level is comparable to the Gleisberg minimum that occurred in the late 19th century, whereas in the extreme scenario, it is considerably deeper, and reaches a Maunder-type minimum. The extreme scenario lingers in that state, whereas the reference one recovers to a climatological mean that is comparable to levels observed during the 1st half of the 20th century. Let us stress that none of the forecasts-constructed scenarios exhibits a grand solar maximum similar to the one that just ended.

3.5 Future Solar Cycle Definition and Scaling Procedure

10 Future cycles are constructed from historical cycles by projecting them into the future. The average solar activity level of the projected historical cycles was thereby scaled in accordance to the predicted activity level of the scenarios. Solar activity variations on time scales shorter than a solar cycle are hence preserved. This strategy ensures consistency between the different

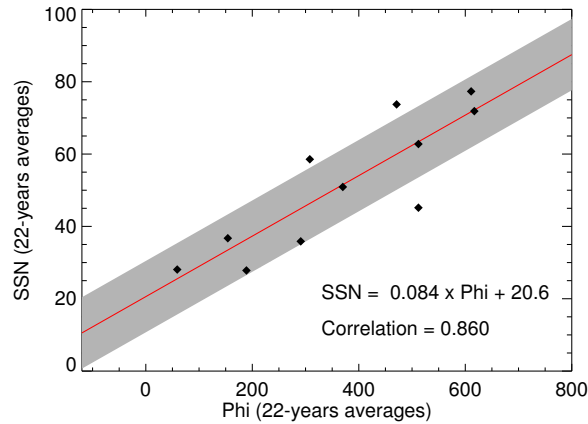


Figure 23. Regression of 22-year averaged SSN to the modulation potential Φ . The grey-shaded area represents the 1σ uncertainty range of the fit. Regression coefficients and the correlation coefficient are also indicated.

types of radiative and particle forcing on all time scales also in the future. The historical cycles used for projection into the future are listed in Table 6 of Appendix G.

We assume a linear dependence of the 22-year average sunspot number $\langle \text{SSN} \rangle_{22}$ on Φ for the scaling of future solar cycles:

$$5 \quad \langle \text{SSN} \rangle_{22} = 0.084 \Phi + 20.6. \quad (4)$$

The coefficients of Eq. 4 have been obtained from a regression fit, based on SSN and Φ in the time period 1768–2010 (see Fig. 23). We use international sunspot number version 1.0, because most SSI models rely on that version (see Sec. 2.1.1).

The resulting SSN time series of both future scenarios have then been used to calculate the SSI with the SATIRE and NRLSSI2 models with annual time resolution. As for the historical CMIP6 dataset, we took for each scenario the arithmetic mean of the two model results. SSI variations on shorter time scales are taken from the corresponding past solar cycles, and are scaled to a comparable cycle-average level of activity by means of a dedicated scaling procedure, as described in Appendix H. F10.7 radio flux data has been constructed from the resulting future SSI record as described in Sec. 2.1.2.

A similar approach has also been chosen for the future particle forcing. Magnetospheric particle forcing (Sec. 2.2.1) relies on the geomagnetic indices Ap and Kp, being closely related to sunspot number on decadal time scales (e.g., Cliver et al., 1998). The scaling of these indices in past solar cycles into the future on basis of $\langle \text{SSN} \rangle$ is described in Appendix I. The 2015–2300 Ap time series we obtained have then been used to calculate MEE ionization rates for the REF and EXT scenarios. Similarly, odd nitrogen upper boundary conditions for the consideration of the EPP indirect effect in climate models with their upper lid in the mesosphere can be computed on basis of the future Ap index with the recommended UBC model (Funke et al., 2016). Future GCR-induced ionization (see Sec. 2.2.3) is calculated from the Φ of the respective scenarios and interpolated to interannual timescales by using the future SSN time series. The proton forcing of past solar cycles (Sec. 2.2.2) has also been

projected into the future, however, no scaling of the proton ionization in dependence of the future cycles' activity level has been made. This is primarily motivated by the lack of knowledge on long-term variations of proton fluxes, related to the short availability of observational records (since 1962).

3.6 Solar Forcing in Future Scenarios

- 5 As mentioned before, we provide two scenarios of future solar activity: the reference one is based on the most likely evolution of solar activity from 2015 to 2300, while the extreme one corresponds to the lower 5th percentile of all forecasts. We first forecast the modulation potential Φ with the three approaches described in Sec. 3.1.1 to 3.1.3, and define then the reference scenario as their average, weighted by their inverse forecast error (Eq. 2). Note that the analogue forecast, and to a lesser degree, the AR forecast tend to converge toward a climatological mean, whereas the harmonic forecast keeps on oscillating.
- 10 Because of that, our forecasts are likely to exhibit somewhat less variability than the observed Φ .

Figures 24 and 25 present an overview of the entire daily CMIP6 solar forcing file from 1850 through 2300, respectively for the reference and extreme scenarios. Both show the the TSI, the F10.7cm solar radio flux, which is a good proxy for Lyman- α line, and three different SSI wavelength ranges in the UV, VIS, and NIR. Also shown are the Ap index as a proxy for auroral electron precipitation, and the ionization rates due to solar protons and galactic cosmic rays. In Fig.25, MEE instead of proton

- 15 ionization rates are shown, as the latter are identical in both scenarios.

As explained in Appendix G, our scenarios are built out of past solar cycles; therefore, both the solar cycles and their daily variations are consistent with the average level of heliospheric potential. In this sense, the future scenarios for CMIP6 are much more realistic than the stationary Sun scenario that went into CMIP5.

4 Pre-industrial (PI) Control Forcing

- 20 For the PI control experiment, we recommend to use one constant (solar cycle averaged) value for the TSI and SSI spectrum representative for 1850 conditions (Fig.26). The average in TSI, SSI, Ap, Kp, F10.7, as well as the ion-pair production rate by GCRs covers the time period from 1.1.1850 to 28.1.1873, which is two full solar cycles. For the ion-pair production rates by SPEs and MEEs median values representative for the background are provided in order to avoid the occurrence of large sporadic events in the PI control experiment.

- 25 As usual the PI control run is supposed to provide an estimate of the unforced climate system to understand internal model variability. It is also used for detection and attribution studies to disentangle contributions from different natural and anthropogenic forcings (some of which include a long-term trend, such as GHGs, aerosols, solar forcing).

For those groups that are interested, we also provide a 1000-year solar forcing time series with 11-year solar cycle variability included but without long-term trend (Fig. 26). This time series still has slightly different solar cycle amplitudes and also

30 preserves the variable phase of the solar cycle, however, the solar cycle mean activity level is held constant as compared to the reference scenario in Fig. 24. By running a second PI control experiment with solar cycle variability, this provides one additional periodic forcing on top of the seasonal cycle. Since the PI control is also used to determine model variability at

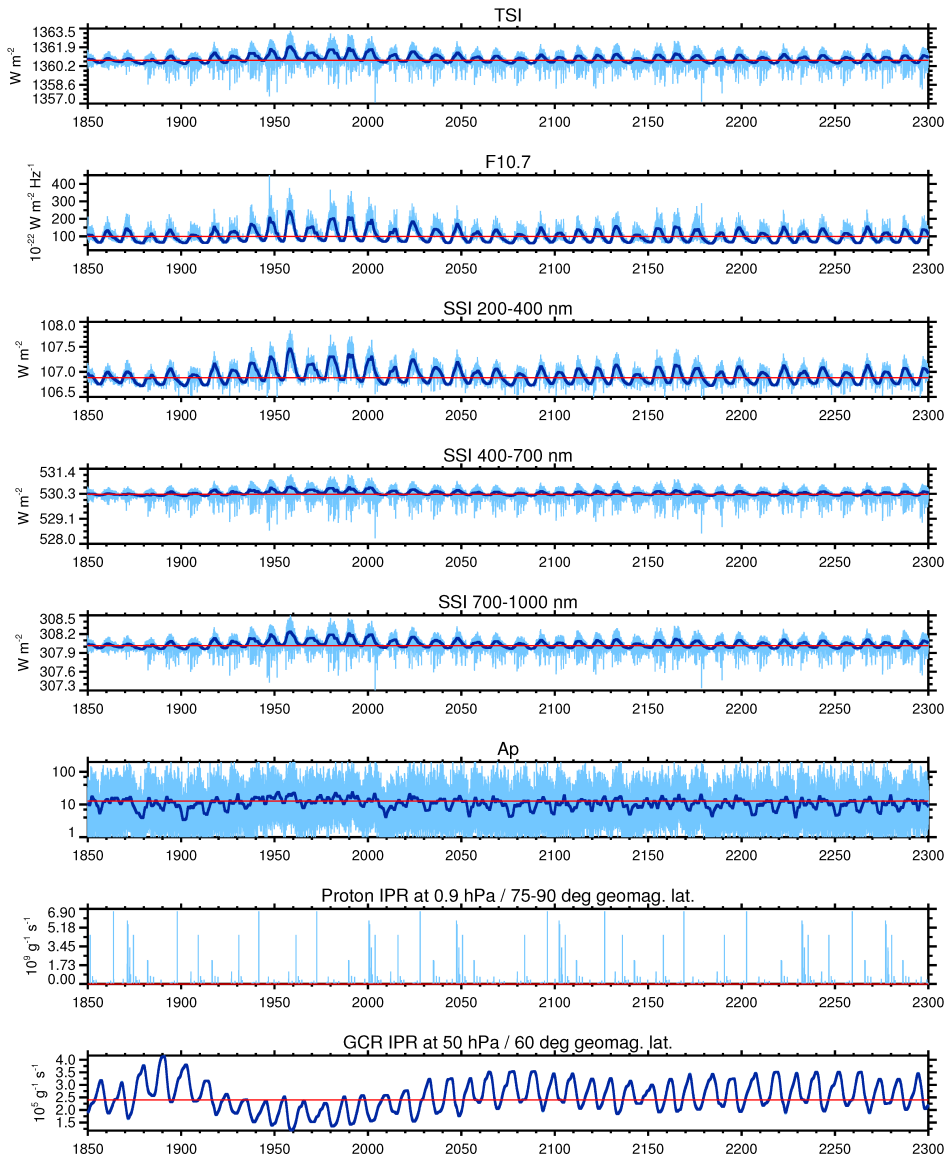


Figure 24. CMIP6 Reference (REF) scenario forcing shown for (from top to bottom) TSI, F10.7, SSI at 200–400 nm, SSI at 400–700 nm, SSI at 700-1000 nm, Ap, proton IPR at 1 hPa and 70° geomagnetic latitude, and GCR IPR 50 hPa and 60° geomagnetic latitude. Annually smoothed values are shown by dark blue lines. Constant values of the PI control forcing (see Sec. 4) are shown with red lines as reference.

decadal timescales, including a solar cycle would certainly change the mean climate and the variance of the control experiment as compared to the “standard” control experiment with constant 1850 solar forcing. However, not including the solar cycle variability may underestimate the variance of the climate system and may lead to climate system biases. Ideally the groups would do two PI control experiments: one with and one without solar cycle variability.

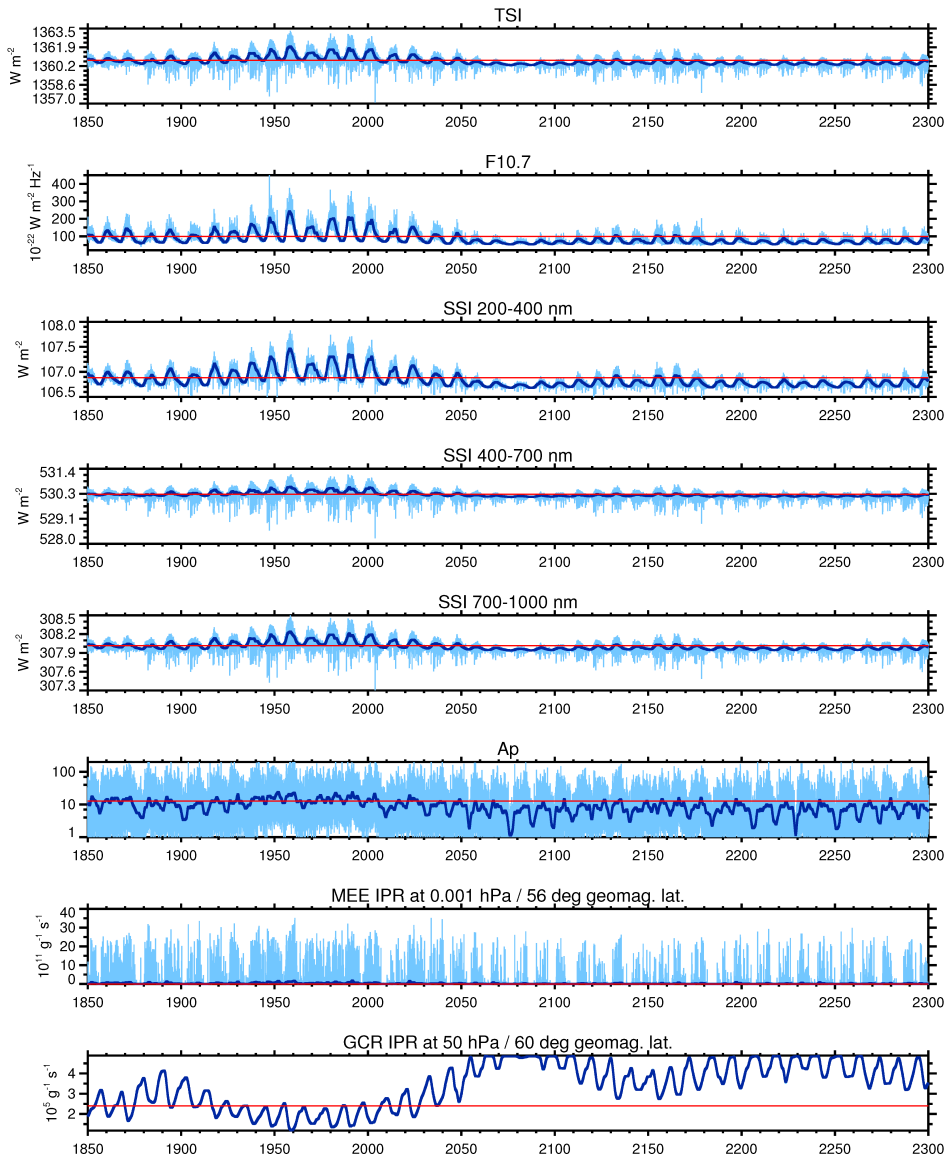


Figure 25. CMIP6 Deep minimum (EXT) scenario forcing shown for (from top to bottom) TSI, F10.7, SSI at 200–400 nm, SSI at 400–700 nm, SSI at 700–1000 nm, Ap, MEE IPR at 0.001 hPa and 56° geomagnetic latitude, and GCR IPR 50hPa and 60° geomagnetic latitude. Annually smoothed values are shown by dark blue lines. Constant values of the PI control forcing (see Sec. 4) are shown with red lines as reference.

Note that the variable PI control dataset is meant solely for sensitivity experiments in order to understand physical mechanisms for internal natural climate variability such as a potential synchronization of North Atlantic climate variability by the 11-year solar cycle (Thieblemont et al., 2015) in the atmosphere-ocean system. It avoids on purpose any long-term trend in

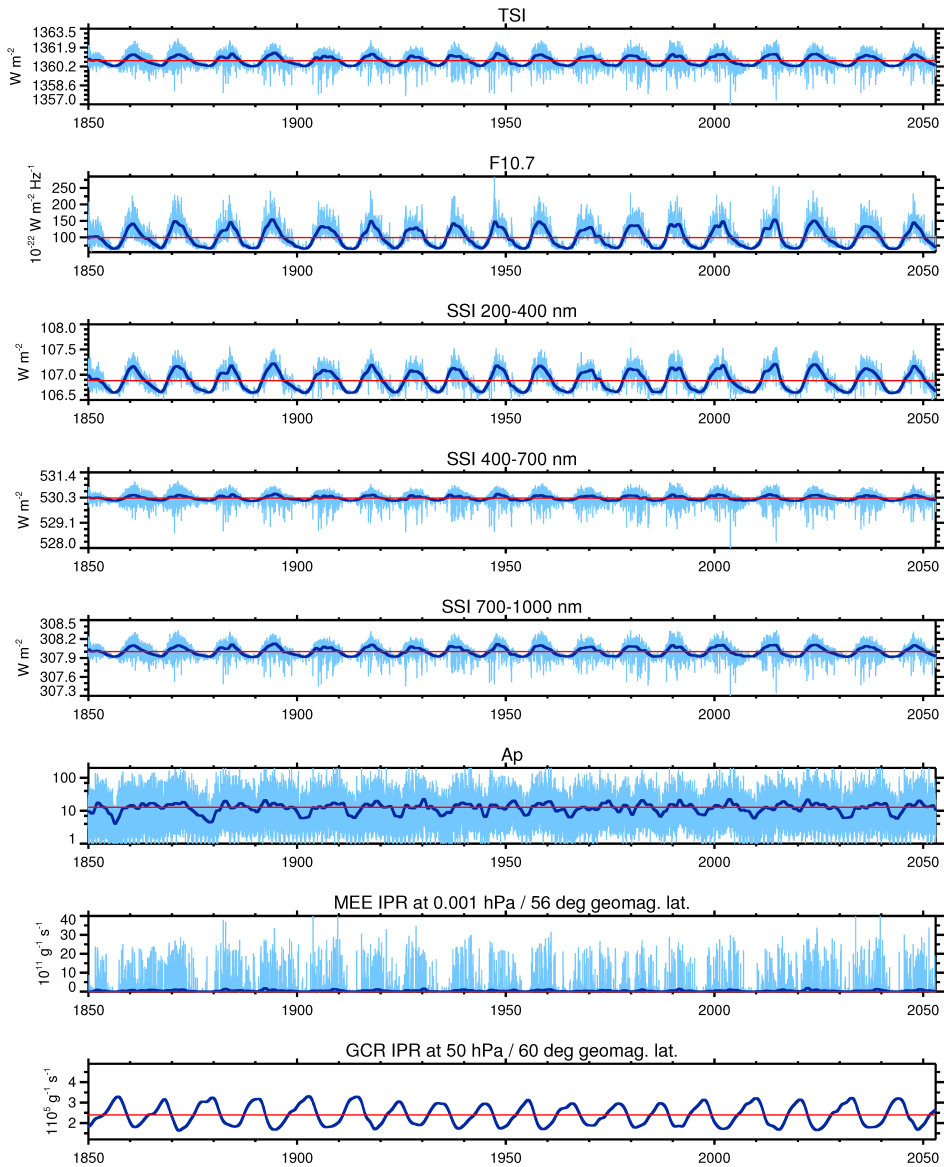


Figure 26. CMIP6 Variable (light blue) and constant PI-control (red) forcing shown for (from top to bottom) TSI, F10.7, SSI at 200–400 nm, SSI at 400–700 nm, SSI at 700–1000 nm, Ap, MEE IPR at 0.001 hPa and 56° geomagnetic latitude, and GCR IPR 50 hPa and 60° geomagnetic latitude. Annually smoothed values are shown by dark blue lines. Note the different scale for F10.7 in comparison with Figures 24 and 25.

solar activity, and should therefore not be used for historical model simulations and/or solar forcing reconstructions. More realistic solar forcing timeseries for the past 1000 years are provided within the PMIP (Paleoclimate Modeling Intercomparison Project) exercise (Kageyama et al., 2016) and the solar forcing is described in more detail in (Jungclauss et al., 2016).

The radiative part of the variable PI control forcing has been generated by scaling the annual and sub-annual components of the REF forcing dataset to a constant solar cycle mean activity level. The scaling procedure for SSI and F10.7 is described in Appendix H. Constant background components have been added. These have been adjusted such that the mean values of the resulting SSI and F10.7 time series are consistent with the constant PI control forcing. In order to enhance the contrast for this sensitivity experiment, we scale the annual and sub-annual components of SSI at wavelengths greater than 115 nm to the mean activity level of solar cycles 18–22 (grand solar maximum) rather than to 1850–1873 conditions. For the EUV channels (10–115 nm) and for F10.7, such an enhanced mean activity level would result in unreasonably low background values (due to the adjustment to the constant PI control forcing). Therefore, the annual and sub-annual components of these quantities were scaled to 1850–1873 conditions.

Similarly, the particle part of the variable PI control forcing has been generated by scaling the annual and sub-annual components of the REF forcing dataset to the 1850–1873 mean activity level. The scaling of geomagnetic Ap and Kp indices is described in Appendix I. MEE-induced ion-pair production rates for the variable PI control forcing have then been calculated from the scaled Ap data. GCR-induced ion-pair production rates have been calculated using a constant value of Φ representative for the 1850–1873 period. Solar cycle variations have been added, however, scaled to the 1850–1873 mean activity level. The variable PI control proton forcing is identical to the REF forcing since it does not include any long-term trend. Note that the temporal averages of SSI, TSI, F10.7, Ap, Kp, as well as GCR-induced ion-pair production rates are fully consistent with the values provided in the constant PI control forcing dataset. This, however, is not the case for the proton and MEE forcings, which, in the latter case, do not account for large, sporadic events.

The variable PI control dataset (see Fig. 26) covers the time period from 1.1.1850 until 9.9.2053 (end of solar cycle 27). The dataset can be extended to cover 1000 years by multiple repetition of the solar cycle sequence 12–27. The first 450 years of the resulting forcing time series are consistent in solar cycle phase and short-term fluctuations with the REF and EXT datasets. Solar forcing only experiments based on variable PI control, REF, and EXT forcing data would therefore be ideally suited to address the impact of long-term solar activity variations on the climate system.

5 Solar Cycle Signal in Stratospheric Ozone

The climate response to solar variability depends not only on the ‘direct’ impact of changes in TSI and SSI on atmospheric and surface heating rates, but also on the ‘indirect’ effects on stratospheric and mesospheric ozone abundances (e.g. Haigh, 1994). ~~The In some regions, the~~ associated solar-ozone response can contribute ~~to~~ more than 50% of the ~~total stratospheric heating response to solar variability in some regions~~ change in stratospheric heating rates between solar cycle maximum and minimum (Shibata and Kodera, 2005; Gray et al., 2009). It is therefore important to include the solar-ozone response in global model simulations to realistically capture the impacts of solar variability on climate.

In reality, the ‘direct’ and ‘indirect’ parts of the heating are highly coupled, since they reflect the same fundamental process (i.e. absorption of solar photons by molecules). In (chemistry-)climate models, the effects of these processes on atmospheric heating rates and temperatures are incorporated through the radiation scheme as a result of variations in the ozone field and

the specified values of TSI and SSI (see Tab. 3). The ozone field in a model can be produced by an interactive photochemical scheme, as presented above for CESM1(WACCM) and EMAC, or it can be externally prescribed in models that do not have a chemistry scheme. Models with a chemistry scheme must adequately represent SSI variability in their photolysis schemes (e.g. in the UV part of the spectrum) to simulate a realistic solar-ozone response. As described above, variations in EPP also affect stratospheric and mesospheric ozone abundances. These effects will be implicitly captured in CCMs with the capability of prescribing EPP and/or their effects on chemical processes (e.g. NO_x).

Several CMIP5 models included stratospheric chemical schemes (Hood et al., 2015), and it seems likely that more models will have this capability in CMIP6. However, there will be CMIP6 models that do not include chemistry but which resolve the stratosphere and specify SSI, and thus have some of the major ingredients for simulating a top-down pathway for solar-climate coupling (Mitchell et al., 2015b). For these models, the simulated climate response to solar variability will partly depend on the representation of the solar-ozone response in their prescribed ozone field.

CMIP5 models without chemistry were recommended to use the SPARC/AC&C Ozone Database (Cionni et al., 2011). The historical part of this dataset for the stratosphere provided monthly and zonal mean ozone concentrations based on a multiple regression analysis of measurements from the Stratospheric Aerosol and Gas Experiment (SAGE) satellite instruments. The regression coefficients for various key drivers (e.g. ODS, GHG, solar forcing) were used to reconstruct ozone values back to 1850 as a function of latitude and pressure. The historical part of the CMIP5 ozone dataset therefore implicitly included a solar-ozone response derived from satellite observations. However, uncertainties in the amplitude of the solar-ozone response in SAGE II measurements, which cover only around two solar cycles, have been recently documented by Maycock et al. (2016). It is therefore desirable to update the representation of the solar-ozone response in the WCRP/SPARC Chemistry Climate Model Initiative (CCMI) Ozone Database for CMIP6 (Hegglin et al., 2017). At the time of writing, this database is still under development and readers are referred to Hegglin et al. (2017) for final details. However, for illustrative purposes, Figure 27 shows the monthly mean fractional solar-ozone response per 130 units of the F10.7cm solar flux that has been diagnosed using a multiple linear regression ~~model analysis~~ (see Maycock et al. (2016)) for the period 1960-99 from the CMIP6 historical ozone files (file: vmro3_input4MIPs_ozone_CMIP_UReading-CCMI-1-0_gr_195001-199912.nc) recently made available through input4MIPs (<https://pcmdi.llnl.gov/projects/input4mips/>). There is currently no information available about how the solar-ozone response will be represented in the ~~ozone files~~ [CMIP6 Ozone Database](#) for the future period and readers are referred to Hegglin et al. (2017) for details.

Figure 27 shows a solar-ozone response of up to ~2% in the tropical mid-stratosphere which peaks at ~5 hPa. Since the peak amplitude of the solar-ozone response in Figure 27 is considerably smaller, and exhibits a different vertical structure, compared to the ~~SAGE data used in the SPARC/AC&C~~ CMIP5 Ozone Database (~~Maycock et al., 2016~~) ([Maycock et al., 2017](#)), we anticipate that the ~~peak~~ magnitude of the ~~solar cycle temperature response~~ [stratospheric temperature response over the solar cycle may also be smaller](#) in models using the ~~CCMI~~ CMIP6 Ozone Database ~~may also be smaller~~ ([Maycock et al., 2017](#)).

We recommend that CMIP6 models without interactive chemistry use the ~~recommended SSI forcing~~ [SSi forcing dataset](#) described above and the ~~CCMI~~ CMIP6 Ozone Database described by Hegglin et al. (2017) to ensure consistency in the representation of the solar cycle forcing across models. If CMIP6 models ~~opt to~~ use an alternative ozone dataset ~~with~~ [containing](#) a

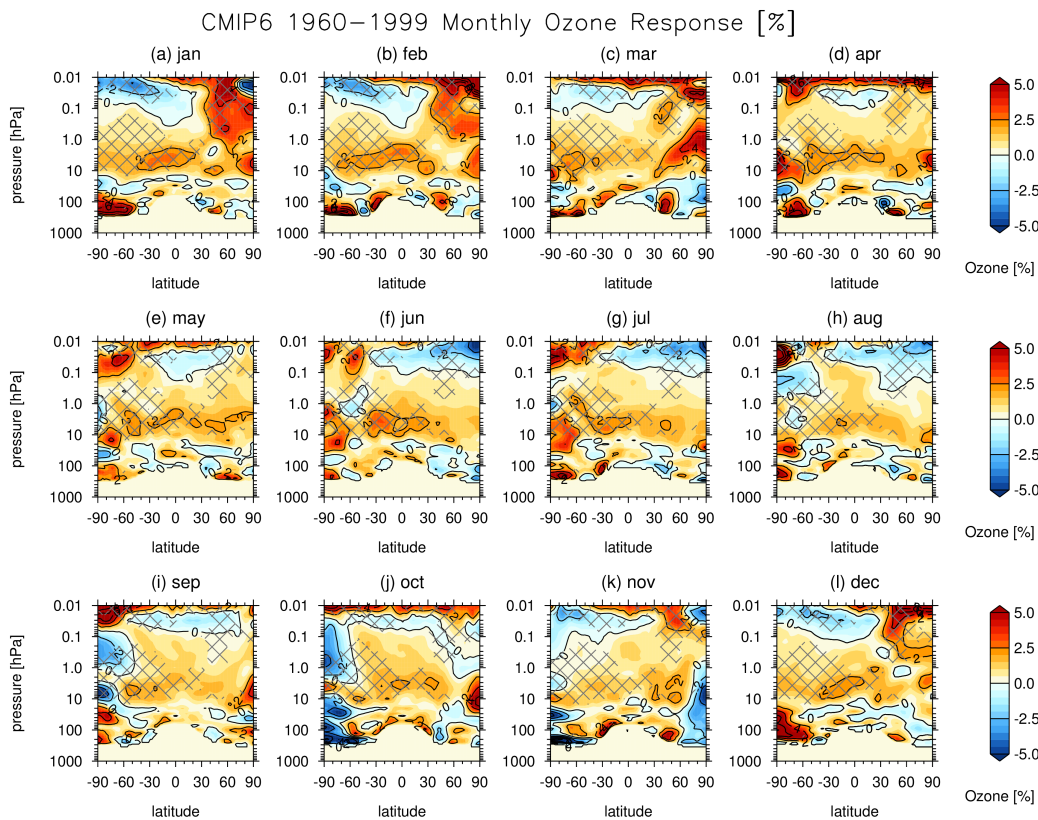


Figure 27. A preliminary estimate of the fractional (%) monthly solar-ozone response per 130 units of the F10.7cm flux in the [CCMI CMIP6 Ozone Database](#) for [CMIP6-extracted-using-multiple-linear-regression-for](#) the period 1960-99 using the ozone mixing ratio [files file](#) (vmro3_input4MIPs_ozone_CMIP_UReading-CCMI-1-0_gr_195001-199912.nc) downloaded from inputs4MIPs. The hatching denotes regions where the [extracted-solar-ozone response diagnosed using multiple regression analysis](#) is [estimated-found](#) to be significantly different from zero at the 95% confidence level. Please note that the [details-of-the-CMIP6 Ozone Database are-still-being-finalised-for-the-future simulations has-not-been-released](#) at the time of writing and [we-refer](#) readers [are-referred](#) to Hegglin et al. (2017) for further details.

different representation of the solar-ozone response it would be very valuable for this to be documented [by modelling groups](#), so that differences in [modelled-responses-to-the-solar-cycle-might-be-simulated-responses-to-solar-forcing-might-be-better](#) understood (Mitchell et al., 2015b).

6 Conclusions

This paper provides a comprehensive description of the ~~solar forcing~~ recommended solar forcing dataset for CMIP6. The dataset consists of time series ~~from 1850 through 2300 of covering 1850-2300 of solar~~ radiative (TSI, SSI, F10.7cm) and particle (Ap, Kp, ionization rates due to SPEs, MEEs, and GCRs) forcings. This is the first time that solar-driven particle forcing has been included as part of the CMIP recommendation and represents a new capability for CMIP6. TSI and SSI time series for the historical period are defined as averages of two solar irradiance models; the empirical NRLTSI2/NRLSSI2 model and the semi-empirical SATIRE model, which have been adapted to CMIP6 needs as described above. Since this represents a change from the CMIP5 recommended NRLTSI1 and NRLSSI1 dataset, ~~the paper puts this paper places~~ special emphasis on the comparison between the radiative properties of the CMIP5 and CMIP6 solar forcing ~~recommendation. Solar forcing is provided~~ in daily as well as monthly resolution separately for the reference period of the historical simulation recommendations. The solar forcing components are provided separately at daily and monthly resolutions for the historical simulations, i.e. 1850–2014, for the future period, i.e. 2015–2300, including an additional extreme Maunder Minimum-like sensitivity scenario, ~~as well as for a constant and a time-varying PI-Control forcing and as constant and time-dependent variants for the preindustrial control simulation~~. The particle forcing is only included in the daily resolution files. The dataset as well as a metadata description and a number of tools to convert and implement the solar forcing data can be found here: <http://solarisheppa.geomar.de/cmip6>. In the following we ~~highlight the most important points~~ summarise the key features of the CMIP6 solar forcing dataset in comparison to CMIP5 that provide the reader with an overview without reading the paper in detail.

Radiative Forcing

- A new and lower TSI value is recommended: the contemporary solar cycle-average is now $1361.0 \pm 0.5 \text{ W/m}^2$ (Prša et al., 2016).
- ~~During Over~~ the last three solar cycles in the satellite era there is a slight negative TSI trend in the CMIP6 ~~which is statistically indistinguishable from available observations (Dudok de Wit et al., 2017). This dataset. A recent reconstruction of the TSI, with a proper estimation of its uncertainties, suggests that this downward trend between the solar minima of 1986 and 2009 is not statistically significant (Dudok de Wit et al., 2017). The TSI trend leads to a~~ an estimated radiative forcing on a global scale of -0.04 W/m^2 , which is small in comparison with other forcings over this period.
- The new CMIP6 SSI dataset is the arithmetic mean of the empirical NRLSSI2 and the ~~semi-empirical~~ semi-empirical SATIRE irradiance models adapted to meet CMIP6 needs and covers wavelengths from 10–10,000 nm.
- The CMIP6 SSI dataset agrees very well with available satellite measurements (i.e. those which are used for building the SOLID observational composite) in the contribution of solar cycle variability to TSI in the 120–200 nm wavelength range. In the 200–400 nm range, which is also important for ozone photochemistry, the CMIP6 dataset shows a larger ~~solar cycle variability contribution to TSI than~~ contribution to solar cycle TSI variability than in CMIP5 (50% as compared to 35%). However, there is a lack of accurate satellite measurements to validate variations in this spectral region. In

the VIS part of the spectrum, the CMIP6 dataset shows smaller solar cycle variability than in CMIP5 (25% as compared to 40%). In the NIR, the CMIP6 dataset shows slightly larger variability than in CMIP5.

The implications of the differences in the spectral characteristics of SSI between CMIP5 and CMIP6 ~~on~~ for climatological and solar cycle variability in atmospheric heating rates and ozone photochemistry have been tested using two state-of-the art CCMs, EMAC and CESM1(WACCM), and a line-by-line radiative transfer model, libradtran.

- When comparing ~~the annual mean climatological differences~~ differences in annual mean climatologies under perpetual solar minimum conditions, the CMIP6-SSI irradiances lead to lower SW heating rates (-0.35 K/day at the stratopause), cooler stratospheric temperatures (-1.5 K in the upper stratosphere), lower ozone abundances in the lower stratosphere (-3%), and higher ozone abundances (+1.5%) in the upper stratosphere and lower mesosphere, as compared to the CMIP5-SSI irradiances. These radiative effects lead to a weakening of the meridional temperature gradient between the tropics and high latitudes and hence to a statistically significant weakening of the stratospheric polar night jet in early winter.
- The ~~changes in solar irradiances between~~ differences in irradiances between 11-year solar cycle maximum and minimum in the CMIP6-SSI dataset result in increases in SW heating rates (+0.2 K/day at the stratopause), temperatures (~1 K at the stratopause), and ozone (+2.5% in the upper stratosphere) in the tropical upper stratosphere. These direct radiative effects lead to a strengthening of the meridional temperature gradient between the tropics and high latitudes and a statistically significant strengthening of the stratospheric polar night jet in early winter, which propagates poleward and downward during mid-winter and affects tropospheric weather, with a positive Arctic Oscillation signal in late winter. This regional surface climate response is similar and statistically significant in both CCMs. The CMIP6-SSI irradiances lead to slightly enhanced solar cycle signals in SW heating rates, temperatures and ozone, as compared to the CMIP5-SSI. However, the differences ~~between the in the 11-year~~ solar cycle signals ~~for~~ between the two SSI datasets are generally not statistically significant and ~~the solar signal is~~ are smaller than the ~~before mentioned climatological differences~~ differences in climatological conditions between CMIP6 and CMIP5 described above.

Particle Forcing

- The reconstruction of geomagnetic Ap and Kp indices backwards in time (starting in 1850) ~~allowed to generate~~ enabled a consistent historical dataset of geomagnetic particle forcing ~~for the consideration of the~~ to be created in order to capture the atmospheric impact of precipitating auroral and radiation belt electrons. Regarding the latter, we employed a novel precipitation model for mid-energy electrons (MEE), based on the Ap index. Computed MEE ~~ionisation~~ ionization rates have been successfully tested in the (CESM1)WACCM model. ~~For the consideration~~ To capture the effects of polar winter descent of EPP-generated NO_x in climate models ~~with their~~ that have an upper lid in the mesosphere (i.e., below the EPP source region), recommendations for the implementation of an odd nitrogen upper boundary condition (UBC) are provided. The UBC has been successfully tested ~~with in~~ in the EMAC model by comparison to observations. Inclusion of the ~~recommened CMIP~~ CMIP6 recommended magnetospheric particle forcing in climate model simulations

~~improves significantly~~ significantly improves the agreement with observed NO_x, HO_x, and ozone distributions in the polar stratosphere and mesosphere.

- Solar proton and Galactic Cosmic Ray forcings have been built from well-established datasets ~~which that~~ have been used in many atmospheric model studies. ~~Observed proton fluxes, however,~~ However, observed proton fluxes are only available since 1963. ~~Before,~~ Therefore, prior to this date the proton forcing included in our dataset is fictitious, although ~~resembling the expected~~ it broadly captures the expected variation in overall strength and distribution ~~along the solar cycle~~ throughout the 11-year solar cycle.
- In most cases, particle forcing can be expressed in terms of ion pair production rates. We have provided detailed recommendations for their implementation into atmospheric chemistry schemes.
- CMIP6 model simulations utilizing the recommended particle forcing for the ~~historic~~ historical period (1850–2014) ~~period will allow to address~~ will enable an assessment of the potential long-term ~~effect of particles as planned to be assessed~~ effects of solar particles on the atmosphere and climate as planned in upcoming coordinated WCRP/SPARC SOLARIS-HEPPA studies.

Future Forcing Scenarios

- 15 In CMIP5, future solar irradiances assumed no long-term changes in the Sun and were obtained by simply repeating solar cycle 23 into the future. In CMIP6, we include a more realistic evolution for future solar forcing based on the weighted average of three statistical ~~forecast models~~ models constrained by past long-term solar proxy data; this shows a moderate decrease to a Gleissberg-type level of solar activity until 2100 for the reference (REF) scenario. We ignore scenarios with high levels of solar activity because the Sun just left such an episode (called a grand solar maximum), and several studies suggest that it is very
- 20 unlikely to return to it in the next 300 years. In addition, we provide an extreme (EXT) scenario ~~to~~ for the future that can be used for sensitivity studies, which includes an evolution to an exceptionally low level of solar activity during the 21st century similar to that estimated for the Maunder Minimum.

PI-Control Forcing

For the PI control experiment, we recommend to use one constant (solar cycle averaged) value for the TSI and SSI spectrum

25 representative ~~for of~~ 1850 conditions. The average values in TSI, SSI, Ap, Kp, F10.7, as well as the ion-pair production rate by GCRs are derived from the time period 1.1.1850 to 28.1.1873, which is two full solar cycles. For the ion-pair production rates by SPEs and MEEs, median values representative of background conditions are provided in order to avoid the occurrence of large sporadic events in the PI control experiment.

We also provide a second PI control forcing time series ~~with a time-varying solar cycle component~~ that includes variations in

30 solar forcing on timescales of the 11-year solar cycle and shorter, but without any long-term trend. This time series contains some variation in 11-year solar cycle amplitude, and also preserves the variable phase of the solar cycle, however, the mean

level of solar activity is held constant. The PI control experiment with solar cycle variability included may better reproduce decadal scale climate variability ~~better. Ideally the~~. Ideally CMIP6 modelling groups will run two PI control experiments: one with and one without solar cycle variability.

Solar Ozone Forcing

- 5 CMIP6 models with interactive chemistry are recommended to include a consistent prescription of the CMIP6-SSI variations in their radiation and photolysis schemes, so that they include an internally-consistent representation of the solar-ozone response. Climate models that do not calculate ozone interactively are recommended to use the SPARC/CCMI Ozone Database for CMIP6 (Hegglin et al., 2017), which ~~includes a~~ has been constructed from existing CCM simulations. This differs from the representation of the solar-ozone response ~~derived from CCM simulations. in the CMIP5 Ozone Database, which was based on~~ satellite ozone measurements (Cionni et al., 2011). Multiple linear regression analysis of the CMIP6 Ozone Database over the period 1960-99 reveals that an 11-year solar cycle ozone response is implicitly included in the dataset and resembles previous results from CCM studies. An analysis of the representation of particle-induced ozone anomalies in the CMIP6 Ozone Database has not been performed. Readers are referred to Hegglin et al. (2017) for further details. ~~Please note that particle-induced ozone anomalies are not yet explicitly considered in this ozone database.~~ CMIP6 models that include both CMIP6-SSI and
- 15 solar induced-ozone variations are expected to show a better representation of solar climate variability compared to models that exclude the solar-ozone response.

7 Data Availability

- The CMIP6 solar forcing dataset described in this paper as well as the metadata description ~~will be~~ have been published at <http://solarisheppa.geomar.de/cmip6> and linked to the Earth System Grid Federation (ESGF) <https://pcmdi.llnl.gov/search/input4mips/> with version control and digital objective identifiers (DOIs) assigned. An overview of the CMIP6 Special Issue can be found in Eyring et al. (2016).
- 20

Appendix A: Reconstruction of the SSI in the EUV

- The EUV spectrum is a complex mix of spectral lines and continua that are associated with different elements, and have each their specific variability in time. In spite of this, there is strong observational evidence for the spectral variability in the EUV
- 25 to have remarkably few degrees of freedom (Amblard et al., 2008). We make use of this property to reconstruct the EUV at wavelengths shortward of 105 nm (in a range that is not covered by NRLSSI2 and SATIRE) as a function of the SSI provided by these same models between 115.5 and 123.5 nm (i.e. including the intense Lyman- α line).

- Let $\Phi(\lambda, t)$ denote the logarithm of the SSI in the EUV, and $\bar{\Phi}(t)$ its value averaged between 115.5 and 123.5 nm. The logarithm is used mainly to guarantee that the SSI, whose amplitude spans several orders of magnitude, never goes negative.
- 30 The ratio between solar-cycle amplitude and short-term variability is strongly wavelength-dependent. For that reason, the SSI

is frequently decomposed into short- and long-timescale terms, with a cutoff around 81 days (e.g. Woods et al., 2005). Let the 81-day average Φ be $\langle \Phi \rangle_{81}$. Our empirical model then reduces to

$$\Phi(\lambda, t) = A(\lambda) \langle \bar{\Phi}(t) \rangle_{81} + B(\lambda) (\bar{\Phi}(t) - \langle \bar{\Phi}(t) \rangle_{81}) + C(\lambda) \quad (\text{A1})$$

The model coefficients $A(\lambda)$, $B(\lambda)$ and $C(\lambda)$ are estimated from 9 years of EUV observations by the TIMED/SEE instrument (Woods et al., 2005), spanning the period from February 2002 to February 2011.

This simple model matches the SOLID observational composite well within its uncertainty range. Note, however, that TIMED/SEE data below 28 nm, and between 115–129 nm are partly modeled, and thus the variability of the EUV spectrum prior to the space age should be considered with great care.

Appendix B: Recommendations for Model Implementation of SSI

10 The SSI dataset recommended for CMIP6 covers the solar spectrum from 10 to 100,000 nm. It is provided as irradiance averages for 3890 spectral bins (in $\text{W}/(\text{m}^2 \text{ nm})$). Sampling and equivalently bin width range from 1 nm (UV and VIS) to 50 nm (NIR). Tab. 4 contains more details regarding the resolution changing with wavelength.

Table 4. Sampling and bin width of CMIP6-SSI

spectral range	sampling/bin width
10-750 nm	1 nm
750-5,000 nm	5 nm
5,000-10,000 nm	10 nm
10,000-100,000 nm	50 nm

Most climate models prescribe either TSI or SSI in their respective radiation schemes. If the model’s radiation code is able to handle spectrally resolved solar irradiance changes, SSI needs be integrated over the specific wavelength bands to generate Top of the Atmosphere (TOA) fluxes. Using CMIP6-SSI this is done for a given spectral band by simply summing up the irradiances of all (partially) contained bins, each multiplied by the bin width (subtracting potential bin parts that reach beyond the boundaries of the target band). A sample routine for the integration can be found here: <http://solarisheppa.geomar.de/cmip6>. Climate models that calculate ozone interactively also have to integrate SSI to the respective wavelength bands in their photolysis code. An example of the numbers of bands in the radiation and photolysis schemes of two state-of-the-art CCMs, WACCM and EMAC, is shown in Section 2.1.3.

Appendix C: Recommendations for Geographic Projection of IPR Data

In order to characterize the electron precipitation into the atmosphere since 1850 we must take into account the offset between geographic and magnetic field coordinates, and how the relationship between them changes with time. We recommend the

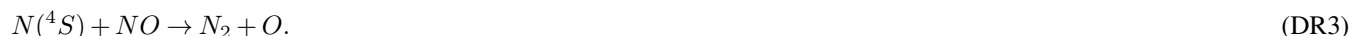
following approach. For years 1850–1900, the gufm1 model may be used (Jackson et al., 2000). Note that this model would allow calculations earlier in time (1590). From 1900–2015 magnetic field conversions should use the current International Geomagnetic Reference Field (IGRF), which at the time of writing is IGRF-12 (Thébault, 2015). It is highly likely that the magnetic field will continue to evolve in the future, and as such we do not recommend fixing the field in any set configuration based on a specific year. Physics-based simulations are now providing representations of future geomagnetic field changes. For the years 2015–2115, Gauss coefficients based on the predicted evolution of the geodynamo can be used from the [modelling modeling](#) of Aubert (2015). For years after 2115, secular variation values from 2115 (also from the Aubert (2015) model) are used to extrapolate forward in time, though obviously with increasing uncertainty. Matlab [modelling-modeling](#) code implementing the above recommendations is available on the SOLARIS-HEPPA CMIP6 website, which allows users to calculate the geomagnetic latitude for any given date, geographic location and altitude for the period 1590 onwards.

Appendix D: NO_x Production by Particle-Induced Ionization

Following Porter et al. (1976) it is assumed that 1.25 N atoms are produced per ion pair. This study also further divided the proton impact of N atom production between the ground state N(⁴S) (45% or 0.55 per ion pair) and the excited state N(²D) (55% or 0.7 per ion pair). Ground state [N(⁴S)] nitrogen atoms can create other NO_y constituents, such as NO, through



or can lead to NO_y destruction through



Generally, excited states of atomic nitrogen, such as N(²D), result in the production of NO through



(e.g., Rusch et al., 1981; Rees, 1989) and do not cause significant destruction of NO_y. If a model does not include the excited state of atomic nitrogen in their computations, the NO_y production from EPP can still be included by assuming that its production is instantaneously converted into NO, resulting in a N(⁴S) production of 0.55 per ion pair and a NO production of 0.7 per ion pair.

Appendix E: HO_x Production by Particle-Induced Ionization

The production of HO_x relies on complicated ion chemistry that takes place after the initial formation of ion pairs (Swider and Keneshea, 1973; Frederick, 1976; Solomon et al., 1981; Sinnhuber et al., 2012). Solomon et al. (1981) computed HO_x

production rates as a function of altitude and ion pair production rate. Each ion pair typically results in the production of around two HO_x constituents in the stratosphere and lower mesosphere. Sinnhuber et al. (2012) have shown that HO_x is formed as H and OH in nearly equal amounts, with small differences of less than 10% due to different ion reaction chains. In the middle and upper mesosphere, one ion pair is computed to produce less than two HO_x constituents per ion pair because water vapor decreases sharply with altitude there, and is no longer available as a source of HO_x. For models which do not include D-region ion chemistry, we recommend to use the parameterisation of Solomon et al. (1981), which is summarized following Jackman et al. (2005b) in Table 5. If the partitioning between HO_x species is considered in the model, H and OH should be formed in equal amounts. Below 40 km altitude and for ionization rates less than 10²cm⁻³s⁻¹ below 70 km altitude, two HO_x can be formed per ion pair. Above 90 km altitude, HO_x-production can be set to zero; between 70 and 90 km, values need to be extrapolated for ion pair production rates smaller than 10²cm⁻³s⁻¹ and larger than 10⁴cm⁻³s⁻¹, taking care not to exceed zero and two.

Table 5. HO_x production per ion pair as a function of altitude and ion pair production rate (IPR). Table adapted from Jackman et al. (2005b).

Altitude [km]	HO _x production per ion pair (no units)		
	IPR [$cm^{-3}s^{-1}$]		
	10 ²	10 ³	10 ⁴
40	2.00	2.00	1.99
45	2.00	1.99	1.99
50	1.99	1.99	1.98
55	1.99	1.98	1.97
60	1.98	1.97	1.94
65	1.98	1.94	1.87
70	1.94	1.87	1.77
75	1.84	1.73	1.60
80	1.40	1.20	0.95
85	0.15	0.10	0.00
90	0.00	0.00	0.00

Appendix F: Minor Constituent Changes due to Particle-Induced Ionization

If available, the use of more comprehensive parameterizations for productions of individual HO_x (OH and H) and NO_y (N(⁴S), N(²D), NO, NO₂, NO₃, N₂O₅, HNO₂, and HNO₃) compounds (e.g., Verronen and Lehmann, 2013; Nieder et al., 2014) is encouraged. Similarly, if atmospheric models include detailed cluster ion chemistry of the lower ionosphere (D region), then the ionization rates should be used to drive the production rates of the primary ions (N₂⁺, N⁺, O₂⁺, O⁺) and neutrals (N, O) produced in particle impact ionization/dissociation (Sinnhuber et al., 2012). Since such a comprehensive treatment of EPP

effects on minor species may introduce more sensitive composition changes via chemical feedbacks, it would be important to document the adopted approaches.

Appendix G: Projection of Historical Solar Cycles in Future Scenarios

Table 6. Historical solar cycles used for construction of future cycles (starting on 2015-01-01).

Current cycle nb.	Historic cycle nb.	Start current cycle yyyy-mm-dd	Start hist. cycle yyyy-mm-dd
24	12	2015-01-01	1883-02-01
25	13	2020-02-02	1890-01-28
26	14	2031-12-18	1901-12-14
27	15	2043-06-19	1913-06-15
28	12	2053-09-10	1878-12-13
29	13	2064-10-26	1890-01-28
30	14	2076-09-10	1901-12-14
31	15	2088-03-12	1913-06-15
32	16	2098-06-04	1923-09-07
33	17	2108-07-05	1933-10-07
34	18	2118-11-21	1944-02-23
35	19	2129-01-16	1954-04-20
36	20	2139-07-02	1964-10-03
37	21	2150-12-04	1976-03-07
38	22	2161-04-21	1986-07-24
39	23	2171-05-21	1996-08-22
40	24	2183-08-19	2008-11-20
	12	2189-11-07	1883-02-01
41	13	2194-10-31	1890-01-28
42	14	2206-09-16	1901-12-14
43	15	2218-03-18	1913-06-15
44	12	2228-06-09	1878-12-13
45	13	2239-07-26	1890-01-28
46	14	2251-06-10	1901-12-14
47	15	2262-12-10	1913-06-15
48	16	2273-03-03	1923-09-07
49	17	2283-04-03	1933-10-07
50	18	2293-08-19	1944-02-23

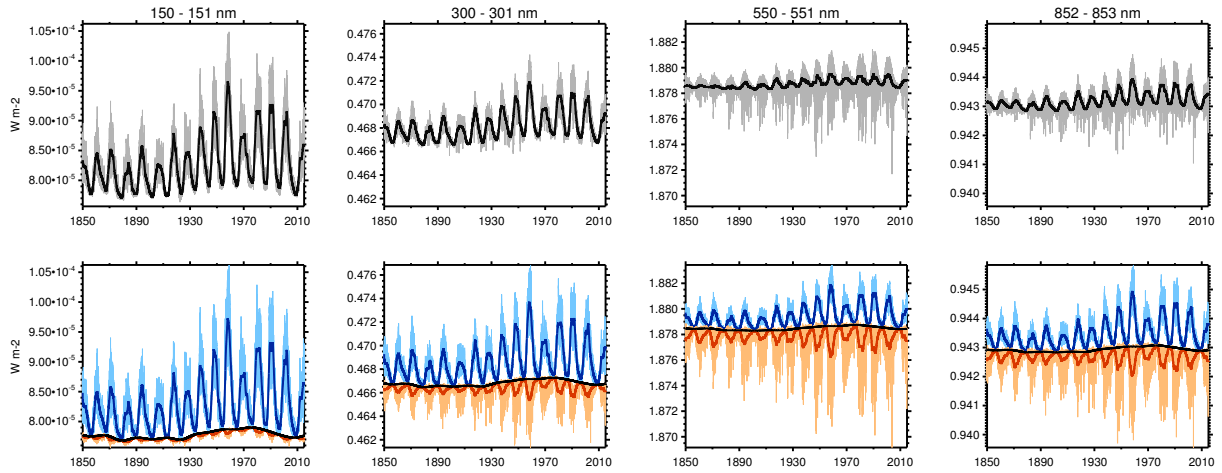


Figure 28. Decomposition of SSI in the scaling procedure (shown for wavelength bins centered at 150.5, 300.5, 550.5, and 852.5 nm, from left to right). Upper panels: daily (grey) and annually (black) resolved SSI. Lower panels: Individual components after decomposition: background SSI^{bg} (black solid); facular brightening related SSI^+ annual, A^+ , (dark-blue) and sub-annual, D^+ , (light-blue); sunspot darkening related SSI^- annual, A^- , (dark-red) and sub-annual, D^- , (light-red).

Appendix H: Scaling of SSI in Future Scenarios and Variable PI-Control Forcing

SSI variability is closely linked to solar magnetic activity variations, and hence sunspot number. However, the form of this relationship may differ significantly at different wavelengths, and time scales (i.e., decadal, annual, sub-annual). Indeed, the contribution to the SSI from different solar features such as faculae, sunspots, the network and ephemeral regions, show 5 different temporal responses (e.g. Vieira and Solanki, 2010). As a consequence, a simple, wavelength-independent scaling of historic SSI sequences for projection into the future or for the generation of the variable PI control forcing would lead to unrealistic results

Instead, we first decompose the SSI time series at individual wavelength bins λ into components corresponding to the background variability $SSI^{bg}(\lambda)$ (i.e., long-term variations of the SSI at solar minima), to facular brightening-related variability $SSI^+(\lambda)$, and to sunspot darkening related variability $SSI^-(\lambda)$. The latter two components are further decomposed into annual (A^+ and A^-) and sub-annual (D^+ and D^-) contributions (see Fig. 28). 10

For the projection of past solar cycles into the future only the D^+ and D^- components need to be scaled since the annually resolved SSI is already provided by the SSI models. These components are shown in Fig. 29 for selected wavelength bins. The distributions of D^+ values within a given solar cycle are rather symmetric around zero and show a close to normal distribution. Variability differences between solar cycles are therefore well represented by the corresponding standard deviations $SD(D^+)_{SC}$ of individual cycles. This quantity also shows good correlation with $\langle SSN \rangle$ and we therefore use it to construct time-resolved scaling functions. The distributions of D^- values are largely skewed towards negative values and do not exhibit 15 the characteristics of a normal distribution. This behavior is expected because of the more intermittent response of SSI to

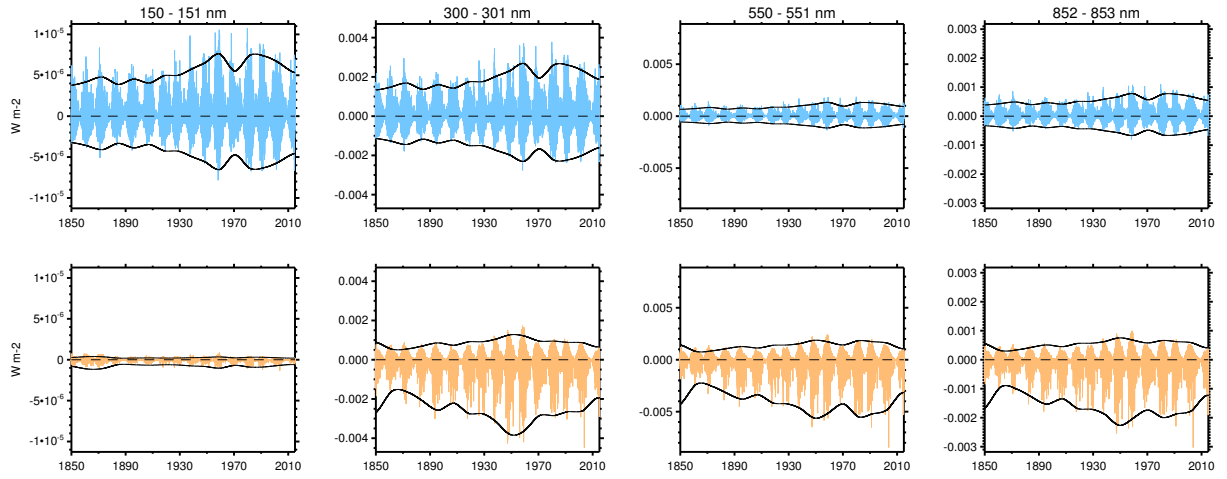


Figure 29. D^+ (top, light blue) and D^- (bottom, light red) components of SSI at wavelength bins centered at 150.5, 300.5, 550.5, and 852.5 nm (from left to right). The corresponding scaling functions $SD(D^+)$ (top) and $MAD(D^-)$ (bottom), multiplied by 3.5 and -3 in the case of $SD(D^+)$ (5 and -15 in the case of $MAD(D^-)$) are shown by black solid lines.

sunspot darkening, as compared to facular brightening. Variability differences between solar cycles are therefore best represented by the corresponding median absolute deviations $MAD(D^-)_{SC}$, which are therefore used to construct the time-resolved scaling functions for the D^- components.

The coefficients for the scaling of SSI variability with $\langle SSN \rangle$ have been obtained from linear regression fits of $SD(D^+)_{SC}$ and $MAD(D^-)_{SC}$ to $\langle SSN \rangle$ for each individual wavelength bin (see Fig. 30). In all fits, a nonzero offset is obtained, with particularly large values in the case of $MAD(D^-)_{SC}$. Sub-annual SSI variations are expected to be very low in the absence of sunspots, with variations mainly coming from the solar network (Bolduc et al., 2014). For that reason, we apply a non-linear correction in the scaling for low $\langle SSN \rangle$ values in order to obtain realistic results for solar cycles with very low activity in the EXT scenario. This has been achieved by multiplying a $\langle SSN \rangle$ -dependent exponential correction f to the obtained offsets:

$$10 \quad f = \frac{1 - \exp(-0.1\langle SSN \rangle)}{1 + \exp(-0.1\langle SSN \rangle)} \quad (H1)$$

For the construction of the variable PI control forcing, annual and sub-annual SSI components are scaled individually to a constant solar cycle mean activity level at each wavelength bin. The scaling has been performed for the D^+ and D^- components based on $SD(D^+)$ and $MAD(D^-)$, respectively, as in the future scenario construction. For A^+ and A^- , we use the corresponding solar cycle averages to construct time-resolved scaling functions. The background contributions SSI^{bg} were set to constant values. The same procedure was also applied to the F10.7 radio flux.

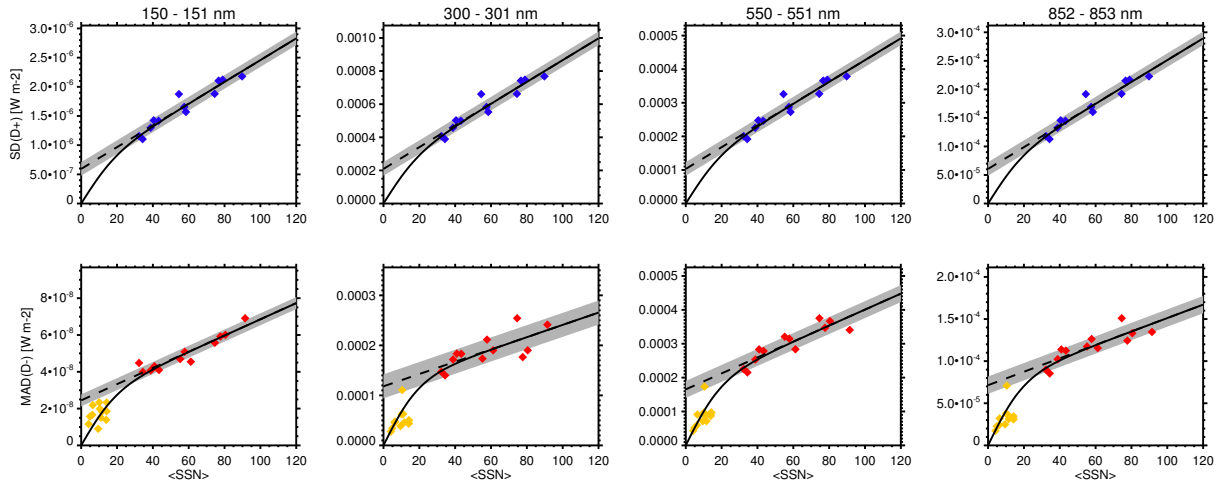


Figure 30. Regression of $SD(D^+)_{SC}$ (top, blue symbols) and $MAD(D^-)_{SC}$ (bottom, red symbols) to $\langle SSN \rangle$ at wavelength bins centered at 150.5, 300.5, 550.5, and 852.5 nm (from left to right). The resulting linear fit is shown by dashed black lines, the grey shaded areas reflect the RMS errors. The solid black lines show the functional dependence used in the scaling after application of a non-linear correction for low $\langle SSN \rangle$ values. $MAD(D^-)$ values calculated from the low activity part of the solar cycles provide an estimate for very weak solar cycles and are shown with orange symbols (only lower panels).

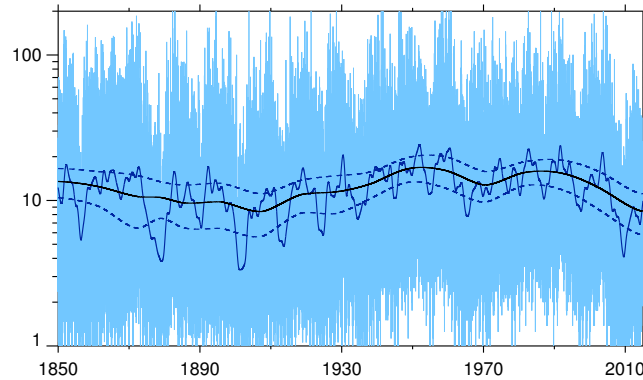


Figure 31. Decomposition of the reconstructed Ap index in the scaling procedure. Light blue: daily resolved Ap ; black: background component Ap^{bg} ; solid dark blue: annual component Ap^a ; dashed dark blue: scaling function $SD(Ap^a)$, multiplied by 1 and -1, used to scale the annual component.

Appendix I: Scaling of Geomagnetic Indices in Future Scenarios and Variable PI-Control Forcing

The geomagnetic activity level is strongly linked to solar activity by the solar wind – magnetosphere interaction. The relationship of geomagnetic activity (and hence geomagnetic indices) and SSN depends strongly on the considered time scales.

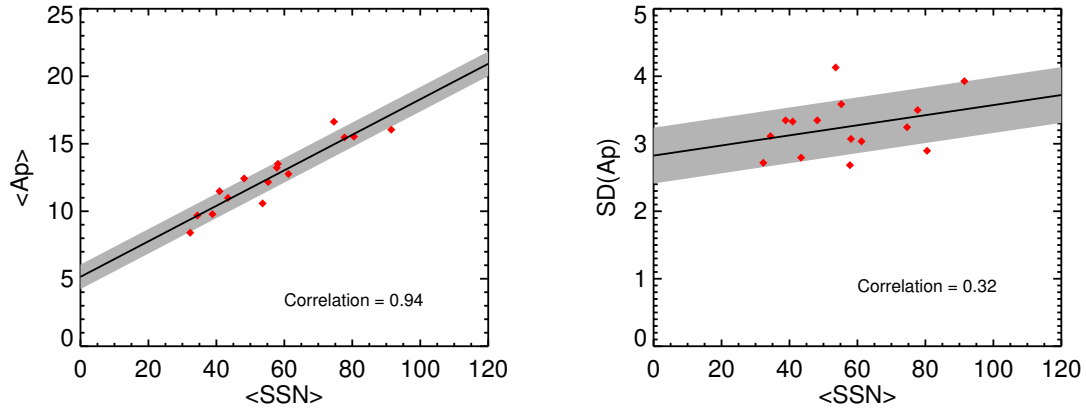


Figure 32. Regression of Ap^{bg} (red symbols, left) and $SD(Ap^a)_{SC}$ (red symbols, right) to $\langle SSN \rangle$. The resulting linear fit is shown by black lines, the grey shaded areas reflect the RMS errors.

Therefore, we decompose the Ap index in components corresponding to different time scales in order to scale them individually for projection of historic Ap sequences into the future or for the generation of the variable PI control forcing (see Fig. 31). The magnitude of sub-annual Ap variations is large and ruled by the mid-term geomagnetic activity level. Since there is strong evidence for Ap to be described by a multiplicative process (Watkins et al., 2005), we decompose Ap as follows:

$$5 \quad Ap(t) = \left(Ap^{bg}(t) + Ap^a(t) \right) D(t), \quad (I1)$$

where Ap^{bg} is the background component obtained from the Ap solar cycle averages, Ap^a the annually averaged component, and D a multiplicative daily component, the latter characterized by a nearly constant magnitude of variability on decadal to secular time scales. The Ap^a variability shows only a weak dependence on the long-term geomagnetic activity level. We use its standard deviation from individual solar cycles for construction of a time-dependent scaling function $SD(Ap^a)$.

10 For the projection of past solar cycles into the future, the components Ap^{bg} and Ap^a need to be scaled in relation to $\langle SSN \rangle$. Linear regression fits of Ap^{bg} and $SD(Ap^a)$ to $\langle SSN \rangle$ are shown in Fig. 32. The correlation of Ap^{bg} and $\langle SSN \rangle$ is very tight with a correlation coefficient of 0.94. As expected, this is not the case for $SD(Ap^a)$. The pronounced offsets of the regression fits at $\langle SSN \rangle = 0$ suggest residual geomagnetic activity for very low solar activity (i.e., Maunder Minimum) conditions in agreement with previous studies (e.g., Cliver et al., 1998).

15 For the construction of the variable PI control forcing, the Ap index is scaled to 1850–1873 average conditions. The scaling has been performed for the Ap^a component on basis of $SD(Ap^a)$. The background contributions Ap^{bg} was set to a constant value corresponding to the 1850–1873 average.

In both future scenario and variable PI control forcing constructions, Ap has been converted into Kp using a statistical correction to account for biases related to the conversion from hourly to daily indices as described in Sec. 2.2.1.

Author contributions. This paper was initiated, coordinated, and edited by K. Matthes and B. Funke. M. E. Andersson made WACCM simulations for Sec. 2.2 and made Figure 15. L. Barnard contributed text to Sections 2.2 and 3.1, and made Fig.22. M. A. Clilverd and C. J. Rodgers led the processing and analysis of the SEM-2 MEPED precipitating electron flux data and wrote part of the text in Sec. 2.2. T. Dudok de Wit wrote parts of Sections 1, 2.1.1, 3, and made Figures 1 and 21. B. Funke developed and conducted the extrapolation and scaling of geomagnetic indices, F10.7, and SSI data, made Figures 12, 16, 23–26, 28–32, and wrote parts of Sections 1–4, 6, C–H. M. Haberleiter contributed to writing and interpretations in Sec. 2.1.1. A. Hendry developed the code for geographic-to-geomagnetic conversions with support from C. J. Rodger and M. E. Andersson. C. H. Jackman provided the solar proton IPR dataset and wrote Sec. 2.2.2. M. Kretzschmar contributed to writing and interpretations in Sec. 2.1.1 and made Figures 2–4. T. Kruschke set up and conducted the CESM1(WACCM) simulations for Sec. 2.1.3, made Figs. 6, 8, 10–11, and contributed to the text in Sections 2.1.3 and B. M. Kunze performed the EMAC model runs for Sec. 2.1.3, made Figures 7 and 9, and contributed to the text in Sec. 2.1.3. U. Langematz contributed to the design, analysis and interpretation of the CCM simulations in Sec. 2.1.3 and assisted in editing the manuscript. D. R. Marsh made WACCM simulations for Sec. 2.2 and provided Fig. 13. K. Matthes wrote the abstract and parts of Sections 1–6, A, and coordinated the design, analysis and interpretation of the CCM and libradtran simulations in Sec. 2.1.3. A. Maycock made Fig. 27 and wrote Sec. 5. S. Misios performed the libradtran simulations and contributed to the text in Sec. 2.1.3. M. Shangguan performed the radiative forcing calculations with libradtran in Sec. 2.1.2. M. Sinnhuber contributed to the analysis of the EMAC tests of the NOy UBC and wrote parts of the text in Sections 1 and 2.2. K. Tourpali contributed to the design and analysis of the libradtran simulations and to the text in Sec. 2.1.3. I. Usoskin provided the GCR ionization data, wrote Sec. 2.2.3, and made Figures 19 and 20. M. van de Kamp developed the MEE precipitation model and calculated the spectral parameters with support and coordination from A. Seppälä, P. T. Verronen, M. A. Clilverd and C. J. Rodger. P. T. Verronen calculated the MEE ionization rates, provided Fig. 14, and wrote the MEE text in Sec. 2.2. S. Versick made Figures 17 and 18, did the EMAC model setup, performed the model runs, and contributed to the analysis of the EMAC tests with the NOy UBC. L. Barnard, J. Beer, P. Charbonneau, T. Dudok de Wit, B. Funke, K. Matthes, A. Maycock, I. Usoskin, and A. Scaife designed the future solar activity scenarios and assisted in editing the manuscript. The final solar forcing dataset for CMIP6 available at <http://solarisheppa.geomar.de/cmip6> was generated by B. Funke and T. Kruschke.

Acknowledgements. We are very grateful to the SATIRE and NRL teams for providing their respective solar irradiance reconstructions. Without these datasets the CMIP6 solar forcing recommendation as well as this paper wouldn't have been possible. We also thank the researchers and engineers of NOAA's Space Environment Center for the provision of the data and the operation of the SEM-2 instrument carried on-board the POES spacecraft. This work has been conducted in the frame of the WCRP/SPARC SOLARIS-HEPPA activity, and an early part inside the EU COST Action ES1005 (TOSCA) which some authors were involved in. This work contributes to the ROSMIC activity within the SCOSTEP VarSITI programme. Part of the work described in this article emanates from two teams at the International Space Science Institute (ISSI) in Bern, i.e. *Quantifying Hemispheric Differences in Particle Forcing Effects on Stratospheric Ozone* (Leader: D. R. Marsh) and *Scenarios of Future Solar Activity for Climate Modelling* (Leader: T. Dudok de Wit), which we gratefully acknowledge for hospitality. MK, TD, MH, KT and SM acknowledge that the research leading to the results has received funding from the European Community's Seventh Framework Programme (FP7 2012) under grant agreement no 313188 (SOLID, <http://projects.pmodwrc.ch/solid>). PTV, MEA, AS, and MvdK were supported by the Academy of Finland projects #276926 (SECTIC: Sun-Earth Connection Through Ion Chemistry) and #258165/#265005 (CLASP: Climate and Solar Particle Forcing). KM, TK, MK, UL, SV and MS gratefully acknowledge funding by the German Ministry of Research (BMBF) within the nationally funded project ROMIC-SOLIC (grant number 01LG1219). KM also acknowledges support from the Helmholtz-University Young Investigators Group NATHAN funded by the Helmholtz-Association through the President's

Initiative and Networking Fund and the GEOMAR Helmholtz Centre for Ocean Research Kiel. MS gratefully acknowledges funding by the Helmholtz Association of German Research Centres (HGF), grant 608 VH-NG-624. BF was supported by the Spanish MCINN under grant ESP2014-54362-P and EC FEDER funds. LB thanks the Science and Technology Facilities Council (STFC) for support under grant ST/M000885/1. AS was supported by the joint DECC/Defra Met Office Hadley Centre Climate Programme (GA01101) and the EU SPECS project (GA308378). UL and MK thank the North-German Supercomputing Alliance (HLRN) for support and computer time. KM and TK thank the computing centre at Kiel University for support and computer time.

References

- Abreu, J. A., Beer, J., Steinhilber, F., Tobias, S. M., and Weiss, N. O.: For how long will the current grand maximum of solar activity persist?, *Geophysical Research Letters*, 35, 20109, doi:10.1029/2008GL035442, 2008.
- Alley, R. B., Berntsen, T., and Bindoff, N. L.: *Climate Change 2007 - The Physical Science Basis. Working Group I Contribution to the Fourth Assessment Report of the IPCC*, Cambridge University Press, Cambridge, 2007.
- Amblard, P., Moussaoui, S., Dudok de Wit, T., Aboudarham, J., Kretzschmar, M., Lilensten, J., and Auchère, F.: The EUV Sun as the superposition of elementary Suns, *Astronomy and Astrophysics*, 487, L13–L16, doi:10.1051/0004-6361/200809588, 2008.
- Andersson, M. E., Verronen, P. T., Rodger, C. J., Clilverd, M. A., and Seppälä, A.: Missing driver in the Sun–Earth connection from energetic electron precipitation impacts mesospheric ozone, *Nature Commun.*, 5, doi:10.1038/ncomms6197, 2014a.
- Andersson, M. E., Verronen, P. T., Rodger, C. J., Clilverd, M. A., and Wang, S.: Longitudinal hotspots in the mesospheric OH variations due to energetic electron precipitation, *Atmos. Chem. Phys.*, 14, 1095–1105, doi:10.5194/acp-14-1095-2014, 2014b.
- Anet, J. G., Rozanov, E. V., Muthers, S., Peter, T., Brönnimann, S., Arfeuille, F., Beer, J., Shapiro, A. I., Raible, C. C., Steinhilber, F., and Schmutz, W. K.: Impact of a potential 21st century "grand solar minimum" on surface temperatures and stratospheric ozone, *Geophysical Research Letters*, 40, 4420–4425, doi:10.1002/grl.50806, 2013.
- Aubert, J.: Geomagnetic forecasts driven by thermal wind dynamics in the Earth's core, *Geophysical Journal International*, 203, 1738–1751, doi:10.1093/gji/ggv394, 2015.
- Austin, J., Tourpali, K., Rozanov, E., Akiyoshi, H., Bekki, S., Bodeker, G., Brühl, C., Butchart, N., Chipperfield, M., Deushi, M., Fomichev, V. I., Giorgetta, M. A., Gray, L., Kodera, K., Lott, F., Manzini, E., Marsh, D., Matthes, K., Nagashima, T., Shibata, K., Stolarski, R. S., Struthers, H., and Tian, W.: Coupled chemistry climate model simulations of the solar cycle in ozone and temperature, *J. Geophys. Res.*, 113, D11306, 2008.
- Ball, W. T., Unruh, Y. C., Krivova, N. A., Solanki, S., Wenzler, T., Mortlock, D. J., and Jaffe, A. H.: Reconstruction of total solar irradiance 1974–2009, *Astronomy & Astrophysics*, 541, A27, doi:10.1051/0004-6361/201118702, 2012.
- Ball, W. T., Haigh, J. D., Rozanov, E. V., Kuchar, A., Sukhodolov, T., Tummon, F., Shapiro, A. V., and Schmutz, W.: High solar cycle spectral variations inconsistent with stratospheric ozone observations, *Nature Geoscience*, 9, 206–209, doi:10.1038/ngeo2640, 2016.
- Barnard, L., Lockwood, M., Hapgood, M. A., Owens, M. J., Davis, C. J., and Steinhilber, F.: Predicting space climate change, *Geophys. Res. Lett.*, 38, doi:10.1029/2011GL048489, 2011.
- Bartels, J.: The standardized index, Ks, and the planetary index, Kp, *IATME Bulletin*, 12b, 97, 1949.
- Baumgaertner, A., Seppälä, A., Jöckel, P., and Clilverd, M.: Geomagnetic activity related NO_x enhancements and polar surface air temperature variability in a chemistry climate model: modulation of the NAM index, *Atmospheric Chemistry and Physics*, 11, 4521–4531, doi:10.5194/acp-11-4521-2011, 2011.
- Baumgaertner, A. J. G., Jöckel, P., and Brühl, C.: Energetic particle precipitation in ECHAM5/MESSy – Part 1: Downward transport of upper atmospheric NO_x produced by low energy electrons, *Atmos. Chem. Phys.*, 9, 2729–2740, doi:10.5194/acp-9-2729-2009, 2009.
- Beer, J., McCracken, K., and von Steiger, R.: *Cosmogenic Radionuclides*, Springer Verlag, Berlin, 2012.
- Bolduc, C., Charbonneau, P., Barnabé, R., and Bourqui, M. S.: A Reconstruction of Ultraviolet Spectral Irradiance During the Maunder Minimum, *Solar Physics*, 289, 2891–2906, doi:10.1007/s11207-014-0503-0, 2014.
- Box, G. E. P., Jenkins, G. M., Reinsel, G. C., and Ljung, G. M.: *Time Series Analysis: Forecasting and Control*, Wiley Series in Probability and Statistics, Wiley, 5th edn., 2015.

- Brockwell, P. J. and Davis, R. A.: Introduction to time series and forecasting, Springer Texts in Statistics, Springer, Berlin, 2nd edn., 2010.
- Caballero-Lopez, R. A. and Moraal, H.: Limitations of the force field equation to describe cosmic ray modulation, *J. Geophys. Res.*, 109, doi:10.1029/2003JA010098, a01101, 2004.
- Calisto, M., Usoskin, I., Rozanov, E., and Peter, T.: Influence of Galactic Cosmic Rays on atmospheric composition and dynamics, *Atmos. Chem. Phys.*, 11, 4547–4556, doi:10.5194/acp-11-4547-2011, 2011.
- 5 Callis, L. B., Boughner, R. E., Baker, D. N., Mewaldt, R. A., Bernard Blake, J., Selesnick, R. S., Cummings, J. R., Natarajan, M., Mason, G. M., and Mazur, J. E.: Precipitating electrons: Evidence for effects on mesospheric odd nitrogen, *Geophys. Res. Lett.*, 23, 1901–1904, doi:10.1029/96GL01787, 1996.
- Charbonneau, P.: Dynamo Models of the Solar Cycle, *Living Reviews in Solar Physics*, 7, 3, doi:10.12942/lrsp-2010-3, 2010.
- 10 Charbonneau, P.: Solar Dynamo Theory, *Annual Review of Astronomy and Astrophysics*, 52, 251–290, doi:10.1146/annurev-astro-081913-040012, 2014.
- Chiodo, G., Calvo, N., Marsh, D. R., and Garcia-Herrera, R.: The 11 year solar cycle signal in transient simulations from the Whole Atmosphere Community Climate Model, *J. Geophys. Res.*, 117, doi:10.1029/2011JD016393, 2012.
- Chiodo, G., Garcia-Herrera, R., Calvo, N., Vaquero, J. M., A?el, J. A., Barriopedro, D., and Matthes, K.: The impact of a future solar minimum on climate change projections in the Northern Hemisphere, *Environmental Research Letters*, 11, 034015, doi:10.1088/1748-9326/11/3/034015, 2016.
- 15 Cionni, I., Eyring, V., Lamarque, J.-F., Randel, W. J., Stevenson, D. S., Wu, F., Bodeker, G. E., Shepherd, T. G., Shindell, D. T., and Waugh, D. W.: Ozone database in support of CMIP5 simulations: Results and corresponding radiative forcing, *Atmos. Chem. Phys.*, 11, 11,267–11,292, 2011.
- 20 Clette, F., Svalgaard, L., Vaquero, J. M., and Cliver, E. W.: Revisiting the Sunspot Number, *Space Science Reviews*, 186, 35–103, doi:10.1007/s11214-014-0074-2, 2014.
- Cliver, E. W., Boriakoff, V., and Bounar, K. H.: Geomagnetic activity and the solar wind during the Maunder Minimum, *Geophysical Research Letters*, 25, 897–900, doi:10.1029/98GL00500, 1998.
- Coddington, O., Lean, J. L., Pilewskie, P., Snow, M., and Lindholm, D.: A Solar Irradiance Climate Data Record, *Bulletin of the American Meteorological Society*, 97, 1265, doi:BAMS-D-14-00265.1, 2016.
- 25 Codrescu, M. V., Fuller-Rowell, T. J., Roble, R. G., and Evans, D. S.: Medium energy particle precipitation influences on the mesosphere and lower thermosphere, *J. Geophys. Res.*, 102, 19977–19987, doi:10.1029/97JA01728, 1997.
- Collins, W. D.: A global signature of enhanced shortwave absorption by clouds, *J. Geophys. Res.*, 103, 31 669–31 679, 1998.
- Cooke, D. J., Humble, J. E., Shea, M. A., Smart, D. F., Lund, N., Rasmussen, I. L., Byrnek, B., Goret, P., and Petrou, N.: On cosmic-ray cut-off terminology, *Il Nuovo Cimento C*, 14, 213–234, doi:10.1007/BF02509357, 1991.
- 30 Damiani, A., Storini, M., Laurenza, M., and Rafanelli, C.: Solar particle effects on minor components of the Polar atmosphere, *Annales Geophysicae*, 26, 361–370, doi:10.5194/angeo-26-361-2008, 2008.
- Damiani, A., Funke, B., Marsh, D. R., López-Puertas, M., Santee, M. L., Froidevaux, L., Wang, S., Jackman, C. H., von Clarmann, T., Gardini, A., Cordero, R. R., and Storini, M.: Impact of January 2005 Solar Proton Events on chlorine species, *Atmos. Chem. Phys.*, 12, 4159–4179, doi:10.5194/acp-12-4259-2012, 2012.
- 35 Damiani, A., Funke, B., López-Puertas, M., Santee, M. L., Cordero, R. R., Laurenza, M., and Watanabe, S.: Energetic particle precipitation: a major driver of the ozone budget in the Antarctic upper stratosphere, *Geophys. Res. Lett.*, doi:10.1002/2016GL068279, 2016GL068279, 2016.

- Dee, D. P., Uppala, S. M., Simmons, A. J., Berrisford, P., Poli, P., Kobayashi, S., Andrae, U., Balmaseda, M. A., Balsamo, G., Bauer, P., Bechtold, P., Beljaars, A. C. M., van de Berg, L., Bidlot, J., Bormann, N., Delsol, C., Dragani, R., Fuentes, M., Geer, A. J., Haimberger, L., Healy, S. B., Hersbach, H., Hólm, E. V., Isaksen, I., Kållberg, P., Köhler, M., Matricardi, M., McNally, A. P., Monge-Sanz, B. M., Morcrette, J.-J., Park, B.-K., Peubey, C., de Rosnay, P., Tavolato, C., Thépaut, J.-N., and Vitart, F.: The ERA-Interim reanalysis: configuration and performance of the data assimilation system, *Quarterly Journal of the Royal Meteorological Society*, 137, 553–597, doi:10.1002/qj.828, 2011.
- Desorgher, L., Flückiger, E. O., Gurtner, M., Moser, M. R., and Büttikofer, R.: Atmocomics: a Geant 4 Code for Computing the Interaction of Cosmic Rays with the Earth’s Atmosphere, *Internat. J. Modern Physics A*, 20, 6802–6804, doi:10.1142/S0217751X05030132, 2005.
- Dietmüller, S., Jöckel, P., Tost, H., Kunze, M., Gellhorn, C., Brinkop, S., Frömming, C., Ponater, M., Steil, B., Lauer, A., and Hendricks, J.: *Geosci. Model Dev.*, 9, 2209–2222, doi:10.5194/gmd-9-2209-2016, 2016.
- Dudok de Wit, T.: A method for filling gaps in solar irradiance and solar proxy data, *Astronomy and Astrophysics*, 533, A29, doi:10.1051/0004-6361/201117024, 2011.
- Dudok de Wit, T., Kopp, G., Fröhlich, C., and Schöll, M.: Methodology to create a new Total Solar Irradiance record: Making a composite out of multiple data records, *Geophysical Research Letters*, accepted, doi:10.1002/2016GL071866, 2017.
- 15 Ermolli, I., Matthes, K., Dudok de Wit, T., Krivova, N. A., Tourpali, K., Weber, M., Unruh, Y. C., Gray, L., Langematz, U., Pilewskie, P., Rozanov, E., Schmutz, W., Shapiro, A., Solanki, S. K., and Woods, T. N.: Recent variability of the solar spectral irradiance and its impact on climate modelling, *Atmospheric Chemistry and Physics*, 13, 3945–3977, doi:10.5194/acp-13-3945-2013, 2013.
- Evans, D. and Greer, M.: Polar Orbiting Environmental Satellite Space Environment Monitor - 2: Instrument Descriptions and Archive Data Documentation, NOAA Technical Memorandum OAR version 1.4 SEC-93, Oceanic and Atmospheric Research Laboratories, Space Environment Center, Boulder, Colorado, 2000.
- 20 Eyring, V., Bony, S., Meehl, G. A., Senior, C. A., Stevens, B., Stouffer, R. J., and Taylor, K. E.: Overview of the Coupled Model Intercomparison Project Phase 6 (CMIP6) experimental design and organization, *Geosci. Model Dev.*, 9, 1937–1958, doi:10.5194/gmd-9-1937-2016, 2016.
- Fang, X., Randall, C., Lummerzheim, D., Solomon, S., Mills, M., Marsh, D., Jackman, C., Wang, W., and Lu, G.: Electron impact ionization: A new parameterization for 100 eV to 1 MeV electrons, *Journal of Geophysical Research*, 113, doi:10.1029/2008JA013384, 2008.
- 25 Fang, X., Randall, C. E., Lummerzheim, D., Wang, W., Lu, G., Solomon, S. C., and Frahm, R. A.: Parameterization of monoenergetic electron impact ionization, *Geophys. Res. Lett.*, 37, n/a–n/a, doi:10.1029/2010GL045406, l22106, 2010.
- Feulner, G. and Rahmstorf, S.: On the effect of a new grand minimum of solar activity on the future climate on Earth, *Geophysical Research Letters*, 37, L05707, doi:10.1029/2010GL042710, 2010.
- 30 Fligge, M., Solanki, S. K., and Unruh, Y. C.: Modelling irradiance variations from the surface distribution of the solar magnetic field, *Astronomy & Astrophysics*, 353, 380–388, 2000.
- Forster, P. M., Fomichev, V. I., Rozanov, E., Cagnazzo, C., Jonsson, A. I., Langematz, U., Fomin, B., Iacono, M. J., Mayer, B., Mlawer, E., Myhre, G., Portmann, R. W., Akiyoshi, H., Falaleeva, V., Gillett, N., Karpechko, A., Li, J., Lemennais, P., Morgenstern, O., Oberländer, S., Sigmond, M., and Shibata, K.: Evaluation of radiation scheme performance within chemistry climate models, *J. Geophys. Res.*, 116, 2156–2202, 2011.
- 35 Fouquart, Y. and Bonnel, B.: Computations of solar heating of the Earth’s atmosphere: A new parameterization, *Beitr. Phys. Atmos.*, 53, 35–62, 1980.

- Frahm, R. A., Winningham, J. D., Sharber, J. R., Link, R., Crowley, G., Gaines, E. E., Chenette, D. L., Anderson, B. J., and Potemra, T. A.: The diffuse aurora: A significant source of ionization in the middle atmosphere, *J. Geophys. Res.*, 102, 28 203–28 214, doi:10.1029/97JD02430, 1997.
- Frederick, J. E.: Solar corpuscular emission and neutral chemistry in the Earth's middle atmosphere, *J. Geophys. Res.*, 81, 3179–3186, doi:10.1029/JA081i019p03179, 1976.
- 5 Friederich, F., von Clarmann, T., Funke, B., Nieder, H., Orphal, J., Sinnhuber, M., Stiller, G. P., and Wissing, J. M.: Lifetime and production rate of NO_x in the upper stratosphere and lower mesosphere in the Southern Hemisphere after the solar proton event in October–November 200, *Atmos. Chem. Phys.*, 13, 2531–2539, doi:10.5194/acp-13-2531-2013, 2013.
- Funke, B., López-Puertas, M., Gil-López, S., von Clarmann, T., Stiller, G. P., Fischer, H., and Kellmann, S.: Downward transport of upper atmospheric NO_x into the polar stratosphere and lower mesosphere during the Antarctic 2003 and Arctic 2002/2003 winters, *J. Geophys. Res.*, 110, D24308, doi:10.1029/2005JD006463, 2005.
- 10 Funke, B., López-Puertas, M., García-Comas, M., Stiller, G. P., von Clarmann, T., and Glatthor, N.: Mesospheric N₂O enhancements as observed by MIPAS on Envisat during the polar winters in 2002–2004, *Atmos. Chem. Phys.*, 8, 5787–5800, doi:10.5194/acp-8-5787-2008, 2008.
- 15 Funke, B., Baumgaertner, A., Calisto, M., Egorova, T., Jackman, C. H., Kieser, J., Krivolutsky, A., López-Puertas, M., Marsh, D. R., Reddmann, T., Rozanov, E., Salmi, S.-M., Sinnhuber, M., Stiller, G. P., Verronen, P. T., Versick, S., von Clarmann, T., Vyushkova, T. Y., Wieters, N., and Wissing, J. M.: Composition changes after the "Halloween" solar proton event: the High-Energy Particle Precipitation in the Atmosphere (HEPPA) model versus MIPAS data intercomparison study, *Atmos. Chem. Phys.*, 11, 9089–9139, doi:10.5194/acp-11-9089-2011, 2011.
- 20 Funke, B., López-Puertas, M., Stiller, G. P., and von Clarmann, T.: Mesospheric and stratospheric NO_y produced by energetic particle precipitation during 2002–2012, *J. Geophys. Res.*, 119, doi:10.1002/2013JD021404, 2014a.
- Funke, B., Puertas, M. L., Holt, L., Randall, C. E., Stiller, G. P., and von Clarmann, T.: Hemispheric distributions and interannual variability of NO_y produced by energetic particle precipitation in 2002–2012, *J. Geophys. Res.*, 119, 13 565–13 582, doi:10.1002/2014JD022423, 2014b.
- 25 Funke, B., López-Puertas, M., Stiller, G. P., Versick, S., and von Clarmann, T.: A semi-empirical model for mesospheric and stratospheric NO_y produced by energetic particle precipitation, *Atmos. Chem. Phys.*, 2016, 8667–8693, doi:10.5194/acp-16-8667-2016, 2016.
- Fytterer, T., Mlynčzak, M., Nieder, H., Perot, K., Sinnhuber, M., Stiller, G., and Urban, J.: Energetic particle induced intra-seasonal variability of ozone inside the Antarctic polar vortex observed in satellite data, *Atmospheric Chemistry and Physics*, 15, doi:10.5194/acp-15-3327-2015, 2015a.
- 30 Fytterer, T., Santee, M. L., Sinnhuber, M., and Wang, S.: The 27day solar rotational effect on mesospheric nighttime OH and O₃ observations induced by geomagnetic activity, *Journal of Geophysical Research*, 120, doi:10.1002/2015JA021183, 2015b.
- Giorgetta, M. A. and Bengtsson, L.: Potential role of the quasi-biennial oscillation in the stratosphere-troposphere exchange as found in water vapor in general circulation model experiments, *J. Geophys. Res.: Atmos.*, 104, 6003–6019, doi:10.1029/1998JD200112, 1999.
- Gray, L., Scaife, A., Mitchell, D., Osprey, S., Ineson, S., Hardiman, S., Butchart, N., Knight, J., Sutton, R., and Kodera, K.: A Lagged Response to the 11-year Solar Cycle in Observed Winter Atlantic/European Weather Patterns, *J. Geophys. Res.*, 118, 1–16, 2013.
- 35 Gray, L. J., Rumbold, S., and Shine, K. P.: Stratospheric temperatures and radiative forcing response to 11-year solar cycle changes in irradiance and ozone, *J. Atmos. Sci.*, 66, 2402–2417, 2009.

- Gray, L. J., Beer, J., Geller, M., Haigh, J. D., Lockwood, M., Matthes, K., Cubasch, U., Fleitmann, D., Harrison, G., Hood, L., Luterbacher, J., Meehl, G. A., Shindell, D., van Geel, B., and White, W.: Solar influences on climate, *Rev. Geophys.*, 48, 1–53, doi:10.1029/2009RG000282, 2010.
- Haberreiter, M., Schöll, M., Dudok de Wit, T., Kretschmar, M., Misios, S., Tourpali, K., and Schmutz, W.: A new observational solar irradiance composite, *Journal of Geophysical Research (Space Physics)*, submitted, 2017.
- Haigh, J.: The impact of solar variability on climate, *SCIENCE*, 272, 981–984, doi:10.1126/science.272.5264.981, <http://dx.doi.org/10.1126/science.272.5264.981>, 1996.
- Haigh, J. D.: The Role of Stratospheric Ozone in Modulating the Solar Radiative Forcing of Climate, *Nature*, 370, 544–546, doi:10.1038/370544a0, 1994.
- 10 Hanslmeier, A. and Brajša, R.: The chaotic solar cycle. I. Analysis of cosmogenic ^{14}C -data, *Astronomy & Astrophysics*, 509, A6, doi:10.1051/0004-6361/200913095, 2010.
- Harder, J. W., Lawrence, G., Fontenla, J., Rottman, G., and Woods, T.: The Spectral Irradiance Monitor: Scientific Requirements, Instrument Design, and Operation Modes, *Solar Physics*, 230, 141–167, doi:10.1007/s11207-005-5007-5, 2005.
- Harder, J. W., Fontenla, J. M., Pilewskie, P., Richard, E. C., and Woods, T. N.: Trends in solar spectral irradiance variability in the visible and infrared, *Geophysical Research Letters*, 36, doi:10.1029/2008GL036797, 2009.
- 15 Hastie, T., Tibshirani, R., and Friedman, J.: *The Elements of Statistical Learning: Data Mining, Inference, and Prediction*, Springer, New York, 2nd edn., 2009.
- Heath, D. F., Krueger, A. J., and Crutzen, P. J.: Solar proton event: influence on stratospheric ozone, *Science*, 197, 886–889, 1977.
- Heggin, M. I., Plummer, D., and Morgenstern, O.: A CCM1 Ozone Database for CMIP6, *Glob. Mod. Devel. Disc.*, in preparation, 2017.
- 20 Hendrickx, K., Megner, L., Gumbel, J., Siskind, D. E., Orsolini, Y. J., Tyssøy, H. N., and Hervig, M.: Observation of 27day solar cycles in the production and mesospheric descent of EPP-produced NO, *J. Geophys. Res.*, 120, 8978–8988, doi:10.1002/2015JA021441, 2015.
- Holt, L. A., Randall, C. E., Peck, E. D., Marsh, D. R., Smith, A. K., and Lynn Harvey, V.: The influence of major sudden stratospheric warming and elevated stratopause events on the effects of energetic particle precipitation in WACCM, *J. Geophys. Res.*, doi:10.1002/2013JD020294, 2013.
- 25 Hood, L. L., Misios, S., Mitchell, D. M., Rozanov, E., Gray, L. J., Tourpali, K., Matthes, K., Schmidt, H., Chiodo, G., Thiéblemont, R., Shindell, D., and Krivolutsky, A.: Solar signals in CMIP-5 simulations: The ozone response, *Q. J. Roy. Meteorol. Soc.*, 141, 2670–2689, doi:10.1002/qj.2553, 2015.
- Horne, R., Lam, M., and Green, J.: Energetic electron precipitation from the outer radiation belt during geomagnetic storms, *Geophysical Research Letters*, 36, doi:10.1029/2009GL040236, 2009.
- 30 Hoyt, D. V. and Schatten, K. H.: Group Sunspot Numbers: A New Solar Activity Reconstruction, *Solar Physics*, 181, 491–491, doi:10.1023/A:1005056326158, 1998.
- Hurrell, J. W., Holland, M. M., Gent, P. R., Ghan, S., Kay, J. E., Kushner, P. J., Lamarque, J. F., Large, W. G., Lawrence, D., Lindsay, K., Lipscomb, W. H., Long, M. C., Mahowald, N., Marsh, D. R., Neale, R. B., Rasch, P., Vavrus, S., Vertenstein, M., Bader, D., Collins, W. D., Hack, J. J., Kiehl, J., and Marshall, S.: The Community Earth System Model: A Framework for Collaborative Research, *Bull. Amer. Meteor. Soc.*, 94, 1339–1360, doi:10.1175/bams-d-12-00121.1, 2013.
- 35 Inceoglu, F., Simoniello, R., Knudsen, M. F., Karoff, C., Olsen, J., and Turck-Chièze, S.: On the Current Solar Magnetic Activity in the Light of Its Behaviour During the Holocene, *Solar Physics*, 291, 303–315, doi:10.1007/s11207-015-0805-x, 2016.

- Ineson, S., Scaife, A. A., Knight, J. R., Manners, J. C., Dunstone, N. J., Gray, L. J., and Haigh, J. D.: Solar forcing of winter climate variability in the Northern Hemisphere, *Nature Geoscience*, 4, 753–757, doi:10.1038/ngeo1282, 2011.
- Ineson, S., Maycock, A. C., Gray, L. J., Scaife, A. A., Dunstone, N. J., Harder, J. W., Knight, J. R., Lockwood, M., Manners, J. C., and Wood, R. A.: Regional climate impacts of a possible future grand solar minimum, *Nature Communications*, 6, doi:10.1038/ncomms8535, 2015.
- 5 Jackman, C. H. and McPeters, R. D.: The Effect of solar proton events on ozone and other constituents, *Solar Variability and its Effects on Climate*, *Geophys. Mon.*, 141, 305–319, 2004.
- Jackman, C. H., Frederick, J. E., and Stolarski, R. S.: Production of odd nitrogen in the stratosphere and mesosphere: An intercomparison of source strengths, *J. Geophys. Res.*, 85, 7495–7505, doi:10.1029/JC085iC12p07495, 1980.
- Jackman, C. H., Douglass, A. R., Rood, R. B., McPeters, R. D., and Meade, P. E.: Effect of solar proton events on the middle atmosphere during the past two solar cycles as computed using a two-dimensional model, *J. Geophys. Res.*, 95, 7417–7428, doi:10.1029/JD095iD06p07417, 1990.
- 10 Jackman, C. H., Cerniglia, M. C., Nielsen, J. E., Allen, D. J., Zawodny, J. M., McPeters, R. D., Douglass, A. R., Rosenfield, J. E., and Rood, R. B.: Two-dimensional and three-dimensional model simulations, measurements, and interpretation of the influence of the October 1989 solar proton events on the middle atmosphere, *Journal of Geophysical Research: Atmospheres*, 100, 11 641–11 660, doi:10.1029/95JD00369, 1995.
- 15 Jackman, C. H., McPeters, R. D., Labow, G. J., Fleming, E. L., Praderas, C. J., and Russell, J. M.: Northern Hemisphere atmospheric effects due to the July 2000 solar proton event, *Geophys. Res. Lett.*, 28, 2883–2886, 2001.
- Jackman, C. H., DeLand, M. T., Labow, G. J., Fleming, E. L., Weisenstein, D. K., Ko, M. K. W., Sinnhuber, M., Anderson, J., and Russell, J. M.: The Influence of the Several Very Large Solar Proton Events in Years 2000–2003 on the Neutral Middle Atmosphere, *Adv. Space Res.*, 35, 445–450, 2005a.
- 20 Jackman, C. H., DeLand, M. T., Labow, G. J., Fleming, E. L., Weisenstein, D. K., Ko, M. K. W., Sinnhuber, M., and Russell, J. M.: Neutral atmospheric influences of the solar proton events in October–November 2003, *J. Geophys. Res.*, 110, A09S27, doi:10.1029/2004JA010888, 2005b.
- Jackman, C. H., Marsh, D. R., Vitt, F. M., Garcia, R. R., Fleming, E. L., Labow, G. J., Randall, C. E., López-Puertas, M., Funke, B., von Clarmann, T., and Stiller, G. P.: Short- and medium-term atmospheric effects of very large solar proton events, *Atmos. Chem. Phys.*, 8, 765–785, doi:10.5194/acp-8-765-2008, 2008.
- 25 Jackman, C. H., Marsh, D. R., Vitt, F. M., Roble, R. G., Randall, C. E., Bernath, P. F., Funke, B., López-Puertas, M., Versick, S., Stiller, G. P., Tylka, A. J., and Fleming, E. L.: Northern Hemisphere atmospheric influence of the solar proton events and ground level enhancement in January 2005, *Atmos. Chem. Phys.*, 11, 6153–6166, doi:10.5194/acp-11-6153-2011, 2011.
- 30 Jackman, C. H., Randall, C. E., Harvey, V. L., Wang, S., Fleming, E. L., López-Puertas, M., Funke, B., and Bernath, P. F.: Middle atmospheric changes caused by the January and March 2012 solar proton events, *Atmos. Chem. Phys.*, 14, 1025–1038, doi:10.5194/acp-14-1025-2014, 2014.
- Jackman, C. H., Marsh, D. R., Kinnison, D. E., Mertens, C. J., and Fleming, E. L.: Atmospheric changes caused by galactic cosmic rays over the period 1960–2010, *Atmos. Chem. Phys. Discuss.*, 15, 33 931–33 966, doi:10.5194/acpd-15-33931-2015, 2015.
- 35 Jackson, A., Jonkers, A. R. T., and Walker, M. R.: Four centuries of geomagnetic secular variation from historical records, *Phil. Trans. R. Soc. Lond. A*, 358, 957–990, doi:10.1098/rsta.2000.0569, 2000.
- Jöckel, P., Kerkweg, A., Pozzer, A., Sander, R., Tost, H., Riede, H., Baumgaertner, A., Gromov, S., and Kern, B.: Development cycle 2 of the Modular Earth Submodel System (MESSy2), *Geosci. Model Dev.*, 3, 717–752, doi:10.5194/gmd-3-717-2010, 2010.

- Jöckel, P., Tost, H., Pozzer, A., Kunze, M., Kirner, O., Brenninkmeijer, C. A. M., Brinkop, S., Cai, D. S., Dyroff, C., Eckstein, J., Frank, F., Garny, H., Gottschaldt, K.-D., Graf, P., Grewe, V., Kerkweg, A., Kern, B., Matthes, S., Mertens, M., Meul, S., Neumaier, M., Nützel, M., Oberländer-Hayn, S., Ruhnke, R., Runde, T., Sander, R., Scharffe, D., and Zahn, A.: Earth System Chemistry integrated Modelling (ESCiMo) with the Modular Earth Submodel System (MESSy) version2.51, *Geosci. Model Dev.*, 9, 1153–1200, doi:10.5194/gmd-9-1153-2016, 2016.
- 5 Jones, A., Qin, G., Strong, K., Walker, K. A., McLinden, C. A., Toohey, M., Kerzenmacher, T., Bernath, P. F., and Boone, C. D.: A global inventory of stratospheric NO_y from ACE-FTS, *J. Geophys. Res.*, 116, n/a–n/a, doi:10.1029/2010JD015465, d17304, 2011.
- Jungclaus, J. H., Bard, E., Baroni, M., Braconnot, P., Cao, J., Chini, L. P., Egorova, T., Evans, M., González-Rouco, J. F., Goosse, H., Hurtt, G. C., Joos, F., Kaplan, J. O., Khodri, M., Klein Goldewijk, K., Krivova, N., LeGrande, A. N., Lorenz, S. J., Luterbacher, J., Man, W., Meinshausen, M., Moberg, A., Nehrbass-Ahles, C., Otto-Bliesner, B. I., Phipps, S. J., Pongratz, J., Rozanov, E., Schmidt, G. A., Schmidt, H., Schmutz, W., Schurer, A., Shapiro, A. I., Sigl, M., Smerdon, J. E., Solanki, S. K., Timmreck, C., Toohey, M., Usoskin, I. G., Wagner, S., Wu, C.-Y., Yeo, K. L., Zanchettin, D., Zhang, Q., and Zorita, E.: The PMIP4 contribution to CMIP6 – Part 3: the Last Millennium, Scientific Objective and Experimental Design for the PMIP4 *past1000* simulations, *Geosci. Model Dev. Discuss.*, 2016, 1–34, doi:10.5194/gmd-2016-278, 2016.
- 10 Kageyama, M., Braconnot, P., Harrison, S. P., Haywood, A. M., Jungclaus, J., Otto-Bliesner, B. L., Peterschmitt, J.-Y., Abe-Ouchi, A., Albani, S., Bartlein, P. J., Brierley, C., Crucifix, M., Dolan, A., Fernandez-Donado, L., Fischer, H., Hopcroft, P. O., Ivanovic, R. F., Lambert, F., Lunt, D. J., Mahowald, N. M., Peltier, W. R., Phipps, S. J., Roche, D. M., Schmidt, G. A., Tarasov, L., Valdes, P. J., Zhang, Q., and Zhou, T.: PMIP4-CMIP6: the contribution of the Paleoclimate Modelling Intercomparison Project to CMIP6, *Geosci. Model Dev. Discuss.*, pp. n/a–n/a, doi:doi:10.5194/gmd-2016-106, 2016.
- 15 Kinnison, D. E., Brasseur, G. P., Walters, S., Garcia, R. R., Marsh, D. R., Sassi, F., Harvey, V. L., Randall, C. E., Emmons, L., Lamarque, J. F., Hess, P., Orlando, J. J., Tie, X. X., Randel, W., Pan, L. L., Gettelman, A., Granier, C., Diehl, T., Niemeier, U., and Simmons, A. J.: Sensitivity of chemical tracers to meteorological parameters in the MOZART-3 chemical transport model, *J. Geophys. Res.*, 112, D20302, doi:10.1029/2006JD007879, 2007.
- Kodera, K.: Solar cycle modulation of the North Atlantic Oscillation: Implication in the spatial structure of the NAO, *Geophys. Res. Lett.*, 29, doi:10.1029/2001GL014557, 2002.
- 25 Kopp, G. and Lean, J. L.: A new, lower value of total solar irradiance: Evidence and climate significance, *Geophysical Research Letters*, 38, L01 706, doi:10.1029/2010GL045777, 2011.
- Kopp, G., Lawrence, G., and Rottman, G.: The Total Irradiance Monitor (TIM): Science Results, *Solar Physics*, 230, 129–139, doi:10.1007/s11207-005-7433-9, 2005.
- 30 Kopp, G., Krivova, N., Lean, J., and Wu, C. J.: The Impact of the Revised Sunspot Record on Solar Irradiance Reconstructions, *Solar Physics*, in press, doi:10.1007/s11207-016-0853, 2016.
- Kremliovsky, M.: Limits of Predictability of Solar Activity, *Solar Phys.*, 159, 371–380, doi:10.1007/BF00686538, 1995.
- Krivolutsky, A., Bazilevskaya, G., Vyushkova, T., and Knyazeva, G.: Influence of cosmic rays on chemical composition of the atmosphere: data analysis and photochemical modelling, *Physics and Chemistry of the Earth, Parts A/B/C*, 27, 471 – 476, doi:10.1016/S1474-7065(02)00028-1, 2002.
- 35 Krivolutsky, A. A., Kuminov, A. A., Kukoleva, A. A., Repnev, A. I., Pereyaslova, N. K., and Nazarova, M. N.: Solar proton activity during cycle 23 and changes in the ozonosphere: Numerical simulation and analysis of observational data, *Geomagnetism and Aeronomy*, 48, 432–445, doi:10.1134/S0016793208040038, 2008.

- Krivova, N. A., Solanki, S. K., Fligge, M., and Unruh, Y. C.: Reconstruction of solar irradiance variations in cycle 23: Is solar surface magnetism the cause?, *Astronomy & Astrophysics*, 399, L1–L4, doi:10.1051/0004-6361:20030029, 2003.
- Krivova, N. A., Vieira, L. E. A., and Solanki, S. K.: Reconstruction of solar spectral irradiance since the Maunder minimum, *Journal of Geophysical Research (Space Physics)*, 115, doi:10.1029/2010JA015431, 2010.
- 5 Krivova, N. A., Solanki, S. K., and Unruh, Y. C.: Towards a long-term record of solar total and spectral irradiance, *Journal of Atmospheric and Solar-Terrestrial Physics*, 73, 223–234, doi:10.1016/j.jastp.2009.11.013, 2011.
- Kunze, M., Godolt, M., Langematz, U., Grenfell, J., Hamann-Reinus, A., and Rauer, H.: Investigating the early Earth faint young Sun problem with a general circulation model, *Planet. Space Sci.*, 98, 77–92, doi:10.1016/j.pss.2013.09.011, planetary evolution and life, 2014.
- Laken, B. A. and Čalogović, J.: Composite analysis with Monte Carlo methods: an example with cosmic rays and clouds, *Journal of Space*
10 *Weather and Space Climate*, 3, A29, doi:10.1051/swsc/2013051, 2013.
- Lam, M. M., Horne, R. B., Meredith, N. P., Glauert, S. A., Moffat-Griffin, T., and Green, J. C.: Origin of energetic electron precipitation >30 keV into the atmosphere, *J. Geophys. Res. (Space Physics)*, 115, A00F08, doi:10.1029/2009JA014619, 2010.
- Langematz, U., Kubin, A., Brühl, C., Baumgaertner, A., Cubasch, U., and Spanghel, T.: Solar effects on chemistry and climate including ocean interactions in Climate And Weather of the Sun-Earth System (CAWSES): Highlights from a Priority Program, pp. 541–571,
15 Springer, Dordrecht, The Netherlands, doi:10.1007/978-94-007-4348-9, 2013.
- Lean, J. L.: The Sun's Variable Radiation and Its Relevance For Earth, *Annual Review Astronomy Astrophysics*, 35, 33–67, doi:10.1146/annurev.astro.35.1.33, 1997.
- Lean, J. L.: Evolution of the Sun's spectral irradiance since the Maunder Minimum, *Geophysical Research Letters*, 27, 2425–2428, doi:10.1029/2000GL000043, 2000.
- 20 Lean, J. L. and DeLand, M. T.: How Does the Sun's Spectrum Vary?, *Journal of Climate*, 25, 2555–2560, doi:10.1175/JCLI-D-11-00571.1, 2012.
- Lean, J. L. and Rind, D. H.: How natural and anthropogenic influences alter global and regional surface temperatures: 1889 to 2006, *Geophysical Research Letters*, 35, n/a–n/a, doi:10.1029/2008GL034864, <http://dx.doi.org/10.1029/2008GL034864>, 118701, 2008.
- Lean, J. L. and Rind, D. H.: How will Earth's surface temperature change in future decades?, *Geophysical Research Letters*, 36, 15 708,
25 doi:10.1029/2009GL038932, 2009.
- Lean, J. L., Cook, J., Marquette, W., and Johannesson, A.: Magnetic Sources of the Solar Irradiance Cycle, *The Astronomical Journal*, 492, 390–401, doi:10.1086/305015, 1998.
- Lean, J. L., Woods, T. N., Eparvier, F. G., Meier, R. R., Strickland, D. J., Correia, J. T., and Evans, J. S.: Solar extreme ultraviolet irradiance: Present, past, and future, *Journal of Geophysical Research (Space Physics)*, 116, A01 102, doi:10.1029/2010JA015901, 2011.
- 30 Lilensten, J., Dudok de Wit, T., and Matthes, K., eds.: Earth's climate response to a changing Sun, EDP Sciences, Paris, 2015.
- Ljung, L.: *System Identification: Theory for the User*, Prentice-Hall, Englewood Cliffs, New Jersey, 2nd edn., 1997.
- Lockwood, M., Harrison, R. G., Woollings, T., and Solanki, S.: Are cold winters in Europe associated with low solar activity?, *Environ. Res. Lett.*, 5, doi:10.1088/1748-9326/5/2/024001, 2010.
- Lockwood, M., Barnard, L., Nevanlinna, H., Owens, M. J., Harrison, R. G., Rouillard, A. P., and Davis, C. J.: Reconstruction of geomagnetic activity and near-Earth interplanetary conditions over the past 167 yr – Part 1: A new geomagnetic data composite, *Annales Geophysicae*,
35 31, 1957–1977, doi:10.5194/angeo-31-1957-2013, 2013.

- Lockwood, M., Nevanlinna, H., Barnard, L., Owens, Harrison, R. G., Rouillard, A. P., and Scott, C. J.: Reconstruction of geomagnetic activity and near-Earth interplanetary conditions over the past 167 yr - Part 4: Near-Earth solar wind speed, IMF, and open solar flux, *Annales Geophysicae*, 32, 383–399, doi:10.5194/angeo-32-383-2014, 2014.
- López-Puertas, M., Funke, B., Gil-López, S., von Clarmann, T., Stiller, G. P., Höpfner, M., Kellmann, S., Fischer, H., and Jackman, C. H.: 5 Observation of NO_x Enhancement and Ozone Depletion in the Northern and Southern Hemispheres after the October–November 2003 Solar Proton Events, *J. Geophys. Res.*, 110, A09S43, doi:10.1029/2005JA011050, 2005a.
- López-Puertas, M., Funke, B., Gil-López, S., von Clarmann, T., Stiller, G. P., Höpfner, M., Kellmann, S., Mengistu Tsidu, G., Fischer, H., and Jackman, C. H.: HNO₃, N₂O₅ and ClONO₂ Enhancements after the October–November 2003 Solar Proton Events, *J. Geophys. Res.*, 110, A09S44, doi:10.1029/2005JA011051, 2005b.
- 10 Maliniemi, V., Asikainen, T., and Mursula, K.: Spatial distribution of Northern Hemisphere winter temperatures during different phases of the solar cycle, *J. Geophys. Res.*, 119, 9752–9764, doi:10.1002/2013JD021343, 2014.
- Marsh, D. R., Solomon, S. C., and Reynolds, A. E.: Empirical model of nitric oxide in the lower thermosphere, *J. Geophys. Res.*, 109, A07301, doi:10.1029/2003JA010199, 2004.
- Marsh, D. R., Garcia, R. R., Kinnison, D. E., Boville, B. A., Sassi, F., Solomon, S. C., and Matthes, K.: Modeling the whole atmosphere 15 response to solar cycle changes in radiative and geomagnetic forcing, *J. Geophys. Res.*, 112, D23306, doi:10.1029/2006JD008306, 2007.
- Marsh, D. R., Mills, M. J., Kinnison, D. E., Lamarque, J.-F., Calvo, N., and Polvani, L. M.: Climate Change from 1850 to 2005 Simulated in CESM1(WACCM), *J. Climate*, 26(19), 7372–7391, doi:10.1175/JCLI-D-12-00558.1, 2013.
- Matthes, K., Kodera, K., Haigh, J., Shindell, D., Shibata, K., Langematz, U., Rozanov, E., and Kuroda, Y.: GRIPS solar experiments inter-comparison project: Initial results, *Papers in Meteorology and Geophysics*, 54, 71–90, 2003.
- 20 Matthes, K., Kuroda, Y., Kodera, K., and Langematz, U.: Transfer of the solar signal from the stratosphere to the troposphere: Northern winter, *J. Geophys. Res.*, 111, D06108, doi:10.1029/2005JD006283, 2006.
- Matthes, K., Marsh, D. R., Garcia, R. R., Kinnison, D. E., Sassi, F., and Walters, S.: Role of the QBO in modulating the influence of the 11 year solar cycle on the atmosphere using constant forcings, *J. Geophys. Res.*, 115, D18110, doi:10.1029/2009JD013020, 2010.
- Mayaud, P.: The aa indices: A 100-year series characterizing the magnetic activity, *Journal of Geophysical Research*, 77, 6870–6874, 25 doi:10.1029/JA077i034p06870, 1972.
- Mayaud, P.-N.: Derivation, Meaning, and Use of Geomagnetic Indices, *Geophysical Monograph*, 22, 1980.
- Maycock, A. C., Ineson, S., Gray, L. J., Scaife, A. A., Anstey, J. A., Lockwood, M., Butchart, N., Hardiman, S. C., Mitchell, D. M., and Osprey, S. M.: Possible impacts of a future Grand Solar Minimum on climate: Stratospheric and global circulation changes, *Journal of Geophysical Research: Atmospheres*, 120, 9043–9058, doi:10.1002/2014JD022022, 2015.
- 30 Maycock, A. C., Matthes, K., Tegtmeier, S., Thiéblemont, R., and Hood, L. L.: The representation of solar cycles signals in stratospheric ozone. Part I: A comparison of satellite observations, *Atmos. Chem. Phys. Diss.*, 16, 10021–10043, doi:10.5194/acp-16-10021-2016, <http://www.atmos-chem-phys.net/16/10021/2016/>, 2016.
- Maycock, A. C., Matthes, K., Tegtmeier, S., Thiéblemont, R., and Hood, L. L.: The representation of solar cycles signals in stratospheric ozone. Part II: A comparison of global models, *Atmos. Chem. Phys. Diss.*, in preparation, 2017.
- 35 Mayer, B. and Kylling, A.: Technical note: The libRadtran software package for radiative transfer calculations - description and examples of use, *Atmos. Chem. Phys.*, 5, 1855–1877, doi:10.5194/acp-5-1855-2005, 2005.
- McClintock, W. E., Rottman, G. J., and Woods, T. N.: Solar-Stellar Irradiance Comparison Experiment II (Solstice II): Instrument Concept and Design, *Solar Physics*, 230, 225–258, doi:10.1007/s11207-005-7432-x, 2005.

- McCracken, K. G., Beer, J., Steinhilber, F., and Abreu, J.: A Phenomenological Study of the Cosmic Ray Variations over the Past 9400 Years, and Their Implications Regarding Solar Activity and the Solar Dynamo, *Solar Physics*, 286, 609–627, doi:10.1007/s11207-013-0265-0, 2013.
- McIlwain, C. E.: Coordinates for Mapping the Distribution of Magnetically Trapped Particles, *J. Geophys. Res.*, 66, 3681–3691, doi:10.1029/JZ066i011p03681, 1961.
- McPeters, R. D.: A nitric oxide increase observed following the July 1982 solar proton event, *Geophys. Res. Lett.*, 13, 667–670, doi:10.1029/GL013i007p00667, 1986.
- McPeters, R. D. and Jackman, C. H.: The response of ozone to solar proton events during solar cycle 21: The observations, *J. Geophys. Res.*, 90, 7945–7954, doi:10.1029/JD090iD05p07945, 1985.
- 10 McPeters, R. D., Jackman, C. H., and Stassinopoulos, E. G.: Observations of ozone depletion associated with solar proton events, *J. Geophys. Res.*, 86, 12 071–12 081, doi:10.1029/JC086iC12p12071, <http://dx.doi.org/10.1029/JC086iC12p12071>, 1981.
- Meehl, G. A., Arblaster, J. M., and Marsh, D. R.: Could a future “Grand Solar Minimum” like the Maunder Minimum stop global warming?, *Geophysical Research Letters*, 40, 1789–1793, doi:10.1002/grl.50361, 2013.
- Mewaldt, R. A., Cohen, C. M. S., Labrador, A. W., Leske, R. A., Mason, G. M., Desai, M. I.,Looper, M. D., Mazur, J. E., Selesnick, R. S., and Haggerty, D. K.: Proton, helium and electron spectra during the large solar particle events of October–November 2003, *J. Geophys. Res.*, 110, A09S18, doi:10.1029/2005JA011038, 2005.
- 15 Mironova, I. A., Aplin, K. L., Arnold, F., Bazilevskaya, G. A., Harrison, R. G., Krivolutsky, A. A., Nicoll, K. A., Rozanov, E. V., Turunen, E., and Usoskin, I. G.: Energetic Particle Influence on the Earth’s Atmosphere, *Space Sci Rev.*, 194, 1–96, doi:10.1007/s11214-015-0185-4, 2015.
- 20 Misios, S., Mitchell, D. M., Gray, L. J., Tourpali, K., Matthes, K., Hood, L. L., Schmidt, H., Chiodo, G., Thiéblemont, R., Rozanov, E., and Krivolutsky, A.: Solar signals in CMIP-5 simulations: effects of atmosphere–ocean coupling, *Q. J. Roy. Meteorol. Soc.*, 142, 928–941, doi:10.1002/qj.2695, 2016.
- Mitchell, D. M., Gray, L. J., Fujiwara, M., Hibino, T., Anstey, J., Harada, Y., Long, C., Misios, S., Stott, P. A., and Tan, D.: Signatures of naturally induced variability in the atmosphere using multiple reanalysis datasets., *Q. J. Roy. Meteorol. Soc.*, 141, 2011–2031, doi:10.1002/qj.2492, 2015a.
- 25 Mitchell, D. M., Misios, S., Gray, L. J., Tourpali, K., Matthes, K., Hood, L. L., Schmidt, H., Chiodo, G., Thiéblemont, R., Rozanov, E., Shindell, D., and Krivolutsky, A.: Solar signals in CMIP-5 simulations: the stratospheric pathway, *Q. J. Roy. Meteorol. Soc.*, 141, 2390–2403, doi:10.1002/qj.2530, 2015b.
- Morley, S. K., Friedel, R. H. W., Cayton, T. E., and Noveroske, E.: A rapid, global and prolonged electron radiation belt dropout observed with the Global Positioning System constellation, *Geophys. Res. Lett.*, 37, L06102, doi:10.1029/2010GL042772, 2010.
- Mudelsee, M.: *Climate Time Series Analysis: Classical Statistical and Bootstrap Methods*, vol. 42 of *Atmospheric and Oceanographic Sciences Library*, Springer Verlag, doi:10.1007/978-90-481-9482-7, 2010.
- Neal, J. J., Rodger, C. J., Clilverd, M. A., Thomson, N. R., Raita, T., and Ulich, T.: Long-term determination of energetic electron precipitation into the atmosphere from AARDDVARK subionospheric VLF observations, *J. Geophys. Res. (Space Physics)*, 120, 2194–2211, doi:10.1002/2014JA020689, 2015.
- 35 Neale, R. B., Richter, J., Park, S., Lauritzen, P. H., Vavrus, S. J., Rasch, P. J., and Zhang, M.: The Mean Climate of the Community Atmosphere Model (CAM4) in Forced SST and Fully Coupled Experiments, *J. Climate*, 26, 5150–5168, doi:10.1175/jcli-d-12-00236.1, 2013.

- Nevanlinna, H.: Results of the Helsinki magnetic observatory 1844-1912, *Annales Geophysicae*, 22, 1691–1704, doi:10.5194/angeo-22-1691-2004, 2004.
- Nieder, H., Winkler, H., Marsh, D., and Sinnhuber, M.: NO_x production due to energetic particle precipitation in the MLT region: Results from ion chemistry model studies, *Journal of Geophysical Research*, 119, 2137–2148, doi:10.1002/2013JA019044, 2014.
- 5 Nissen, K. M., Matthes, K., Langematz, U., and Mayer, B.: Towards a better representation of the solar cycle in general circulation models, *Atmos. Chem. Phys.*, 7, 5391–5400, doi:10.5194/acp-7-5391-2007, 2007.
- Passos, D., Charbonneau, P., and Beaudoin, P.: An Exploration of Non-kinematic Effects in Flux Transport Dynamos, *Solar Physics*, 279, 1–22, doi:10.1007/s11207-012-9971-2, 2012.
- Pesnell, W. D.: Solar Cycle Predictions, *Solar Physics*, 281, 507–532, doi:10.1007/s11207-012-9997-5, 2012.
- 10 Petrovay, K.: Solar Cycle Prediction, *Living Rev. Solar Phys.*, 7, doi:10.12942/lrsp-2010-6, 2010.
- Picone, J. M., Hedin, A. E., Drob, D. P., and Aikin, A. C.: NRLMSISE-00 empirical model of the atmosphere: Statistical comparisons and scientific issues, *Journal of Geophysical Research (Space Physics)*, 107, 1468, doi:10.1029/2002JA009430, 2002.
- Porter, H. S., Jackman, C. H., and Green, A. E. S.: Efficiencies for production of atomic nitrogen and oxygen by relativistic proton impact in air, *J. Chem. Phys.*, 65, 154–167, doi:10.1063/1.432812, 1976.
- 15 Prša, A., Harmanec, P., Torres, G., Mamajek, E., Asplund, M., Capitaine, N., Christensen-Dalsgaard, J., Depagne, É., Haberreiter, M., Hekker, S., Hilton, J., Kopp, G., Kostov, V., Kurtz, D. W., Laskar, J., Mason, B. D., Milone, E. F., Montgomery, M., Richards, M., Schmutz, W., Schou, J., and Stewart, S. G.: Nominal Values for Selected Solar and Planetary Quantities: IAU 2015 Resolution B3, *The Astronomical Journal*, 152, 41, doi:10.3847/0004-6256/152/2/41, 2016.
- Randall, C. E., Rusch, D. W., Bevilacqua, R. M., Hoppel, K. W., and Lumpe, J. D.: Polar Ozone and Aerosol Measurement (POAM) II stratospheric NO₂, 1993–1996, *J. Geophys. Res.*, 103, 28,361–28,371, 1998.
- 20 Randall, C. E., Siskind, D. E., and Bevilacqua, R. M.: Stratospheric NO_x enhancements in the southern hemisphere vortex in winter/spring of 2000, *Geophys. Res. Lett.*, 28, 2385–2388, 2001.
- Randall, C. E., Harvey, V. L., Singleton, C. S., Bailey, S. M., Bernath, P. F., Codrescu, M., Nakajima, H., and Russell III, J. M.: Energetic particle precipitation effects on the Southern Hemisphere stratosphere in 1992-2005, *J. Geophys. Res.*, 112, D08308, doi:10.1029/2006JD007696, 2007.
- 25 Randall, C. E., Harvey, V. L., Siskind, D. E., France, J., Bernath, P. F., Boone, C. D., and Walker, K. A.: NO_x descent in the Arctic middle atmosphere in early 2009, *Geophys. Res. Lett.*, 36, doi:10.1029/2009GL039706, 2009.
- Rayner, N. A., Parker, D. E., Horton, E. B., Folland, C. K., Alexander, L. V., Rowell, D. P., Kent, E. C., and Kaplan, A.: Global analyses of sea surface temperature, sea ice, and night marine air temperature since the late nineteenth century, *J. Geophys. Res.*, 108, n/a–n/a, doi:10.1029/2002JD002670, 4407, 2003.
- 30 Reames, D.: Particle Acceleration at the Sun and in the Heliosphere, *Space Sciences Reviews*, 90, 413–491, 1999.
- Reddmann, T., Ruhnke, R., Versick, S., and Kouker, W.: Modeling disturbed stratospheric chemistry during solar-induced NO_x enhancements observed with MIPAS/ENVISAT, *J. Geophys. Res.*, 115, D00I11, doi:10.1029/2009JD012569, 2010.
- Rees, M. H.: *Physics and chemistry of the upper atmosphere*, Cambridge University Press, <http://dx.doi.org/10.1017/CBO9780511573118>, 1989.
- 35 Reeves, G. D., McAdams, K. L., Friedel, R. H. W., and O'Brien, T. P.: Acceleration and loss of relativistic electrons during geomagnetic storms, *Geophys. Res. Lett.*, 30, 1529, doi:10.1029/2002GL016513, 2003.

- Richardson, I. and Cane, H.: Near-Earth Interplanetary Coronal Mass Ejections During Solar Cycle 23 (1996 – 2009): Catalog and Summary of Properties, *Solar Physics*, 264, 189–237, doi:10.1007/s11207-010-9568-6, 2010.
- Rienecker, M. M., Suarez, M. J., Gelaro, R., Todling, R., Bacmeister, J., Liu, E., Bosilovich, M. G., Schubert, S. D., Takacs, L., Kim, G.-K., Bloom, S., Chen, J., Collins, D., Conaty, A., da Silva, A., Gu, W., Joiner, J., Koster, R. D., Lucchesi, R., Molod, A., Owens, T., Pawson, S., Pegion, P., Redder, C. R., Reichle, R., Robertson, F. R., Ruddick, A. G., Sienkiewicz, M., and Woollen, J.: MERRA: NASA's Modern-Era Retrospective Analysis for Research and Applications, *J. Climate*, 24, 3624–3648, doi:10.1175/jcli-d-11-00015.1, 2011.
- Rind, D., Lean, J., Lerner, J., Lonergan, P., and Leboissier, A.: Exploring the stratospheric/tropospheric response to solar forcing, *J. Geophys. Res.*, 113, doi:10.1029/2008JD010114, 2008.
- Rodger, C. J., Clilverd, M. A., Green, J. C., and Lam, M. M.: Use of POES SEM-2 observations to examine radiation belt dynamics and energetic electron precipitation into the atmosphere, *J. Geophys. Res.*, 115, A04202, doi:10.1029/2008JA014023, 2010a.
- Rodger, C. J., Kavanagh, A. J., Clilverd, M. A., and Marple, S. R.: Comparison between POES energetic electron precipitation observations and riometer absorptions: Implications for determining true precipitation fluxes, *J. Geophys. Res. (Space Physics)*, 118, 7810–7821, doi:10.1002/2013JA019439, 2013.
- Roeckner, E., Bäuml, G., Bonaventura, L., Brokopf, R., Esch, M., Giorgetta, Hagemann, S., Kirchner, I., Kornbluh, L., Manzini, E., Rhodin, A., Schlese, U., Schulzweida, U., and Tompkins, A.: The atmospheric general circulation model ECHAM5, Part I, Tech. Rep. No. 349, Max-Planck-Institut für Meteorologie, Hamburg, 2003.
- Roeckner, E., Brokopf, R., Esch, M., Giorgetta, M., Hagemann, S., Kornbluh, L., Manzini, E., Schlese, U., and Schulzweida, U.: Sensitivity of Simulated Climate to Horizontal and Vertical Resolution in the ECHAM5 Atmosphere Model, *J. Climate*, 19, 3771–3791, doi:10.1175/JCLI3824.1, 2006.
- Rohen, G. J., von Savigny, C., Sinnhuber, M., Llewellyn, E. J., Kaiser, J. W., Jackman, C. H., Kallenrode, M.-B., Schröter, J., Eichmann, K.-U., Bovensmann, H., and Burrows, J. P.: Ozone depletion during the solar proton events of October/November 2003 as seen by SCIAMACHY, *J. Geophys. Res.*, 110, A09S39, doi:10.1029/2004JA010984, 2005.
- Rottman, G.: The *SORCE* Mission, *Solar Physics*, 230, 7–25, doi:10.1007/s11207-005-8112-6, 2005.
- Rozanov, E., Calisto, M., Egorova, T., Peter, T., and Schmutz, W.: Influence of the Precipitating Energetic Particles on Atmospheric Chemistry and Climate, *Surv. Geophys.*, 33, 483–501, doi:10.1007/s10712-012-9192-0, 2012.
- Rusch, D. W., Gérard, J.-C., Solomon, S., Crutzen, P. J., and Reid, G. C.: The effect of particle precipitation events on the neutral and ion chemistry of the middle atmosphere. I - Odd nitrogen, *Planet. Space Sci.*, 29, 767–774, 1981.
- Salmi, S.-M., Verronen, P. T., Thölix, L., Kyrölä, E., Backman, L., Karpechko, A. Y., and Seppälä, A.: Mesosphere-to-stratosphere descent of odd nitrogen in February–March 2009 after sudden stratospheric warming, *Atmos. Chem. Phys.*, 11, 4645–4655, doi:10.5194/acp-11-4645-2011, 2011.
- Sander, R., Baumgaertner, A., Gromov, S., Harder, H., Jöckel, P., Kerkweg, A., Kubistin, D., Regelin, E., Riede, H., Sandu, A., Taraborrelli, D., Tost, H., and Xie, Z.-Q.: The atmospheric chemistry box model CAABA/MECCA-3.0, *Geosci. Model Dev.*, 4, 373–380, doi:10.5194/gmd-4-373-2011, 2011a.
- Sander, R., Jöckel, P., Kirner, O., Kunert, A. T., Landgraf, J., and Pozzer, A.: The photolysis module JVAL-14, compatible with the MESSy standard, and the JVal PreProcessor (JVPP), *Geosci. Model Dev.*, 7, 2653–2662, doi:10.5194/gmd-7-2653-2014, 2014.
- Sander, S. P., Abbatt, J., Barker, J. R., Burkholder, J. B., Friedl, R. R., Golden, D. M., Huie, R. E., Kolb, C. E., Kurylo, M. J., Moortgat, G. K., Orkin, V. L., and Wine, P. H.: Chemical Kinetics and Photochemical Data for Use in Atmospheric Studies, Tech. Rep. Evaluation No. 17, JPL Publication 10-6, Jet Propulsion Laboratory, Pasadena, <http://jpldataeval.jpl.nasa.gov>, 2011b.

- Scaife, A. A., Ineson, S., Knight, J. R., Gray, L., Kodera, K., and Smith, D. M.: A mechanism for lagged North Atlantic climate response to solar variability, *Geophysical Research Letters*, 40, 434–439, doi:10.1002/grl.50099, 2013.
- Schmidt, H., Brasseur, G., Charron, M., Manzini, E., Giorgetta, M., Diehl, T., Formichev, V., Kinnison, D., Marsh, D., and Walters, S.: The HAMMONIA chemistry climate model: sensitivity of the mesopause region to the 11-year solar cycle and CO₂ doubling, *J. Clim.*, 19, 3903–3931, 2006.
- Schmutz, W., Fehlmann, A., Finsterle, W., Kopp, G., and Thuillier, G.: Total solar irradiance measurements with PREMOS/PICARD, in: AIP conference proceedings, vol. 1531 of *American Institute of Physics Conference Series*, p. 624, doi:10.1063/1.4804847, 2013.
- Schöll, M., de Wit, T. D., Kretzschmar, M., and Haberreiter, M.: Making of a solar spectral irradiance dataset I: observations, uncertainties, and methods, *Journal of Space Weather and Space Climate*, 6, A14, doi:10.1051/swsc/2016007, 2016.
- 10 Semeniuk, K., Fomichev, V. I., McConnell, J. C., Fu, C., Melo, S. M. L., and Usoskin, I. G.: Middle atmosphere response to the solar cycle in irradiance and ionizing particle precipitation, *Atmos. Chem. Phys.*, 11, 5045–5077, doi:10.5194/acp-11-5045-2011, 2011.
- Seppälä, A., Randall, C. E., Clilverd, M. A., Rozanov, E., and Rodger, C. J.: Geomagnetic activity and polar surface air temperature variability, *J. Geophys. Res.*, 114, doi:10.1029/2008JA014029, 2009.
- Seppälä, A., Matthes, K., Randall, C. E., and Mironova, I. A.: What is the solar influence on climate? Overview of activities during CAWSES-II, *Progress in Earth and Planetary Science*, 1, 24, doi:10.1186/s40645-014-0024-3, 2014.
- 15 Seppälä, A. and Clilverd, M. A.: Energetic Particle Forcing of the Northern Hemisphere winter stratosphere: Comparison to solar irradiance forcing, *Frontiers in Physics*, 2, doi:10.3389/fphy.2014.00025, 2014.
- Seppälä, A., Verronen, P. T., Sofieva, V. F., Tamminen, J., Kyrölä, E., Rodger, C. J., and Clilverd, M. A.: Destruction of the tertiary ozone maximum during a solar proton event, *Geophys. Res. Lett.*, 33, n/a–n/a, doi:10.1029/2005GL025571, 107804, 2006.
- 20 Shibata, K. and Kodera, K.: Simulation of radiative and dynamical responses of the middle atmosphere to the 11-year solar cycle, *J. Atmos. Sol. Terr. Phys.*, 67, 125–143, 2005.
- Shindell, D. T., Schmidt, G. A., Mann, M. E., Rind, D., and Waple, A.: Solar Forcing of Regional Climate Change During the Maunder Minimum, *Science*, 294, 2149–2152, doi:10.1126/science.1064363, 2001.
- Sinnhuber, M., Kazeminejad, S., and Wissing, J.-M.: Interannual variation of NO_x from the lower thermosphere to the upper stratosphere in the years 1991–2005, *Journal of Geophysical Research*, 116, doi:10.1029/2010JA015825, 2011.
- 25 Sinnhuber, M., Nieder, H., and Wieters, N.: Energetic particle precipitation and the chemistry of the mesosphere / lower thermosphere, *Surveys in Geophysics*, 33, doi:10.1007/s10712-012-9201-3, 2012.
- Sinnhuber, M., Friederich, F., Bender, S., and Burrows, J.: The response of mesospheric NO to geomagnetic forcing in 2002–2012 as seen by SCIAMACHY, *Journal of Geophysical Research (Space Physics)*, 121, doi:10.1002/2015JA022284, 2016.
- 30 Siskind, D. E.: Atmospheric science across the Stratopause, vol. 123 of *Geophysical Monograph*, chap. On the coupling between middle and upper atmospheric odd nitrogen, pp. 101–116, American Geophysical Union, 2000.
- Smith, D. M., Scaife, A. A., Boer, G. J., Caian, M., Doblus-Reyes, F. J., Guemas, V., Hawkins, E., Hazeleger, W., Hermanson, L., Ho, C. K., Ishii, M., Kharin, V., Kimoto, M., Kirtman, B., Lean, J., Matei, D., Merryfield, W. J., Müller, W. A., Pohlmann, H., Rosati, A., Wouters, B., and Wyser, K.: Real-time multi-model decadal climate predictions, *Climate Dynamics*, 41, 2875–2888, doi:10.1007/s00382-012-1600-0, 2013.
- 35 Solanki, S., Usoskin, I., Kromer, B., Schüssler, M., and Beer, J.: Unusual activity of the Sun during recent decades compared to the previous 11,000 years, *Nature*, 431, 1084–1087, doi:10.1038/nature02995, 2004.

- Solanki, S. K., Krivova, N. A., and Haigh, J. D.: Solar Irradiance Variability and Climate, *Annual Review of Astronomy and Astrophysics*, 51, 311–351, doi:10.1146/annurev-astro-082812-141007, 2013.
- Solomon, S., Rusch, D. W., Gérard, J.-C., Reid, G. C., and Crutzen, P. J.: The effect of particle precipitation events on the neutral and ion chemistry of the middle atmosphere. II - Odd hydrogen, *Planet. Space Sci.*, 29, 885–892, 1981.
- 5 Solomon, S., Crutzen, P. J., and Roble, R. G.: Photochemical coupling of the thermosphere and the lower atmosphere 1. Odd nitrogen from 50 to 120 km, *J. Geophys. Res.*, 87, 7206–7220, 1982.
- Solomon, S. C. and Qian, L.: Solar extreme-ultraviolet irradiance for general circulation models, *J. Geophys. Res.*, 110, A10306, doi:10.1029/2005JA011160, 2005.
- Steinhilber, F. and Beer, J.: Prediction of solar activity for the next 500 years, *Journal of Geophysical Research (Space Physics)*, 118, 1861–1867, doi:10.1002/jgra.50210, 2013.
- 10 Steinhilber, F., Abreu, J. A., Beer, J., Brunner, I., Christl, M., Fischer, H., Heikkilä, U., Kubik, P. W., Mann, M., McCracken, K. G., Miller, H., Miyahara, H., Oerter, H., and Wilhelms, F.: 9,400 years of cosmic radiation and solar activity from ice cores and tree rings, *Proceedings of the National Academy of Sciences*, 109, 5967–5971, doi:10.1073/pnas.1118965109, 2012.
- Stott, P., Jones, G. S., and Mitchell, J. F. B.: Do Models Underestimate the Solar Contribution to Recent Climate Change?, *J. Climate*, 16, 4070–4093, [http://dx.doi.org/10.1175/1520-0442\(2003\)016<4079:DMUTSC>2.0.CO;2](http://dx.doi.org/10.1175/1520-0442(2003)016<4079:DMUTSC>2.0.CO;2), 2003.
- 15 Summers, D., Ni, B., and Meredith, N. P.: Timescales for radiation belt electron acceleration and loss due to resonant wave-particle interactions: 1. Theory, *J. Geophys. Res. (Space Physics)*, 112, A04206, doi:10.1029/2006JA011801, 2007.
- Swider, W. and Keneshea, T.: Decrease of ozone and atomic oxygen in the lower mesosphere during a PCA event, *Planetary and Space Science*, 21, 1969 – 1973, doi:[http://dx.doi.org/10.1016/0032-0633\(73\)90126-8](http://dx.doi.org/10.1016/0032-0633(73)90126-8), 1973.
- 20 Tapping, K. F.: The 10.7 cm solar radio flux (F10.7), *Space Weather*, 11, 394–406, doi:10.1002/swe.20064, 2013.
- Thébaud, E.: International Geomagnetic Reference Field: the 12th generation, *Earth, Planets and Space*, 67, 1–19, doi:10.1186/s40623-015-0228-9, 2015.
- Thieblemont, R., Matthes, K., Omrani, N.-E., Kodera, K., and Hansen, F.: Solar forcing synchronizes decadal North Atlantic climate variability, *Nature Commun.*, 6, 8268, doi:10.1038/ncomms9268, 2015.
- 25 Thomas, R. J., Barth, C. A., Rottman, G. J., Rusch, D. W., Mount, G. H., Lawrence, G. M., Sanders, R. W., Thomas, G. E., and Clemens, L. E.: Mesospheric ozone depletion during the Solar Proton Event of July 13, 1982 Part I Measurement, *Geophys. Res. Lett.*, 10, 253–255, doi:10.1029/GL010i004p00253, 1983.
- Turunen, E., Verronen, P. T., Seppälä, A., Rodger, C. J., Clilverd, M. A., Tamminen, J., Enell, C.-F., and Ulich, T.: Impact of different precipitation energies on NO_x generation during geomagnetic storms, *J. Atmos. Sol.-Terr. Phys.*, 71, 1176–1189, doi:10.1016/j.jastp.2008.07.005, 2009.
- 30 Unruh, Y. C., Solanki, S. K., and Fligge, M.: The spectral dependence of facular contrast and solar irradiance variations, *Astronomy & Astrophysics*, 345, 635–642, 1999.
- Usoskin, I. G.: A History of Solar Activity over Millennia, *Living Reviews in Solar Physics*, 5, 3–67, doi:10.12942/lrsp-2008-3, 2008.
- Usoskin, I. G.: A History of Solar Activity over Millennia, *Living Rev. Solar Phys.*, 10, 1, doi:10.12942/lrsp-2013-1, 2013.
- 35 Usoskin, I. G. and Kovaltsov, G. A.: Cosmic ray induced ionization in the atmosphere: Full modeling and practical applications, *J. Geophys. Res.*, 111, D21206, doi:10.1029/2006JD007150, 2006.
- Usoskin, I. G., Alanko-Huotari, K., Kovaltsov, G. A., and Mursula, K.: Heliospheric modulation of cosmic rays: Monthly reconstruction for 1951–2004, *J. Geophys. Res.*, 110, A12108, doi:10.1029/2005JA011250, 2005.

- Usoskin, I. G., Desorgher, L., Velinov, P., Storini, M., Flückiger, E. O., Bütikofer, R., and Kovaltsov, G. A.: Ionization of the earth's atmosphere by solar and galactic cosmic rays, *Acta Geophys.*, 57, 88–101, doi:10.2478/s11600-008-0019-9, 2009.
- Usoskin, I. G., Kovaltsov, G. A., and Mironova, I. A.: Cosmic ray induced ionization model CRAC:CRII: An extension to the upper atmosphere, *J. Geophys. Res.*, 115, D10302, 2010.
- 5 Usoskin, I. G., Bazilevskaya, G. A., and Kovaltsov, G. A.: Solar modulation parameter for cosmic rays since 1936 reconstructed from ground-based neutron monitors and ionization chambers, *J. Geophys. Res.*, 116, A02104, doi:10.1029/2010JA016105, 2011.
- Usoskin, I. G., Hulot, G., Gallet, Y., Roth, R., Licht, A., Joos, F., Kovaltsov, G. A., Thébault, E., and Khokhlov, A.: Evidence for distinct modes of solar activity, *Astronomy & Astrophysics*, 562, L10, doi:10.1051/0004-6361/201423391, 2014.
- Van Allen, J. A. and Frank, L. A.: Radiation Around the Earth to a Radial Distance of 107,400 km, *Nature*, 183, 430–434, doi:10.1038/183430a0, 1959.
- 10 van de Kamp, M., Seppälä, A., Clilverd, M. A., Rodger, C. J., Verronen, P. T., and Whittaker, I. C.: A model providing long-term datasets of energetic electron precipitation during geomagnetic storms, *J. Geophys. Res. Atmos.*, 121, 12 520–12 540, doi:10.1002/2015JD024212, 2016.
- Verronen, P. T. and Lehmann, R.: Analysis and parameterisation of ionic reactions affecting middle atmospheric HO_x and NO_y during solar proton events, *Ann. Geophys.*, 31, 909–956, doi:10.5194/angeo-31-909-2013, 2013.
- 15 Verronen, P. T., Seppälä, A., Kyrölä, E., Tamminen, J., Pickett, H. M., and Turunen, E.: Production of odd hydrogen in the mesosphere during the January 2005 solar proton event, *Geophys. Res. Lett.*, 33, L24811, doi:10.1029/2006GL028115, 2006.
- Verronen, P. T., Funke, B., López-Puertas, M., Stiller, G. P., von Clarmann, T., Enell, C.-F., Turunen, E., and Tamminen, J.: About the Increase of HNO₃ in the Stratopause Region During the Halloween 2003 Solar Proton Event, *Geophys. Res. Lett.*, 35, L20809, doi:10.1029/2008GL035312, 2008.
- 20 Verronen, P. T., Santee, M. L., Manney, G. L., Lehmann, R., Salmi, S.-M., and Seppälä, A.: Nitric acid enhancements in the mesosphere during the January 2005 and December 2006 solar proton events, *J. Geophys. Res.*, 116, D17 301, doi:10.1029/2011JD016075, 2011a.
- Verronen, P. T., Rodger, C. J., Clilverd, M. A., and Wang, S.: First evidence of mesospheric hydroxyl response to electron precipitation from the radiation belts, *J. Geophys. Res.*, 116, D07 307, doi:10.1029/2010JD014965, 2011b.
- 25 Vieira, L. E. A. and Solanki, S. K.: Evolution of the solar magnetic flux on time scales of years to millenia, *Astronomy & Astrophysics*, 509, A100, doi:10.1051/0004-6361/200913276, 2010.
- Vieira, L. E. A., Solanki, S. K., Krivova, N. A., and Usoskin, I.: Evolution of the solar irradiance during the Holocene, *Astronomy & Astrophysics*, 531, A6, doi:10.1051/0004-6361/201015843, 2011.
- Viereck, R., Puga, L., McMullin, D., Judge, D., Weber, M., and Tobiska, W. K.: The Mg II index: A proxy for solar EUV, *Geophysical Research Letters*, 28, 1343–1346, doi:10.1029/2000GL012551, 2001.
- 30 Vitt, F. M. and Jackman, C. H.: A comparison of sources of odd nitrogen production from 1974 through 1993 in the Earth's middle atmosphere as calculated using a two-dimensional model, *J. Geophys. Res.*, 101, 6729–6739, 1996.
- von Clarmann, T., Glatthor, N., Höpfner, M., Kellmann, S., Ruhnke, R., Stiller, G. P., Fischer, H., Funke, B., Gil-López, S., and López-Puertas, M.: Experimental Evidence of Perturbed Odd Hydrogen and Chlorine Chemistry After the October 2003 Solar Proton Events, *J. Geophys. Res.*, 110, A09S45, doi:10.1029/2005JA011053, 2005.
- 35 von Clarmann, T., Funke, B., López-Puertas, M., Kellmann, S., Linden, A., Stiller, G. P., Jackman, C. H., and Harvey, V. L.: The Solar Proton Events in 2012 as Observed by MIPAS, *Geophys. Res. Lett.*, 40, 1–5, doi:10.1002/grl.50119, 2013.

- Wang, Y.-M., Lean, J. L., and Sheeley, Jr., N. R.: Modeling the Sun's Magnetic Field and Irradiance since 1713, *The Astrophysical Journal*, 625, 522–538, doi:10.1086/429689, 2005.
- Watkins, N. W., Credgington, D., Hnat, B., Chapman, S. C., Freeman, M. P., and Greenhough, J.: Towards Synthesis of Solar Wind and Geomagnetic Scaling Exponents: A Fractional Lévy Motion Model, *Space Science Reviews*, 121, 271–284, doi:10.1007/s11214-006-4578-2, 2005.
- Weeks, L. H., Cuikay, R. S., and Corbin, J. R.: Ozone Measurements in the Mesosphere During The Solar Proton Event of 2 November 1969., *Journal of Atmospheric Sciences*, 29, 1138–1142, doi:10.1175/1520-0469(1972)029<1138:OMITMD>2.0.CO;2, 1972.
- Wenzler, T., Solanki, S. K., and Krivova, N. A.: Can surface magnetic fields reproduce solar irradiance variations in cycles 22 and 23?, *Astronomy & Astrophysics*, 432, 1057–1061, doi:10.1051/0004-6361:20041956, 2005.
- 10 Whittaker, I. C., Gamble, R. J., Rodger, C. J., Clilverd, M. A., and Sauvaud, J.-A.: Determining the spectra of radiation belt electron losses: Fitting DEMETER electron flux observations for typical and storm times, *J. Geophys. Res. (Space Physics)*, 118, 7611–7623, doi:10.1002/2013JA019228, 2013.
- Whittaker, I. C., Clilverd, M. A., and Rodger, C. J.: Characteristics of precipitating energetic electron fluxes relative to the plasmopause during geomagnetic storms, *J. Geophys. Res. (Space Physics)*, 119, 8784–8800, doi:10.1002/2014JA020446, 2014a.
- 15 Whittaker, I. C., Rodger, C. J., Clilverd, M. A., and Sauvaud, J.-A.: The effects and correction of the geometric factor for the POES/MEPED electron flux instrument using a multisatellite comparison, *J. Geophys. Res. (Space Physics)*, 119, 6386–6404, doi:10.1002/2014JA020021, 2014b.
- Winkler, H., Kazeminejad, S., Sinnhuber, M., Kallenrode, M.-B., and Notholt, J.: Conversion of mesospheric HCl into active chlorine during the solar proton event in July 2000 in the northern polar region, *J. Geophys. Res.*, 114, D00I03, doi:10.1029/2008JD011587, 2009.
- 20 Woods, T. N., Tobiska, W. K., Rottman, G. J., and Worden, J. R.: Improved solar Lyman α irradiance modeling from 1947 through 1999 based on UARS observations, *J. Geophys. Res.*, 105, 27 195–27 216, doi:10.1029/2000JA000051, 2000.
- Woods, T. N., Eparvier, F. G., Bailey, S. M., Chamberlin, P. C., Lean, J., Rottman, G. J., Solomon, S. C., Tobiska, W. K., and Woodraska, D. L.: Solar EUV Experiment (SEE): Mission overview and first results, *Journal of Geophysical Research (Space Physics)*, 110, A01 312, doi:10.1029/2004JA010765, 2005.
- 25 Woollings, T., Lockwood, M., Masato, G., Bell, C., and Gray, L.: Enhanced signature of solar variability in Eurasian winter climate, *Geophys. Res. Lett.*, 37, doi:10.1029/2010GL044601, 2010.
- Yando, K., Millan, R. M., Green, J. C., and Evans, D. S.: A Monte Carlo simulation of the NOAA POES Medium Energy Proton and Electron Detector instrument, *J. Geophys. Res.*, 116, A10 231, doi:10.1029/2011JA016671, 2011.
- Yeo, K. L., Krivova, N. A., Solanki, S. K., and Glassmeier, K. H.: Reconstruction of total and spectral solar irradiance from 1974 to 2013 based on KPVT, SoHO/MDI and SDO/HMI observations, *Astronomy & Astrophysics*, 570, doi:10.1051/0004-6361/201423628, 2014.
- 30 Yeo, K. L., Ball, W. T., Krivova, N. A., Solanki, S. K., Unruh, Y. C., and Morrill, J.: UV solar irradiance in observations and the NRLSSI and SATIRE-S models, *J. Geophys. Res.*, 120, 6055–6070, doi:10.1002/2015JA021277, 2015.
- Zadorozhny, A., Tuchkov, G., Kikhtenko, V., Laštovička, J., Boška, J., and Novák, A.: Nitric oxide and lower ionosphere quantities during solar particle events of October 1989 after rocket and ground-based measurements, *Journal of Atmospheric and Terrestrial Physics*, 54, 183 – 192, doi:http://dx.doi.org/10.1016/0021-9169(92)90127-7, 1992.
- 35 Zadorozhny, A. M., Kikhtenko, V. N., Kokin, G. A., Tuchkov, G. A., Tyutin, A. A., Chizhov, A. F., and Shtirkov, O. V.: Middle atmosphere response to the solar proton events of October 1989 using the results of rocket measurements, *J. Geophys. Res.*, 99, 21 059–21 069, doi:10.1029/93JD03194, 1994.

A new observational solar irradiance composite

Margit Haberreiter¹, Micha Schöll^{1,2}, Thierry Dudok de Wit², Matthieu Kretzschmar², Stergios Misios^{3,4}, Klairie Tourpali³, and Werner Schmutz¹

Abstract. Variations in the solar spectral irradiance (SSI) are an important driver of the chemistry, temperature, and dynamics of the Earth's atmosphere, and ultimately the Earth's climate. To investigate the detailed response of the Earth's atmosphere to SSI variations, a reliable SSI dataset is needed. We present an observational SSI composite dataset **that is based on 20 instruments, and has been built by using probabilistic approach** that takes into account the scale-dependent uncertainty of each available SSI observation. We compare the variability of this new composite with available SSI reconstructions and discuss the respective modelled responses in the Earth's atmosphere. As the composite is based on purely statistical means we consider it as a valuable independent dataset.

1. Introduction

The impact of solar variability on the Earth's climate has a long history as a research field, and has also become a hotly debated topic [Haigh, 1994; Haigh *et al.*, 2010; Ermolli *et al.*, 2013; Ball *et al.*, 2016]. This impact is mediated by several mechanisms including direct solar heating of the Earth's surface, changes in stratospheric ozone, and the impact of energetic particles [Haigh, 2007; Gray *et al.*, 2010; Ermolli *et al.*, 2013; Solanki *et al.*, 2013].

Although there is strong evidence for this natural forcing to be weak in comparison to that of man-made greenhouse gases, large uncertainties remain regarding the magnitude of the impacts, and the mechanisms involved [Stocker and Qin, 2014]. Two key mechanisms have been identified and investigated in a number of modelling studies: The first one, known as the *bottom-up* mechanism, involves direct changes in the troposphere, caused by the variability **primarily in the visible part of the solar spectrum**, directly penetrating to the lower troposphere, warming the surface and modulating the atmosphere-ocean interactions [e.g. Meehl *et al.*, 2009]. The second one, named *top-down* mechanism, involves the direct influence of solar ultraviolet (UV) variations – in particular below 200 nm – on the upper atmosphere, causing an increase in stratospheric ozone and related warming, and indirect dynamical effects at lower stratospheric levels, and finally influencing surface climate through stratosphere-troposphere coupling [e.g. Haigh, 1994; Matthes *et al.*, 2006].

For the *top-down* mechanisms the key input variable is the solar UV radiation, on which this paper will concentrate. Direct observations of the spectrally-resolved solar irradiance (or SSI, for Solar Spectral Irradiance) started in the 1970s. These observations however, are fragmented in time and in wavelength. Only in 2003 - with the launch of the SORCE

spacecraft - did the continuous monitoring of the solar spectrum really start. As a consequence, our present knowledge of the solar variability in different parts of the spectrum is limited. However, a continuous SSI dataset is crucially needed to assess decadal, and multi-decadal time scales that are most relevant for climate studies. This paucity of observations is further complicated by numerous problems; making radiometrically accurate SSI observations is notoriously challenging, as instruments degrade in time, have a limited lifetime, and rarely allow in-flight calibration.

To overcome these problems, and reconstruct the SSI over longer periods, several SSI models have been developed and their output, the reconstructed SSI time series, has been widely used to represent solar spectral variations in climate and chemistry-climate modelling studies [Matthes *et al.*, 2006; Austin *et al.*, 2008; Ermolli *et al.*, 2013; Solanki *et al.*, 2013; Hood *et al.*, 2015; Mitchell *et al.*, 2015; Misios *et al.*, 2015].

However, and while most of them correctly reproduce recent SSI observations, large uncertainties remain regarding their ability to reconstruct past variations on multi-decadal time scales. More importantly, all these models are eventually trained and tested on the few available SSI observations. This situation has led to the international collaborative project **SOLID (First European Comprehensive Solar Irradiance Data Exploitation, <http://projects.pmodwrc.ch/solid/>)** with the aim of collecting and merging all available SSI observations into one single composite that will finally offer better conditions for training SSI models, understanding solar variability, and assessing its impact on climate. Such homogeneous datasets are of particular importance for initiatives such as the Climate Model Intercomparison Project (CMIP, <http://www.pcmdi.llnl.gov/projects/cmip/>), which aims at quantifying the contributions of various forcings, including the solar forcing.

Although the SOLID composite addresses the full solar spectrum, including the visible and near-infrared, in this paper we focus on the UV only, from 100 nm to 400 nm because of its key role in Sun-climate studies. Indeed, the visible and near-infrared bands mostly lead to direct heating of the surface and oceans only, and their forcing can be conveniently summarised in the spectrally-integrated SSI, named Total Solar Irradiance (TSI). **The TSI has received considerable attention, and its reconstruction efforts have a long history** [Fröhlich and Lean, 1998; Kopp and Lean, 2011]. In comparison, the SSI has received much less attention, while its variability also raises many questions. Recent observations by the SORCE satellite, for example,

¹Physikalisch-Meteorologisches Observatorium and World Radiation Center, Dorfstrasse 33, CH-7260 Davos Dorf, Switzerland

²LPC2E/CNRS and Université d'Orléans, 3A Av. de la Recherche Scientifique, 45071 Orléans, France

³LAP, Aristotle University of Thessaloniki, 54124 Thessaloniki, Greece

⁴Atmospheric, Oceanic and Planetary Physics, Oxford University, Oxford, UK

have revealed SSI variations in the UV band that depart from past observations, and could potentially lead to a different climate response to the solar cycle [Haigh et al., 2010]. These variations are still hotly debated [Lean and DeLand, 2012], and provide yet another motivation for building a single composite that would allow different periods to be compared. Recently, Ball et al. [2016] investigated the response of the Earth’s atmosphere to different SSI datasets and concluded that the simulated ozone response driven by the SORCE SSI observations cannot be reconciled with ozone observations.

The first attempt to merge different SSI observations in a single UV dataset was made by DeLand and Cebula [2008] who created a dataset with daily spectra covering the 120–400 nm wavelength range from 1978 to 2005. In the presence of multiple simultaneous observations, one single instrument was selected. We go further by including all available datasets, and covering the period from November 8, 1978 to December 31, 2014. In addition, we provide a systematic framework for merging overlapping observations, filling in periods of missing data with solar proxies, and taking into account uncertainties, finally providing uncertainties for the composite too. The first stage, which consists in collecting all the datasets and preprocessing them to enable their merging has already been described by Schöll et al. [2016], henceforth referred to as Paper I.

In the current paper, we concentrate on the making of the SSI composite, including a time-dependent uncertainty of the datasets, and the properties of that composite. Two major assets of the mathematical procedure we propose are its traceability, and the decoupling of the statistical problem (merging SSI datasets) from the scientific one (correcting SSI datasets). Our method can be readily extended to other spectral bands, or to combinations of observations. **At this stage we merge the datasets without attempting to correct them. While the help of additional physical constraints and SSI models should lead to better results, we consider the making of a purely observational composite as an important and mandatory first step toward more elaborate composites.**

The paper is structured as follows. First, in Section 2, we briefly discuss the datasets used for the **observational** UV composite presented here. Then, in Section 3, we present in detail the tools to derive the composite. Third, in Section 4, we present an **experimental version of the SSI composite, labelled SOLID.beta, and compare it with available SSI reconstruction models. In Section 5, we discuss remaining issues, which are solved in Section 6, where we present the final version of the observational composite.** Then, in Section 7.1, the response of atmospheric heating to the SOLID composite is evaluated and compared against other SSI products. Finally, in Section 8, we summarize our findings and list the specific actions that remain to be taken before the composite can be truly considered as being representative of the solar UV variation.

2. SSI observations

Our composite is based on 20 instruments, which are listed in Table 2. In addition, we also took into consideration 9 reference spectra, of which - due to the unknown uncertainty of the other datasets - we only used one, i.e. the ATLAS3 spectrum, and 6 solar proxy datasets, as listed in Table 1. In Paper I, we describe how they are all converted into a unified format, together with independent uncertainty estimates. Several instruments were not included in our composite. ENVISAT/SCIAMACHY, for example, was excluded **at this stage** because it is not degradation corrected. The broadband filter radiometers SOHO/VIRGO-SPM, PROBA2/LYRA, and PICARD/PREMOS also were also omitted because of their coarse spectral resolution.

However, these instruments are valuable for validating the SSI composite, as discussed in Section 5.

Let us stress that none of the original SSI datasets and proxy datasets has been corrected or adjusted as our prime objective is to build a composite that is as objective as possible, before considering what changes will be needed to enhance its value for climate studies. For the same reason, we deliberately excluded inputs coming from model reconstructions of the SSI. While this questionable choice inevitably leads to discrepancies between some of the instruments, it is also an asset, in the sense that it provides us with a fully independent reference dataset for testing models and checking individual instruments. The time-dependent uncertainties are furthermore evaluated by independent means, thus ensuring that all the instruments can be meaningfully compared. This is important for what follows because these uncertainties determine the contribution of each instrument to the composite.

In addition to SSI observations, we consider 6 solar proxies. While they do not strictly correspond to SSI observations, they are known to reproduce SSI variations in given bands, and for specific time scales. The 10.7 cm radio flux (or F10.7 index), for example, has been widely used as a proxy for the EUV band, whereas the 30 cm flux is better suited for reproducing the solar rotational variability at longer UV wavelengths [Dudok de Wit et al., 2014]. The sunspot darkening is a proxy that has been successfully used to reproduce the variability in TSI [Fröhlich and Lean, 2004].

This list does not include the MgII index, which is a widely-used proxy for solar variability in the UV [Viereck et al., 2001]. Indeed, while we concentrate here on the space age only (from 7 November 1978 onward), the full SOLID dataset actually starts in 1950, thus requiring proxies that cover the full period. Most radio fluxes are available for that period, whereas measurements of the MgII index started only in November 1978. This is the reason why for this first version of the SOLID dataset, we did not include the MgII index. Incidentally, because the MgII index is highly correlated with radio fluxes at 15 and 30 cm, most of its variability can be adequately reproduced with a combination of radio fluxes at these two wavelengths [Dudok de Wit et al., 2014].

Resorting to proxies is also questionable choice, but it is the only solution for filling in the numerous data gaps in the composite, while relying on observations that have been shown to be good substitutes for the SSI. Of course, one should interpret such proxy reconstructions with great care when considering time scales in excess of several years, for which they may not properly capture the true solar variability.

2.1. TSI dataset

TSI observations are formally part of the SSI. However, they have received considerably more attention so far, and expectations are high regarding a potential long-term variability, whose assessment requires extra care. For that reason, we processed the TSI independently, and **built its composite** without resorting to proxy data, or TSI models. We also used slightly different approach, which is detailed in a companion paper [Dudok de Wit et al., 2017].

Table 1. Proxies used in addition to the original SSI data in order to fill in data gaps.

Name of proxy	Origin (Observatory)	relevant for
30.0 cm radio flux	Nobeyama/Toyokawa	UV
15.0 cm radio flux	Nobeyama/Toyokawa	UV
10.7 cm radio flux	Penticton/Ottawa	EUV/UV
8.2 cm radio flux	Nobeyama/Toyokawa	EUV/UV
3.2 cm radio flux	Nobeyama/Toyokawa	EUV/UV
sunspot darkening	Greenwich/SOON netw.	VIS

Table 2. List of the instruments used for making the composite, the version of the dataset, if available, as used in the SOLID composite; see Paper I for more details. The observation period corresponds to the data as they are used in the SOLID composite.

Instrument	Version	Wavelength range [nm]	Observation period [mm/yyyy]	Reference
GOES13/EUVS	n.a.	11.7–123.2	07/2006–10/2014	<i>Evans et al.</i> [2010]
GOES14/EUVS	n.a.	11.7–123.2	07/2009–11/2012	<i>Eparvier et al.</i> [2009]
GOES15/EUVS	n.a.	11.7–123.2	04/2010–10/2014	<i>Eparvier et al.</i> [2009]
ISS/SolACES	n.a.	16.5–57.5	01/2011–03/2014	<i>Schmidtke et al.</i> [2014]
NIMBUS7/SBUV	n.a.	170.0–399.0	11/1978–10/1986	<i>DeLand and Cebula</i> [2001]
NOAA9/SBUV2	n.a.	170.0–399.0	03/1985–05/1997	<i>DeLand et al.</i> [2004]
NOAA11/SBUV2	n.a.	170.0–399.0	12/1988–10/1994	<i>Cebula et al.</i> [1998]
SDO/EVE	5	5.8–106.2	04/2010–10/2014	<i>Woods et al.</i> [2012]
SME/UV	n.a.	115.5–302.5	10/1981–04/1989	<i>Rottman et al.</i> [1982]
SNOE/SXP	n.a.	4.5	03/1998–09/2000	<i>Bailey et al.</i> [2000]
SOHO/CDS	3.1	31.4–62.0	04/1998–06/2010	<i>Harrison et al.</i> [1995]
SOHO/SEM	n.a.	25.0–30.0	01/1996–06/2014	<i>Wiemann et al.</i> [2014]
SORCE/SIM	21	240.0–2412.3	04/2003–05/2015	<i>Rottman et al.</i> [2005]
SORCE/SOLSTICE	13	115.0–309.0	04/2003–05/2015	<i>Rottman</i> [2005]
SORCE/XPS	10	0.5–39.5	04/2003–05/2015	<i>Woods and Rottman</i> [2005]
TIMED/SEE-EGS	11	27.1–189.8	02/2002–02/2013	<i>Woods et al.</i> [1994]
TIMED/SEE-XPS	11	1.0–9.0	01/2002–11/2014	<i>Woods et al.</i> [1999]
UARS/SOLSTICE	11	119.5–419.5	10/1991–09/2001	<i>Rottman et al.</i> [1993]
UARS/SUSIM	22	115.5–410.5	10/1991–08/2005	<i>Brueckner et al.</i> [1993]

3. Methodology

The approach we advocate for this is a probabilistic one, in which, at each time step, we consider a weighted average of the different observations. These weights are set by the uncertainty of the observations, for which we thus need a metric that can be consistently applied to all the observations.

An important and novel feature of our approach is its multi-scale character. Simultaneous observations may agree on one particular time scale, and diverge on another one. Among the most debated examples is the difference between the SORCE/SOLSTICE and SORCE/SIM instruments at 240 nm [*Lean and DeLand*, 2012]: both show the same solar rotational variability, but disagree on the presence of a long-term trend. In such a case, direct averaging of the two will mix instrumental artifacts with the solar signal, rather than keep the best of each record. Likewise, it is important to take into account the disparity in the quality of the different datasets by assigning to each of them a time-dependent (and also time scale-dependent) uncertainty. **Another motivation for working scale-by-scale is the occurrence of artificial jumps in the composite whenever different datasets with data gaps are directly averaged.**

As we shall show below, the uncertainty of the datasets is a crucial ingredient of our composite because it allows to weight co-temporal observations at the same wavelength. Ideally, such uncertainties should be provided by the instrument teams. In practice, they are often absent or lack a crisp definition, and therefore cannot be meaningfully compared. Since we need to rely on the same definition for all datasets, we decided to use instead an independent estimation of the uncertainty (see Sec. 3.1) and use it to assign weights.

Our uncertainty is inherently scale-dependent; its high-frequency part (called precision) is the easiest to estimate. We also require a long-term uncertainty and call it stability (Sec. 3.2). The multi-scale approach allows mixing precision and stability at each scale in a natural way. The heuristic idea is as follows: at a specific timescale, every sample incorporates information over a time-interval that is proportional to its scale. As such, the uncertainty at this scale includes both the precision over this time-interval, as well as the stability over the same time-interval weighted by the timescale. As a consequence, the contribution of the precision to the uncertainty decreases with larger time-scales, while the contribution of the stability increases in proportion to the scale.

The creation of the composite involves a multiscale decomposition of the records, followed by a weighted average, and finally the recombination of the different scales. In practice, this procedure requires five steps, which we detail below.

The first direct spectral observations available are from the NIMBUS7/SBUV instrument, which started to provide data in November 8, 1978. Therefore, all datasets are extended back in time to that date and cover the time up to December 31, 2014.

3.1. Precision

In this work we use the term *precision* to quantify in each SSI dataset the high-frequency noise component that is routinely associated with random instrumental fluctuations. **The associated timescales are 3-4 days and below.** As described in Paper I, we determine the precision by using an adapted version of the wavelet noise estimator by *Donoho and Johnstone* [1995]. Let us note, however, that this estimator cannot properly quantify low frequency noise (**i.e. on time scales of several days and beyond**), and therefore is not suited for observations that are contaminated, for example, by red noise. For that purpose, we consider a second, and different estimator, i.e. the long-term uncertainty estimate as discussed in the following.

3.2. Long-term uncertainty

Beyond the uncertainty caused by the short-term noise, referred to as precision here, an additional uncertainty of the measured irradiance comes from the evolution of the instrument’s response in time. The instrument’s response can change because of the instrument’s (detector or filter) degradation, also called *ageing*, but also when changes in the operations of the spacecraft or instrument affect the measurement. When these effects are identified and/or understood, they can be corrected. However, it is not rare that SSI datasets have residual instrumental effects that remain in the signal as part of the real SSI time evolution. The uncertainty on the SSI dataset caused by these effects can be referred to as *long-term precision* or *stability*. We use here the term of stability.

It is out of reach to identify and correct *a posteriori* the instrumental effects affecting the time evolution of the observed SSI. Here, we estimate the uncertainty on SSI time series (i.e. the stability) by **comparing the latter to a two**

time-scale proxy model, and identifying patterns that cannot be reproduced by that very admissible model. More precisely, for each instrumental record $I(\lambda, t)$ we determine the high-frequency and low-frequency coefficients, a_i^{LF} and a_i^{HF} , respectively, of the following model

$$I(\lambda, t) = a_0 + \sum_{i=1}^n (a_i^{\text{LF}} P_i^{\text{LF}}(t) + a_i^{\text{HF}} P_i^{\text{HF}}(t)) \quad (1)$$

where the summation is over different solar proxies P_i and the superscript LF and HF represents the low and high frequency component, respectively. These components are determined using a running average of 108 days, *i.e.*, four solar rotations, a duration that is similar to the lifetime of active regions on the Sun. Using the more traditional 81 days to distinguish short and long timescale does not affect the results, and we found that, qualitatively, 108 days allows to better isolate the long term variations that can include instrumental trends.

It is known that using a 2-time-scale reconstruction model generally improves the fitting of observed time series [Woods *et al.*, 2000]. To build this admissible proxy model we use 6 proxies: the Daily Sunspot Area [Wilson and Hathaway, 2006, DSA], the Mg II index [Skupin *et al.*, 2005] and the radio fluxes at 3.2 cm, 10.7 cm, 15 cm, and 30 cm [Dudok de Wit *et al.*, 2014]. Clearly, the larger the number of simultaneous proxies, the larger the number of degrees of freedom in the model, and the more the model might reproduce non-solar variations. One can therefore decide to be more or less allowable in asking the true SSI to be reproducible by proxies.

Once the observed time series is fitted with this proxy model over the whole record, **we estimate its stability empirically by**

$$s(\lambda, t, \tau) = |\text{slope}(I_{\text{obs}}, t) - \text{slope}(I_{\text{fit}}, t)|, \quad (2)$$

where the slope is computed over a chosen time interval τ . The stability is therefore time-dependent and it is given in

$\text{Wm}^{-2}\text{yr}^{-1}$ (or, **alternatively**, in $\% \text{yr}^{-1}$). This stability represents the ability of a proxy model, adjusted at each time series, to reproduce the observed slope computed over a dedicated time interval τ , which thus also sets the time scale at which the stability is considered. Here we estimate it for a time scale of $\tau = 3$ years in order to focus on trends.

3.3. Temporal extension of SSI datasets

The multi-scale decomposition can only be performed on regularly sampled time series with no missing data. Following the pre-processing stage that is described in Paper I, our input data are SSI time series with daily values, with one record for each 1 nm wavelength bin.

Prior to decomposing the data, we extend each dataset over the interval going from November 8, 1978 to December 31, 2014 in order to make all records of equal length. **This preparatory step has not been covered Paper I.** We fill in the data gaps by expectation-maximization [Dudok de Wit, 2011]. This technique exploits the correlation between specific bands of the SSI and the above-mentioned solar proxies to replace missing values by a linear combination of the latter, after prior decomposition into two different time scales with a cutoff at 81 days. Two separate time scales are needed to properly handle the possibility for the same solar features, such as sunspots, to cause darkening (in the visible), and brightening (in the UV). The 81-day cutoff is commonly used to separate fast variations from slow ones [Woods *et al.*, 2000].

After extending the SSI datasets, we end up with one large table that has 13202 time steps, and as many columns as there are individual wavelengths multiplied by the number of instruments, *i.e.* typically 10^7 records. Let us stress that this temporal extension is required only to decompose the data into different time scales and as such is a technical necessity; the interpolated or extrapolated values enter the composite with a lowered weight, as they are assigned a higher uncertainty.

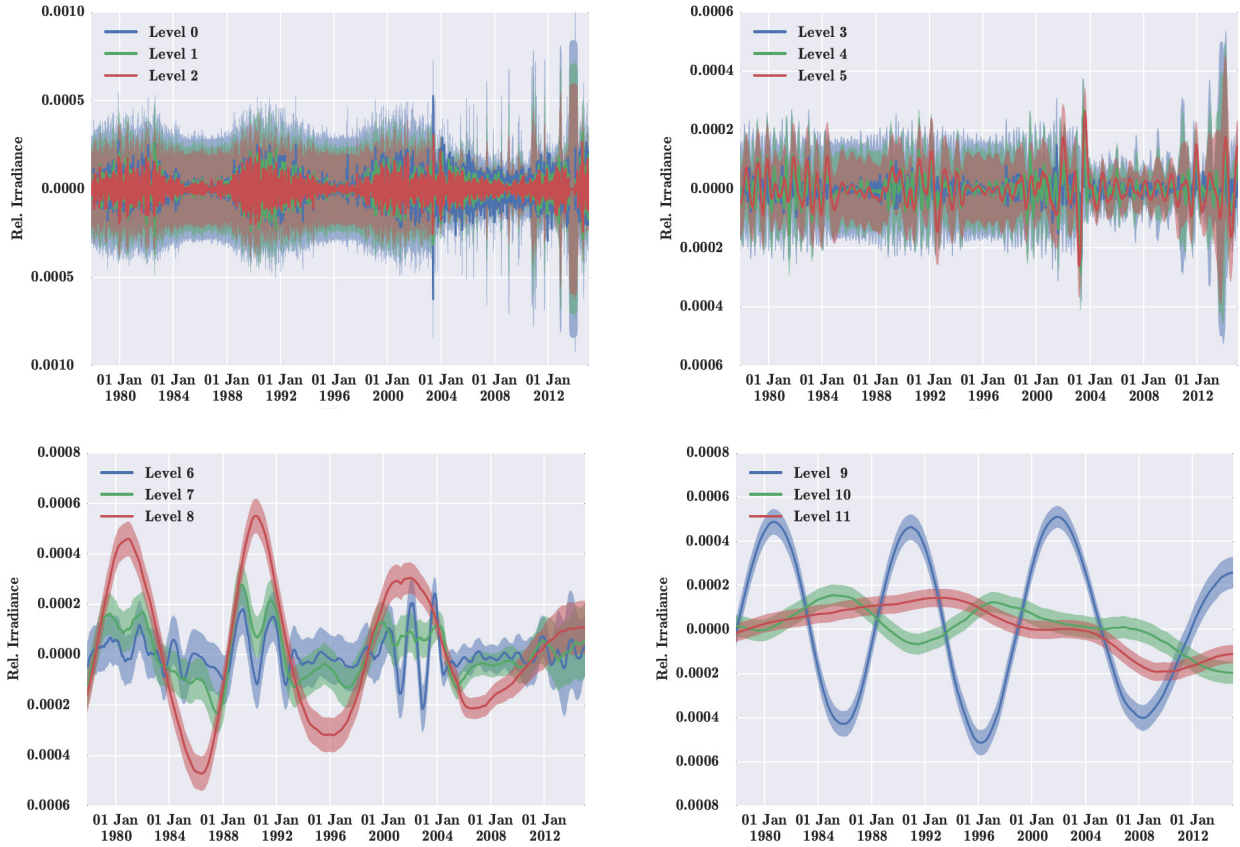


Figure 1. Illustration of the multiscale decomposition of the **extended** SORCE/SOLSTICE data set at 220.5 nm for Levels 0, 1, and 2 (top left), Levels 3, 4, and 5 (top right), Levels 6, 7, and 8 (bottom left), and Levels 9, 10, and 11 (bottom right). Level 12 with a scale of $a^{12} = 4096$ days is not shown as it represents a quasi-constant offset.

3.4. Multiscale decomposition of the SSI records

The natural tool for decomposing time series into different time scales is the wavelet transform, which decomposes each time series into $J + 1$ different records of identical length. Their characteristic scales $a = 2^j$ are numbered by their level $j = 0, 1, 2, \dots, J$. The largest level J is the largest integer such that $a_J = 2^J \leq d$, where d is the duration (in days) of the record.

This wavelet decomposition can be performed in different ways. We need an undecimated (or redundant) transform, so that a precise time stamp can be assigned to each wavelet coefficient. The transform should also be orthogonal in scale, so that operations performed on the wavelet transform at one particular scale do not affect neighbouring scales. The solution we advocate

here, which is widely used in astrophysics, is based on the one-dimensional *à trous* wavelet transform [Starck *et al.*, 2010].

We decompose the time series $d_\lambda(t)$ at wavelength λ and time t into multiple orthogonal time series $d_{j,\lambda}^*$ by convolving it with a Gaussian kernel $\mathcal{G}(t)$ of width (scale) $a = 2^j$, as given in Eq. 3:

$$d_{j,\lambda}^*(t) = d_\lambda(t) \star \mathcal{G}(t, 2^j). \quad (3)$$

For the lowest level $a = 1$ we just take $\mathcal{G}(t, a = 1)$ as the identity function on t , so that

$$d_{0,\lambda}^*(t) = d_\lambda(t) \quad (4)$$

Boundaries are handled by mirroring the data on each side. The wavelet transform at level j now reads

$$d_{j,\lambda} = \begin{cases} d_{j,\lambda}^* - d_{j+1,\lambda}^* & \text{if } j < J \\ d_{j,\lambda}^* & \text{if } j = J. \end{cases} \quad (5)$$

One advantage of this method is the easy recovery of the original time series d_λ simply by adding up its wavelet transforms $d_{j,\lambda}$. Indeed,

$$d_\lambda = \sum_{j=0}^J d_{j,\lambda} . \quad (6)$$

At each level j , both precision and stability contribute to the combined uncertainty. While the precision decreases with larger scales due to the noise averaging out over a larger time-period, the uncertainty associated with the stability increases towards larger scales. What would be really needed here is an estimate of the uncertainty versus time-scale. For the TSI *Dudok de Wit et al.* [2017] find the power spectral density of the uncertainty to be **proportional to** the inverse of the frequency (with frequency = $1/a$), as with so-called 1/f noise, or shot noise. This scaling may not apply to the SSI, whose instruments have different noise characteristics. For that reason, we rely **here on the precision and an empirical stability estimate to obtain the uncertainty** at all scales.

We estimate the uncertainty $\epsilon_{\lambda,j}(t)$ at level j by using a weighted spectrum of the squared precision $\epsilon_\lambda^2(t)$, together with a weighted and scaled sum of the stability $s_\lambda(t)$, where the weights are the Gaussian kernel for both precision and stability and the stability is scaled proportional to the kernel width a .

$$\epsilon_{j,\lambda}(t) = \sqrt{(\epsilon_\lambda(t) \star \mathcal{G}(t, 2^j))^2 + (a s_\lambda(t) \star \mathcal{G}(t, 2^j))^2} \quad (7)$$

As an example of the decomposition of the SSI data records Figure 1 shows the SSI time series and their respective uncertainties for Levels 0, 1, 2 (top left), Levels

3, 4, 5 (top right), Levels 6, 7, 8 (bottom left), and Levels 9, 10, 11 of the **extended** SORCE/SOLSTICE time series (**the result after applying the steps as described in Sec. 3.3**), at 220 nm.

In the following we keep the uncertainties for each time scale constant in time, although the method can easily handle time-varying uncertainties. **In particular, we can incorporate information from the instrument teams and, for example, increase the uncertainty during times when the spacecraft has off-pointing problems.** Such adjustments can also be made at specific time-scales if the observations are known to be affected by band-limited noise. In future version of the dataset, this will be considered, for example for observations by ENVISAT/SCIAMACHY. This instrument adequately reproduces solar variability at short time scales (days to months) but its long-term variability suffers from several interruptions that occurred during its lifetime. When several cotemporal observations with differing variations are averaged, it is eventually their uncertainty which determines how each of them will be weighted. Therefore, it is of great importance to properly estimate such uncertainties by injecting physical information in them. In doing so, we decouple the scientific problem (*What prior information goes into the composite?*) from the statistical one (*What is the best way of making the composite?*). Clearly, the first problem is open-ended, and here we focus on the second one.

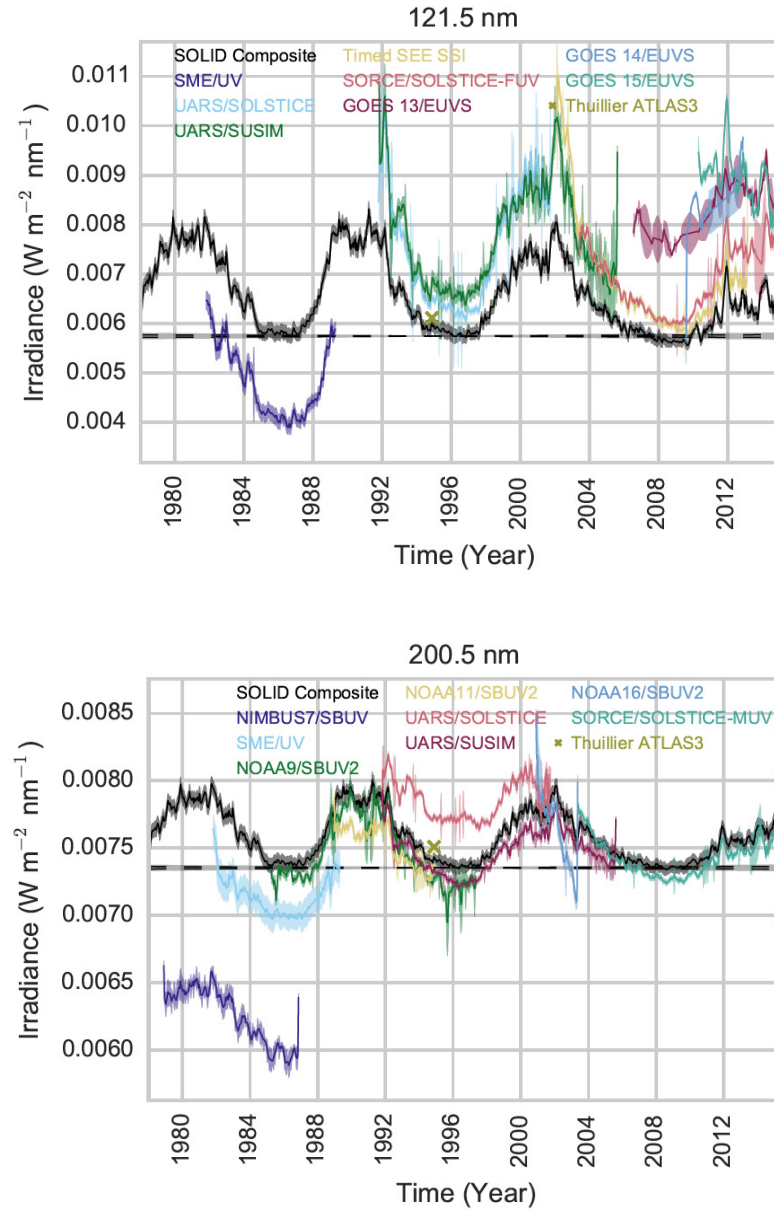


Figure 2. SOLID composite along with the individual irradiance datasets that are used to produce it, shown at 121.5 nm (top panel) and 200.5 nm (bottom panel).

3.5. Averaging the wavelet transformed data

Once we have performed the multiscale decomposition, $d_{j,\lambda}$, of the SSI for each level j (and instrument I , not indicated here), we determine the composite by maximizing its likelihood, which is equivalent to mak-

ing a weighted average of the values of $d_{j,\lambda}$; the weights are given by the inverse variance of each record. **This is done scale-wise.** The uncertainty of the composite can be obtained by classical error propagation. Thanks to the orthogonality of the wavelet transform, uncertainties at different scales can be processed separately, and added as if they were independent.

The equations to derive the scale-wise components, \bar{d}_j , of the composite for each level j and its respective uncertainties, $\bar{\epsilon}_j$, again for each level j are

$$\bar{d}_j = \sum_{i \in I} d_{i,j} w_{i,j} \quad (8)$$

$$\bar{\epsilon}_j = \left(\sum_{i \in I} \epsilon_{i,j}^2 w_{i,j}^2 \right)^{1/2} \quad (9)$$

$$\text{where } w_{i,j} = \frac{\epsilon_{i,j}^{-2}}{\sum_{k \in I} \epsilon_{k,j}^{-2}} .$$

are the weights for level j and instrument i for the wavelength of interest, and $\epsilon_{i,j}$ is the corresponding **uncertainty** at level j . As described in Paper I, we assume purely uncorrelated noise. Therefore, for interpolated and proxy-extended data, after flagging them, we increase the **uncertainty** to the $1\text{-}\sigma$ standard variation of the actual variation of the SSI data of that dataset **scaled with the \sqrt{N} , with N being the number of missing days determined from the onset and end of the data gap**. This results in a substantially lower weight of the interpolated and extrapolated data values in the composite.

3.6. Combining the reconstructed scales

To obtain the final composite, the components of the composite are summed-up scale-wise (i.e. over all levels), as given in Eq. 6. The uncertainty, ϵ_{comp} , of the final composite is obtained by error propagation

$$\epsilon_{\text{comp}} = \left(\sum_{j=0}^J \bar{\epsilon}_j^2 \right)^{1/2} . \quad (10)$$

3.7. Absolute scale of composite

The above procedure results in a time series that combines all available instruments while taking into account the uncertainty of the individual datasets, with both precision and stability. However, the absolute scale also needs to be set. To do so, we re-calibrate the composite to the ATLAS 3 reference spectrum by *Thuillier et al.* [2004] and, at the same time, constrain it to the TSI composite by *Dudok de Wit et al.* [2017] for that particular day when the reference spectrum was measured.

First, we re-scale the ATLAS 3 reference spectrum to make its integrated spectrum match the value of the TSI composite for the day of the ATLAS 3 observation. For this, we first use a black-body model to the unobserved infrared tail of the spectrum, and successively scale the integrated spectrum to the TSI composite. Secondly, we use this modified ATLAS 3 spectrum to re-scale the value of the SOLID composite such that it matches the reference spectrum for its date of the observation.

4. Preliminary observational composite

In the following, we present the **first, preliminary, observational SSI composite** for different wavelengths **and daily resolution** along with the UV datasets that went into the production of the composite. **For practical reasons we set the spectral resolution to 1 nm, but at the longer wavelength ranges (starting at 623 nm) we have a coarser resolution of 2 nm and higher.** Figure 2 shows the observational composite and the available observations it is made of for 121.5 nm (top panel) and 200.5 nm (bottom panel). As expected, the composite closely corresponds to a weighted average of the individual records. Note that most records agree well on their short-term variability, and less so on the long term, hence the importance of merging them scale-wise. Thanks to this multi-scale approach, and to the use of solar proxies for filling in gaps, the stability of the composite is better than what would have been obtained by simply daisy-chaining the records. Most observations and the composite agree better at short wavelengths, where the larger relative variability results in a more favorable signal-to-noise ratio. There are some exceptions, however. At 121.5 nm, for example, the solar cycle variability of SME exceeds that of the other instruments, which suggests the needs for a correction, as already reported by *Woods et al.* [2000]. **One side effect of the use of proxies is their small but significant contribution to the composite. This is evident, for example, in the variation of the Lyman- α line: the large excursion observed in mid-1992 is smaller in the composite than it is in the original observations from UARS/SUSIM. One could easily reduce this contribution from proxies and even set it to 0 if there are cotemporal observations available, as we did for making the TSI composite [Dudok de Wit et al., 2017]. However, for spectral bands that suffer from fragmented observations or from a low signal-to-noise ratio (especially above 300 nm), proxies help constrain the composite.**

Figure 3 compares the observational composite with various existing reconstructions and the SORCE Solar Spectral Irradiance dataset¹ for the following spectral bins: 120–122 nm, 130–200 nm, 200–242 nm, 242–310 nm, 300–350 nm, 350–400 nm, **400–500 nm, and 500–600 nm**. The reconstructions we consider are from the semi-empirical SATIRE-S model [*Yeo et al.*, 2014], the empirical NRLSSI1 model [*Lean*, 2000] and its more recent version NRLSSI2 [*Coddington et al.*, 2016], **and direct observations from SORCE/SOLSTICE and SORCE/SIM as part of the SORCE Solar Irradiance dataset. In this dataset, SIM observations are used from 310 nm onward.**

The first message coming from this figure is the good agreement between the composite and the three mod-

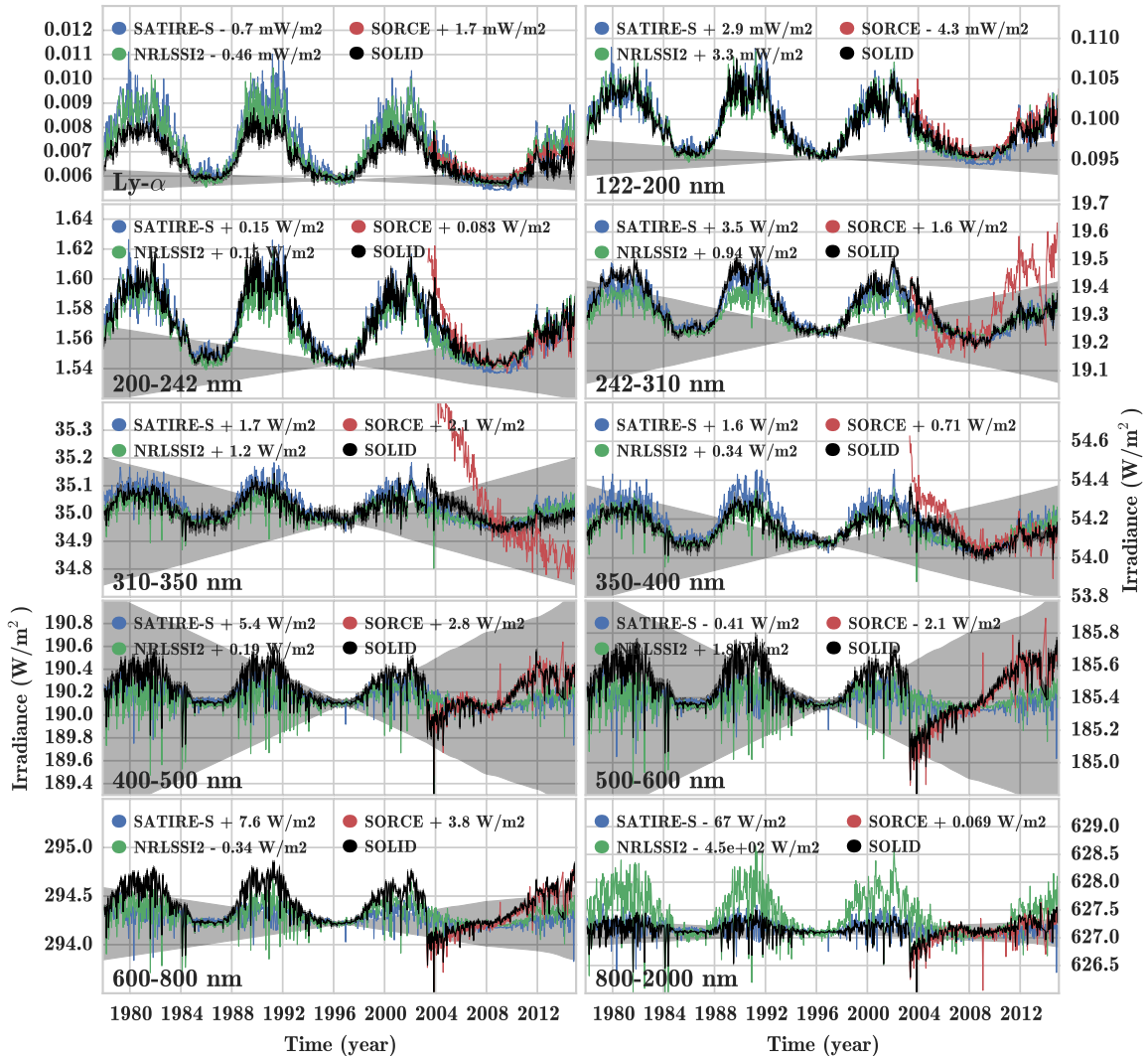


Figure 3. Illustration of the observational SOLID composite (black line), model reconstructions from NRLSSI1 (green line) and SATIRE-S (blue line), and since 2003, the observations from the SORCE mission (red line), with SIM being used from 310 nm onward. These data are integrated over the following spectral intervals: Top row: 120–122 nm (left) and 122–200 nm (right); second row: 200–242 nm (left) and 242–310 nm (right); third row: 310–350 nm (left) and 350–400 nm (right); fourth row: 400–500 nm (left) and 500–600 nm (right); bottom row: 600–800 nm (left) and 800–2000 nm (right). The numbers in the legend given after the name of each dataset indicate the value for the absolute scaling of each of the datasets to the SOLID composite. The gray-shaded area illustrates the cumulated uncertainty of the SOLID composite starting from January 1, 1996.

els for the spectral ranges from 120 – 310 nm (the top 4 panels), for none of which it significantly deviates from, given its confidence intervals. This highlights the difficulty in assessing differences between these models when they are as poorly constrained by the observations. **This also highlights** the need for a sound assessment of the confidence intervals. Clearly, future improvements of the composite should not depend on the individual datasets alone, but also on re-

finements that will be made in the precision and stability estimates.

The second message is the unusual solar cycle variability of the composite after 2003, when SORCE/SIM data start being used. As long as there are alternatives to these observations (i.e. for 200–400 nm, and at lower wavelengths), the composite remains in good agreement with the models. At **longer** wavelengths, when SORCE/SIM is the only observing instrument,

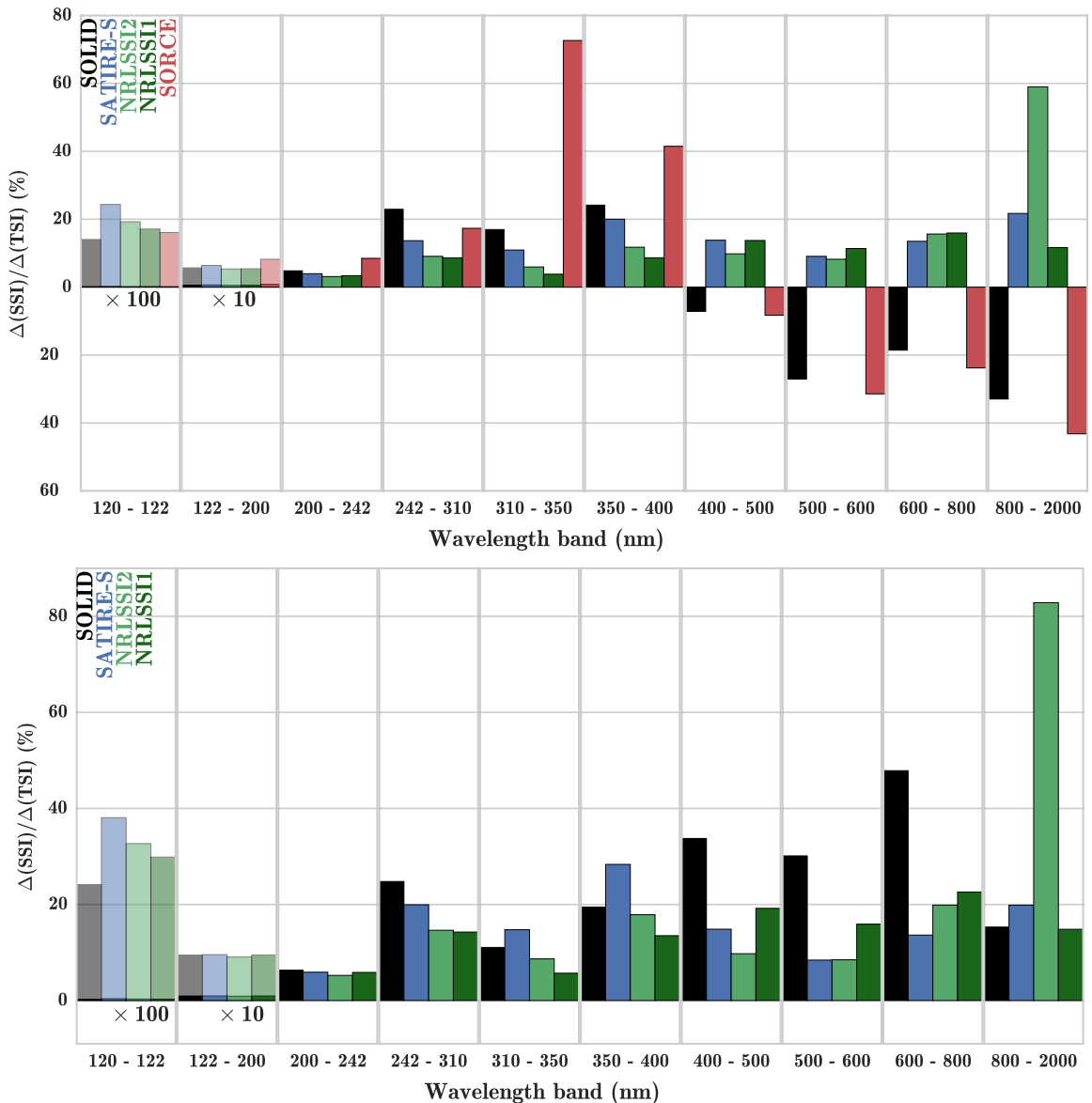


Figure 4. Upper Panel: Change of the annual mean of SSI in different spectral bins from 2003 to 2008 with respect to the variation in TSI for the same time interval. Shown are the relative changes for SOLID.beta (black), SATIRE-S (blue), NRLSSI1 and NRLSSI2 (dark and light green), and the SORCE composite (red) **with SIM being used from 310 nm onward**. For better illustration, the first and second spectral bin, i.e. for 121–122 nm and 130–200 nm is multiplied by a factor of 100 and 10, respectively, additionally shown in partly transparent color. Lower panel: Same as upper panel, but for the annual means of 1989 and 1996, for which no SORCE data is available.

the discrepancy with the models, and with former solar cycles becomes striking, which is in line with previous studies by *Cahalan et al.* [2010] and *Ermolli et al.* [2013]. As the observations from SIM data are the only to cover wavelengths longward of 410 nm we consider that particular dataset further in Sections 5 and 6.

Figure 3 also illustrates the precision and stability of the composite as derived in Paper I and Sec. 3.2 by showing how it increases in time when moving away from a date that has been arbitrarily chosen to be in the center of the in-

terval. The figure thereby reveals how weak the solar cycle variability becomes, as compared to the uncertainty, when moving from the UV to the visible. Note that this representation may actually overestimate the true long-term stability, which does not increase that fast in time. Indeed, for the TSI, *Dudok de Wit et al.* [2017] find that the stability does not increase linearly with time and so these commonly-used fan-shaped structures may need to be revised in future work.

A different representation of the composite is given in Figure 4, which shows the annual mean of the SSI vari-

ation relative to the TSI variation for the spectral intervals 120–122 nm, **122–200 nm**, **200–242 nm**, **242–310 nm**, 310–400 nm, 400–500 nm, 500–600 nm, 600–800 nm, and 800–2000 nm. **We note that the variability of the high-resolution spectrum shows much more detail**, [see *Fontenla et al.*, 2015, Fig. 14] and [see *Ermolli et al.*, 2013, Fig. 6]. To better illustrate the variation of the SSI, Figure 4 shows the change in SSI relative to the change in TSI for the declining phase of solar cycle 23 (annual means from 2003 to 2008 – upper panel) and solar cycle 22 (annual means from 1989 to **1996** – lower panel). For better visibility, the 120–122 nm and 150–200 nm spectral bins are scaled with a factor of 100 and 10, respectively.

For both time intervals, the variation in the Lyman- α line (i.e. the 120–122 nm band) is lowest for the SOLID composite, and highest for SATIRE-S, with NRLSSI2 and NRLSSI1 being in between. **The reason for this is the absence of rescaling of the SME data, whose values are approximately 1.5 times smaller than its expected level** [*Woods et al.*, 2000]. The absence of correction explains the lower solar cycle variability of the SOLID composite as compared to the Lyman- α composite by *Woods et al.* [2000]. We stress again that we took the approach to not change the original observations, with all the consequences this might have.

For the 130–200 nm and 200–242 nm wavelength ranges the variation of all datasets is very close, with a slightly higher variation for the SORCE dataset. Moreover, for the wavelength range 242–310 nm and both time intervals the SOLID composite gives the highest variation, while SATIRE-S, NRLSSI2 and NRLSSI1 give a lower variation.

Then, for the 310–350 nm and 350–400 nm wavelength ranges and for the 2003–2008 time interval the SOLID composite again gives the highest variation, and the variation is successively lower for SATIRE-S, NRLSSI2 and NRLSSI1. In this case, for both spectral ranges, the SORCE variation gives a considerably larger variation than all other datasets. For the 1989–**1994** time interval the variation of the SOLID composite is between the SATIRE-S and NRLSSI2.

And finally, for the 2003–2008 time interval, and the 400–500 and 500–600 nm range, the SOLID and SORCE composite give a negative solar cycle variation, while SATIRE-S, NRLSSI2 and NRLSSI1 show a variation in phase with the solar cycle. The reason is that for this time frame and wavelength range the only dataset available is SORCE/SIM. Therefore, the SOLID composite follows the overall variation as observed by the SORCE/SIM instrument. Whether the unusual variation reported by SIM is real or not is still an open question.

5. Validation of SSI composite

Let us now concentrate on recent observations when SORCE was operating. For that period, the SOLID composite compares well with the observations made by the PREcision Monitoring Sensor [*Schmutz et al.*, 2009] onboard the PICARD mission [*Thuillier et al.*, 2006]. Figure 5 shows the SOLID composite convolved with the broadband filters of the PREMOS instrument and the PREMOS observations [*Cessateur et al.*, 2016] centered at 210 nm (left panel) and 215 nm (right panel). The agreement between both time series for the two wavelength channels is excellent. In particular the temporal evolution of the rotational variability is in very good agreement. Some deviation after however can be seen in the 210-nm channel after 05/2012, and in the 215-nm channel from early 2013 onward. At 210 nm *Cessateur et al.* [2016] find a similar deviation when comparing the PREMOS data with SORCE/SOLSTICE (see their Fig. 13). **We emphasize here that for the comparison shown in Fig. 5 both datasets are in absolute values, and both the PREMOS channels and the SOLID composite are not detrended, i.e. they include the long-term trend. Due to the limited spectral coverage of the PREMOS data this can only be considered as a limited validation.**

Clearly, an issue **with the composite is the variability in the 400–500 nm and 500–600 nm spectral bins.** The only observations available for these spectral bins are from the SIM instrument, and these data have already been discussed controversially, see e.g. [*Haigh et al.*, 2010]. While *Merkel et al.* [2011] conclude from their analysis of observations from the Microwave Limb Sounder (MLS) and Sounding of the Atmosphere using Broadband Emission Radiometry (SABER) and Global climate modeling that a higher UV is consistent with the different ozone solar cycle trends across the stratopause, *Ball et al.* [2016] argue that a higher UV variability is incompatible with the Stratospheric Water and Ozone Satellite Homogenized (SWOOSH) and the Global Ozone Chemistry And Related trace gas Data records for the Stratosphere (GOZCARDS) datasets.

From Figs. 2 and 3 it becomes clear that the overall trend in the SIM data cannot be reproduced by the multi-scale analysis using the proxy data, as discussed above. On the one hand, it could be argued that the approach to extend the observational datasets, as described in Section 3, has limitations. In addition, the reason might be that the degradation correction of the SIM data is incomplete. As pointed out by *Ball et al.* [2016] the observed SSI trend **of the SIM instrument** is inconsistent with observed ozone trends. This highlights the need to add **additional** constraints to future versions of the SOLID composite.

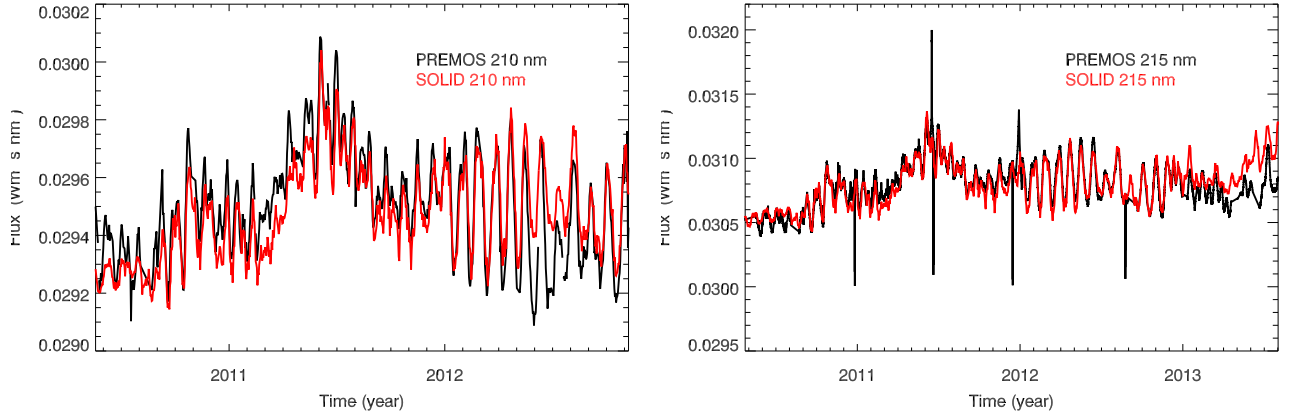


Figure 5. Comparison of the SOLID composite (red line) with the PREMOS observations (black line) for the 210-nm channel (left panel) and 215-nm channel (right panel).

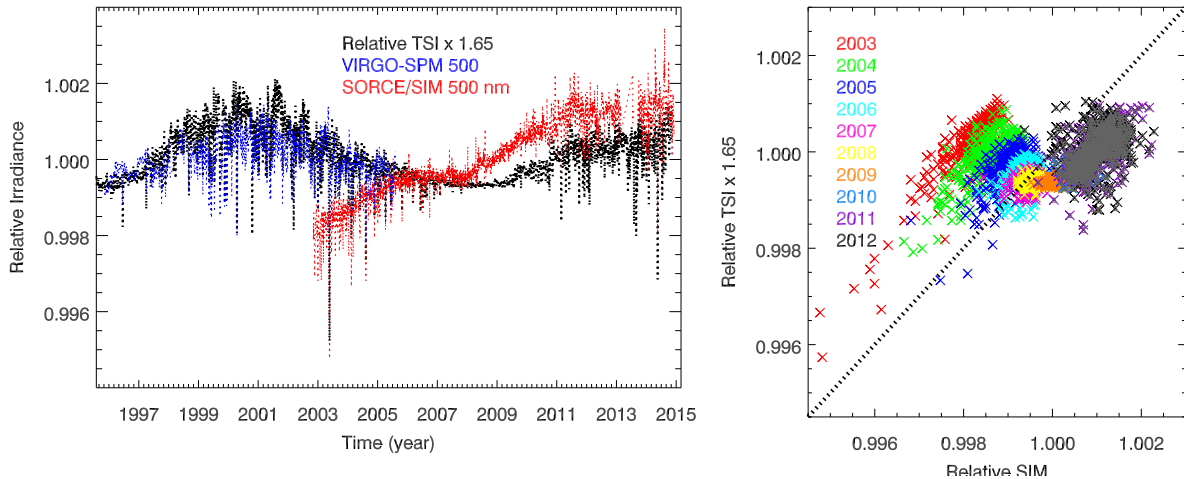


Figure 6. Left panel: comparison of the scaled TSI (black), the VIRGO-SPM 500-nm channel (blue), and SORCE/SIM at 500 nm (red). Following [Wehrli *et al.*, 2013] the relative TSI variability has been multiplied by the regression coefficient 1.65. **Right panel: scatter plot of the relative scaled TSI variation (black line in left panel) and the scaled SIM observations (red curve in left panel).** The color code indicates the different years when the observations were taken. The dotted line is the line with slope equals 1, i.e. the expected gradient following Wehrli *et al.* [2013]. The datapoints for the years 2010 to 2012 (blue to black) that are employed in the revised SSI composite are additionally overlaid with grey triangles.

In order to investigate this **further** we use an additional independent dataset that is not employed in the composite itself. First, we use data taken with the VIRGO-SPM instrument [Fröhlich *et al.*, 1995] onboard SOHO. Wehrli *et al.* [2013] investigated the correlation of the relative annual variability of VIRGO-SPM channels and TSI over the time frame of 2002 to 2012. Interestingly, the relative variation as observed with the VIRGO-SPM channel at 500 nm gave a statistically significant positive correlation with the relative variation of TSI, with a regression factor of 1.65 and a correlation coefficient of $r^2=0.72$.

Figure 6 shows the relative variation of the TSI scaled **with the factor 1.65** (black) along with the relative variation at 500-nm channel of VIRGO-SPM, and the

relative variation at 500 nm as observed with SIM (red). The discrepancy between the observations from SIM and the scaled TSI variation suggests that – at least for the early phase of the SORCE mission until approximately **2010** – **a strong part of the variation seen by SIM may be instrumental.** To further illustrate this, Fig. 6 (right panel) shows the corresponding scatter plot of the relative scaled TSI (black line in left panel) and the relative SIM observation at 500 nm (red line in left panel) for the years from 2003 to 2012, for which SIM observations are available. The color code illustrates the different years of the time series. This plot indicates that the behavior of SIM changed around 2010. While its SSI observations continuously increase, the TSI first decreases from 2003 until

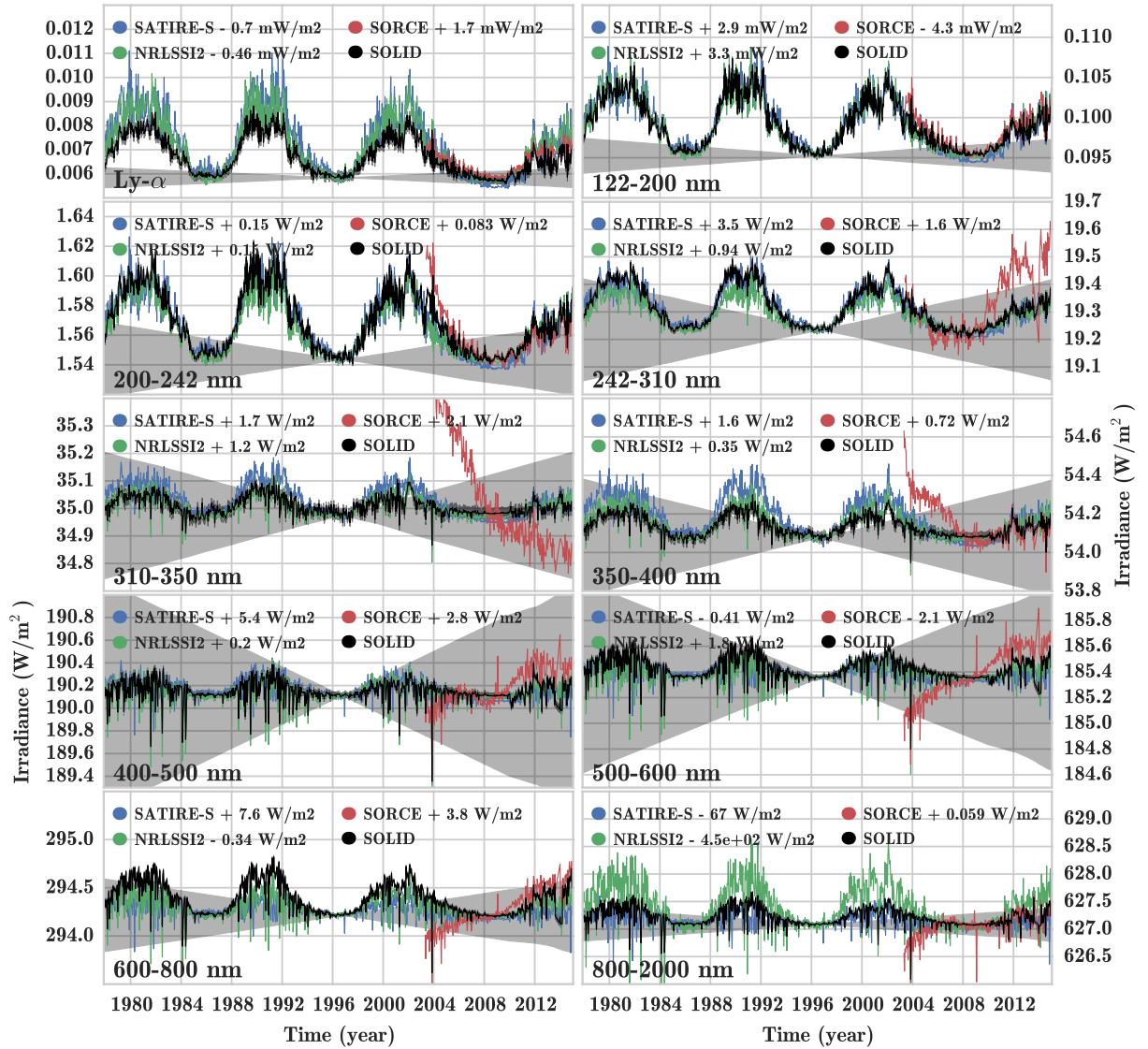


Figure 7. Same as Fig. 3 but for the final SOLID composite.

the solar minimum in 2008 and then increases with the onset of Solar Cycle 24. From *Wehrli et al.* [2013] we know that the SSI at 500 nm is - with high statistical significance - in phase with the TSI solar cycle variability. Therefore, we conclude that the SIM data before 2010 are likely to be unreliable and disregard them for our purposes. SIM seems to have recovered after 2010 and provides observations that are in phase with the TSI variability. So, for the remainder of this paper we shall only use SIM data from January 1, 2010 onward.

6. Final SSI composite

Based on the discussions in Sec. 5 we now provide the final version of the observational composite by only using SIM observations after 1 January 2010. All other observational datasets are kept as described above. Figures 7 and 8 show the relative contribution of the SSI in specific spectral ranges to the TSI. The figures are the same as Figs. 3 and 4 but for the final composite. Not surprisingly, the SOLID composite now also shows a variation from 400 nm onward that is in phase with the solar cycle. In the spectral range between 200–242 nm the SOLID composite is slightly higher than the models, but lower than the **SORCE** composite. For the spectral bins from 310–350 nm and 350–400 nm, the SOLID composite gives the lowest variation of all four (positively correlated datasets) datasets. For 400–500 nm the SOLID composite is slightly lower than the three models. The **SORCE** dataset shows a negative SSI contribution to TSI in this and all other spectral bins longward of that. For 500–600 nm the SOLID composite is almost identical to **NRLSS1**, while both **SATIRE** and **NRLSSI2** give a slightly lower SSI variation. Then, for 600–800 nm the SOLID composite leads to the highest SSI contribution to the TSI variation. And finally, from 800–2000 nm SOLID is slightly higher than **SATIRE** while **NRLSSI2** largely exceeds the other datasets, and **NRLSSI1** gives the lowest SSI contribution.

Overall, the SOLID composite is an extremely valuable dataset to understand how to combine disparate observations, and test SSI models, as well as solar proxies. However, this dataset should be considered as the first step, **with multiple possible improvements**.

While the observational composite is consistent from a statistical point of view, future versions require additional physical knowledge to further reduce the impact of uncorrected instrumental artifacts. One obvious way of moving in that direction would be to build a hybrid dataset that combines observational and modelled SSI. Another important step is to correct some of the observational datasets for instrumental artifacts.

A thorough evaluation of the results and comparisons to observations will help not only to assess differences, weaknesses and strengths of the models, but also to advance knowledge and further understanding of the physical mechanisms that govern the influence of the Sun to the Earth's atmosphere and climate.

7. Sensitivity of atmospheric heating to the SSI dataset

7.1. Radiation scheme

To demonstrate the effects of the different spectra on the atmospheric energy balance, we performed calculations with the **LibRadtran v.2.0** high resolution model [*Emde et al., 2016*], which is a library of radiative transfer equation solvers widely used for UV and heating rate calculations (for a full list of relevant publications see <http://www.libradtran.org>). **LibRadtran** was configured with the pseudo-spherical approximation of **DISORT** solver, which accounts for the sphericity of the atmosphere, running in a six-streams mode. Calculations pertain to a cloud- and aerosol-free tropical atmosphere (0.56°N), the surface reflectivity is set to 0.1 and the effects of Rayleigh scattering are enabled. The atmosphere is portioned into 80 layers extending from the surface to 80 km. Here we show signals above 23 km. The model output is daily averages of spectral heating rates from 120 nm to 700 nm with a 1 nm spectral resolution for the 15th of January, calculated according to the recommendations for the Radiation Intercomparison of the Chemistry-Climate Model Validation Activity (**CCMVal**)². Calculations were performed for **NRLSSI2**, **SATIRE-S**, **SORCE** and **SOLID** for solar maximum (2003) and solar minimum (2008) years using the resolved solar spectra. That is in the 200–310 nm spectral band, which is important for ozone formation and absorption, **NRLSSI2**, **SORCE** and **SOLID** come in 1 nm bins whereas the resolution of **SATIRE-S** is 1 nm up to 289.5 and 2 nm thereafter. For this study the parts of the spectra that come with a coarser spectral resolution than 1 nm are interpolated linearly. As pointed out by *Deland and Cebula [2012]* a different resolution than the **SORCE** native resolution could introduce additional effects in the heating rate calculation for that dataset.

The integrated difference between the solar maximum and solar minimum conditions is shown in Fig. 4a for specific spectral intervals. Since we are primarily concerned here with the direct effect of atmospheric heating, the ozone feedback is not considered and ozone mixing ratios are kept constant to the climatology of a standard atmosphere in all calculations. The ozone response to solar cycle variations in SSI and the impacts of the use of **NRLSSI** and **SORCE** spectral irradiance as forcing functions has been reported by *Swartz et al. [2012]*, who provide a detailed evaluation of the individual mechanisms of atmospheric response to solar cycle variations in SSI through direct solar heating and photolysis.

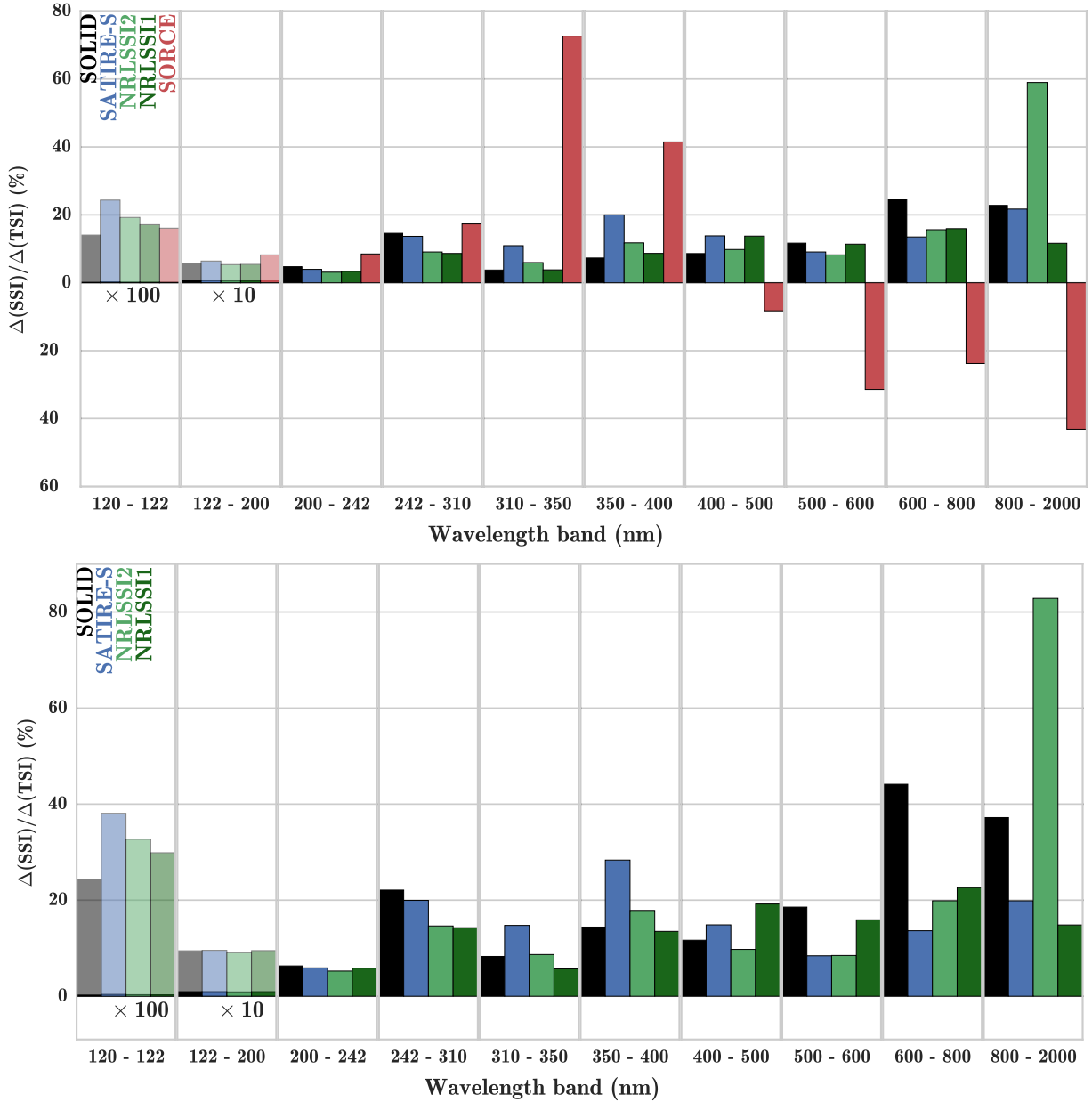


Figure 8. Same as Fig. 4 but for the final SOLID composite.

7.2. Effects in the Earth’s atmosphere

Figure 9a compares solar cycle anomalies of total spectral heating rates (K/day), integrated from 120 to 700 nm, for all SSI datasets. The solar cycle signature in heating rates is characterized by two distinctive maxima in the stratopause (50 km) and upper mesosphere (above 70 km), resulting from the larger solar fluxes available for absorption by O₃ and O₂. The SOLID dataset introduces a solar-cycle related heating of about 0.12 K/day at the stratopause, which is considerably stronger than NRLSSI2 but weaker than SOLAR. The difference in heating rates between SOLID and SATIRE-S is not statistically significant, if the uncertainty in the SOLID irradiances is taken into account

(gray shading in Fig. 9a). The respective uncertainty of heating rate anomalies ranges from 0.09 to 0.14 K/day. **It should be noted that since UARS/SUSIM and UARS/SOLSTICE were taking measurements in 2003, their smaller amplitude for solar cycle variations below 310 nm moderates the SOLID forcing term relative to the SOLAR-only forcing. This leads to weaker heating in the stratosphere between SOLID and SOLID.beta versions.**

The solar cycle heating in the mesosphere is related to absorption in the Lyman- α and the Schumann-Runge bands (175 to 200 nm) (Fig. 9b and Fig. 10). More specifically, irradiance changes in wavelengths between 130 and 200 nm contribute about 30-50% of the total solar heating above 70 km in SOLID, with weaker contribution at higher altitudes as the strong heating in

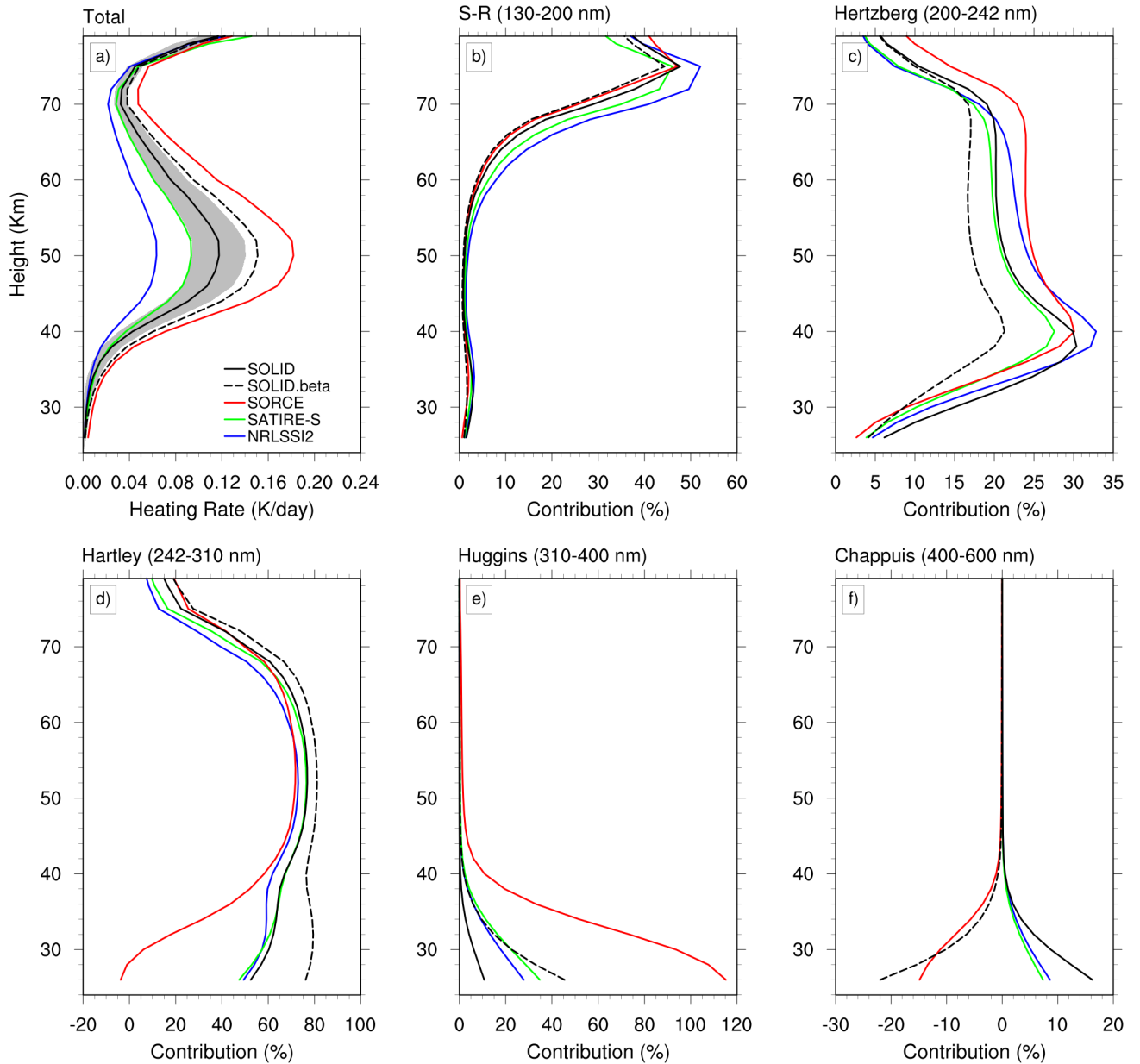


Figure 9. Comparison of solar heating rate differences (K/day) between solar minimum (2008) and maximum (2003) for the **SOLID (black solid)**, **SOLID.beta (black dashed)** composites, NRLSSI2 (green), SATIRE-S (blue) and SORCE (red). Panel a) shows the integrated (120–700 nm) heating rate anomalies whereas panels b)–f) show the relative contribution (%) of the 130–200 nm, 200–242 nm, 242–310 nm, 310–400 nm and 400–600 nm intervals to the integral. Grey shading indicates the uncertainty in the total heating rate anomalies from the SOLID SSI uncertainty (corresponding to the grey-shaded areas in Fig. 3).

Lyman- α is not a part of the integral in Figure 9b. NRLSSI2 shows a slightly stronger contribution in this region whereas SOLID.beta shows the weakest. Figure 9 indicates that anomalous heating in the stratosphere occurs primarily from 220 nm to 310 nm, as expected from the strong ozone absorption in the Hertzberg continuum (200 to 242 nm) and Hartley bands (242 to

310 nm). The heating rate anomalies in the stratosphere in the Hartley bands are **lower in SOLID compared to NRLSSI2 and SATIRE-S**, whereas SORCE shows the strongest anomalies at all heights and spectral bins except from about 290 to 310 nm (Fig. 10). **Nevertheless, SSI changes in this spectral region contributes almost the same to the total heating in all datasets (Fig. 9c,d).**

A notable difference of SOLID compared to the other spectra is the strong **positive** contribution between 400 – 600 nm (Chappuis bands, Fig. 9f) to the total heating of the lower tropical stratosphere. Solar fluxes in this spectral region **increase** by about 20–40 % from solar minimum to maximum. **On the other hand, SOLID.beta shows an opposite contribution with negative effect below 40 Km.** As described in **Sec. 4**, the reason is that the SOLID.beta variability in this spectral range is **essentially determined** by the SIM observations, which in a similar fashion show the same negative SSI change. **The assimilation of SIM observations after 2008 in SOLID now leads to a positive contribution, much stronger than NRLSSI2 and SATIRE, to balance the almost zero effect between 310–400 nm.** Although, the line-by-line calculations do not take into account solar fluxes in wavelengths above 700 nm, the out-of-phase variability in SOLID.beta and SORCE is expected to introduce negative heating rate anomalies in the lower stratosphere and troposphere, **as highlighted in other studies [Cahalan et al., 2010]. Without taking into account the early part of SORCE/SIM observations, we find with SOLID a considerable positive influence in the heating of the lower stratosphere stemming from the Chappuis bands, where, nevertheless the total heating is negligible. Yet, this strong change in the visible may cause significant changes on the surface climate and should be examined with climate model simulations.**

The heating rate calculations of *Oberländer et al.* [2012] demonstrated a stronger solar cycle signal in the stratosphere for SATIRE-S compared to the first version of the NRL model. The SSI variability in NRLSSI2 still shows the weakest solar cycle signal as the heating rate anomalies at 50 km calculated with libRadtran are about 32% and 45% weaker than for SATIRE-S, SOLID respectively (Fig. 9a). As mentioned above, our interest lies in comparing the direct effects of SSI variability on atmospheric heating between the different SSI data sets, thus we have deliberately neglected the ozone feedback. This of course results to the underestimation of the total (radiative and chemistry) solar forcing effect on atmospheric heating, but allows for a more straightforward comparison, since the ozone response and the relevant combined effects strongly depend on **the relative contribution of wavelengths that photolyze molecular oxygen (<240 nm) and ozone (<310 nm), respectively** [e.g. *Haigh et al.*, 2010; *Swartz et al.*, 2012; *Ball et al.*, 2014]. *Gray et al.* [2009] estimated that the ozone feedback amplifies the direct radiative heating in the stratopause by more than 50% but it is less important in the middle stratosphere. On the other hand, the ozone effect was found dominant in the lower tropical stratosphere, contributing about 70–80% of the total solar cycle heating. **The calculations of Swartz et al. [2012] suggested for even a stronger con-**

tribution of ozone feedback on the total stratospheric heating, which adds up linearly to the direct heating throughout the middle and upper stratosphere. A comprehensive assessment of the combined radiative and chemistry contributions shall be made in a future study using a chemistry-climate model.

8. Conclusion

In this study, we have introduced a novel framework for merging different SSI observations into one single homogeneous and continuous composite dataset. Here we combined observations from 20 instruments into a single composite with daily values from November 8, 1978 to December 31, 2014, running from 0.5 to 1991.5 nm, with most bins having a 1 nm spectral resolution. Three important assets of this composite are: 1) its reliance on uncertainty estimates of the instrumental data, which are derived in an independent way, and are used to weigh their individual contribution to the composite; 2) the estimation of the uncertainty of the composite itself, which is essential for testing it against model reconstructions; and 3) the objectivity and traceability of the method, in the sense that the contribution of each instrument, and at specific time-scales, can be controlled, and adapted if necessary.

The present composite is solely based on original (unadjusted) observations, as we consider this to be a mandatory first step toward more elaborate products that will require additional physical information in order to enhance their scientific value. The list of obvious improvements includes:

- improve the uncertainty estimates of the instrumental records at different time-scales, and in particular at long ones (i.e. stability);
- include model reconstructions to fill data gaps and to complement observations when these suffer from large uncertainties;
- include physical constraints, such as the equality between the spectrally-integrated SSI, and the TSI, which is measured independently;
- additionally, exploit the high coherence of the SSI variability to exclude incoherent instrumental noise and thereby improve its signal-to-noise ratio. **This approach, which has already been explored by Cesateur et al. [2011] can be incorporated as an intermediate step of the composite building, before the records are averaged. Since, however, it entails a decrease of the uncertainty, the latter must be carefully reevaluated.**

We recently applied a similar approach to the TSI [*Dudok de Wit et al.*, 2017] and to the sunspot number. Both have challenges on their own. With the TSI, no contributions from solar proxies are allowed. With sunspot numbers, the absence of absolute scale requires an additional normalization step. Although the maximum likelihood framework, which we are using here,

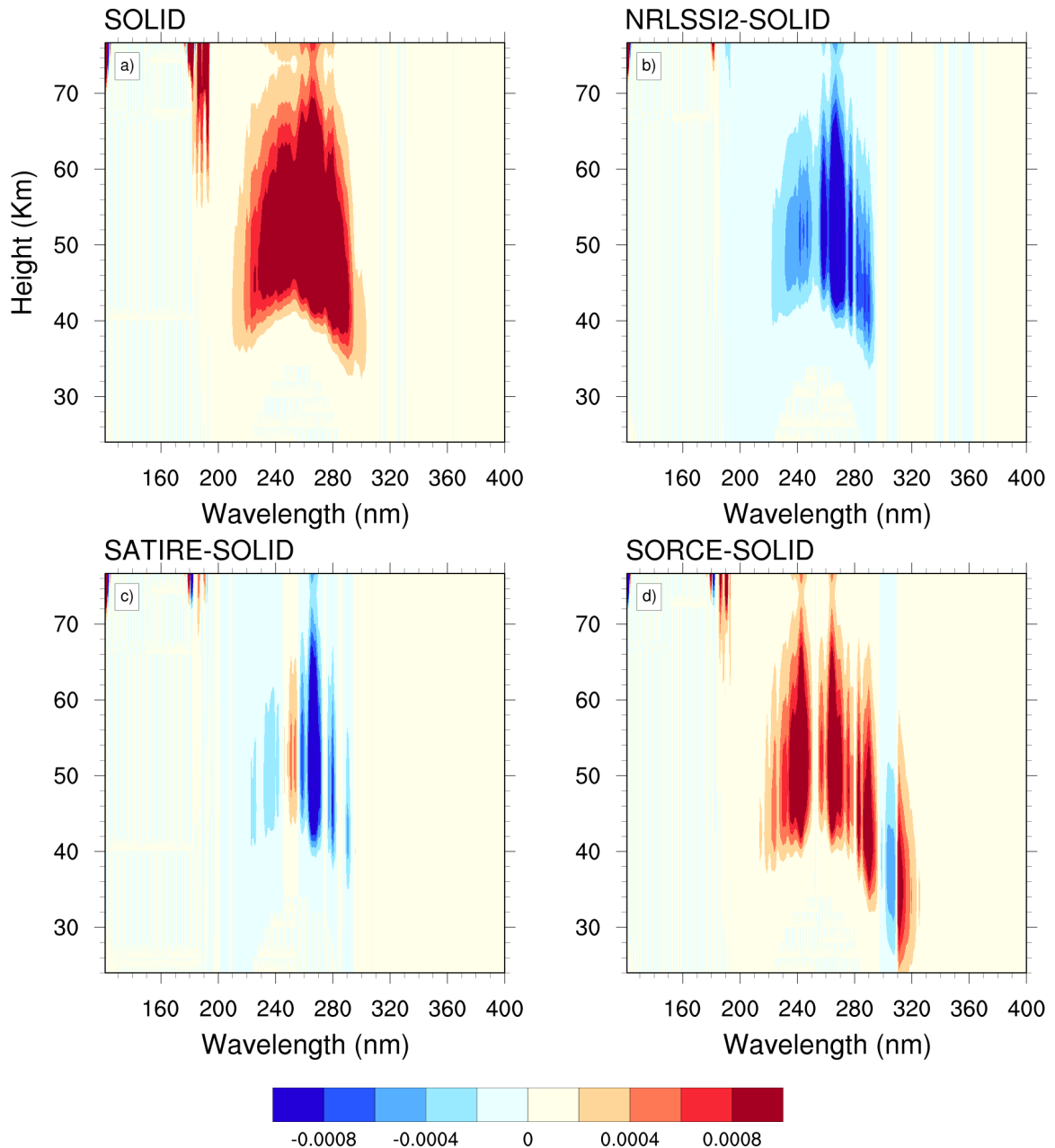


Figure 10. Panel a: Solar spectral heating rate anomalies (K/day/nm) between solar minimum (2008) and maximum (2003) for the **SOLID composite**. The integral gives the total heating anomalies shown in Fig. 9a. Panels b–d: Differences in the solar cycle heating rates (K/day/nm) between SOLID and NRLSSI2, SATIRE-S and SORCE, respectively.

is well suited for such purposes, eventually a Bayesian approach will be required to properly specify the prior information.

In order to understand the role of the Sun as one of the natural forcing mechanisms it is crucial to have a realistic estimate of the solar irradiance variability at hand. With the work presented we are confident we achieved a considerable step closer towards this goal.

Acknowledgments. The authors acknowledge that the research leading to these results has received funding from

the European Community Seventh Framework Programme (FP7 2012) under grant agreement no 313188 (SOLID, <http://projects.pmodwrc.ch/solid>). Moreover, this work was supported by the COST Action ES1005 TOSCA (Towards a more complete assessment of the impact of solar variability on the Earth's climate). This research has made use of NASA's Astrophysics Data System. We gratefully acknowledge all the instrumental teams for making their data freely available.

Notes

1. http://lasp.colorado.edu/lisird/sorce/sorce_ssi/index.html

2. <http://homepages.see.leeds.ac.uk/~earpmf/cmvalrad.shtml>

References

- Austin, J., et al. (2008), Coupled chemistry climate model simulations of the solar cycle in ozone and temperature, *Journal of Geophysical Research-Atmospheres*, *113*(D11), D11,306.
- Bailey, S. M., T. N. Woods, C. A. Barth, S. C. Solomon, L. R. Canfield, and R. Korde (2000), Measurements of the solar soft X-ray irradiance by the Student Nitric Oxide Explorer: First analysis and underflight calibrations, *J. Geophys. Res.*, *105*, 27,179–27,194, doi:10.1029/2000JA000188.
- Ball, W. T., N. A. Krivova, Y. C. Unruh, J. D. Haigh, and S. K. Solanki (2014), A New SATIRE-S Spectral Solar Irradiance Reconstruction for Solar Cycles 21-23 and Its Implications for Stratospheric Ozone*, *Journal of Atmospheric Sciences*, *71*, 4086–4101, doi:10.1175/JAS-D-13-0241.1.
- Ball, W. T., J. D. Haigh, E. V. Rozanov, A. Kuchar, T. Sukhodolov, F. Tummon, A. V. Shapiro, and W. Schmutz (2016), High solar cycle spectral variations inconsistent with stratospheric ozone observations, *Nature Geoscience*, *9*, 206–209, doi:10.1038/ngeo2640.
- Brueckner, G. E., K. L. Edlow, L. E. Floyd, J. L. Lean, and M. E. Vanhoosier (1993), The solar ultraviolet spectral irradiance monitor (SUSIM) experiment on board the Upper Atmosphere Research Satellite (UARS), *J. Geophys. Res.*, *98*, 10,695.
- Cahalan, R. F., G. Wen, J. W. Harder, and P. Pilewskie (2010), Temperature responses to spectral solar variability on decadal time scales, *Geophys. Res. Lett.*, *37*, L07705, doi:10.1029/2009GL041898.
- Cebula, R. P., M. T. DeLand, and E. Hilsenrath (1998), NOAA 11 solar backscattered ultraviolet, model 2 (SBUV/2) instrument solar spectral irradiance measurements in 1989-1994 1. Observations and long-term calibration, *J. Geophys. Res.*, *103*, 16,235–16,250, doi:10.1029/98JD01205.
- Cessateur, G., T. Dudok de Wit, M. Kretschmar, J. Liliensten, and J.-F. Hochedez (2011), Monitoring the Solar UV Irradiance Spectrum from the Observation of a few Passbands, *Astronomy and Astrophysics*, *528*, A68, doi:10.1051/0004-6361/201015903.
- Cessateur, G., et al. (2016), Solar irradiance observations with PREMOS filter radiometers on the PICARD mission: In-flight performance and data release, *Astronomy and Astrophysics*, *588*, A126, doi:10.1051/0004-6361/201527577.
- Coddington, O., J. L. Lean, P. Pilewskie, M. Snow, and D. Lindholm (2016), A Solar Irradiance Climate Data Record, *Bulletin of the American Meteorological Society*, *97*, 1265, doi:10.1175/BAMS-D-14-00265.1.
- DeLand, M. T., and R. P. Cebula (2001), Spectral solar UV irradiance data for cycle 21, *J. Geophys. Res.*, *106*, 21,569–21,584, doi:10.1029/2000JA000436.
- DeLand, M. T., and R. P. Cebula (2008), Creation of a composite solar ultraviolet irradiance data set, *Journal of Geophysical Research (Space Physics)*, *113*, 11,103, doi:10.1029/2008JA013401.
- Deland, M. T., and R. P. Cebula (2012), Solar UV variations during the decline of Cycle 23, *Journal of Atmospheric and Solar-Terrestrial Physics*, *77*, 225–234, doi:10.1016/j.jastp.2012.01.007.
- DeLand, M. T., R. P. Cebula, and E. Hilsenrath (2004), Observations of solar spectral irradiance change during cycle 22 from NOAA-9 Solar Backscattered Ultraviolet Model 2 (SBUV/2), *Journal of Geophysical Research (Atmospheres)*, *109*, D06304, doi:10.1029/2003JD004074.
- Donoho, D. L., and I. M. Johnstone (1995), Adapting to unknown smoothness via wavelet shrinkage, *Journal of the American Statistical Association*, *90*(432), 1200–1224, doi:10.1080/01621459.1995.10476626.
- Dudok de Wit, T. (2011), A method for filling gaps in solar irradiance and solar proxy data, *Astronomy and Astrophysics*, *533*, A29, doi:10.1051/0004-6361/201117024.
- Dudok de Wit, T., S. Bruinsma, and K. Shibasaki (2014), Synoptic radio observations as proxies for upper atmosphere modelling, *Journal of Space Weather and Space Climate*, *4*(26), A06, doi:10.1051/swsc/2014003.
- Dudok de Wit, T., G. Kopp, C. Fröhlich, and M. Schöll (2017), Making a composite out of multiple observations: the new Total Solar Irradiance composite, *Geophys. Res. Lett.*, *accepted*, doi:10.1002/2016GL071866.
- Emde, C., et al. (2016), The libradtran software package for radiative transfer calculations (version 2.0.1), *Geosci. Model Dev.*, *9*(5), 1647–1672, doi:10.5194/gmd-9-1647-2016.
- Eparvier, F. G., D. Crosier, A. R. Jones, W. E. McClintock, M. Snow, and T. N. Woods (2009), The Extreme Ultraviolet Sensor (EUVS) for GOES-R, in *Society of Photo-Optical Instrumentation Engineers (SPIE) Conference Series, Society of Photo-Optical Instrumentation Engineers (SPIE) Conference Series*, vol. 7438, p. 4, doi:10.1117/12.826445.
- Ermolli, I., et al. (2013), Recent variability of the solar spectral irradiance and its impact on climate modelling, *Atmospheric Chemistry & Physics*, *13*, 3945–3977, doi:10.5194/acp-13-3945-2013.
- Evans, J. S., D. J. Strickland, W. K. Woo, D. R. McMullin, S. P. Plunkett, R. A. Viereck, S. M. Hill, T. N. Woods, and F. G. Eparvier (2010), Early Observations by the GOES-13 Solar Extreme Ultraviolet Sensor (EUVS), *Sol. Phys.*, *262*, 71–115, doi:10.1007/s11207-009-9491-x.
- Fontenla, J. M., P. C. Stancil, and E. Landi (2015), Solar Spectral Irradiance, Solar Activity, and the Near-Ultra-Violet, *ApJ*, *809*, 157, doi:10.1088/0004-637X/809/2/157.
- Fröhlich, C., and J. Lean (1998), The Sun's total irradiance: Cycles, trends, and related climate change uncertainties since 1976, *Geophys. Res. Lett.*, *25*, 4377–4380.
- Fröhlich, C., and J. Lean (2004), Solar radiative output and its variability: evidence and mechanisms, *Astron. Astroph. Review*, *12*, 273–320, doi:10.1007/s00159-004-0024-1.
- Fröhlich, C., et al. (1995), VIRGO: Experiment for Helioseismology and Solar Irradiance Monitoring, *Sol. Phys.*, *162*, 101–128, doi:10.1007/BF00733428.
- Gray, L. J., S. T. Rumbold, and K. P. Shine (2009), Stratospheric temperature and radiative forcing response to 11-year solar cycle changes in irradiance and ozone, *Journal of the Atmospheric Sciences*, *66*(8), 2402–2417.
- Gray, L. J., et al. (2010), Solar Influences on Climate, *Reviews of Geophysics*, *48*, RG4001, doi:10.1029/2009RG000282.
- Haigh, J. D. (1994), The role of stratospheric ozone in modulating the solar radiative forcing of climate, *Nature*, *370*(6490), 544–546.
- Haigh, J. D. (2007), The Sun and the Earth's Climate, *Living Reviews in Solar Physics*, *4*, doi:10.12942/lrsp-2007-2.
- Haigh, J. D., A. R. Winning, R. Toumi, and J. W. Harder (2010), An influence of solar spectral variations on radiative forcing of climate, *Nature*, *467*, 696–699, doi:10.1038/nature09426.
- Harrison, R. A., et al. (1995), The Coronal Diagnostic Spectrometer for the Solar and Heliospheric Observatory, *Solar Physics*, *162*, 233–290, doi:10.1007/BF00733431.
- Hood, L., et al. (2015), Solar signals in cmip-5 simulations: The ozone response, *Quarterly Journal of the Royal Meteorological Society*, *141*, 26702689.
- Kopp, G., and J. L. Lean (2011), A new, lower value of total solar irradiance: Evidence and climate significance, *Geophys. Res. Lett.*, *38*, L01706, doi:10.1029/2010GL045777.
- Lean, J. (2000), Evolution of the Sun's Spectral Irradiance Since the Maunder Minimum, *Geophys. Res. Lett.*, *27*, 2425–2428, doi:10.1029/2000GL000043.
- Lean, J. L., and M. T. DeLand (2012), How Does the Sun's Spectrum Vary?, *Journal of Climate*, *25*, 2555–2560, doi:10.1175/JCLI-D-11-00571.1.
- Matthes, K., Y. Kuroda, K. Kodera, and U. Langematz (2006), Transfer of the solar signal from the stratosphere to the troposphere: Northern winter, *Journal of Geophysical Research-Atmospheres*, *111*(D6), D06,108, doi:10.1029/2005JD006283.
- Meehl, G. A., J. M. Arblaster, K. Matthes, F. Sassi, and H. van Loon (2009), Amplifying the pacific climate system response to a small 11-year solar cycle forcing, *Science*, *325*(5944), 1114–1118, doi:10.1126/science.1172872.
- Merkel, A. W., J. W. Harder, D. R. Marsh, A. K. Smith, J. M. Fontenla, and T. N. Woods (2011), The impact of solar spectral irradiance variability on middle atmospheric ozone, *Geophys. Res. Lett.*, *38*, L13802, doi:10.1029/2011GL047561.
- Misios, S., et al. (2015), Solar signals in cmip-5 simulations: Effects of atmosphere ocean coupling, *Quarterly Journal of the Royal Meteorological Society*.

- Mitchell, D., et al. (2015), Solar signals in cmip-5 simulations: The stratospheric pathway, *Quarterly Journal of the Royal Meteorological Society*, *141*, 2390–2403.
- Oberländer, S., et al. (2012), The influence of spectral solar irradiance data on stratospheric heating rates during the 11 year solar cycle, *Geophysical Research Letters*, *39*(1), L01,801, doi:10.1029/2011gl049539.
- Rottman, G. (2005), The SORCE Mission, *Sol. Phys.*, *230*, 7–25, doi:10.1007/s11207-005-8112-6.
- Rottman, G., J. Harder, J. Fontenla, T. Woods, O. R. White, and G. M. Lawrence (2005), The Spectral Irradiance Monitor (SIM): Early Observations, *Sol. Phys.*, *230*, 205–224, doi:10.1007/s11207-005-1530-7.
- Rottman, G. J., C. A. Barth, R. J. Thomas, G. H. Mount, G. M. Lawrence, D. W. Rusch, R. W. Sanders, G. E. Thomas, and J. London (1982), Solar spectral irradiance, 120 to 190 nm, October 13, 1981 - January 3, 1982, *Geophys. Res. Lett.*, *9*, 587–590, doi:10.1029/GL009i005p00587.
- Rottman, G. J., T. N. Woods, and T. P. Sparn (1993), Solar-Stellar Irradiance Comparison Experiment 1. I - Instrument design and operation, *J. Geophys. Res.*, *98*, 10,667, doi:10.1029/93JD00462.
- Schmidtke, G., B. Nikutowski, C. Jacobi, R. Brunner, C. Erhardt, S. Knecht, J. Scherle, and J. Schlagenhauf (2014), Solar EUV Irradiance Measurements by the Auto-Calibrating EUV Spectrometers (SolACES) Aboard the International Space Station (ISS), *Sol. Phys.*, *289*, 1863–1883, doi:10.1007/s11207-013-0430-5.
- Schmutz, W., et al. (2009), The PREMOS/PICARD instrument calibration, *Metrologia*, *46*, 202–206, doi:10.1088/0026-1394/46/4/S13.
- Schöll, M., T. Dudok de Wit, M. Kretzschmar, and M. Haberreiter (2016), Making of a solar spectral irradiance dataset I: observations, uncertainties, and methods, *Journal of Space Weather and Space Climate*, *6*(27), A14, doi:10.1051/swsc/2016007.
- Skupin, J., M. Weber, S. Noël, H. Bovensmann, and J. P. Burrows (2005), GOME and SCIAMACHY solar measurements: Solar spectral irradiance and Mg II solar activity proxy indicator, *Mem. Soc. Astron. Italiana*, *76*, 1038.
- Solanki, S. K., N. A. Krivova, and J. D. Haigh (2013), Solar Irradiance Variability and Climate, *ARA&A*, *51*, 311–351, doi:10.1146/annurev-astro-082812-141007.
- Starck, J.-L., F. Murtagh, and J. M. Fadili (2010), *Sparse image and signal processing: wavelets, curvelets, morphological diversity*, Cambridge University Press, Cambridge.
- Stocker, T., and D. Qin (Eds.) (2014), *Climate Change 2013 - The Physical Science Basis. Working Group I Contribution to the Fifth Assessment Report of the IPCC.*, Cambridge University Press, Cambridge.
- Swartz, W. H., R. S. Stolarski, L. D. Oman, E. L. Fleming, and C. H. Jackman (2012), Middle atmosphere response to different descriptions of the 11-yr solar cycle in spectral irradiance in a chemistry-climate model, *Atmospheric Chemistry & Physics*, *12*, 5937–5948, doi:10.5194/acp-12-5937-2012.
- Thuillier, G., L. Floyd, T. N. Woods, R. Cebula, E. Hilsenrath, M. Hersé, and D. Labs (2004), Solar irradiance reference spectra for two solar active levels, *Advances in Space Research*, *34*, 256–261, doi:10.1016/j.asr.2002.12.004.
- Thuillier, G., S. Dewitte, W. Schmutz, and Picard Team (2006), Simultaneous measurement of the total solar irradiance and solar diameter by the PICARD mission, *Advances in Space Research*, *38*, 1792–1806, doi:10.1016/j.asr.2006.04.034.
- Viereck, R., L. Puga, D. McMullin, D. Judge, M. Weber, and W. K. Tobiska (2001), The Mg II index: A proxy for solar EUV, *Geophysical Research Letters*, *28*, 1343–1346, doi:10.1029/2000GL012551.
- Wehrli, C., W. Schmutz, and A. I. Shapiro (2013), Correlation of spectral solar irradiance with solar activity as measured by VIRGO, *A&A*, *556*, L3, doi:10.1051/0004-6361/201220864.
- Wieman, S. R., L. V. Didkovsky, and D. L. Judge (2014), Resolving Differences in Absolute Irradiance Measurements Between the SOHO/CELIAS/SEM and the SDO/EVE, *Solar Physics*, *289*, 2907–2925, doi:10.1007/s11207-014-0519-5.
- Wilson, R. M., and D. H. Hathaway (2006), On the Relation Between Sunspot Area and Sunspot Number, *NASA STI/Recon Technical Report N*, *6*, 20,186.
- Woods, T. N., and G. Rottman (2005), XUV Photometer System (XPS): Solar Variations during the SORCE Mission, *Sol. Phys.*, *230*, 375–387, doi:10.1007/s11207-005-2555-7.
- Woods, T. N., G. J. Rottman, R. G. Roble, O. R. White, S. C. Solomon, G. M. Lawrence, J. Lean, and W. K. Tobiska (1994), Thermosphere-Ionsphere-Mesosphere Energetics and Dynamics (TIMED) Solar EUV Experiment, in *Optical Spectroscopic Techniques and Instrumentation for Atmospheric and Space Research, Society of Photo-Optical Instrumentation Engineers (SPIE) Conference Series*, vol. 2266, edited by J. Wang and P. B. Hays, pp. 467–478.
- Woods, T. N., E. M. Rodgers, S. M. Bailey, F. G. Eparvier, and G. J. Ucker (1999), TIMED solar EUV experiment: preflight calibration results for the XUV photometer system, in *Optical Spectroscopic Techniques and Instrumentation for Atmospheric and Space Research III, Society of Photo-Optical Instrumentation Engineers (SPIE) Conference Series*, vol. 3756, edited by A. M. Larar, pp. 255–264.
- Woods, T. N., W. K. Tobiska, G. J. Rottman, and J. R. Worden (2000), Improved solar Lyman α irradiance modeling from 1947 through 1999 based on UARS observations, *J. Geophys. Res.*, *105*, 27,195–27,216, doi:10.1029/2000JA000051.
- Woods, T. N., et al. (2012), Extreme Ultraviolet Variability Experiment (EVE) on the Solar Dynamics Observatory (SDO): Overview of Science Objectives, Instrument Design, Data Products, and Model Developments, *Solar Physics*, *275*, 115–143, doi:10.1007/s11207-009-9487-6.
- Yeo, K. L., N. A. Krivova, S. K. Solanki, and K. H. Glassmeier (2014), Reconstruction of total and spectral solar irradiance from 1974 to 2013 based on KPVT, SoHO/MDI, and SDO/HMI observations, *A&A*, *570*, A85, doi:10.1051/0004-6361/201423628.